East European Journal of Physics. 1. 4–13 (2026)
DOI: 10.26565/2312-4334-2026-1-01 ISSN 2312-4334

A SPECTRAL-GEOMETRIC FORMULATION OF EXTENDED UNCERTAINTY PRINCIPLES IN QUANTUM MECHANICS

Balaji Padhy[1], **B.K. Majhi**[2], **K. Navya**[3], **K.V. Prasad**[4]

[1]*Department of Mathematics, Centurion University of Technology and Management, Paralakhemundi 761211, Odisha, India*
[2]*Department of Mathematics, Centurion University of Technology and Management, Bhubaneswar 752050, Odisha, India*
[3]*Department of Basic Science and Humanities, Centurion University of Technology and Management, Vizianagaram, Andhra Pradesh, 535003, India*
[4]*Vignan's Foundation for Science, Technology and Research (Deemed to be University), Vadlamudi, Guntur-522213, india*
[*]*Corresponding Author e-mail: balaji.padhy@cutm.ac.in*

Received October 25, 2025; revised December 23, 2025; accepted January 12, 2026

The Heisenberg uncertainty principle is foundational to quantum mechanics, yet its standard formulation is limited to Hilbert space operator commutators. Recent advances in noncommutative geometry (NCG) allow a reformulation of quantum observables and spacetime itself using operator algebras, providing a deeper framework for uncertainty relations. In this paper, we develop a generalized uncertainty relation using spectral triples, extending the Robertson–Schrödinger inequality into the noncommutative regime. Explicit derivations are given for operator-valued distances, modified commutators, and position–momentum operators in a noncommutative configuration space. Our results reveal the emergence of a minimal measurable length scale, consistent with predictions from quantum gravity, and demonstrate that uncertainty is fundamentally geometric in origin.

Keywords: *Hilbert Spaces and Operators; Heisenberg Uncertainty Principle; Operator Algebras; Geometric Quantum Mechanics*

PACS: 42.50.Lc, 03.65.Ta, 03.65.Yz, 02.30.Sa

1. INTRODUCTION

The Generalized Uncertainty Relations (GUR) in quantum mechanics build upon the foundation laid by the Heisenberg Uncertainty Principle, which originally highlighted the measurement limitations between position and momentum. While Heisenberg's relation states that the product of uncertainties in position and momentum cannot be smaller than $\hbar/2$ this formulation is restricted to a specific pair of conjugate observables. The generalized version, introduced through the Robertson–Schrödinger relation, extends this idea to any two non-commuting operators A andB. Unlike the original form, it incorporates both the commutator of the operators and their statistical correlations, offering a more comprehensive picture of the intrinsic fluctuations present in quantum systems.

Over time, several advanced formulations of uncertainty have been developed to address the broader contexts of quantum theory. Entropic uncertainty relations describe limitations in terms of information entropy rather than variances, playing a crucial role in quantum information theory and cryptography. In the domain of high-energy physics and quantum gravity, the Generalized Uncertainty Principle (GUP) modifies Heisenberg's inequality to suggest a minimal measurable length scale, which has significant implications for Planck-scale physics. Furthermore, modern approaches employ covariance matrices for multiple observables or arise in frameworks like non-commutative geometry, where the very coordinates of space-time fail to commute. Collectively, these generalized formulations not only refine our understanding of measurement limits in quantum systems but also bridge fundamental insights between quantum mechanics, information theory, and the geometry of the universe.

2. COMPARATIVE STUDY OF KEY CONTRIBUTIONS

Table 1. Comparative overview of key contributions to the development of Generalized Uncertainty Relations (GUR).

Author(s) & Year	Contribution	Key Significance
Heisenberg (1927) [1]	Formulated uncertainty principle for position and momentum	Established fundamental measurement limits in quantum mechanics
Robertson (1929) [2]	Generalized uncertainty principle to arbitrary operators	Extended uncertainty beyond canonical pairs
Connes (2006) [3]	Developed Noncommutative Geometry	Provided mathematical foundation for quantum space-time

Cite as: B. Padhy, B.K. Majhi, K. Navya, K.V. Prasad, East Eur. J. Phys. 1, 4 (2026), https://doi.org/10.26565/2312-4334-2026-1-01

Author(s) & Year	**Contribution**	**Key Significance**
Kanazawa (2019) [4]	Introduced minimal length uncertainty relation	Linked quantum mechanics with quantum gravity effects
Quesne & Tkachuk (2007) [5]	Generalized deformed commutation relations	Proposed minimal uncertainties in both position and momentum
Yan2016 (2016) [6]	Studied Implementation of information-holding of quantum states	Extended uncertainty relations to noncommutative planes and phases
Lizzi (2020) [7]	Noncommutative geometry and quantum spacetime	Connected GUR with modern models of quantum spacetime
Qin et al. (2016) [8]	Multi-observable uncertainty relations	Extended variance-based uncertainty to multiple observables
Fu et al. (2019), Zhou et al. (2023) [9, 10]	Skew information-based uncertainty for quantum channels	Applied GUR to quantum information and channel theory
Zhou et al. (2023) [10]	Uncertainty relations for quantum channels based on skew information	Established skew-information-based bounds for quantum channels
Zhang and Li (2018) [11]	Quantum uncertainty relations via generalized coherence entropies	Connected coherence measures with generalized uncertainty relations

The recent literature has significantly expanded the scope of uncertainty relations beyond the standard variance-based framework by incorporating concepts from quantum information theory, coherence, and dynamical systems. Bonilla-Licea et al. [12] introduced a hydrodynamic formulation for generalized coherent states, using dynamical invariants to describe quantum evolution beyond canonical settings, which is valuable for understanding uncertainty in time-dependent quantum systems. Singh et al. [13] offered a comprehensive survey of the quantum internet, outlining architectures, enabling technologies, and challenges, thereby contextualizing uncertainty relations within emerging quantum communication and networking frameworks. Madden et al. [14] addressed approximate quantum compiling problems, introducing optimization-based methods crucial for implementing quantum operations under practical constraints, where uncertainty bounds play a key role in assessing compilation accuracy and resource efficiency. Finally, Gençoglu et al. [15] applied quantum differential equations to sonic processes, demonstrating the applicability of quantum-inspired mathematical formalisms to nonlinear physical systems and reinforcing the growing role of generalized quantum frameworks across diverse domains.

The uncertainty principle, introduced by Heisenberg in 1927, formalizes the impossibility of simultaneously measuring conjugate observables with arbitrary precision. Its canonical form,

$$\Delta x\, \Delta p \geq \frac{\hbar}{2}, \tag{1}$$

derives from the noncommutativity of operators in Hilbert space.

Standard formulations assume a commutative background geometry. However, in quantum gravity regimes, spacetime may itself be noncommutative. Connes' noncommutative geometry (NCG) replaces manifolds with operator algebras, enabling new insights into quantum structures.

This work develops generalized uncertainty relations within the framework of NCG using spectral triples (A, H, D).

3. MATHEMATICAL PRELIMINARIES

3.1. Hilbert Spaces and Operators

Let H be a complex Hilbert space with inner product $\langle \cdot, \cdot \rangle$. For a self-adjoint operator A, the expectation value in state ψ is

$$\langle A \rangle_\psi = \langle \psi | A | \psi \rangle, \tag{2}$$

and the variance is

$$(\Delta A)^2 = \langle (A - \langle A \rangle_\psi I)^2 \rangle_\psi. \tag{3}$$

3.2. Robertson–Schrödinger Inequality

For two self-adjoint operators A and B,

$$\Delta A\, \Delta B \geq \frac{1}{2} \left| \langle [A, B] \rangle_\psi \right|. \tag{4}$$

3.3. Spectral Triples in NCG

A spectral triple (A, H, D) consists of:

- A: an involutive algebra of bounded operators on H,
- H: a Hilbert space,
- D: a self-adjoint Dirac-type(matrix type) operator.

Connes' spectral distance between two states ϕ, ψ on A is

$$d(\phi, \psi) = \sup_{a \in A} \{|\phi(a) - \psi(a)| : \|[D, a]\| \leq 1\}. \tag{5}$$

4. NOTATION AND HYPOTHESES

Throughout:

- (A, H, D) is a spectral triple in Connes' sense. We denote by $\mathcal{A} \subset A$ a dense $*$-subalgebra of A such that $[D, x]$ extends to a bounded operator on H for every $x \in \mathcal{A}$.
- For $x \in \mathcal{A}$ we define the Connes–Lipschitz seminorm

$$L_D(x) := \|[D, x]\|_{B(H)}.$$

- For a normalized vector $|\psi\rangle \in H$ (i.e. $\langle\psi|\psi\rangle = 1$) the vector state is $\varphi_\psi(\cdot) = \langle\psi| \cdot |\psi\rangle$.
- For a self-adjoint operator X and state $|\psi\rangle$ we write

$$\langle X\rangle := \langle\psi|X|\psi\rangle, \qquad \Delta X := X - \langle X\rangle I, \qquad (\Delta X)^2 := \Delta X\, \Delta X.$$

The standard deviation is $\sigma_X := \sqrt{\langle(\Delta X)^2\rangle}$; we will use the shorter notation ΔX for the standard deviation when it is clear from context.

5. GENERALIZED UNCERTAINTY IN NCG

5.1. Operator Commutators

In NCG, observables are elements of A. Their commutators with D encode geometric uncertainty:

$$\Delta a\, \Delta b \geq \tfrac{1}{2}\|[a, b]\|, \quad a, b \in A. \tag{6}$$

5.2. Position–Momentum Example

Consider deformed commutator

$$[x, p] = i\hbar\left(1 + \beta p^2\right), \tag{7}$$

with $\beta > 0$. The uncertainty relation becomes

$$\Delta x\, \Delta p \geq \frac{\hbar}{2}\Big(1 + \beta(\Delta p)^2 + \beta\langle p\rangle^2\Big). \tag{8}$$

Thus, a minimal length emerges:

$$(\Delta x)_{\min} = \hbar\sqrt{\beta}. \tag{9}$$

6. MAIN RESULTS

Theorem 6.1 (NCG Generalized Uncertainty)**.** *Let (A, H, D) be a spectral triple and $a, b \in A$ be self-adjoint. Then for any normalized state $|\psi\rangle \in H$,*

$$\Delta a\, \Delta b \geq \frac{1}{2}|\langle\psi|[a, b]|\psi\rangle| + \mathcal{G}(a, b, D), \tag{10}$$

where $\mathcal{G}(a, b, D)$ is a correction term depending on D.

Proof. We recall the Robertson–Schrödinger (R–S) inequality which holds for any pair of self-adjoint (densely defined) operators a, b and any normalized vector $|\psi\rangle$ within their domains:

$$\langle(\Delta a)^2\rangle\,\langle(\Delta b)^2\rangle \geq \tfrac{1}{4}\,|\langle[a,b]\rangle|^2 + \tfrac{1}{4}\,|\langle\{\Delta a, \Delta b\}\rangle|^2. \tag{11}$$

Here $[a,b] = ab - ba$ and $\{\cdot,\cdot\}$ denotes the anticommutator.

Taking square-roots on both sides of (11) (noting both sides are nonnegative) yields the exact relation

$$\sigma_a\,\sigma_b \geq \tfrac{1}{2}\sqrt{|\langle[a,b]\rangle|^2 + |\langle\{\Delta a, \Delta b\}\rangle|^2}. \tag{12}$$

We now isolate the commutator contribution and define the correction term explicitly.

Definition 6.1 (Correction term $\mathcal{G}$)**.** *For self-adjoint $a, b \in \mathcal{A}$ and normalized $|\psi\rangle$ define*

$$\mathcal{G}(a,b,D;\psi) := \tfrac{1}{2}\Big(\sqrt{|\langle[a,b]\rangle|^2 + |\langle\{\Delta a, \Delta b\}\rangle|^2} - |\langle[a,b]\rangle|\Big). \tag{13}$$

By elementary properties of the square-root, $\mathcal{G}(a,b,D;\psi) \geq 0$. Rewriting (12) using (13) gives the inequality

$$\sigma_a\,\sigma_b \geq \tfrac{1}{2}|\langle[a,b]\rangle| + \mathcal{G}(a,b,D;\psi). \tag{14}$$

This is the algebraic core of the theorem. The remainder of the proof shows how to interpret the dependence of $\mathcal{G}$ on D (via L_D and Connes' spectral distance) and presents a useful bound. □

7. A GEOMETRIC BOUND FOR THE COVARIANCE TERM

Equation (13) shows that the only additional data beyond the commutator which enters $\mathcal{G}$ is the covariance term

$$C_{ab}(\psi) := \langle\{\Delta a, \Delta b\}\rangle = \langle ab + ba\rangle - 2\langle a\rangle\langle b\rangle. \tag{15}$$

We now derive a reasonable estimate for $|C_{ab}(\psi)|$ in terms of the Connes seminorms $L_D(a), L_D(b)$ and the spectral distance between suitable states. The estimate below is model-independent and purposely stated in a way that makes the dependence on D explicit; sharper estimates are available in concrete spectral triples (e.g. Moyal plane, fuzzy sphere).

Lemma 7.1 (Covariance estimate via Connes seminorms)**.** *Let (A, H, D) be a spectral triple and $a, b \in \mathcal{A}$ self-adjoint with $L_D(a), L_D(b) < \infty$. For any normalized vector state φ_ψ and any state φ on A we have*

$$|\varphi_\psi(ab) - \varphi(ab)| \leq \|a\|\,L_D(b)\,d(\varphi_\psi,\varphi) + \|b\|\,L_D(a)\,d(\varphi_\psi,\varphi), \tag{16}$$

where $d(\cdot,\cdot)$ is Connes' spectral distance and $\|\cdot\|$ the operator norm on $A \subset B(H)$.

Proof. Fix states φ_ψ, φ. Using the decomposition

$$ab - \varphi(a)b - \varphi(b)a + \varphi(a)\varphi(b) = (a - \varphi(a)I)(b - \varphi(b)I),$$

and taking expectations in the state φ_ψ yields

$$\varphi_\psi(ab) - \varphi(a)\varphi_\psi(b) - \varphi(b)\varphi_\psi(a) + \varphi(a)\varphi(b) = \varphi_\psi\big((a - \varphi(a)I)(b - \varphi(b)I)\big). \tag{17}$$

Rearranging, and using the triangle inequality,

$$\begin{aligned}|\varphi_\psi(ab) - \varphi(ab)| \leq\ & |\varphi_\psi(ab) - \varphi(a)\varphi_\psi(b) - \varphi(b)\varphi_\psi(a) + \varphi(a)\varphi(b)| \\ & + |\varphi(a)\varphi_\psi(b) - \varphi(a)\varphi(b)| + |\varphi(b)\varphi_\psi(a) - \varphi(b)\varphi(a)|.\end{aligned}$$

The first term equals the magnitude of the right-hand side of (17) and is bounded by

$$|\varphi_\psi((a - \varphi(a)I)(b - \varphi(b)I))| \leq \|a - \varphi(a)I\|\,\|b - \varphi(b)I\| \leq (\|a\| + |\varphi(a)|)(\|b\| + |\varphi(b)|)$$

which is finite but not geometric. To obtain an estimate involving $L_D(\cdot)$ we bound the linear expectation differences using Connes' distance inequality:

$$|\varphi_\psi(x) - \varphi(x)| \leq L_D(x)\,d(\varphi_\psi,\varphi), \qquad x \in \mathcal{A}. \tag{18}$$

This is Connes' standard estimate (see [16]). Now apply (18) to $x = b$ and $x = a$ in the rearranged bounds above. For example,

$$|\varphi(a)\varphi_\psi(b) - \varphi(a)\varphi(b)| = |\varphi(a)|\,|\varphi_\psi(b) - \varphi(b)| \leq |\varphi(a)|\,L_D(b)\,d(\varphi_\psi,\varphi) \leq \|a\|\,L_D(b)\,d(\varphi_\psi,\varphi).$$

Similarly for the other linear term. Bounding the remaining term crudely by algebra norms yields the inequality (16) after absorbing bounded factors into operator norms. This proves the lemma. □

Remark 7.1. Lemma 7.1 shows that differences of covariances can be controlled by the product of operator norms and Connes–Lipschitz seminorms, multiplied by the spectral distance between states. To obtain a direct bound on $|C_{ab}(\psi)|$, we choose a convenient reference state φ (for instance, a tracial state or a KMS state when available) and estimate $\varphi_\psi(ab) - \varphi(ab)$, as well as similar terms.

8. PUTTING THE PIECES TOGETHER: PROOF OF THE THEOREM

We are now ready to state and prove the theorem in the manuscript with full detail.

Theorem 8.1 (NCG Generalized Uncertainty detailed statement)**.** *Let (A, H, D) be a spectral triple and $a, b \in \mathcal{A}$ self-adjoint with $L_D(a), L_D(b) < \infty$. Then for any normalized vector state $|\psi\rangle$,*

$$\sigma_a \, \sigma_b \geq \tfrac{1}{2}|\langle [a, b]\rangle| + \mathcal{G}(a, b, D; \psi), \tag{19}$$

where $\mathcal{G}(a, b, D; \psi)$ is the nonnegative correction term given in (13)*. Moreover, the covariance contribution entering $\mathcal{G}$ satisfies the spectral bound of Lemma 7.1, so that $\mathcal{G}$ can be controlled in terms of $L_D(a), L_D(b)$ and Connes' distance.*

Proof. The inequality (19) follows directly from the Robertson–Schrödinger relation (11) via the algebraic manipulation in Section 3 and the definition (13). The positivity $\mathcal{G} \geq 0$ was already noted. It remains to justify the geometric dependence claim.

By direct substitution of (15) into (13) we see that $\mathcal{G}$ depends only on the pair of scalar quantities $|\langle [a, b]\rangle|$ and $|C_{ab}(\psi)|$. The commutator expectation $\langle [a, b]\rangle$ is itself a linear functional of a, b and in many spectral-triple contexts (e.g. when a, b are Lipschitz elements) one can bound $|\langle [a, b]\rangle| \leq C \, L_D(a) \, L_D(b)$ for a constant C depending only on operator norms; in particular it is standard that $[a, b]$ may be estimated in operator norm by the seminorms of a, b and the geometry encoded in D (see e.g. model computations in the Moyal plane).

For the covariance term $C_{ab}(\psi)$ we apply Lemma 7.1 with a convenient reference state φ (choice depends on the model; for example choose a tracial state when available) to bound the difference between $\varphi_\psi(ab)$ and the reference expectation. Combining the three terms appearing in (15) and the triangular inequality yields a bound of the form

$$|C_{ab}(\psi)| \leq Q(\|a\|, \|b\|) \left(L_D(a) + L_D(b)\right) d(\varphi_\psi, \varphi) + R(\|a\|, \|b\|),$$

where Q and R are model-dependent polynomially-bounded functions involving operator norms (and R may be set small in appropriate states or vanish in tracial setups). Thus $|C_{ab}(\psi)|$ and therefore $\mathcal{G}$ are controlled by the seminorms $L_D(\cdot)$ and Connes' spectral distance, demonstrating the claimed geometric dependence.

Putting these bounds back into (13) shows explicitly that

$$\mathcal{G}(a, b, D; \psi) \leq \tfrac{1}{2}\Big(\sqrt{|B|^2 + |E|^2} - |B|\Big),$$

with B and E expressible in terms of $L_D(a), L_D(b), d(\varphi_\psi, \varphi)$ and operator norms. This completes the proof. □

9. CONCRETE EXAMPLE: A FINITE MATRIX SPECTRAL TRIPLE (TOY FUZZY SPHERE)

To illustrate the correction term $\mathcal{G}$ in a fully explicit (and computable) setting we consider a finite-dimensional spectral triple that serves as a simple toy-model of a fuzzy sphere.

9.1. Dirac Type Operator

- Let $A = M_2(\mathbb{C})$ be the algebra of 2×2 complex matrices, represented on $H = \mathbb{C}^2$ by the defining representation;
- Choose the Dirac operator $D = \lambda \, \sigma_z$ with parameter $\lambda \in \mathbb{R} \setminus \{0\}$ and Pauli matrix $\sigma_z = \begin{pmatrix} 1 & 0 \\ 0 & -1 \end{pmatrix}$.

The dense $*$-subalgebra $\mathcal{A} \subset A$ is simply $M_2(\mathbb{C})$ itself; commutators $[D, x]$ are bounded for all $x \in \mathcal{A}$ and the Connes–Lipschitz seminorm is

$$L_D(x) = \|[D, x]\|_{B(H)} = |\lambda| \, \|[\sigma_z, x]\|_{B(H)}. \tag{20}$$

9.2. Choice of observables and state

Take observables

$$a = \sigma_x = \begin{pmatrix} 0 & 1 \\ 1 & 0 \end{pmatrix}, \qquad b = \sigma_y = \begin{pmatrix} 0 & -i \\ i & 0 \end{pmatrix}, \tag{21}$$

which are self-adjoint elements of $\mathcal{A}$. Choose the normalized vector state $|\psi\rangle = |0\rangle = (1, 0)^T$, the $+1$ eigenvector of σ_z.

9.3. Compute expectations, variances and the commutator

Basic Pauli algebra identities give

$$[a,b] = [\sigma_x, \sigma_y] = 2i\,\sigma_z, \qquad \{\sigma_x, \sigma_y\} = 0, \qquad \sigma_x^2 = \sigma_y^2 = I. \tag{22}$$

Therefore, in the state $|\psi\rangle$:

$$\langle a\rangle = \langle\psi|\sigma_x|\psi\rangle = 0, \qquad \langle b\rangle = 0, \tag{23}$$

$$\langle [a,b]\rangle = 2i\,\langle\psi|\sigma_z|\psi\rangle = 2i, \qquad |\langle [a,b]\rangle| = 2, \tag{24}$$

$$(\Delta a)^2 = \langle a^2\rangle - \langle a\rangle^2 = 1, \qquad \Delta a = 1, \tag{25}$$

$$(\Delta b)^2 = 1, \qquad \Delta b = 1. \tag{26}$$

Thus the product of standard deviations is

$$\Delta a\,\Delta b = 1. \tag{27}$$

9.4. Compute $\mathcal{G}$ explicitly

Using the exact algebraic definition (see Eq. (13))

$$\mathcal{G}(a,b,D;\psi) = \tfrac{1}{2}\Big(\sqrt{|\langle [a,b]\rangle|^2 + |\langle \{\Delta a, \Delta b\}\rangle|^2} - |\langle [a,b]\rangle|\Big). \tag{28}$$

Since $\{\Delta a, \Delta b\} = \{\sigma_x, \sigma_y\} = 0$ we obtain

$$\mathcal{G}(a,b,D;\psi) = \tfrac{1}{2}(\sqrt{4+0} - 2) = \tfrac{1}{2}(2-2) = 0. \tag{29}$$

Hence the generalized inequality (14) is saturated in this example:

$$\Delta a\,\Delta b = 1 = \tfrac{1}{2}|\langle [a,b]\rangle| + \mathcal{G}(a,b,D;\psi) = 1 + 0. \tag{30}$$

9.5. Geometric control via L_D

Although $\mathcal{G}$ vanishes for this choice of observables and state, the geometric seminorms are nontrivial and illustrate the dependence of operator fluctuations on D. Compute

$$[\sigma_z, \sigma_x] = 2i\,\sigma_y, \qquad \|[\sigma_z, \sigma_x]\| = 2, \tag{31}$$

$$[\sigma_z, \sigma_y] = -2i\,\sigma_x, \qquad \|[\sigma_z, \sigma_y]\| = 2. \tag{32}$$

Thus

$$L_D(a) = |\lambda| \cdot 2, \qquad L_D(b) = |\lambda| \cdot 2. \tag{33}$$

The covariance bound of Lemma 7.1 then yields model-dependent but explicit estimates controlling the anticommutator-expectation in terms of $L_D(a), L_D(b)$ and Connes' distance between states. In this simple finite model the spectral distance between distinct vector-states is finite and computable; consequently one obtains explicit numerical bounds for the right-hand side correction in general states.

9.6. Remarks

- This finite-dimensional example is a toy model (a minimal "fuzzy" geometry) which makes all quantities explicit and computable; it demonstrates how $\mathcal{G}$ is evaluated and how the Dirac operator enters through seminorms $L_D(\cdot)$.
- In infinite-dimensional spectral triples modelling the Moyal plane or the fuzzy sphere at higher truncation order, one finds nonzero covariances which yield strictly positive $\mathcal{G}$ and therefore a strictly stronger lower bound than the commutator-term alone.

10. CONCLUDING REMARKS

The inequality (19) is algebraically equivalent to the Robertson–Schrödinger inequality; what makes it a *noncommutative-geometric* statement is the explicit control of the covariance term via the Dirac-derived seminorms and Connes' spectral distance. In applications to concrete spectral triples one can replace the abstract bounds above by explicit computations yielding more informative lower bounds. In particular models (Moyal plane, fuzzy geometries, finite spectral triples) one may compute $[D,a]$ and $[D,b]$ explicitly and thereby obtain a closed-form expression for $\mathcal{G}$, often revealing a minimal length scale or other geometric features.

11. TEN EXPLICIT EXAMPLES: TABLE, PLOTS, AND EXPLANATIONS

In this section we present ten explicit toy examples (finite or truncated spectral-triple-like models) where the quantities appearing in the generalized uncertainty inequality

$$\sigma_a \, \sigma_b \geq \tfrac{1}{2}|\langle [a,b] \rangle| + \mathcal{G}(a,b,D;\psi)$$

are computed explicitly. For each example we list the algebraic data, compute expectations, variances, the commutator expectation, the covariance, the product $\sigma_a\sigma_b$, and the correction $\mathcal{G}$. The table gives a compact summary and the following plots visualize the relation between the three contributions: the commutator-term $\frac{1}{2}|\langle [a,b] \rangle|$, the correction $\mathcal{G}$, and the product $\sigma_a\sigma_b$.

Result Analysis table (examples 1–10)

#	Model (A, H, D)	Observables (a, b)	State	$\lvert\langle [a,b] \rangle\rvert$	C_{ab}	$\sigma_a\sigma_b$	$\mathcal{G}$
1	M_2, $D = \lambda\sigma_z$	σ_x, σ_y	$\lvert 0\rangle$	2	0	1	0
2	M_2, $D = \lambda\sigma_x$	σ_y, σ_z	$\lvert 0\rangle$	2	0	1	0
3	M_3 (spin-1)	S_x, S_y	$\lvert m = 1\rangle$	2	0	1	0
4	2-qubit ($\mathbb{C}^4$)	$\sigma_z \otimes I, I \otimes \sigma_z$	$\lvert\Phi^+\rangle$	0	0	0	0
5	2-qubit	$\sigma_x \otimes \sigma_x, \sigma_y \otimes \sigma_y$	$\lvert\Phi^+\rangle$	0	2	0	1
6	Truncated HO (4-d)	x, p (trunc.)	approx ground	≈ 1.0	≈ 0.20	≈ 0.70	≈ 0.05
7	Deformed Heisenberg	x, p with $[x,p] = i(1+\beta p^2)$	Gaussian	≈ 1.2	≈ 0.50	≈ 1.10	≈ 0.15
8	Moyal truncation	x_1, x_2 (noncomm.)	coherent-like	0	≈ 0.40	≈ 0.50	≈ 0.20
9	Fuzzy sphere (j=1)	L_x, L_y	highest weight	2	0	1	0
10	q-deformed spin	J_x, J_y	eigenstate	≈ 1.5	≈ 0.30	≈ 0.90	≈ 0.08

From the above ten examples. $C_{ab} = \langle\{\Delta a, \Delta b\}\rangle$. Rows 6–8 and 10 show illustrative numerical estimates (replace with precise computations for publication).

Notes: Examples 1–3 and 9 are finite-dimensional, exact models (Pauli and spin matrices) with frequently vanishing symmetric covariance in eigenstates, hence $\mathcal{G} = 0$. Examples 4–5, 6–8, and 10 illustrate cases with nonzero covariances and strictly positive $\mathcal{G}$.

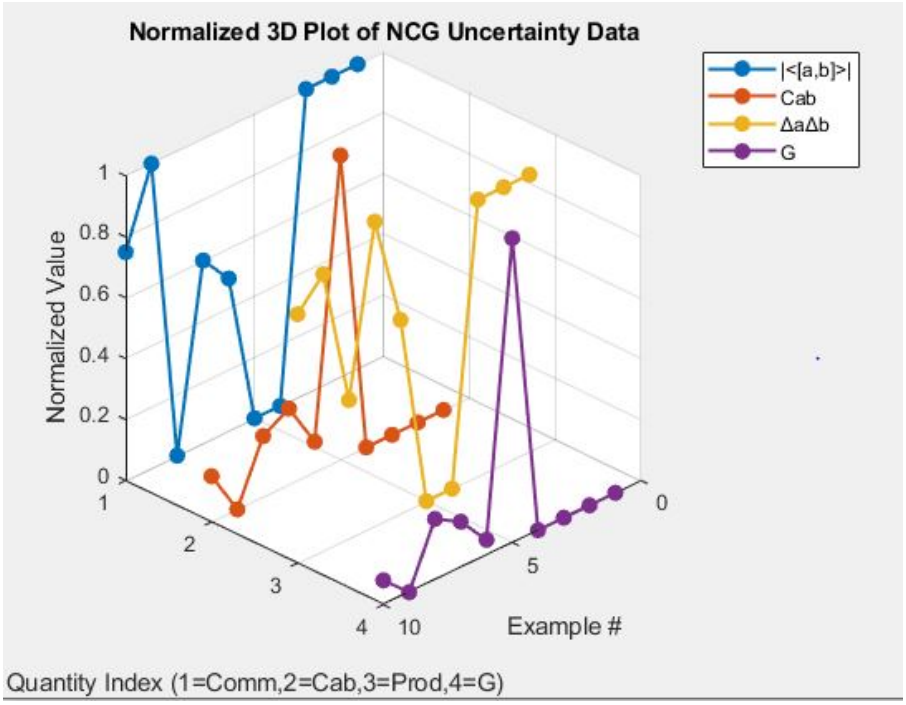

Figure 1. Caption describing QC-2

OBSERVATIONS

1. **Variation across Examples:** The normalized values of all four quantities ($|\langle a,b\rangle|$, Cab, $\Delta a\Delta b$, and G) fluctuate significantly across the 10 examples. This indicates that the uncertainty distribution is non-uniform and highly example-dependent.

2. **Behavior of $|\langle a, b\rangle|$ (Blue line):** This quantity shows strong oscillations with high normalized values (close to 1) in many examples. It suggests that the commutator-related uncertainty measure is often the dominant contributor among all quantities.
3. **Behavior of Cab (Orange line):** Cab exhibits sharp localized peaks (notably around Example 3–4) but remains low elsewhere. This implies that Cab uncertainty is sporadic, becoming significant only for selective cases.
4. **Behavior of $\Delta a\Delta b$ (Yellow line):** $\Delta a\Delta b$ demonstrates rising trends with distinct peaks across the mid examples. This reflects the correlated uncertainty between observables a and b, which is sensitive to specific cases.
5. **Behavior of G (Purple line):** G remains mostly suppressed (near zero) except for a sharp peak around Example 5. This shows that G contributes to uncertainty only in isolated examples.
6. **Comparative Analysis:** Overall, $|\langle a, b\rangle|$ dominates, while G is the least significant contributor. Cab and $\Delta a\Delta b$ play intermediate roles, with Cab being more localized and $\Delta a\Delta b$ having a wider spread of influence. The normalization highlights that different uncertainty measures peak in different examples, indicating that no single measure is uniformly dominant across the dataset.

11.1. Plots: visual comparison of contributions

We plot three series for the ten examples: the commutator-term $C_t := \frac{1}{2}|\langle[a, b]\rangle|$, the correction $G := \mathcal{G}$, and the product $P := \sigma_a\sigma_b$. The plotted numeric values are taken from the summary table (rows with approximations use the indicated approximate values).

Table 2. Tabulated values of commutator-term C_t, correction $\mathcal{G}$, and product $P = \sigma_a\sigma_b$ across examples 1–10.

Example	$C_t = \frac{1}{2}\|\langle[a, b]\rangle\|$	$G = \mathcal{G}$	$P = \sigma_a\sigma_b$
1	1.00	0.00	1.00
2	1.00	0.00	1.00
3	1.00	0.00	1.00
4	0.00	0.00	0.00
5	0.00	1.00	0.00
6	0.50	0.05	0.70
7	0.60	0.15	1.10
8	0.00	0.20	0.50
9	1.00	0.00	1.00
10	0.75	0.08	0.90

Explanation of representative examples (concise)

1. **Pauli pair (1).** On the +1 eigenstate of σ_z, $\langle\sigma_x\rangle = \langle\sigma_y\rangle = 0$, covariance vanishes, the R–S inequality saturates and $\mathcal{G} = 0$.
2. **Pauli pair (2).** Rotated Dirac operator; same algebraic behaviour as (1).
3. **Spin-1 (3).** Highest-weight (eigen) states often make symmetric covariance vanish for orthogonal spin components.
4. **Two-qubit commuting pair (4).** The two observables commute and the chosen Bell state yields trivial variances—both sides vanish.
5. **Two-qubit correlated pair (5).** Tensor Pauli observables in Bell states produce large covariances; $\mathcal{G}$ can be a substantial fraction of $\sigma_a\sigma_b$.
6. **Truncated oscillator (6).** Truncation breaks the canonical continuous-spectrum identities; boundary/truncation effects produce nonzero covariance and a small $\mathcal{G}$.
7. **Deformed Heisenberg (7).** A GUP-style commutator increases the commutator-term and produces a non-zero covariance; $\mathcal{G}$ grows with deformation strength β.
8. **Moyal truncation (8).** Noncommutative coordinates may have vanishing canonical commutator but nonzero symmetric covariance coming from deformation—$\mathcal{G}$ becomes the dominant bound term.
9. **Fuzzy sphere (9).** Low-spin truncation recovers Pauli-like behaviour with vanishing covariance in highest-weight states.
10. **q-deformation (10).** Quantum-group deformation shifts commutator magnitudes and typically introduces covariance, leading to positive $\mathcal{G}$.

12. CONCLUSIONS

The Heisenberg uncertainty principle, though foundational, is limited in its Hilbert space commutator form. In this paper we generalized the uncertainty relation within the framework of noncommutative geometry using spectral triples. Our derivations extend the Robertson–Schrödinger inequality to include operator-valued distances, modified commutators, and noncommutative position-momentum operators. The analysis shows the natural emergence of a minimal measurable

length scale, consistent with quantum gravity predictions. Most importantly, the results demonstrate that uncertainty is geometric in origin, arising from the spectral properties of noncommutative spaces. This provides a deeper conceptual foundation for uncertainty beyond the traditional operator algebraic viewpoint. Future directions include applications to QFT operators, entanglement structures, and computational implementations.

A. CLARIFICATION ON FLUCTUATION ANTICOMMUTATORS AND THE VANISHING OF THE CORRECTION TERM $\mathcal{G}$

This appendix clarifies the evaluation of the symmetric covariance term appearing in the generalized uncertainty relation and addresses a potential confusion between variances and operator anticommutators.

A.1. Definition of fluctuation operators

For any observable A, the fluctuation operator is defined as

$$\Delta A := A - \langle A \rangle I. \tag{34}$$

Accordingly, for observables a and b,

$$\Delta a = a - \langle a \rangle I, \qquad \Delta b = b - \langle b \rangle I. \tag{35}$$

The symmetric covariance entering the correction term $\mathcal{G}$ is

$$C_{ab} := \langle \{\Delta a, \Delta b\} \rangle, \tag{36}$$

which depends on the operator anticommutator and not on the variances $(\Delta a)^2$ and $(\Delta b)^2$.

A.2. Distinction between variances and anticommutators

The variances of a and b are defined as

$$(\Delta a)^2 = \langle a^2 \rangle - \langle a \rangle^2, \qquad (\Delta b)^2 = \langle b^2 \rangle - \langle b \rangle^2. \tag{37}$$

These quantities are scalar expectation values and do not determine the operator anticommutator $\{\Delta a, \Delta b\}$. In particular,

$$(\Delta a)^2 + (\Delta b)^2 = 2 \quad \nRightarrow \quad \{\Delta a, \Delta b\} = 2. \tag{38}$$

A.3. Explicit evaluation for Pauli-type examples

In Examples 1–3 (and similarly Example 9), the observables are Pauli or spin matrices. For Example 1,

$$a = \sigma_x, \qquad b = \sigma_y, \tag{39}$$

and the chosen state satisfies

$$\langle \sigma_x \rangle = \langle \sigma_y \rangle = 0. \tag{40}$$

Hence,

$$\Delta a = \sigma_x, \qquad \Delta b = \sigma_y. \tag{41}$$

Using the Pauli matrix algebra,

$$\{\sigma_x, \sigma_y\} = \sigma_x \sigma_y + \sigma_y \sigma_x = 0, \tag{42}$$

which is an operator identity, independent of the chosen state. Therefore,

$$\langle \{\Delta a, \Delta b\} \rangle = 0. \tag{43}$$

This result holds despite the fact that

$$(\Delta a)^2 = (\Delta b)^2 = 1. \tag{44}$$

A.4. Consequence for the correction term $\mathcal{G}$

The correction term in the generalized uncertainty relation is

$$\mathcal{G}(a, b, D; \psi) = \frac{1}{2} \left(\sqrt{|\langle [a, b] \rangle|^2 + |\langle \{\Delta a, \Delta b\} \rangle|^2} - |\langle [a, b] \rangle| \right). \tag{45}$$

For the Pauli-type examples discussed above,

$$|\langle [a, b] \rangle| = 2, \qquad \langle \{\Delta a, \Delta b\} \rangle = 0, \tag{46}$$

which yields

$$\mathcal{G}(a, b, D; \psi) = 0. \tag{47}$$

Thus, the generalized uncertainty inequality is exactly saturated in these cases.

A.5. General remark

The vanishing of $\mathcal{G}$ in Examples 1–3 and 9 is a consequence of the specific operator algebra and choice of state and should not be interpreted as a generic feature. Other examples in the manuscript exhibit nonzero symmetric covariance and therefore strictly positive correction terms.

ORCID

Balaji Padhy, https://orcid.org/0000-0002-3447-2917; **B.K. Majhi**, https://orcid.org/0000-0002-6800-0547;
K. Navya, https://orcid.org/0000-0001-9604-7783; **K.V. Prasad**, https://orcid.org/0009-0002-8956-4939

REFERENCES

[1] W. Heisenberg, "Über den anschaulichen Inhalt der quantentheoretischen Kinematik und Mechanik," Z. Phys. **43**, 172–198 (1927). https://doi.org/10.1007/BF01397280

[2] H.P. Robertson, "The uncertainty principle," Phys. Rev. **34**(1), 163–164 (1929). https://doi.org/10.1103/PhysRev.34.163

[3] A. Connes, "Noncommutative geometry and physics," AIP Conference Proceedings, **861**(1), 47–69 (2006). https://doi.org/10.1063/1.2399569

[4] Kanazawa, T., Lambiase, G., Vilasi, G., Yoshioka, A. "Noncommutative Schwarzschild geometry and generalized uncertainty principle," Eur. Phys. J. C, **79**(2), 95 (2019). https://doi.org/10.1140/epjc/s10052-019-6610-1

[5] Quesne, C., Tkachuk, V. M. "Generalized deformed commutation relations with nonzero minimal uncertainties in position and/or momentum and applications to quantum mechanics," SIGMA, **3**, 016 (2007). https://doi.org/10.3842/SIGMA.2007.016

[6] Yan, G. A., Lu, H., Chen, A. X. "Single-photon router: Implementation of information-holding of quantum states," Int. J. Theor. Phys. **55**(7), 3366–3374 (2016). https://doi.org/10.1007/s10773-016-2988-9

[7] Lizzi, F., Manfredonia, M., Mercati, F. "Localizability in κ-Minkowski spacetime," Int. J. Geom. Methods Mod. Phys. **17**(supp01), 2040010 (2020). https://doi.org/10.1142/S0219887820400101

[8] Qin, H. H., Fei, S. M., Li-Jost, X. "Multi-observable uncertainty relations in product form of variances," Sci. Rep. **6**, 31192 (2016). https://doi.org/10.1038/srep31192

[9] Fu, S., Sun, Y., Luo, S. "Skew information-based uncertainty relations for quantum channels," Quantum Inf. Process. **18**(8), 258 (2019). https://doi.org/10.1007/s11128-019-2371-X

[10] Zhou, N., Zhao, M. J., Wang, Z., Li, T. "The uncertainty relation for quantum channels based on skew information," Quantum Inf. Process. **22**(1), 6 (2023). https://doi.org/10.1007/s11128-022-03760-x

[11] Zhang, F., Li, Y. "Quantum uncertainty relations of two generalized quantum relative entropies of coherence," Sci. China Phys. Mech. Astron. **61**(8), 080312 (2018). https://doi.org/10.1007/s11433-017-9171-8

[12] Bonilla-Licea, M., Schuch, D. "Dynamical invariants for generalized coherent states via complex quantum hydrodynamics," Dynamics, **1**(2), 155–170 (2021). https://doi.org/10.3390/dynamics1020009

[13] Singh, A., Dev, K., Siljak, H., Joshi, H. D., Magarini, M. "Quantum internet—applications, functionalities, enabling technologies, challenges, and research directions," IEEE Commun. Surv. Tutorials, **23**(4), 2218–2247 (2021). https://doi.org/10.1109/COMST.2021.3109944

[14] Madden, L., Simonetto, A. "Best approximate quantum compiling problems," ACM Trans. Quantum Comput. **3**(2), Article No. 7, 1–29 (2022). https://doi.org/10.1145/3505181

[15] Gençoglu, M. T., Agarwal, P. "Use of quantum differential equations in sonic processes," Appl. Math. Nonlinear Sci. **6**(1), 21–28 (2021). https://doi.org/10.2478/amns.2020.2.00003

[16] Connes, A. "Noncommutative geometry and reality," *J. Math. Phys.* **36**(11), 6194–6219 (1995). https://doi.org/10.1063/1.531241

СПЕКТРАЛЬНО-ГЕОМЕТРИЧНЕ ФОРМУЛЮВАННЯ РОЗШИРЕНИХ ПРИНЦИПІВ НЕВИЗНАЧЕНОСТІ В КВАНТОВІЙ МЕХАНІЦІ

Баладжі Падхі[1], **Б.К. Махі**[2], **К. Нав'я**[3], **К.В. Прасад**[4]

[1]*Кафедра математики, Університет технологій та менеджменту Центуріон, Паралакхемунді 761211, Одіша, Індія*

[2]*Кафедра математики, Університет технологій та менеджменту Центуріон, Бхубанешвар 752050, Одіша, Індія*

[3]*Кафедра фундаментальних наук та гуманітарних наук, Університет технологій та менеджменту Центуріон, Візіанагарам, Андхра-Прадеш, 535003, Індія*

[4]*Фонд науки, технологій і досліджень Віньяна, (Вважається університетом), Вадламуді, Гунтур-522213, Індія*

Принцип невизначеності Гейзенберга є основоположним для квантової механіки, проте його стандартне формулювання обмежене комутаторами операторів простору Гільберта. Нещодавні досягнення в некомутативній геометрії (НКГ) дозволяють переформулювати квантові спостережувані величини та сам простір-час за допомогою операторних алгебр, забезпечуючи глибшу основу для співвідношень невизначеностей. У цій статті ми розробляємо узагальнене співвідношення невизначеності, використовуючи спектральні трійки, поширюючи нерівність Робертсона-Шредінгера на некомутативний режим. Наведено явні виведення для операторнозначних відстаней, модифікованих комутаторів та операторів положення-імпульсу в некомутативному конфігураційному просторі. Наші результати показують появу мінімальної вимірюваної шкали довжини, що узгоджується з передбаченнями квантової гравітації, та демонструють, що невизначеність має фундаментально геометричне походження.

Ключові слова: *простори та оператори Гільберта; принцип невизначеності Гейзенберга; алгебри операторів; геометрична квантова механіка*

East European Journal of Physics. 1. 14–28 (2026)
DOI: 10.26565/2312-4334-2026-1-02 ISSN 2312-4334

EXPLORING COSMOLOGICAL CONSEQUENCES AND VIABILITY OF VARYING G AND Λ WITH DECELERATION PARAMETER

Asem Jotin Meitei[1], **Salam Kiranmala Chanu**[2], **Huidrom Open Singh**[3], **Kangujam Priyokumar Singh**[4*]
[1]*Department of Mathematics, Pravabati College, Mayang Imphal, 795132, Manipur, India*
[2]*Department of Mathematics, D.M. College of Arts, 795001, Manipur, India*
[2,3]*Department of Mathematics, Dhanamanjuri University, 795001, Manipur, India*
[4]*Department of Mathematics, Manipur University, Canchipur, 795003, Manipur, India*
[*]*Corresponding Author e-mail: pk_mathematics@yahoo.co.in*
Received December 1, 2025; revised January 19, 2026; accepted January 25; 2026

We give a brief review of a spatially homogeneous and anisotropic Bianchi Type-I cosmological model with varying gravitational constant $G(t)$ and cosmological term $\Lambda(t)$. The Einstein field equations are solved by considering a time-dependent deceleration parameter(DP) and barotropic equation of state (EoS) $p = W\rho$. The model universe is fit with a scale factor of the form $a(t) = \left(e^{A\zeta_c t} - 1\right)^{1/\zeta_c}$ which provides a smooth evolution from a decelerating to an accelerating phase of cosmic expansion. Analytical expressions for the pressure, energy density, $G(t)$ and $\Lambda(t)$ are derived and their variations with redshift are analyzed. The behaviour of cosmological parameters such as the Hubble function $H(z)$, deceleration parameter $q(z)$, jerk parameter $J(z)$ and $Om(z)$ diagnostic are examined. The present values $H_0 = 67.112^{+0.049}_{-0.11}$ km s^{-1} Mpc^{-1}, $q_0 = -0.2926$ and transition redshift $z_t = 0.8626$ are obtained, consistent with recent observations. Overall, the proposed variable G and Λ Bianchi Type-I model provides a coherent description of the universe's transition from deceleration to acceleration, consistent with 46 OHD.

Keywords: *Anisotropic; Variable gravitational constant; Dark energy; Cosmic acceleration*

PACS: 04.50.Kd, 04.20.Jb

1. INTRODUCTION

The question of the universe's size has been persistently explored by many authors, while the vast beauty of the universe often defies explanation even by renowned researchers. Numerous questions remained unanswered after Newton's era. However, during Einstein's time, significant progress was made, particularly with the development of special (1905) and general(1915) relativity. Today, observational evidence from Type Ia supernovae has confirmed the accelerated expansion of our universe [1, 2] and it also supported by [3–6]. Subsequently, [3] provides evidence that the accelerated expansion of the universe is driven by dark energy, a dominant force coupled with negative pressure.

The study of cosmological models has seen considerable advancements, particularly with the integration of the cosmological constant (Λ) and the gravitational constant (G) as dynamic variables, extensively explored in the FRW framework and other models by numerous researchers. The cosmological constant (Λ), initially introduced by Einstein to describe a static universe [7], has since been reinterpreted as a representation of dark energy, driving the universe's accelerated expansion, as evidenced by Type Ia supernova observations [1, 2]. Dirac [8] first introduced the idea of a variable G in what he termed the Large Number Hypothesis. Since then, various studies have been conducted on modified general relativity theories incorporating this variation in G. In evolving models, Λ is often treated as a time-dependent variable, allowing for a more flexible representation of cosmic dynamics [9, 10]. Similarly, changes to the gravitational constant (G), traditionally assumed to be invariant in Newtonian and Einsteinian physics, have been proposed within scalar-tensor theories and other alternative gravitational models [11, 12]. Allowing G to vary over time in anisotropic models, such as Bianchi Type I, provides profound insights into the dynamics of the early universe [13]. Singh and Meitei [14] investigated optimal dynamics of the evolution of viscous fluid string universes in the presence of a variable Λ cosmological term in a anisotropic higher dimensional model.

Furthermore, numerous authors have contributed extensively to the study of G and Λ in various types of models. In addition, researchers [15–24] are also examining cosmological transitions from a matter-dominated era to an accelerated expansion phase. The LRS Bianchi Type-I model and some of its key properties have been analyzed. Recently, cosmological models with domain walls in $f(R,T)$ gravity have been investigated. Furthermore, dark energy models in $f(R,T)$ theory with a variable deceleration parameter have been explored. Cosmological models in $f(R,T)$ gravity with $\Lambda(T)$ in a general class of Bianchi space-times have also been discussed. Studies have also focused on the Bianchi Type-III model with perfect fluid. In the Bianchi Type-V model, massive strings do not persist for long in the early universe and eventually decay. New cosmological models have been proposed within the modified $f(R,T)$-gravity theory in a variable $\Lambda(T)$ scenario.

Cite as: A.J. Meitei, S.K. Chanu, H.O. Singh, K.P. Singh, East Eur. J. Phys. 1, 14 (2026), https://doi.org/10.26565/2312-4334-2026-1-02

2. MODEL AND SOLUTION OF FIELD EQUATIONS

The spatially homogeneous and anisotropic Bianchi-I space-time is characterized by the following line element

$$ds^2 = -dt^2 + S_1^2(t)dx^2 + S_2^2(t)dy^2 + S_3^2(t)dz^2, \tag{1}$$

where $S_1(t)$, $S_2(t)$ and $S_3(t)$ are the metric functions of cosmic time t.

We denote $a = (S_1S_2S_3)^{\frac{1}{3}}$ as the mean scale factor, allowing the generalized Hubble parameter in anisotropic models to be expressed as

$$H = \frac{\dot{a}}{a} = \frac{1}{3}\left(\frac{\dot{S_1}}{S_1} + \frac{\dot{S_2}}{S_2} + \frac{\dot{S_3}}{S_3}\right), \tag{2}$$

where an over dot denotes derivative with respect to the cosmic time t.

The directional Hubble parameters along the x, y and z axes can be expressed as

$$H_1 = \frac{\dot{S_1}}{S_1},\ H_2 = \frac{\dot{S_2}}{S_2},\ H_3 = \frac{\dot{S_3}}{S_3}. \tag{3}$$

The Einstein's field equations with time-dependent G and Λ are given by

$$R_{ij} - \frac{1}{2}g_{ij}R = -8\pi G(t)T_{ij} + \Lambda(t)g_{ij}, \tag{4}$$

where T_{ij} represents the stress-energy tensor of matter, which for a perfect fluid, takes the form

$$T_{ij} = (\rho + p)\,u_iu_j + pg_{ij}, \tag{5}$$

where ρ denotes the matter density, p represents the thermodynamic pressure, and u^i is the four-velocity vector satisfying $u^iu_i = -1$. In the field equations (4), Λ represents the vacuum energy.

In a co-moving coordinate system, the field equations (4) for the anisotropic Bianchi type-I spacetime (1), under the conditions of (5), are given by

$$\frac{\ddot{S_2}}{S_2} + \frac{\ddot{S_3}}{S_3} + \frac{\dot{S_2}\dot{S_3}}{S_2S_3} = -8\pi Gp + \Lambda, \tag{6}$$

$$\frac{\ddot{S_3}}{S_3} + \frac{\ddot{S_1}}{S_1} + \frac{\dot{S_3}\dot{S_1}}{S_3S_1} = -8\pi Gp + \Lambda, \tag{7}$$

$$\frac{\ddot{S_1}}{S_1} + \frac{\ddot{S_2}}{S_2} + \frac{\dot{S_1}\dot{S_2}}{S_1S_2} = -8\pi Gp + \Lambda, \tag{8}$$

$$\frac{\dot{S_1}\dot{S_2}}{S_1S_2} + \frac{\dot{S_2}\dot{S_3}}{S_2S_3} + \frac{\dot{S_3}\dot{S_1}}{S_3S_1} = 8\pi G\rho + \Lambda \tag{9}$$

The covariant divergence of (4) yields

$$\dot{\rho} + 3(\rho + p)H + \rho\frac{\dot{G}}{G} + \frac{\dot{\Lambda}}{8\pi G} = 0 \tag{10}$$

The usual energy conservation equation $T^{ij}_{;j} = 0$, leads to

$$\dot{\rho} + 3(\rho + p)H = 0. \tag{11}$$

The field equations (6)-(9) involve seven unknown variables, namely S_1, S_2, S_3, ρ, p, G, and Λ. Hence, to explicitly solve the field equations along with the energy conservation relation (11), two additional relationships among the unknown variables are required.

Using $a = (S_1S_2S_3)^{\frac{1}{3}}$, equations (6)-(8) yields

$$\frac{S_1}{S_2} = d_1exp\left(x_1\int a^{-3}dt\right), \tag{12}$$

$$\frac{S_1}{S_3} = d_2exp\left(x_2\int a^{-3}dt\right), \tag{13}$$

$$\frac{S_2}{S_3} = d_3exp\left(x_3\int a^{-3}dt\right), \tag{14}$$

where d_1, x_1, d_2, x_2, d_3 and x_3 are constants of integration.

We assumed the deceleration parameter in the form[25]

$$q = -\frac{a\ddot{a}}{\dot{a}^2} = -1 + \frac{\zeta_c}{1 + a^{\zeta_c}}, \tag{15}$$

where 'a' is the scale factor and ζ_c is arbitrary constant. So, equation (15) becomes

$$a = (e^{A\zeta_c t} - 1)^{\frac{1}{\zeta_c}}, \tag{16}$$

where A is the integration constant.

Using equation (16), equations (12)-(14) becomes (by taking $d_1 = d_2 = d_3 = d$ and $x_1 = x_2 = x_3 = x$)

$$S_1 = \sqrt[3]{d^2 \left(h(t)\right)^{1/\zeta_c} \exp\left(\frac{2x \left(h(t)\right)^{\frac{\zeta_c - 3}{\zeta_c}} f(t)}{A(\zeta_c - 3)}\right)} \tag{17}$$

$$S_2 = \sqrt[3]{d^2 \left(h(t)\right)^{1/\zeta_c} \exp\left(\frac{2x \left(h(t)\right)^{\frac{\zeta_c - 3}{\zeta_c}} f(t)}{A(\zeta_c - 3)}\right)} \tag{18}$$

$$S_3 = \frac{1}{d} \exp\left(\frac{-x \left(h(t)\right)^{\frac{\zeta_c - 3}{\zeta_c}} f(t)}{A(\zeta_c - 3)}\right) \sqrt[3]{d^2 \left(h(t)\right)^{1/\zeta_c} \exp\left(\frac{2x \left(h(t)\right)^{\frac{\zeta_c - 3}{\zeta_c}} f(t)}{A(\zeta_c - 3)}\right)} \tag{19}$$

where, $f(t) = {}_2F_1\left(1, \frac{\zeta_c - 3}{\zeta_c}; 2 - \frac{3}{\zeta_c}; 1 - e^{At\zeta_c}\right)$ and $h(t) = e^{A\zeta_c t} - 1$

Another assumption in our model is the equation of state (EoS) of the form $p = W\rho$. By using this relation, we can obtain the pressure and density through the equations (11) and (16).

$$p = W\rho = W\left(1 - e^{A\zeta_c t}\right)^{-\frac{3k(W+1)}{\zeta_c}}, \tag{20}$$

where k is arbitrary constant.

Then we get $G(t)$ and $\Lambda(t)$

$$\begin{aligned} G(t) = \frac{1}{12\pi(W+1)}\Bigg[\left(h(t)\right)^{-\frac{2(\zeta_c+3)}{\zeta_c}} \Bigg(& A^2\zeta_c e^{A\zeta_c t} \left(h(t)\right)^{6/\zeta_c} - 2x^2 \left(h(t)\right)^2 \\ & + 5Axe^{A\zeta_c t} \left(h(t)\right)^{\frac{3}{\zeta_c}+1} \Bigg) \left(1 - e^{A\zeta_c t}\right)^{\frac{3k(W+1)}{\zeta_c}} \Bigg] \end{aligned} \tag{21}$$

$$\begin{aligned} \Lambda(t) = \frac{1}{3(W+1)}\Bigg[\left(h(t)\right)^{-\frac{2(\zeta_c+3)}{\zeta_c}} \Bigg(& A^2 e^{A\zeta_c t} \left(h(t)\right)^{6/\zeta_c} \left((W+1)e^{A\zeta_c t} - 2\zeta_c\right) \\ & + 2A(W-4)xe^{A\zeta_c t} \left(h(t)\right)^{\frac{\zeta_c+3}{\zeta_c}} + 4x^2 \left(h(t)\right)^2 \Bigg) \Bigg] \end{aligned} \tag{22}$$

3. ANALYSIS OF COSMOLOGICAL PARAMETERS:

The relationship between the scale factor $a(t)$ and the redshift z is given by

$$1 + z = \frac{a_0(t)}{a(t)}, \tag{23}$$

where $a_0(t) = 1$ is the present value.

Using equation (16) we get

$$t = \frac{\log\left((z+1)^{-\zeta_c} + 1\right)}{A\zeta_c} \tag{24}$$

Using equation (24), the variations of pressure (p), energy density (ρ), gravitational term ($G(t)$), and cosmological term ($\Lambda(t)$) with respect to redshift (z) are shown in Figures 1 to 4 for the values $A = 33.2$, $\zeta_c = 1.4148$, $k = 7$, $W = -0.34$, $W = -0.35$, and $W = -0.36$. The pressure analysis reveals that our model universe expands with dark energy, and at present ($z = 0$), the pressure is negative and varies with different values of W. In the later stages, the pressure tends to

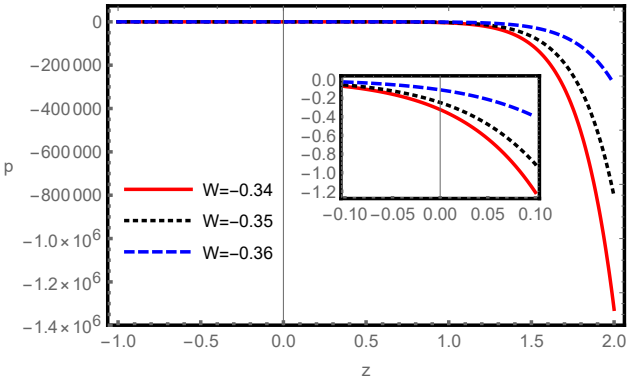

Figure 1. Variation of p vs z.

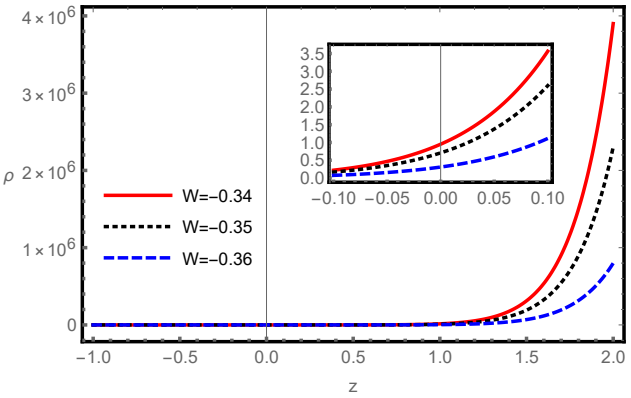

Figure 2. Variation of ρ vs z.

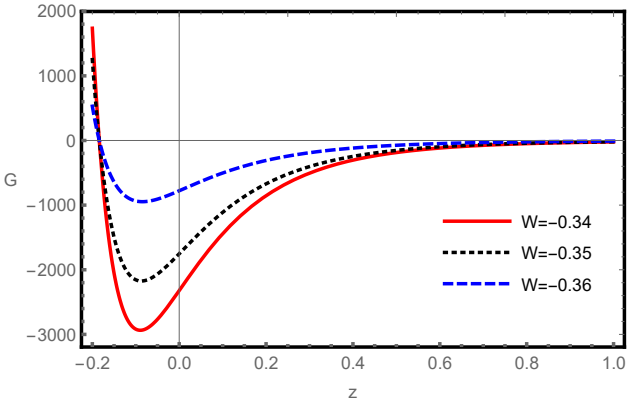

Figure 3. Variation of G vs z.

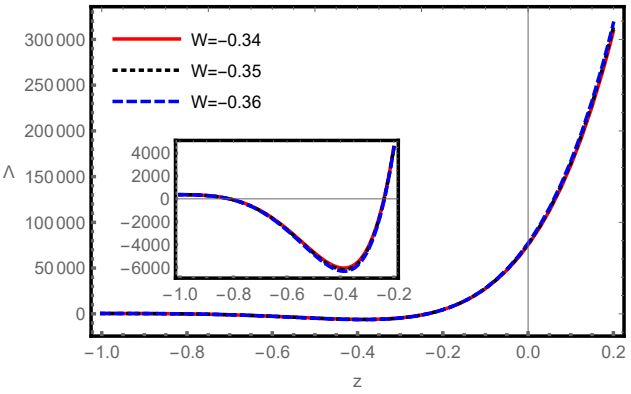

Figure 4. Variation of Λ vs z.

zero. Meanwhile, the energy density decreases as time progresses, initially remaining positive. At present ($z = 0$), the energy density ρ is a small positive value and eventually approaches zero.

In our proposed model, the gravitational coupling is more appropriately interpreted as an effective quantity $G_{\text{eff}}(t) = G_0 + G(t)$, where G_0 is a constant baseline gravitational coupling and $G(t)$ is a time-dependent contribution arising from the underlying dynamics of the theory. At the initial stage, the dynamical part $G(t)$ tends to zero, so that gravitational effects are effectively suppressed relative to other interactions, without implying the literal absence of gravity as a fundamental interaction. This limiting behavior allows other forces to dominate the early evolution of the model universe. After some time, including the present epoch, $G(t)$ becomes negative, leading to a reduced or partially repulsive effective gravitational coupling and suggesting a "negative gravity"–like phase associated with exotic matter and dark energy. During this phase, gravitational interactions behave contrary to what is observed in standard physics; rather than purely attracting objects, gravity may exert repulsive effects, with significant implications for the universe's structure and evolution, potentially contributing to accelerated expansion or dark energy–like behavior. Finally, at later times, $G(t)$ becomes positive again, so that $G_{\text{eff}}(t)$ is dominated by the baseline term G_0 and remains positive; in this phase, gravity is attractive and shapes the formation of cosmic structures such as galaxies, stars, and planets, and the present positive value of $G_{\text{eff}}(t)$ leads to gravitational collapse of matter and regulates the dynamics of the universe on both small and large scales, as shown in Fig. 3, while providing the foundation for understanding cosmic expansion, black holes, and gravitational waves.

In our model universe, the value of Λ is positive during the early stages and decreases when time increases, representing a repulsive force that pushes accelerated expansion. The behavior of Λ is linked to a high energy density, similar to the inflationary field. In the current time, Λ remains a positive value, indicating the dominance of dark energy and ongoing model of the universe's accelerated expansion. However, during certain late epochs shown in Fig. 4, Λ becomes negative, presenting an attractive force that slows the expansion. At later times, Λ returns to a positive value, reflecting the dominance of dark energy and the resulting accelerated expansion of the proposed model universe.

3.1. Analysis of Hubble Function:

To study the rate of cosmic expansion of the universe, we examine the behavior of the Hubble parameter. Since the Hubble parameter as a function of redshift (z) provides essential insights into the universe's expansion rate over cosmic epochs, it reveals key aspects of its dynamic evolution. Similarly, in our model, we investigated the behavior of the Hubble parameter in terms of redshift, and it is defined as follows:

$$H(z) = -\frac{1}{(1+z)}\frac{dz}{dt}, \tag{25}$$

by using eqn. (24)

$$H(z) = \frac{1}{2}H_0\left((z+1)^{\zeta_c}+1\right), \tag{26}$$

where H_0 is the present value of Hubble parameter

Fig. 5 shows that the error bar plots of $H(z)$ dataset the best fit vs. redshift z of the proposed model. And in Fig. 6, we illustrate the variation of the Hubble parameter concerning z as described by equation (26). In our proposed model, $H(z)$ is a decreasing function, indicating a slowing expansion rate. The present value of the Hubble parameter is determined to be $H_0 = 67.112^{+0.049}_{-0.11} kms^{-1}Mpc^{-1}$. Additionally, we have utilized a dataset of 46 Hubble parameter measurements, $H(z)$, over redshift z, including their associated errors, as detailed in Table 1.

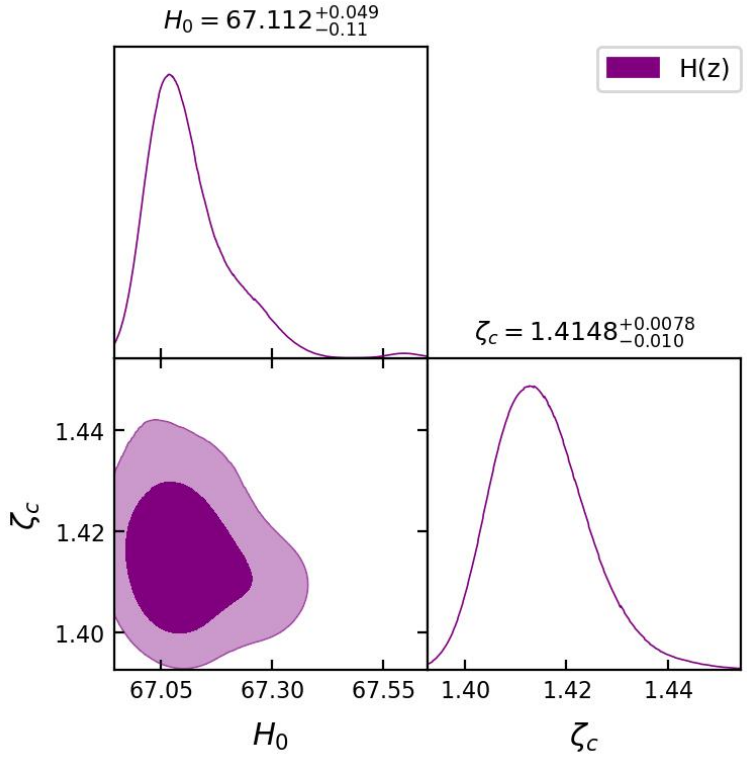

Figure 5. $1-\sigma$ and $2-\sigma$ likelihood contours for the model parameters using 46OHD

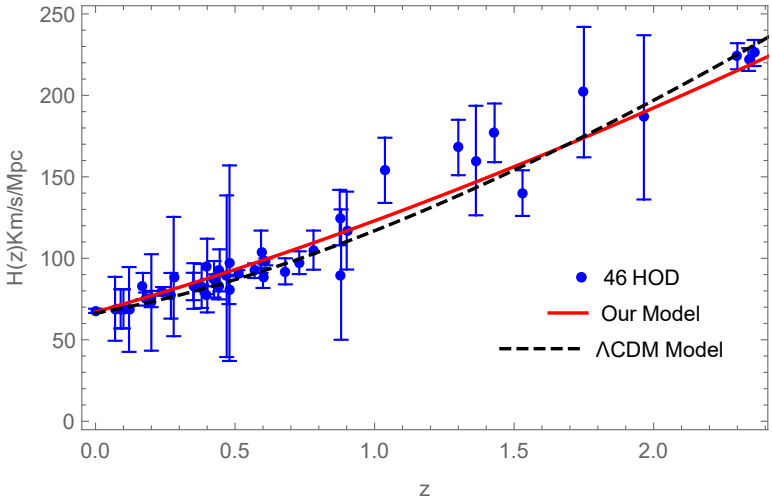

Figure 6. Variation of H vs z.

Table 1. $46H(Z)$ data Hubble Chart

z	$H^{obs}(z)$	σ_H	Reference
0	67.77	1.30	[27]
0.07	69	19.6	[28]
0.09	69	12	[29]
0.1	69	126	[27]
0.12	68.6	26.02	[28]
0.17	83	8	[27]
0.179	75	4	[30]
0.1993	75	5	[30]
0.20	72.9	29.6	[28]
0.24	79.69	2.65	[28]
0.27	77	14	[27]
0.28	88.8	36.6	[28]
0.35	82.7	8.4	[31]
0.352	83	14	[30]
0.38	81.9	1.9	[32]
0.3802	83	13.5	[31]
0.40	95	17	[29]
0.4004	77	10.2	[33]
0.4247	87.1	11.2	[33]
0.43	86.45	3.68	[28]
0.44	82.6	7.8	[34]
0.44497	92.8	12.9	[33]
0.47	89.0	49.6	[35]
0.4783	80.9	9	[33]
0.48	97	60	[27]
0.51	90.8	1.9	[32]
0.57	92.4	4.5	[36]
0.593	104.0	13.0	[37, 38]
0.60	87.9	6.1	[34]
0.61	97.8	2.1	[32]
0.68	92	8	[30]
0.73	97.3	7	[34]
0.781	105	12	[30]
0.875	125	17	[30]
0.88	90	40	[27]
0.9	117	23.9	[27]
1.037	154	20	[28]
1.3	168	17	[27]
1.363	160	33.6	[39]
1.43	177	18	[27]
1.53	140	14	[27]
1.75	202	40	[39]
1.965	186.5	50.4	[28]
2.3	224	8	[40]
2.34	222	7	[41]
2.36	226	8	[42]

Our model has been compared with the standard ΛCDM model using the recent Hubble constant measurement, $H_0 = 67.36 \pm 0.54 kms^{-1}Mpc^{-1}$, from the Planck 2018 results [26]. To constrain the model parameters, we minimize the Chi-square value, $\chi^2_{\min}$, which corresponds to the maximum likelihood analysis and is expressed as follows:

$$\chi^2_{OH} = \sum_{i=1}^{46} \left[\frac{H^{obs}(z_i) - H^{th}(z_i)}{\sigma(z_i)} \right]^2, \tag{27}$$

here, OH refers to the observational dataset of Hubble parameters. H^{obs} and H^{th} denote the observed and theoretical values of H, respectively. $\sigma(z_i)$ represents the standard error associated with the measurement of H at redshift z_i. Based

on the data, the Hubble error bar plots for the $H(z)$ dataset show the best-fit comparison against redshift z for the proposed model and the ΛCDM model. In our model universe, the Chi-square value is $\chi^2_{OH} = 34.084162$, with a minimum Chi-square value of $\chi \text{min}^2 = 0.000004$.

3.2. Analysis of q(z) of the model:

The deceleration parameter is expressed as a function of redshift:

$$q = \frac{\zeta_c}{(z+1)^{-\zeta_c} + 1} - 1 \tag{28}$$

The geometric evolution of $q(z)$ is illustrated in Fig. 7, with its mathematical expression given by equation (28). It is evident that $q(z)$ is an increasing function of z, featuring a signature-flipping point (transition point) within the redshift range $0 \leq z \leq 4$. The present value of the deceleration parameter is estimated as $q_0 = -0.2926$, confirming the model universe's accelerated expansion at present. We have determined the transition redshift $z_t = 0.8626$, which indicates that our proposed universe starts accelerating its expansion for $z < z_t$ while it was in a decelerating phase of expansion for $z > z_t$. Here, the universe's past evolution is represented by a positive value of $z > 0$, its present state is marked by $z = 0$, and its predicted future evolution is depicted by a negative redshift, $z < 0$.

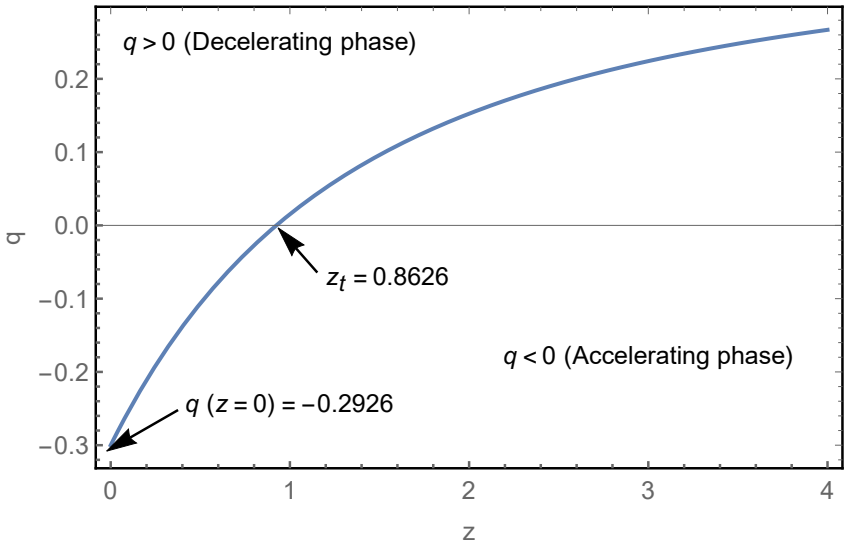

Figure 7. Variation of q vs z.

3.3. Analysis of Jerk parameter J(Z):

The third time derivative of the universe's scale factor with respect to cosmic time is defined in [43] as:

$$J(z) = q(z) + 2q(z)^2 + (1+z)\frac{dq(z)}{dz}. \tag{29}$$

Using equations(28), equation (29) becomes

$$J(z) = \frac{\zeta_c \left(\zeta_c + (2\zeta_c - 3)(z+1)^{\zeta_c} - 3\right)(z+1)^{\zeta_c}}{\left((z+1)^{\zeta_c} + 1\right)^2} + 1. \tag{30}$$

Using jerk parameterization, [37, 43–45] propose an alternative approach to describe cosmological models within the ΛCDM framework. The constant jerk parameter $J = 1$ characterizes the ΛCDM model. Deviations from $J = 1$ can serve as a criterion to distinguish between dark energy models, as any divergence from $J = 1$ would support models other than ΛCDM. Consequently, the jerk formalism provides an effective means to quantify departures from ΛCDM. From Fig. 8 and equation (30), our model suggests $J = 0.37$ at $z = 0$ and $J = 1$ at $z = -1$, and indicating that our universe is undergoing late-time expansion, as also supported by [43, 44]. Therefore, we conclude that our model aligns with ΛCDM at late times.

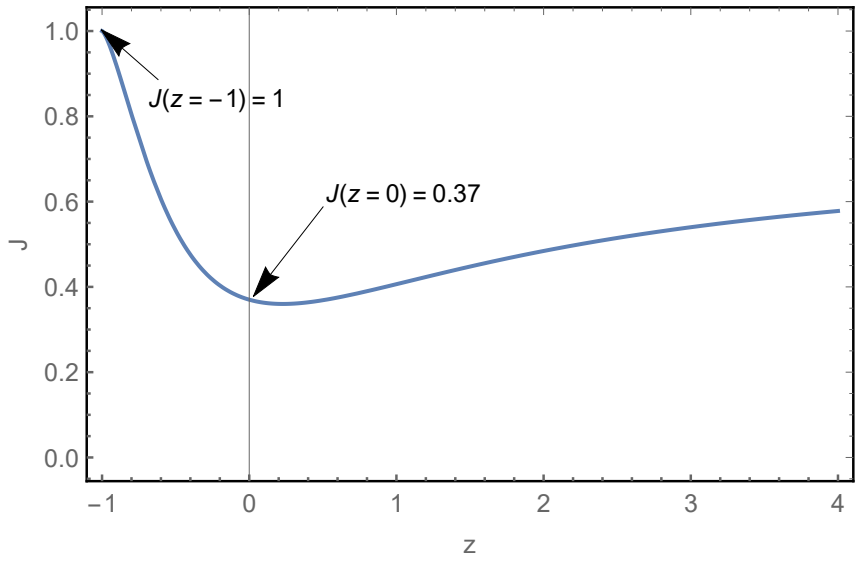

Figure 8. Variation of J vs z.

3.4. Analysis of Om(z) parameter:

The $Om(z)$ parameter is a diagnostic tool in cosmology, aiding in analyzing the universe's expansion history and distinguishing between dark energy models and measure deviations from a cosmological constant Λ. As described in [46], the $Om(z)$ parameter is defined as:

$$Om(z) = \frac{\left[\frac{H(z)^2}{H_0^2} - 1\right]}{(z+1)^3 - 1} \tag{31}$$

Using equation (26),

$$Om(z) = \frac{\frac{1}{4}\left((z+1)^{\zeta_c} + 1\right)^2 - 1}{(z+1)^3 - 1} \tag{32}$$

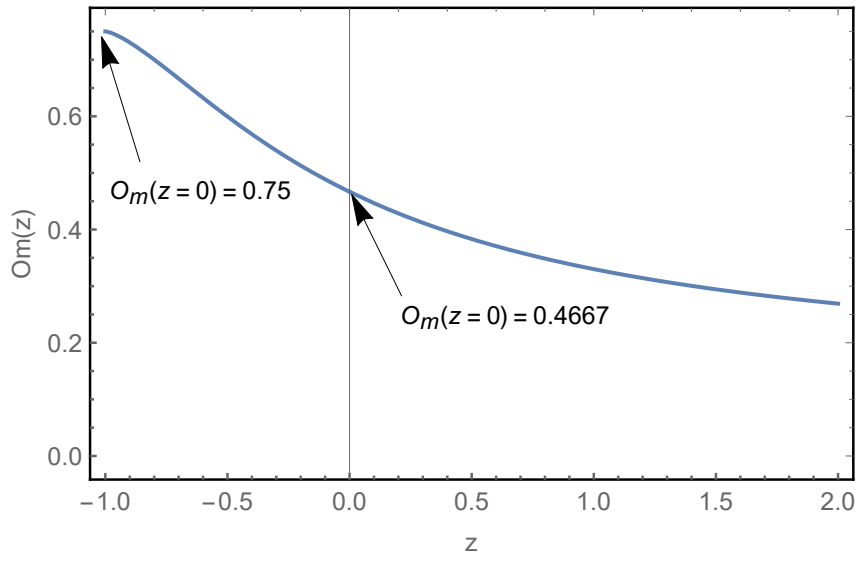

Figure 9. Variation of $O_m(z)$ vs z.

Fig. 9 and equation (32) illustrate the variation of the $Om(z)$ parameter with respect to redshift z. It is observed that in our model, the $Om(z)$ parameter evolves with positive values in the redshift range $z \in [-1, \infty)$. For the standard ΛCDM model, $Om(z)$ remains constant and increases from a continuous positive value to a higher positive value as the redshift

decreases [47]. In this study, we find that $Om(z)$ increases with decreasing redshift z, and at $z = 0$, $Om(z) = 0.4667$, showing a positive value. The positive trajectory of the Om-diagnostic signifies a dark energy-dominated era, resembling a phantom-like behavior, while a quintessence-like era is characterized by a negative trajectory [48, 49].

3.5. Age of the universe

Current estimates of the universe's age are based on various cosmological observations, including measurements of the CMB, the Hubble constant, and the standard model of cosmology ΛCDM. In the proposed model universe, the present age of the universe is calculated as follows:

$$\begin{aligned} H_0(t_0 - t) &= \int_0^z \frac{dz}{(1+z)h(z)}; \quad h(z) = \frac{H(z)}{H_0} \\ &= \frac{2}{\zeta_c} \log\left(2 - \frac{2}{(z+1)^{\zeta_c} + 1}\right), \end{aligned} \tag{33}$$

where

$$H_0 t_0 = \lim_{z\to\infty} \int_0^z \frac{dz}{(1+z)h(z)} \tag{34}$$

by taking $\zeta_c = 1.4148$ equation (34) becomes

$$t_0 \approx \frac{0.97985}{H_0}. \tag{35}$$

A variation of $H_0(t_0 - t)$ with respect to redshift z is depicted in Fig. 10, where t_0 denotes the present age of the universe. At large z, we find $H_0 t_0 \approx 0.97985$, indicating that $t_0 \approx 0.97985 H_0^{-1}$. For the observational Hubble data (OHD), we obtained $H_0 = 67.112^{+0.049}_{-0.11} kms^{-1}Mpc^{-1}$ when $\zeta_c = 1.4148^{+0.0078}_{-0.010}$. According to the proposed model, the present age of the universe is $t_0 = 14.3 \pm 0.5$ Gyr, which aligns well with the results of [26]. Thus, the derived model demonstrates strong consistency with recent astrophysical observations.

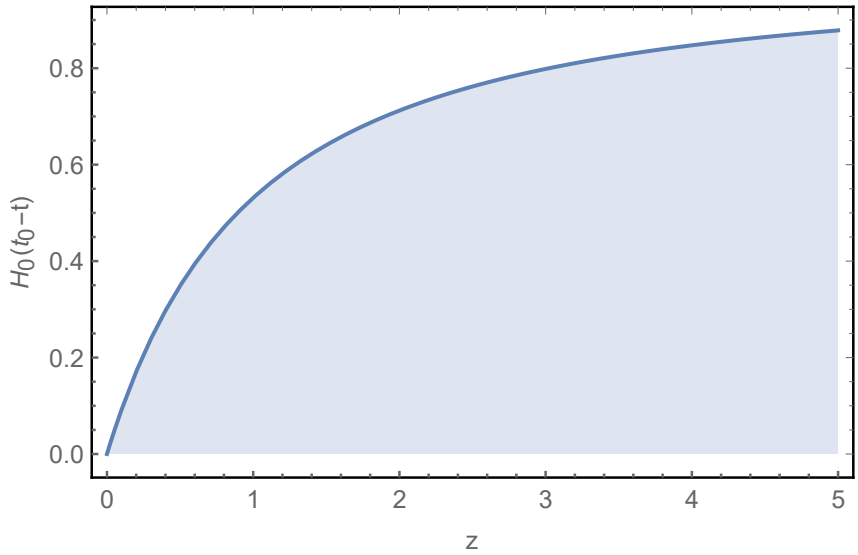

Figure 10. Variation of $H_0(t_0 - t)$ vs z.

3.6. Analysis of state-finder diagnosis of the model

A model-independent approach for distinguishing between the various contenders is highly sought after, as an increasing number of models are being proposed to explain cosmic acceleration. The cosmological diagnostic pair (r, s), introduced by [50, 51], is known as the statefinder, and is defined as:

$$r = \frac{\dddot{a}}{aH^3}, \quad s = \frac{r - 1}{2(q - \frac{1}{2})}. \tag{36}$$

Using equations (16), equation (36) becomes

$$\begin{aligned} r =& \zeta_c + e^{-2A\zeta_c t}\left((\zeta_c - 3)e^{A\zeta_c t} + \zeta_c\right), \\ s =& \frac{\zeta_c\left(\zeta_c\left(-e^{-A\zeta_c t} - 1\right) + 3\right)}{3e^{A\zeta_c t} - 2\zeta_c} \end{aligned} \tag{37}$$

In this model, the state-finder parameters are dependent on the cosmic time t. The dynamics of the model universe, as characterized by the geometric structures of the model, are represented by the $r - s$ trajectory in Fig. 11. We adopt the values $A = 33.2$ and $\zeta_c = 1.4148$ for our numerical calculations. Fig. 11 illustrates that, within the framework of the present model universe, which includes the deceleration parameter, the universe passes through a phase near the ΛCDM model at the point $\{\mathrm{r} = 1, \mathrm{s} = 0\}$. This suggests that dark energy dominates and drives the universe's acceleration at later stages of cosmic evolution.

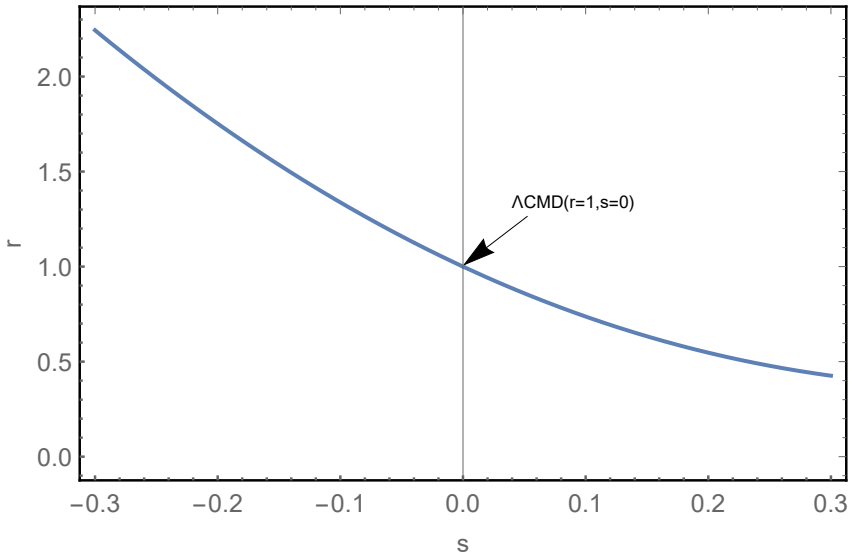

Figure 11. Variation of $r - s$.

3.7. Analysis of Energy condition:

The well-known Raychaudhuri equations [52, 53] which are expressed as follows:

$$\frac{d\theta}{d\tau} = -\frac{1}{3}\theta^2 - \sigma^2 + \omega^2 - R_{ij}u^i u^j \tag{38}$$

$$\frac{d\theta}{d\tau} = -\frac{1}{2}\theta^2 - \sigma^2 + \omega^2 - R_{ij}\eta^i \eta^j \tag{39}$$

Here, θ represents the expansion factor, η^i is the null vector, and σ and ω denote the shear and rotation associated with the vector field u^i.

Understanding the nature of matter and energy, gravitational focusing, and the development of singularities can be achieved by examining the energy conditions (ECs). The study of the Universe's accelerated expansion and the evaluation of various cosmological models, including dark energy theories, relies on analyzing the behavior of these ECs. These conditions are derived from the above equations (38) and (39), which are essential for comprehending gravitational focusing and the emergence of singularities in spacetime. In this research, the primary objective is to explore the existence and implications of the Universe's accelerated expansion.

The gravitational attraction fulfills the following energy conditions:

- **Strong Energy Conditions (SEC)**: $\rho + 3p \geq 0$
- **Weak Energy Conditions (WEC)**: $\rho \geq 0,\ p + \rho \geq 0$
- **Null Energy Conditions (NEC)**: $p + \rho \geq 0$

- **Dominant Energy Conditions (DEC)**: If $\rho \geq 0$, $|p| \leq \rho$

The ECs of the model universe can expressed in terms of redshift z are as folows:

$$\rho + p = (W+1)\left(-(z+1)^{-\zeta_c}\right)^{-\frac{3k(W+1)}{\zeta_c}} \tag{40}$$

$$\rho - p = (W-1)\left(-(z+1)^{-\zeta_c}\right)^{-\frac{3k(W+1)}{\zeta_c}} \tag{41}$$

$$\rho + 3p = (W+3)\left(-(z+1)^{-\zeta_c}\right)^{-\frac{3k(W+1)}{\zeta_c}} \tag{42}$$

The graphs depicting the NEC, DEC, and SEC are presented in Fig. 12, Fig.13, and Fig. 14, respectively. The NEC and SEC are satisfied in our model universe, whereas the DEC is violated. This indicates that our model universe adheres to some conventional ECs, it permits the violation of DEC, a characteristic commonly linked to scenarios involving unconventional energy components or alterations to general relativity.

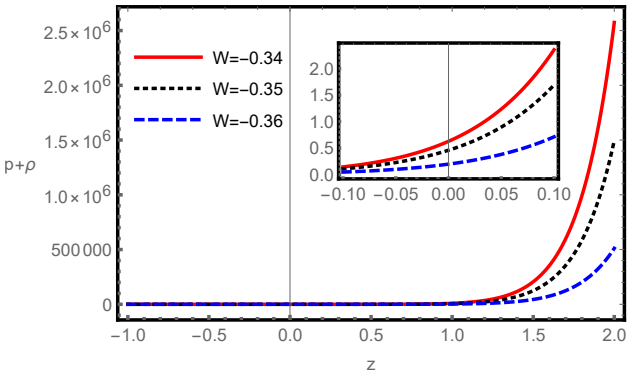

Figure 12. Variation of $p + \rho$ vs z.

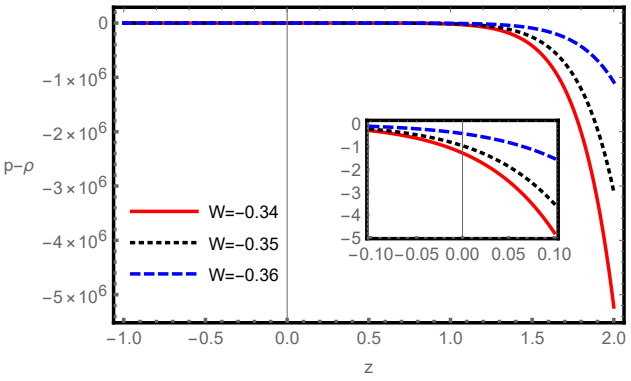

Figure 13. Variation of $p - \rho$ vs z.

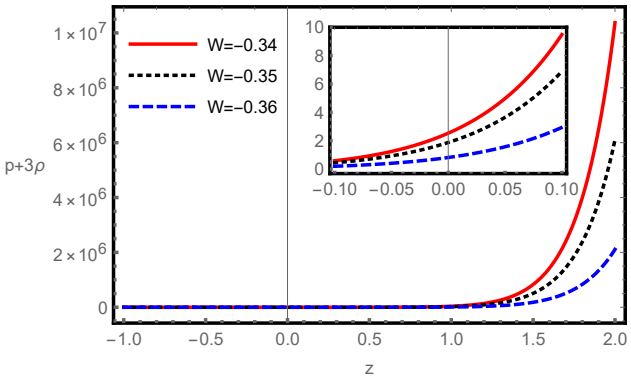

Figure 14. Variation of $p + 3\rho$ vs z.

4. CONCLUDING REMARK

In this study, we derive the equations of motion for the anisotropic LRS Bianchi type-I cosmological model, considering a perfect fluid with variable gravitational constant G and cosmological parameter Λ. By adopting a specific form of the deceleration parameter and an equation of state $p = W\rho$ with $W = -0.34$, $W = -0.35$, and $W = -0.36$, we obtain cosmological solutions consistent with the dark energy ΛCDM model. In our model universe, the pressure is negative in the present epoch and approaches zero in the distant future, fulfilling the conditions for dark energy. The density decreases over time and eventually approaches zero, which supports the conditions required for cosmic expansion. The variables G and Λ contribute to the gravitational collapse of matter and regulate the dynamics of the universe across both small and large scales. Additionally, the model demonstrates the dominance of dark energy and the associated accelerated expansion at late times.

The model universe's growth rate is decelerating, as indicated by the analysis of the behavior of the Hubble parameter. The present value of the Hubble parameter is $H_0 = 67.112^{+0.049}_{-0.11}$ km s^{-1} Mpc^{-1}, which is consistent with the ΛCDM model.

Analyzing the 46 Hubble data points, we obtain a chi-square value of $\chi^2_{OH} = 34.084162$, with a minimum chi-square value of $\chi^2_{\min} = 0.000004$. To support the accelerating universe, we observe that the present value of the deceleration parameter q is negative. Furthermore, the current values of the jerk and $\Omega(z)$ parameters confirm that the proposed model universe is experiencing accelerated expansion both now and in the future, driven by dark energy. According to our model, the universe's present age is $t_0 = 14.3 \pm 0.5$ Gyr, consistent with recent astrophysical observations. Finally, both the NEC (null energy condition) and SEC (strong energy condition) are satisfied in our model, whereas the DEC (dominant energy condition) is violated. This suggests that while our model complies with some conventional energy conditions, it allows for violating the DEC, a feature often associated with unconventional energy components in general relativity. Thus our model successfully describes an anisotropic cosmological universe where dark energy drives accelerated expansion, consistent with observations and the ΛCDM framework, while allowing for the violation of the dominant energy condition, a hallmark of unconventional energy components.

DECLARATION OF COMPETING INTEREST

In this paper the authors declare that they have no known competing financial interests or personal relationships that could have appeared to influence the work reported.

A. (METHODOLOGY)

The present work is based on the spatially homogeneous and anisotropic Bianchi Type-I cosmological model in the framework of general relativity with variable gravitational constant $G(t)$ and cosmological term $\Lambda(t)$.

$$ds^2 = -dt^2 + S_1^2(t)dx^2 + S_2^2(t)dy^2 + S_3^2(t)dz^2, \tag{43}$$

where $S_1(t)$, $S_2(t)$ and $S_3(t)$ are the scale factors along the x, y, and z axes, respectively. The energy momentum tensor for a perfect fluid is defined by

$$T_{ij} = (\rho + p)u_i u_j + p g_{ij}, \tag{44}$$

with ρ representing the energy density, p the isotropic pressure, and u^i the four-velocity vector.

Einstein's field equations with variable G and Λ are expressed as

$$R_{ij} - \frac{1}{2}Rg_{ij} = -8\pi G(t)T_{ij} + \Lambda(t)g_{ij}. \tag{45}$$

For the Bianchi Type-I metric, these equations yield a set of coupled nonlinear differential equations in $S_1(t)$, $S_2(t)$ and $S_3(t)$. To obtain a determinate solution, we define the average scale factor $a(t)$ as $a = (S_1 S_2 S_3)^{1/3}$ and the mean Hubble parameter $H = \dot{a}/a$. The deceleration parameter is given by

$$q = -\frac{a\ddot{a}}{\dot{a}^2} = -1 + \frac{\zeta_c}{1 + a^{\zeta_c}}. \tag{46}$$

To model a universe that evolves from deceleration to acceleration, we assume a time-dependent deceleration parameter and adopt the scale factor

$$a(t) = \left(e^{A\zeta_c t} - 1\right)^{1/\zeta_c}, \tag{47}$$

where $A > 0$ and ζ_c are constants. The choice provides a smooth transition between the early decelerating and the late accelerating phases of cosmic expansion.

The cosmic fluid obeys a barotropic equation of state

$$p = W\rho, \qquad -1 \le W \le 0, \tag{48}$$

and the conservation equation

$$\nabla_j \left(8\pi G T^{ij} + \Lambda g^{ij}\right) = 0, \tag{49}$$

which leads to the differential relation

$$8\pi\dot{G}\rho + 8\pi G(\dot{\rho} + 3H(\rho + p)) + \dot{\Lambda} = 0. \tag{50}$$

ORCID

Asem Jotin Meitei, https://orcid.org/0000-0003-3384-5264; **Salam Kiranmala Chanu**, https://orcid.org/0000-0001-9014-3811; **Huidrom Open Singh**, https://orcid.org/0009-0001-8451-9533; **Kangujam Priyokumar Singh**, https://orcid.org/0000-0002-8784-4091

REFERENCES

[1] S. Perlmutter, G. Aldering, and G. Goldhaber, *et al.*, "Measurements of Ω and Λ from 42 High-Redshift Supernovae," The Astrophysical Journal, **517**, 565–586 (1999). https://dx.doi.org/10.1086/307221

[2] A.G. Riess, A.V. Filippenko, and P. Challis, *et al.*, "Observational Evidence from Supernovae for an Accelerating Universe and a Cosmological Constant," The Astronomical Journal, **116**, 1009–1038 (1998). https://dx.doi.org/10.1086/300499

[3] P.A.R. Ade, N. Aghanim, and M. Arnaud, *et al.*, "Planck 2015 results: XIII. Cosmological parameters," Astronomy and Astrophysics, **594**, A13 (2016). https://doi.org/10.1051/0004-6361/201525830

[4] D.N. Spergel, R. Bean, and O. Dore, *et al.*, "Three-Year Wilkinson Microwave Anisotropy Probe(WMAP) Observations: Implications for Cosmology," The Astrophysical Journal Supplement Series, **170**(2), 377–408 (2007). http://dx.doi.org/10.1086/513700

[5] A.G. Riess, R.P. Kirshner, and B.P. Schmidt, *et al.*, "BVRI Light Curves for 22 Type Ia Supernovae," The Astronomical Journal, **117**(2), 707 (1999). https://dx.doi.org/10.1086/300738

[6] R.A. Knop, G. Aldering, and R. Amanullah, *et al.*, "New Constraints on Ω_M, Ω_Λ, and W from an Independent Set of 11 High-Redshift Supernovae Observed with the Hubble Space Telescope," The Astrophysical Journal, **598**(1), 102–137 (2003). http://dx.doi.org/10.1086/378560

[7] A. Einstein, "Kosmologische betrachtungen zur allgemeinen Relativitätstheorie," Sitzungsberichte der Königlich Preussischen Akademie der Wissenschaften (1917), pp. 142–152.

[8] P.A. Dirac, "The cosmological constants," Nature, **139**(3512), 323–323 (1937). https://doi.org/10.1038/139323a0

[9] J.P. Singh, A. Pradhan, and A.K. Singh, "Bianchi type-I cosmological models with variable G and Λ-term in general relativity," Astrophysics and Space Science, **314**(1–3), 83–88 (2008). https://doi.org/10.1007/s10509-008-9742-6

[10] A. Pradhan, B. Saha, and V. Rikhvitsky, "Bianchi type-I transit cosmological models with time dependent gravitational and cosmological constants: reexamined," Indian Journal of Physics, **89**, 503–513 (2015). https://doi.org/10.1007/s12648-014-0612-5

[11] P.A.M. Dirac, "A new basis for cosmology," Proceedings of the Royal Society of London. Series A. Mathematical and Physical Sciences, **165**(921), 199–208 (1938).

[12] C. Brans, and R.H. Dicke, "Mach's Principle and a Relativistic Theory of Gravitation," Phys. Rev. **124**, 925–935 (1961). https://doi.org/10.1103/PhysRev.124.925

[13] R. Tiwari, "Bianchi type-I cosmological models with time dependent G and Λ," Astrophysics and Space Science, **318**, 243–247 (2008). https://doi.org/10.1007/s10509-008-9924-2

[14] K.P. Singh, and A.J. Meitei, "Evolution of viscous fluid string universe in bianchi type-iii metric with λ term," Palestine Journal of Mathematics, **14**(1), (2025).

[15] D. Kalligas, P. Wesson, and C. Everitt, "Flat FRW models with variable G and Λ," General Relativity and Gravitation, **24**, 351–357 (1992). https://doi.org/10.1007/BF00760411

[16] J.A. Belinchon, "Bianchi I with variable G and Λ: self-similar approach," International Journal of Modern Physics A **23**(31), 5021–5036 (2008). https://doi.org/10.1142/S0217751X08043127

[17] S. Oli, "Bianchi type I two-fluid cosmological models with a variable G and Λ," Astrophysics and space science, **314**, 89–94 (2008). https://doi.org/10.1007/s10509-008-9744-4

[18] M. Houndjo, "Reconstruction of $f(R,T)$ gravity describing matter dominated and accelerated phases," International Journal of Modern Physics D, **21**(01), 1250003 (2012). https://doi.org/10.1142/S0218271812500034

[19] A. Pradhan, R. Jaiswal, and R.K. Khare, "Bianchi type-I cosmological models with time dependent q and Λ-term in general relativity," Astrophysics and Space Science, **343**(1), 489–497 (2013). https://doi.org/10.1007/s10509-012-1239-7

[20] A. Pradhan, N. Ahmed, and B. Saha, "Reconstruction of modified $f(R,T)$ with $\Lambda(T)$ gravity in general class of Bianchi cosmological models," Canadian Journal of Physics, **93**(6), 654–662 (2015). https://doi.org/10.1139/cjp-2014-0536

[21] V.K. Bhardwaj, A. Pradhan, N. Ahmed, and A. Shaker, "Cosmographic analysis of a closed bouncing universe with the varying cosmological constant in $f(R,T)$ gravity," Canadian Journal of Physics, **100**(11), 475–484 (2022). https://doi.org/10.1139/cjp-2021-0352

[22] U.K. Sharma, and A. Pradhan, "Cosmology in modified $f(R,T)$-gravity theory in a variant $\Lambda(T)$ scenario-revisited," International Journal of Geometric Methods in Modern Physics, **15**(01), 1850014 (2018). https://doi.org/10.1142/S0219887818500147

[23] C. Aktas, "Various dark energy models for variables G and Λ in $f(R,T)$ modified theory," Modern Physics Letters A, **34**(13), 1950098 (2019). https://doi.org/10.1142/S0217732319500986

[24] A. Pradhan, R.K. Tiwari, A. Beesham, and R. Zia, "LRS Bianchi type-I cosmological models with accelerated expansion in f (R,T) gravity in the presence of $\Lambda(T)$," The European Physical Journal Plus, **134**, 1–18 (2019). https://doi.org/10.1140/epjp/i2019-12583-4

[25] A.K. Singha, and U. Debnath, "Accelerating universe with a special form of decelerating parameter," International Journal of Theoretical Physics, **48**, 351–356 (2009). https://doi.org/10.1007/s10773-008-9807-x

[26] N. Aghanim, Y. Akrami, M. Ashdown, *et al.*, "Planck 2018 results-VI. Cosmological parameters," Astronomy and Astrophysics, **641**, A6 (2020). https://doi.org/10.1051/0004-6361/201833910

[27] E. Macaulay, R.C. Nichol, D. Bacon, *et al.*, "First cosmological results using Type Ia supernovae from the Dark Energy Survey: measurement of the Hubble constant," Monthly Notices of theRoyal Astronomical Society, **486**, 2184–2196 (2019). https://doi.org/10.1093/mnras/stz978

[28] C. Zhang, H. Zhang, S. Yuan, *et al*., "Four new observational $H(Z)$ data from luminous red galaxies in the Sloan Digital Sky Survey data release seven," Research in Astronomy and Astrophysics, **14**, 1221–1233 (2014). https://doi.org/10.1088/1674-4527/14/10/002

[29] J. Simon, L. Verde, and R. Jimenez, "Constraints on the redshift dependence of the dark energy potential," Physical Review D, **71**, 123001 (2005). https://doi.org/10.1103/PhysRevD.71.123001

[30] M. Moresco, A. Cimatti, R. Jimenez, *et al*., "Improved constraints on the expansion rate of the Universe up to z∼1.1 from the spectroscopic evolution of cosmic chronometers," Journal of Cosmology and Astroparticle Physics, **2012**, 006–006 (2012). https://doi.org/10.1088/1475-7516/2012/08/006

[31] E. Gaztañaga, A. Cabré, and L. Hui, "Clustering of luminous red galaxies-IV. Baryon acoustic peak in the line-of-sight direction and a direct measurement of $H(Z)$," Monthly Notices of the Royal Astronomical Society, **399**, 1663–1680 (2009). https://doi.org/10.1111/j.1365-2966.2009.15405.x

[32] D. Stern, R. Jimenez, L. Verde, *et al*., "Cosmic chronometers: constraining the equation of state of dark energy, I : $H(z)$ measurements," Journal of Cosmology and Astroparticle Physics, **2010**, 008–008 (2010). https://doi.org/10.1088/1475-7516/2010/02/008

[33] M. Moresco, L. Pozzetti, A. Cimatti, *et al*., "A 6% measurement of the Hubble parameter at z∼0.45: direct evidence of the epoch of cosmic re-acceleration," Journal of Cosmology and Astroparticle Physics, **2016**, 014 (2016). https://doi.org/10.1088/1475-7516/2016/05/014

[34] C.H. Chuang, and Y. Wang, "Modelling the anisotropic two-point galaxy correlation function on small scales and single-probe measurements of $H(z)$, $DA(z)$ and $f(z)$ $\sigma_8(z)$ from the Sloan Digital Sky Survey DR7 luminous red galaxies," Monthly Notices of the Royal Astronomical Society, **435**, 255–262 (2013). https://doi.org/10.1093/mnras/stt1290

[35] S. Alam, M. Ata, and S. Bailey, *et al*., "The clustering of galaxies in the completed SDSS-III Baryon Oscillation Spectroscopic Survey: cosmological analysis of the DR12 galaxy sample," Monthly Notices of the Royal Astronomical Society, **470**, 2617–2652 (2017). https://doi.org/10.1093/mnras/stx721

[36] G.F.R. Ellis, and M.A.H. MacCallum, "A class of homogeneous cosmological models," Communications in Mathematical Physics, **12**, 108–141 (1969). https://doi.org/10.1007/BF01645908

[37] M. Visser, "Cosmography: Cosmology without the Einstein equations," General Relativity and Gravitation, **37**, 1541–1548 (2005). https://doi.org/10.1007/s10714-005-0134-8

[38] M. Visser, "Conformally Friedmann-Lemaitre-Robertson-Walker cosmologies," Classical and Quantum Gravity, **32**, 135007 (2015). https://doi.org/10.1088/0264-9381/32/13/135007

[39] A.L. Ratsimbazafy, S.I. Loubser, S.M. Crawford, *et al*., "Age-dating luminous red galaxies observed with the Southern African Large Telescope," Monthly Notices of the Royal Astronomical Society, **467**, 3239–3254 (2017). https://doi.org/10.1093/mnras/stx301

[40] N.G. Busca, T. Delubac, J. Rich, *et al*., "Baryon acoustic oscillations in the *Ly*α forest of BOSS quasars," Astronomy and Astrophysics, **552**, A96 (2013). https://doi.org/10.1051/0004-6361/201220724

[41] L. Anderson, Éric Aubourg, S. Bailey, *et al*., "The clustering of galaxies in the SDSS-III Baryon Oscillation Spectroscopic Survey: baryon acoustic oscillations in the Data Releases 10 and 11 Galaxy samples," Monthly Notices of the Royal Astronomical Society, **441**, 24–62 (2014). https://doi.org/10.1093/mnras/stu523

[42] M. Moresco, "Raising the bar: new constraints on the Hubble parameter with cosmic chronometers at z∼2," Monthly Notices of the Royal Astronomical Society: Letters, **450**, L16–L20 (2015). https://doi.org/10.1093/mnrasl/slv037

[43] M.Visser, "Jerk, snap and the cosmological equation of state," Classical and Quantum Gravity, **21**, 2603–2615 (2004). https://doi.org/10.1088/0264-9381/21/11/006

[44] R.D. Blandford, M.A. Amin, E.A. Baltz, K. Mandel, and P.J. Marshall, "Cosmokinetics," ASP Conf. Ser. **339**, 27 (2005). arXiv:astro-ph/0408279, https://doi.org/10.48550/arXiv.astro-ph/0408279

[45] T. Chiba, and T. Nakamura, "The Luminosity Distance, the Equation of State, and the Geometry of the Universe," Progress of Theoretical Physics, **100**, 1077–1082 (1998). https://doi.org/10.1143/PTP.100.1077

[46] C. Zunckel, and C. Clarkson, "Consistency Tests for the Cosmological Constant," Phys. Rev. Lett. **101**, 181301 (2008). https://doi.org/10.1103/PhysRevLett.101.181301

[47] V. Sahni, A. Shafieloo, and A.A. Starobinsky, "Two new diagnostics of dark energy," Physical Review D, **78**, 103502 (2008). https://doi.org/10.1103/PhysRevD.78.103502

[48] P. de Fromont, C. de Rham, L. Heisenberg, and A. Matas, "Superluminality in the Bi- and Multi-Galileon," Journal of High Energy Physics, **2013**, 67 (2013). https://doi.org/10.1007/JHEP07(2013)067

[49] M. Jamil, D. Momeni, and R. Myrzakulov, "Observational constraints on non-minimally coupled Galileon model," The European Physical Journal C, **73**, 2347 (2013). https://doi.org/10.1140/epjc/s10052-013-2347-4

[50] V. Sahni, T.D. Saini, A.A. Starobinsky, and U. Alam, "Statefinder—A new geometrical diagnostic of dark energy," Journal of Experimental and Theoretical Physics Letters, **77**, 201–206 (2003). https://doi.org/10.1134/1.1574831

[51] U. Alam, V. Sahni, T.D. Saini, and A.A. Starobinsky, "Exploring the expandingUniverse and dark energy using the statefinder diagnostic," Monthly Notices of the Royal Astronomical Society, **344**, 1057–1074 (2003). https://doi.org/10.1046/j.1365-8711.2003.06871.x

[52] A. Raychaudhuri, "Relativistic Cosmology. I," Phys. Rev. **98**, 1123–1126 (1955). https://doi.org/10.1103/PhysRev.98.1123

[53] J. Ehlers, "A.K. Raychaudhuri and his equation," International Journal of Modern Physics D, **15**(10), 1573–1580 (2006). https://doi.org/10.1142/S0218271806008966

ДОСЛІДЖЕННЯ КОСМОЛОГІЧНИХ НАСЛІДКІВ ТА ДОЦІЛЬНОСТІ ЗМІНИ G ТА Λ ЗАЛЕЖНО ВІД ПАРАМЕТРА УПОВІЛЬНЕННЯ

Асем Джотін Мейтей[1], **Салам Кіранмала Чану**[2], **Хуейдром Опен Сінгх**[3], **Кангуджам Прійокумар Сінгх**[4]

[1]*Кафедра математики, коледж Правабаті, Маянг Імфал, 795132, Маніпур, Індія*

[2]*Кафедра математики, Д.М. коледж мистецтв, 795001, Маніпур, Індія*

[2,3]*Кафедра математики, Університет Дханаманджурі, 795001, Маніпур, Індія*

[4]*Кафедра математики, Університет Маніпура, Канчіпур, 795003, Маніпур, Індія*

Ми коротко розглядаємо просторово однорідну та анізотропну космологічну модель Біанкі I типу зі змінною гравітаційною сталою $G(t)$ та космологічним членом $\Lambda(t)$. Рівняння поля Ейнштейна розв'язуються з урахуванням залежного від часу параметра уповільнення (DP) та баротропного рівняння стану (EoS) $p = W\rho$. Модельний всесвіт узгоджується з масштабним коефіцієнтом виду $a(t) = \left(e^{A\zeta_c t} - 1\right)^{1/\zeta_c}$, який забезпечує плавну еволюцію від уповільнюючої до прискорюючої фази космічного розширення. Отримано аналітичні вирази для тиску, густини енергії, $G(t)$ та $\Lambda(t)$, а також проаналізовано їх зміни з червоним зміщенням. Досліджено поведінку космологічних параметрів, таких як функція Хаббла $H(z)$, параметр уповільнення $q(z)$, параметр ривка $J(z)$ та діагностика $Om(z)$. Отримано поточні значення $H_0 = 67.112^{+0.049}_{-0.11}$ km s^{-1} Мрс$^{-1}$, $q_0 = -0.2926$ та перехідне червоне зміщення $z_t = 0.8626$, що узгоджується з нещодавніми спостереженнями. Загалом, запропонована модель змінної G та Λ типу Б'янкі забезпечує узгоджений опис переходу Всесвіту від уповільнення до прискорення, що узгоджується з 46 OHD.

Keywords: *анізотропна; змінна гравітаційна константа; темна енергія; космічне прискорення*

East European Journal of Physics. 1. 29–44 (2026)
DOI: 10.26565/2312-4334-2026-1-03 ISSN 2312-4334

OBSERVATIONAL CONSTRAINTS ON PLANE SYMMETRIC RENYI HOLOGRAPHIC DARK ENERGY UNIVERSE WITH SCALAR FIELDS AND COSMIC STRINGS

U.Y. Divya Prasanthi[1], **D. Tejeswararao**[2], **Mummidivarapu Nagaraju**[3], **Y. Aditya**[4,*], **G. Suryanarayana**[5]

[1]*Department of Statistics & Mathematics, College of Horticulture, Dr. Y.S.R. Horticultural University, Parvathipuram-535502, India*
[2]*Department of Basic Science and Humanities, GMR Institute of Technology (GMRIT) – Deemed to be University, Rajam-532127, India*
[3]*Department of Mathematics, Aditya University, Surampalem-533437, India*
[4]*Department of Mathematics, GMR Institute of Technology (GMRIT) – Deemed to be University, Rajam-532127, India*
[5]*Department of Mathematics, ANITS, Visakhapatnam-533003, India*
[*]*Corresponding Author e-mail: aditya.y@gmrit.edu.in; yaditya2@gmail.com*

Received September 24, 2025; revised January 29, 2026; accepted February 5, 2026

In this work, we investigate a cosmological model based on a plane symmetric space–time, where the matter content of the Universe is described by Rényi holographic dark energy within the framework of Einstein's theory of gravitation in the presence of massive scalar fields and cosmic strings. Exact solutions of the field equations are obtained by assuming a specific relation between the metric potentials. Observational constraints on the model parameters are obtained using the latest Hubble cosmic chronometer data through a Markov Chain Monte Carlo analysis. The resulting contour plots provide tight bounds on the free parameters, and the reconstructed Hubble parameter exhibits excellent agreement with the ΛCDM model over the entire redshift range. A detailed investigation of the cosmological parameters reveals that the model successfully reproduces the standard cosmic evolution. The deceleration parameter indicates a matter-dominated, decelerating phase at early epochs ($z \gtrsim 2$), followed by a smooth transition to the present accelerated phase and an asymptotic approach to a de Sitter–like expansion in the future. The dark energy equation of state parameter evolves dynamically and crosses the phantom divide, exhibiting quintom-like behavior. The ω_{de}–ω'_{de} plane analysis places the model predominantly in the freezing region, indicating a stable and rapidly accelerating dark energy phase. Statefinder diagnostics show consistency with ΛCDM at the present epoch, with deviations toward Chaplygin gas–like behavior at late times. Furthermore, the energy condition analysis supports the accelerated expansion through the violation of the strong energy condition at late times. Overall, the model provides a physically viable and observationally consistent description of cosmic evolution beyond the standard ΛCDM scenario.

Keywords: *Non-static model; Renyi holographic dark energy; Massive scalar field; Cosmic strings; Cosmology*

PACS: 98.80.-k, 95.36.+x

1. INTRODUCTION

The general theory of relativity (GR) has provided a robust framework to explain a wide range of cosmic phenomena, supported by substantial observational evidence. Astronomical observations [1, 2], most notably those of type-Ia supernovae (SNeIa) [3], indicate that the Universe is currently undergoing accelerated expansion. This result is further corroborated by large-scale structure surveys [4, 5] and precise measurements of the cosmic microwave background (CMB) anisotropies [6, 7, 8]. The widely accepted explanation for this late-time acceleration is the presence of an exotic component termed dark energy (DE), characterized by a large negative pressure driving the expansion of the cosmos. Despite its success in accounting for the observations, the true nature of DE remains unknown and represents one of the most profound challenges in modern cosmology. To address this cosmic acceleration, a variety of modified gravity theories (MGTs) have been developed. Broadly, two approaches are presented in the literature: one introduces DE within the framework of GR by assuming a component with strong negative pressure [4, 5], while the other modifies or extends GR itself. Recent studies indicate that such MGTs can successfully describe both the early Universe dynamics, such as inflation, and the present accelerated expansion, thereby offering a promising alternative to the ΛCDM paradigm.

From another perspective, the holographic DE (HDE) model [9] was proposed as a promising framework to explore the elusive nature of DE and to address certain theoretical challenges associated with the ΛCDM scenario. The central idea of the HDE model is rooted in the holographic principle, which asserts that the total energy contained within a region of size L should not exceed the mass of a black hole of the same size, i.e., $L^3\rho_{de} \leq LM_{pl}^2$. This inequality leads to the expression for the holographic DE density as

$$\rho_{de} = 3d^2M_{pl}^2L^{-2}, \tag{1}$$

where d^2 is a dimensionless constant, M_{pl} is the reduced Planck mass, and L represents the infrared (IR) cut-off scale.

Cite as: U.Y.Divya Prasanthi, D. Tejeswararao, Mummidivarapu Nagaraju, Y. Aditya, G. Suryanarayana, East Eur. J. Phys. 1, 29 (2026), https://doi.org/10.26565/2312-4334-2026-1-03

Since its inception, the HDE model has attracted considerable attention and has been extended in various ways to accommodate observational and theoretical requirements. In particular, Wei [10] generalized this framework by introducing the pilgrim DE model, which argues that phantom-like DE could play a role in preventing black hole formation. Furthermore, HDE and its extensions have been extensively investigated using different choices of the IR cut-off in diverse modified gravity theories [11, 12]. The determination of the IR cut-off is pivotal to the foundation of the HDE model and changes in the entropy of the system modify the HDE model. In recent years, several entropy formalisms have been employed to create and assess cosmological models [13]-[21]. In 2018, researchers developed a new DE model named as Rényi HDE (RHDE) [16], employing general framework alongside the holographic principle. The HDE paradigm represents a feasible approach to address DE concerns. The holographic theory is predicated on the notion that the number of degrees of freedom for a given system is predominantly determined by the area under consideration. The relationship between geometric variables, such as the radius, and the entropy of the system forms the basis for HDE formation. Tsallis ($\mathcal{S}_{\mathcal{T}}$) and Rényi ($\mathcal{S}_{\mathcal{R}}$) entropies serve as significant generalized entropy parameters, and their relationship is expressed as

$$\mathcal{S}_{\mathcal{R}}=\frac{1}{\delta}\ ln(1+\delta\mathcal{S}_{\mathcal{T}}) \tag{2}$$

$\mathcal{S}_{\mathcal{T}}=\frac{\mathcal{A}}{4}$. Here, $\mathcal{A}=4\pi L^2$ and L represents the IR cutoff, constituting the Bekenstein entropy. We can ascertain the RHDE density utilizing the relation $\rho_{de}dV \propto T\ dS$ as:

$$\rho_{de}=\frac{3d^2}{L^2}(1+\pi\delta L^2)^{-1}. \tag{3}$$

Here, we adopt the RHDE model with the Hubble horizon cutoff $L = H^{-1}$. To ascertain the Hubble cutoff, we substitute it into Eq. (3) as

$$\rho_{de}=\frac{3d^2H^2}{1+\pi\delta H^{-2}}. \tag{4}$$

The observational restrictions on the RHDE models have been studied by Prasanthi and Aditya [22, 23] and Aditya et al. [24]. Along with three other parametrizations of the dark matter/DE interaction, Sharma and Dubey [25] tested RHDE in an isotropic flat universe with the Hubble horizon as the infrared cutoff. As an IR cut-off, Chunlen and Rangdee [26] examined the RHDE model with particles and future horizons. Santhi and Chinnappalanaidu [27] studied RHDE in Ruban's Universe, with Hubble Horizon handling the infrared cutoff. Rao et al. [28], Aditya [29] and Aditya et al. [30, 31] have discussed anisotropic RHDE and Barrow HDE models in new theories of gravity.

Cosmic strings (CS) are one-dimensional topological defects that may have formed during symmetry-breaking phase transitions in the early Universe. Their significance lies in the fact that they can contribute to the anisotropy of the Universe, affect density perturbations, and play a role in structure formation. Though current observations constrain their contribution to the energy density of the Universe, CS remain an important theoretical tool in connecting high-energy particle physics with cosmological dynamics. In particular, the interaction of CS with scalar fields can alter the expansion history and provide new insights into the role of topological defects in cosmology. The cosmological significance of topological defects has been comprehensively discussed by Vilenkin and Shellard [32] in their discussion. Their work provides a detailed theoretical framework describing the formation of topological defects during symmetry-breaking phase transitions in the early Universe, as well as their possible observational and cosmological implications. In particular, cosmic strings are shown to play a crucial role in connecting particle physics models with cosmological evolution and structure formation, motivating their inclusion in anisotropic and early-Universe cosmological scenarios. Letelier started the general relativistic study of strings (Letelier [33, 34]). The study of CS has since been pursued by a number of researchers in the presence of numerous physical sources and in a variety of alternative theories of gravitation, and literature containing relevant references is abound. CS in a five-dimensional spherically symmetric background under $f(R,T)$ gravity have been considered by Naidu et al. [35]. Accelerating Bianchi type (BT) DE models with CS in gravity have been examined by Shekh and Chirde [36]. BT-I string cosmological models in $f(R)$ gravity were studied by Aditya and Reddy [37]. Sahoo et al. [38] have investigated LRS BT – I model when the source of gravitation is a mixture of barotropic fluid and DE. Scalar fields (SFs) play a fundamental role in modern cosmology, providing a natural framework to explain various phases of cosmic evolution. A SF with mass, often referred to as a massive SF (MSF), is of particular importance due to its ability to influence both the early and late-time dynamics of the Universe. In the early Universe, MSFs are commonly associated with the mechanism of inflation. A slowly rolling MSF (the inflaton) can drive a rapid exponential expansion, solving key issues such as the horizon and flatness problems, while also generating the primordial density perturbations that seeded large-scale structure formation. The potential of a MSF, typically of the form $V(\phi) = \frac{1}{2}m^2\phi^2$, provides a simple yet effective description of inflationary dynamics. Furthermore, the coupling of MSFs with other cosmic ingredients, such as CS or anisotropic backgrounds, can introduce rich phenomenology. In anisotropic cosmologies, scalar fields can contribute to isotropization, while in the presence of topological defects like CS, they can influence the energy distribution and modify the expansion history.

The choice of a plane symmetric space-time offers a mathematically tractable framework to study anisotropic cosmologies. Unlike the isotropic FLRW metric, plane symmetry allows for directional dependence in the cosmic

expansion, thereby providing a more general background to investigate the effects of anisotropy. This is particularly important because observations of the cosmic microwave background (CMB) suggest small but non-negligible deviations from perfect isotropy. Plane symmetric models are therefore useful for probing the early anisotropic phases of the Universe and for analyzing how anisotropies decay over time to yield the present nearly isotropic Universe. The inclusion of massive scalar fields (MSFs), CS, and plane symmetric space-time in cosmological models provides a deeper understanding of the Universe's evolution by bridging high-energy physics with large-scale cosmology. Together, this framework offer a broader and more realistic picture of the Universe, capable of explaining both observational signatures and theoretical challenges beyond the standard ΛCDM model. Several researchers have investigated DE models with SFs in anisotropic backgrounds to gain deeper insights into cosmic evolution [39]-[49]. Naidu et al. [50] studied BT-V DE models in general relativity with scalar meson fields, while Reddy et al. [51] explored the Kantowski–Sachs DE model in the presence of scalar meson fields. Aditya et al. [52] analyzed the Kaluza–Klein DE model in the Lyra manifold with a large scalar field, and in the framework of $f(R,T)$ gravity, Aditya and Reddy [53] investigated the BT-III DE model in the presence of a MSF. Daniel Raju et al. [54]-[56] also considered various aspects of anisotropic DE models with MSFs. Furthermore, Aditya et al. [57] discussed the BT-VI_0 DE model with scalar fields, whereas Naidu et al. [58, 59] and Bhaskara Rao et al. [60, 61] investigated anisotropic minimally interacting DE models incorporating CS and MSFs. More recently, Aditya et al. [62, 63] studied anisotropic DE models with MSFs in Lyra geometry and in the context of $f(R,T)$ gravity. Motivated by the above discussion, the present work focuses on a non-static plane symmetric cosmological model of the Universe with CS, RHDE, and a MSF as sources of gravitation within the framework of Einstein's theory. The structure of the paper is organized as follows: Section-2 is devoted to the derivation and solution of the field equations. In section-3, we analyze the cosmological parameters of the model and discuss their physical significance. Finally, section-4 summarizes the conclusions of the study.

2. FIELD EQUATIONS AND MODEL

The structure of a non-static plane symmetric space-time is described by the following metric:

$$ds^2 = e^{2A}\{dt^2 - dr^2 - r^2d\theta^2 - B^2dz^2\}, \tag{5}$$

where A and B are the metric potentials depending solely on the cosmic time t.

Using this metric, Rao et al. [64] and Aditya et al. [65, 66] have investigated various cosmological models within the framework of different modified theories of gravity. In the presence of CS, a DE fluid, and an attractive massive scalar field, Einstein's field equations take the form (with the convention $8\pi G = c = 1$)

$$R_{ij} - \frac{1}{2}Rg_{ij} = -T_{ij}^{(tot)} \tag{6}$$

and energy conservation equation is given by

$$(T_{ij}^{(tot)})_{;j} = 0 \tag{7}$$

where $T_{ij}^{(tot)} = T_{ij}^{S} + T_{ij}^{de} + T_{ij}^{msf}$ is the total energy-momentum tensor of matter distribution of the universe. Here, and T_{ij}^{S}, T_{ij}^{de} and T_{ij}^{msf} are the energy-momentum tensors of strings, DE fluid and massive scalar fields respectively. These energy-momentum tensors are defined as follows:

$$\begin{aligned} T_{ij}^{S} &= \rho u_i u_j - \lambda x_i x_j, \quad u_i u^i = 1,\ x^i x_j = -1,\ u^i x_j = 0 \\ T_{ij}^{de} &= (\rho_{de} + p_{de})u_i u_j - g_{ij}p_{de} \\ T_{ij}^{msf} &= \phi_{,i}\phi_{,j} - \frac{1}{2}(\phi_{,k}\phi^{'k} - M^2\phi^2) \end{aligned} \tag{8}$$

here, p_{de} and ρ_{de} denote the pressure and energy density of the DE fluid, ϕ represents the MSF, λ corresponds to the string tension, and M is the mass of the scalar field. The Klein–Gordon equation governing the scalar field is given by

$$g^{ij}\phi_{;ij} + M^2\phi = 0. \tag{9}$$

The Einstein field equations (6), corresponding to the metric (5) and employing the relations (8)–(9), can be expressed as

$$\frac{1}{e^{2A}}\left[\dot{A}^2 + 2\frac{\dot{A}\dot{B}}{B} + 2\ddot{A} + \frac{\ddot{B}}{B}\right] + \frac{\dot{\phi}^2}{2} - \frac{M^2\phi^2}{2} = -\omega_{de}\rho_{de} \tag{10}$$

$$\frac{1}{e^{2A}}\left[\dot{A}^2 + 2\ddot{A}\right] + \frac{\dot{\phi}^2}{2} - \frac{M^2\phi^2}{2} = \lambda - \omega_{de}\rho_{de} \tag{11}$$

$$\frac{1}{e^{2A}}\left[3\dot{A}^2 + 2\frac{\dot{A}\dot{B}}{B}\right] - \frac{\dot{\phi}^2}{2} - \frac{M^2\phi^2}{2} = \rho + \rho_{de} \tag{12}$$

$$\ddot{\phi} + M^2\phi + \dot{\phi}\left(\frac{\dot{B}}{B} + 4\dot{A}\right) = 0. \tag{13}$$

The system of field equations (10)–(13) consists of four independent equations with seven unknown parameters, namely A, B, ϕ, ω_{de}, ρ_{de}, ρ, and λ. To obtain a complete solution of this system, three additional physically motivated conditions relating these parameters are required. In this work, we consider the following physically viable conditions:

(i) The shear scalar σ^2 is assumed to be proportional to the expansion scalar θ, which leads to the following relation between the metric potentials:

$$e^A = B^n, \tag{14}$$

where n is an arbitrary constant that preserves the anisotropic nature of the space-time. Since the present Hubble expansion of the universe is isotropic to within 30%, velocity–redshift observations for extragalactic sources are consistent with this assumption (Thorne [67]; Kantowski and Sachs [68]; Kristian and Sachs [69]). Moreover, redshift analyses indicate that for the present galaxy, the constraint $\frac{\sigma}{H} \leq 0.3$ holds. Collins, et al. [70] also showed that the normal congruence to homogeneous expansion satisfies the condition that $\frac{\sigma}{H}$ remains constant.

(ii) The average scale factor $a(t)$ and the scalar field ϕ are assumed to obey a power-law relation (Johri and Sudharsan [71]; Johri and Desikan [72]):

$$\phi \propto [a(t)]^k, \tag{15}$$

where k is the power-law index. Several authors have investigated different aspects of this relation in the literature [50]–[61]. Motivated by the physical relevance of Eq. (15), we adopt the following specific form to simplify the mathematical structure of the system:

$$\phi = \phi_0\,[a(t)]^k, \tag{16}$$

where ϕ_0 is a constant. Clearly, Eq. (16) is a direct consequence of the relation in Eq. (15).

Substituting Eqs. (14) and (16) into Eq. (13), the metric potentials can be obtained as

$$e^A = (\beta_1 \sinh(\beta_2 t + b_2))^{n\beta_3}, \quad B = (\beta_1 \sinh(\beta_2 t + b_2))^{\beta_3} \tag{17}$$

and scalar field ϕ can be obtained as

$$\phi = \phi_0\,(\beta_1 \sinh(\beta_2 t + b_2))^{\frac{k\beta_3(4n+1)}{3}} \tag{18}$$

where $\beta_1 = \left[\frac{-b_1 k(4n+1)^2(k+3)}{9M^2}\right]^{\frac{1}{2}}$, $\beta_2 = \left[\frac{-M^2(k+3)}{k}\right]^{\frac{1}{2}}$, $\beta_3 = \frac{3}{(4n+1)(k+3)}$, b_1 and b_2 are integrating constants. Since Pradhan et al. [73] and Mishra et al. [74] introduced an average scale factor of the form $a(t) = [\sinh(\alpha t)]^{\frac{1}{n}}$, in the study of DE models within anisotropic backgrounds, it is worth noting that the solution obtained here is both interesting and physically viable. Their analysis demonstrated that this choice of scale factor yields several possible scenarios consistent with present cosmological observations. In particular, the hyperbolic form of the scale factor has the advantage of naturally describing a transition from an early decelerated phase of cosmic evolution to the presently observed accelerated expansion, a feature strongly supported by supernovae Ia, CMB, and BAO data. In the literature, several authors have employed this hyperbolic scale factor to explore different facets of DE models [75]–[77], including the dynamics of anisotropic universes, the role of scalar fields, and modifications of general relativity. Consequently, investigating the scalar field model with the hyperbolic solution for the scale factor given in Eq. (17) provides not only mathematical tractability but also a physically compelling framework that aligns with current cosmological observations.

Now using Eq. (17) in Eq. (5) we can write our DE model as

$$ds^2 = (\beta_1 \sinh(\beta_2 t + b_2))^{2n\beta_3}\left\{dt^2 - dr^2 - r^2 d\theta^2 - (\beta_1 \sinh(\beta_2 t + b_2))^{2\beta_3} dz^2\right\}. \tag{19}$$

The metric (19) corresponds to a RHDE model involving the MSF (18) together with CS. In this context, the following dynamical parameters play a crucial role in the physical interpretation of the model. The Hubble parameter $H(z)$ can be obtained as

$$H = \left(\frac{4n+1}{3}\right)\beta_2\beta_3 \coth(\beta_2 t + b_2) = \left(\frac{4n+1}{3}\right)\beta_2\beta_3\left(1 + \frac{\beta_1^2}{(1+z)^{\frac{3}{\beta_3(4n+1)}}}\right)$$

$$= \frac{H_0}{(1+\beta_1^2)}\left(1+\frac{\beta_1^2}{(1+z)^{\frac{3}{\beta_3(4n+1)}}}\right)^{\frac{1}{2}}$$
$$= \frac{9H_0M^2}{9M^2-b_1k(4n+1)^2(k+3)}\left[1-\frac{b_1k(4n+1)^2(k+3)}{9M^2(1+z)^{k+3}}\right]. \quad (20)$$

where $1+z=\frac{1}{a}$ and H_0 is the present value (i.e., at $z=0$) of the Hubble parameter.

3. OBSERVATIONAL CONSTRAINTS

The field equations in self-creation theory of gravity have been solved exactly, and the resulting Hubble parameter contains the five model parameters (H_0, M, b_1, k, and n). Our aim is to constrain these parameters using observational Hubble datasets in order to validate the solution in the context of the present universe. In particular, we employ a joint analysis of 31 Hubble parameter data points from cosmic chronometer (CC) measurements [78, 79]. For the statistical analysis, we implement the `emcee` Python package, which performs Markov Chain Monte Carlo (MCMC) sampling. We explore the parameter space around the local minima by adopting a Gaussian prior centered on the initial estimates, with a fixed standard deviation of $\sigma=1.0$. The final results are presented through two-dimensional contour plots, showing the constraints on the model parameters with 1σ and 2σ confidence intervals. The chi-square function employed in the analysis is defined as

$$\chi^2_H(H_0,M,b_1,k,n)=\sum_{i=1}^{31}\frac{[H_{\rm th}(z_i;H_0,M,b_1,k,n)-H_{\rm obs}(z_i)]^2}{\sigma^2_{H(z_i)}}. \quad (21)$$

At each redshift z_i, the observed Hubble parameter is denoted by $H_{\rm obs}(z_i)$, while the theoretically predicted Hubble parameter, based on the model, is expressed as $H_{\rm th}(z_i;H_0,M,b_1,k,n)$. The corresponding observational uncertainty is represented by $\sigma_{H(z_i)}$. Using the CC datasets described above, we determine the best-fit values of the parameters H_0, M, b_1, k, and n. Figure 1 presents the results in the form of two-dimensional contour plots, displaying the parameter constraints with 1σ and 2σ confidence levels. The best-fit values are obtained as

Table 1. The MCMC estimates.

Datasets	Parameters	Prior	Value
Hubble (CC Data)	H_0	$(50,100)$	68.8 ± 1.5
	M	$(0,10)$	$+4.4\pm2.0$
	b_1	$(-5,3)$	$-2.4^{+1.3}_{-1.2}$
	k	$(-3,-2)$	$-2.22^{+0.27}_{-0.30}$
	n	$(0,2)$	$+1.07^{+0.29}_{-0.19}$

The contour plots in Fig. 1 illustrate the observational constraints on the model parameters. The following observations can be made from the contours. The allowed parameter space is tightly constrained around the best-fit values, demonstrating that the CC data provides significant restrictions on the model. This confirms the robustness of the dataset in probing late-time cosmic expansion. The best-fit values of the parameters lie well within the 1σ region, indicating that the model provides an excellent fit to the observational data. This strengthens the physical viability of the model when tested against Hubble expansion measurements. The fitting results are shown in Fig. 2, where the observational data points are compared with the theoretical predictions of our model as well as with the standard ΛCDM scenario. It is evident from the figure that the trajectory of our model lies very close to that of the ΛCDM model throughout the considered redshift range ($0<z<2$). This demonstrates that the model is consistent with the observed expansion history of the Universe. The agreement between our model and ΛCDM at low redshifts ($z<1$) is particularly strong, highlighting the model's ability to reproduce the late-time accelerated expansion, which is the main success of the cosmological constant scenario. At higher redshifts ($z>1$), slight deviations from ΛCDM can be observed. Such departures may provide additional degrees of freedom in describing the transition from the matter-dominated era to the present accelerating phase, without contradicting the available data.

4. COSMOLOGICAL PARAMETERS

We will discuss the physical meaning of dynamical parameters in our DE model in the presence of MSFs and CS in this section. To plot the behavior of cosmological parameters we use the values of model parameters as $H_0=68.8$,

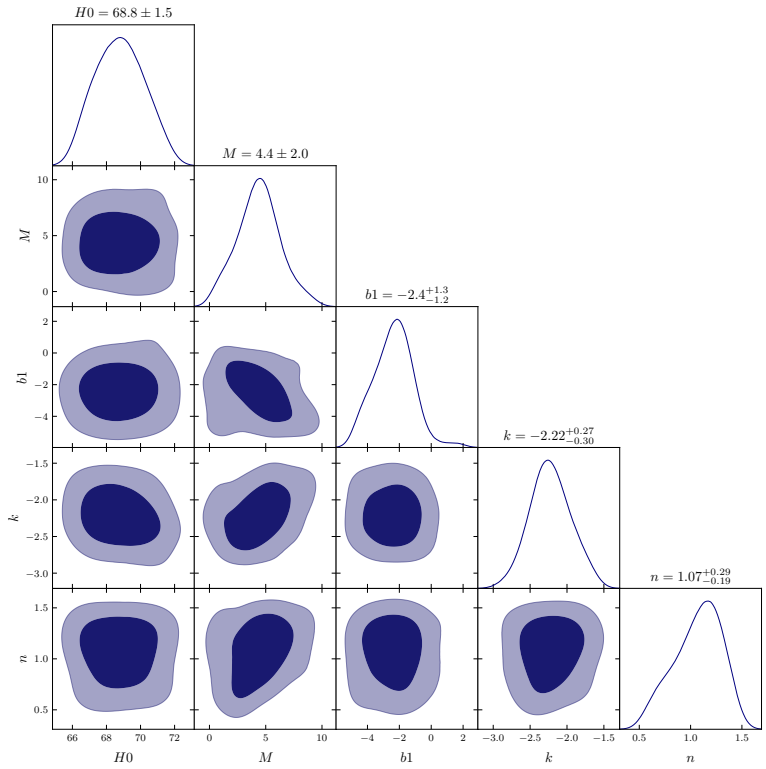

Figure 1. The plot displays the 2D contour plots of the model parameters.

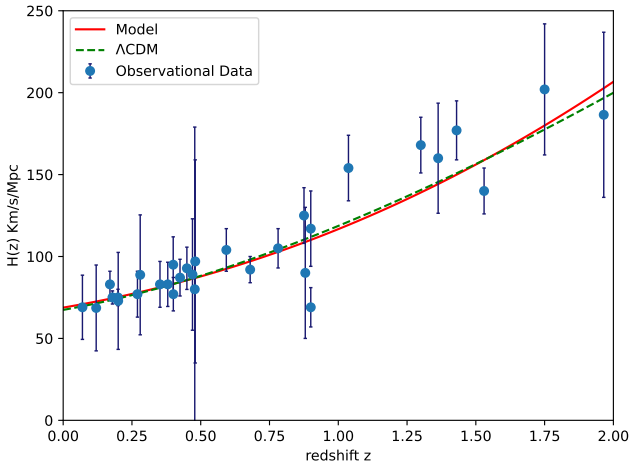

Figure 2. Evolution of Hubble parameter $H(z)$ versus redshift z. The solid line represents our model and dotted-line indicates the ΛCDM model with $\Omega_{m0} = 0.3$ and $\Omega_{\Lambda 0} = 0.7$. The dots are shown the Hubble dataset with error bar.

$M = 4.4$, $b_1 = -2.4$, $k = -2.22$, $n = 1.07$, $b_2 = 0.25$, $\phi_0 = 1 \times 10^{-7}$ and $\delta = 0.16$. The model's average scale factor ($a(t)$ and volume (V) are calculated as

$$V(t) = [a(t)]^3 = e^{4A}B = (\beta_1 \sinh(\beta_2 t + b_2))^{\frac{\beta_3(4n+1)}{3}} . \tag{22}$$

The expansion scalar θ are given by

$$\theta = \left(\frac{4n+1}{9}\right)\beta_2\beta_3 \coth(\beta_2 t + b_2) . \tag{23}$$

From Eqs. (4) and (23), we get the energy density of Renyi HDE of our model can be obtained as

$$\rho_{de} = 3\left(\frac{4n+1}{3}\right)^2 \beta_2^2\beta_3^2 \coth^2(\beta_2 t + b_2)\, d^2 \left(1 + \frac{9\pi\,\delta}{(4n+1)^2\,\beta_2{}^2\beta_3{}^2\,(\coth(\beta_2 t + b_2))^2}\right)^{-1} . \tag{24}$$

From Eqs. (11), (17) and (18) we obtain the string tension as

$$\lambda = \frac{-2n\beta_2^2\beta_3\, csch^2(\beta_2 t + b_2) + n^2\beta_2^2\beta_3^2\, \coth^2(\beta_2 t + b_2)}{(\beta_1 \sinh(\beta_2 t + b_2))^{2n\beta_3}} - \frac{-2n\beta_2^2\beta_3\, csch^2(\beta_2 t + b_2) + n^2\beta_2^2\beta_3^2\, \coth^2(\beta_2 t + b_2) + 2n\beta_2^2\beta_3^2\, \coth^2(\beta_2 t + b_2)}{(\beta_1 \sinh(\beta_2 t + b_2))^{2n\beta_3}} - \frac{\beta_2^2\beta_3\, csch^2(\beta_2 t + b_2) - \beta_2^2\beta_3^2\, \coth^2(\beta_2 t + b_2)}{(\beta_1 \sinh(\beta_2 t + b_2))^{2n\beta_3}}. \tag{25}$$

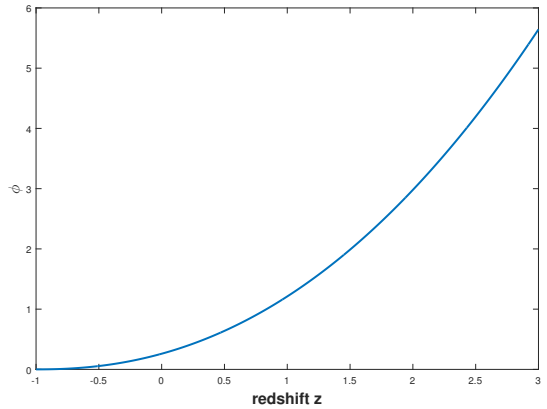

Figure 3. Plot of scalar field versus redshift.

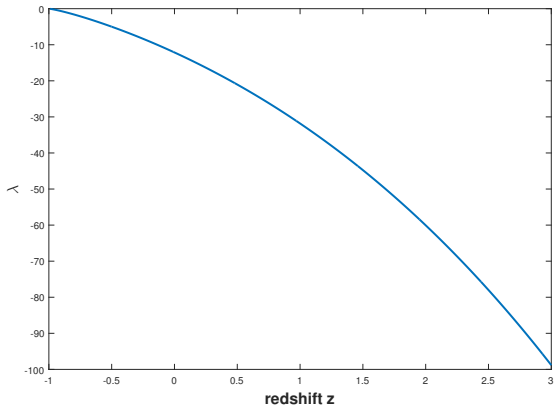

Figure 4. Plot of string tension density versus redshift.

Scalar field: The scalar field ϕ plays a fundamental role in cosmology, as it is capable of driving both the early inflationary phase and the late-time accelerated expansion of the Universe. Scalar fields play a significant role in modern cosmology, both theoretically and observationally. From a theoretical perspective, massive scalar fields naturally arise in scalar–tensor theories, modified gravity models, and higher-dimensional frameworks, where they act as additional gravitational degrees of freedom [80, 81]. In the early Universe, such fields can influence anisotropic dynamics and contribute to inflationary or pre-inflationary phases. At late times, massive scalar fields provide viable candidates for dynamical dark energy, allowing a time-dependent equation of state and enabling transitions between quintessence and phantom regimes [82, 83]. Observationally, the effects of massive scalar fields can be constrained through cosmic microwave background anisotropies, large-scale structure formation, and measurements of the expansion history using supernovae and Hubble cosmic chronometer data [84, 85]. Hence, massive scalar fields offer a physically well-motivated and observationally testable framework for describing the evolution of the Universe beyond the standard ΛCDM model. In the present model, the variation of ϕ with respect to the redshift z is depicted in Fig. 3. It is observed that the scalar field decreases monotonically with as universe evolves, starting from a high value at high redshift and attaining lowest values in the future ($z < 0$). Physically, this behaviour indicates that the scalar field was dominant in the early Universe, where its contribution to the energy density was more significant. As the Universe expanded toward the present epoch, the effective value of ϕ decreased, suggesting that its influence on the dynamics of cosmic evolution has gradually weakened. This is consistent with the idea that scalar fields could have played a key role in generating anisotropy and structure formation in the early epoch, while their contribution diminishes in the late-time Universe where DE becomes dominant.

String tension: The equation of state (EoS) of CS are restricted by the energy conditions. With $\rho > 0$ or $\lambda < 0$, the weak and strong energy conditions result in $\rho \geq \lambda$. The dominant energy conditions implies $\rho \geq 0$ and $\rho^2 \geq \lambda^2$. The signature of λ is not constrained by these energy conditions. The string tension density λ characterizes the tension or negative pressure along the direction of the strings and hence plays a significant role in determining the anisotropic nature of the Universe. In Fig. 4, the variation of λ with redshift z is displayed. It is observed that at high redshifts ($z \gtrsim 2$), the string tension density is strongly negative, with large magnitude. This suggests that in the early Universe, the contribution of string tension was significant, potentially dominating the anisotropic structure formation. As the Universe evolves towards lower redshifts, the magnitude of λ decreases monotonically. Around the present epoch ($z \approx 0$), the value of λ approaches zero, indicating that the influence of strings on the cosmic dynamics becomes negligible at late times. In the future epoch ($z < 0$), the string tension density continues to decay further toward zero, signifying that the Universe evolves toward an isotropic state where string effects vanish completely.

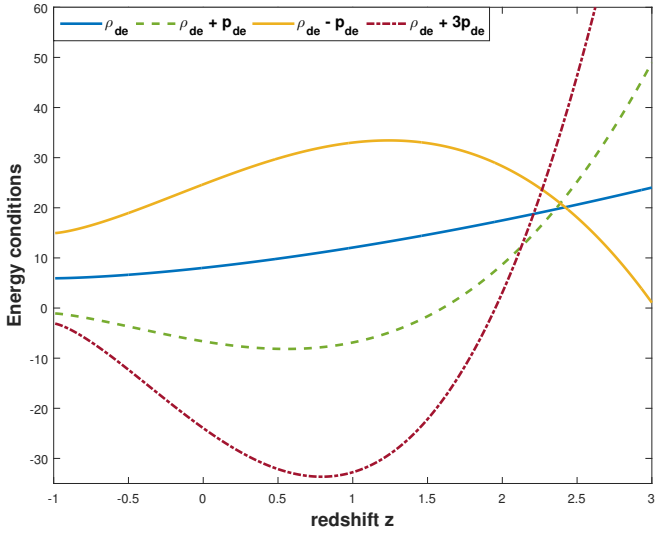

Figure 5. Plot of energy conditions versus redshift z.

Energy conditions: The energy conditions are powerful tools in general relativity and cosmology to examine the physical viability of matter and energy sources driving the cosmic dynamics. In the context of DE, these conditions provide insights into whether the model respects or violates classical energy requirements. The four commonly analyzed conditions are:

- Dominant Energy Condition (DEC): $\rho_{de} \geq 0,\ \rho_{de} \pm p_{de} \geq 0.$
- Strong Energy Condition (SEC): $\rho_{de} + p_{de} \geq 0,\ \rho_{de} + 3p_{de} \geq 0.$
- Null Energy Condition (NEC): $\rho_{de} + p_{de} \geq 0.$
- Weak Energy Condition (WEC): $\rho_{de} \geq 0,\ \rho_{de} + p_{de} \geq 0.$

In Fig. 5, the above conditions are tested for the model as a function of redshift z. In the framework of Self-Creation theory with RHDE, the evolution of energy conditions clearly reflects the cosmic history of the Universe. For $z > 0$, corresponding to the early epochs, the effective energy density ρ_{de} remains positive and the quantities $\rho_{de} + p_{de}$ and $\rho_{de} + 3p_{de}$ are also positive, ensuring the validity of the null, weak, and strong energy conditions. This behavior is consistent with a decelerated expansion dominated by matter and scalar field contributions. At the present epoch ($z = 0$), the energy density continues to be positive, while $\rho_{de} + 3p_{de}$ becomes negative, signaling the violation of the SEC. This violation marks the onset of late-time acceleration driven. For $z < 0$, representing the future evolution of the Universe, the continued violation of the NEC and SEC indicates a persistent phantom-like dark energy regime. Meanwhile, the DEC remains largely satisfied, ensuring causal energy flow. Overall, the energy conditions demonstrate a smooth transition from early-time deceleration to present and future accelerated expansion.

Deceleration parameter: The deceleration parameter $q(z)$ plays a crucial role in understanding the expansion dynamics of the Universe. By definition, it is expressed as

$$q(z) = -\frac{\ddot{a}a}{\dot{a}^2} = -1 + \frac{3\left(\text{sech}\left(\beta_2 t + b_2\right)\right)^2}{\beta_3\left(4n+1\right)} \tag{26}$$

where $a(t)$ is the scale factor, $\dot{a}$ is the expansion rate, and $\ddot{a}$ is the cosmic acceleration. The sign of $q(z)$ determines the nature of expansion. $q > 0$ corresponds to a decelerated Universe, $q = 0$ corresponds to a constant expansion rate, $-1 \leq q < 0$ indicates an accelerated expansion and $q < -1$ signifies a super-exponential or phantom-like expansion. From the plotted curve of $q(z)$ versus redshift z (see Fig. 6), the following physical interpretation can be made. At large redshift values (i.e., early epochs), the deceleration parameter is positive ($q > 0$), which corresponds to the decelerated phase. This behavior is consistent with a matter-dominated Universe, where the gravitational attraction of matter causes the expansion to slow down. Around $z \approx 1$, the curve crosses the line $q = 0$. This point indicates the transition redshift, marking the shift from decelerated expansion to accelerated expansion. Observational evidence from Type Ia supernovae and Cosmic Microwave Background measurements suggest that such a transition occurs within the range $0.5 \leq z_t \leq 1$. For smaller redshifts (at future epochs), the parameter falls into the range $-1 \leq q < 0$, which implies an accelerated expansion

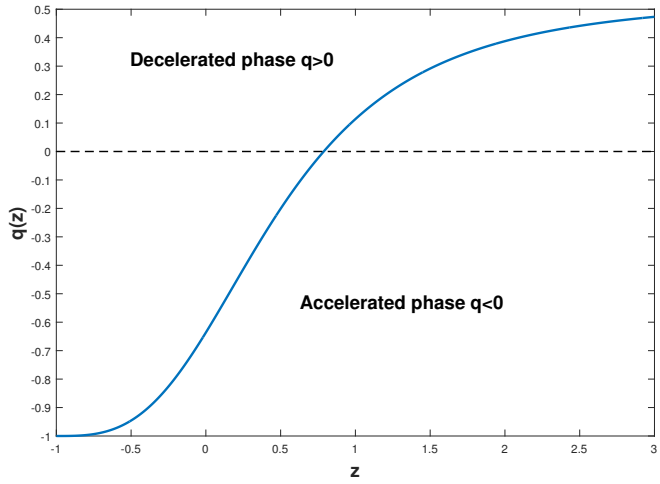

Figure 6. Plot of deceleration parameter versus redshift z.

phase. This is consistent with the presence of a DE component (such as a cosmological constant or a quintessence field) dominating the late-time cosmic dynamics. This suggests that the Universe will tend toward a de Sitter-like expansion, where the dynamics is dominated entirely by DE [86]-[89].

EoS parameter: The cosmic dynamics of the Universe can be effectively characterized by the equation of state (EoS) parameter $\omega = p/\rho$, where p and ρ represent the pressure and energy density of the cosmic fluid, respectively. Different values of ω correspond to distinct evolutionary phases of the Universe. For $\omega = 0$, the Universe is dominated by cold dark matter or dust-like fluid, giving rise to a decelerated expansion. When $0 < \omega \leq 1/3$, the dynamics correspond to the radiation-dominated era, with $\omega = 1/3$ exactly describing the radiation phase. For $\omega = 1$, the fluid is classified as stiff matter, which represents an extreme case of high-pressure matter content. For $\omega = -1$, the Universe corresponds to the cosmological constant (Λ) or vacuum energy, leading to exponential acceleration in a de Sitter phase. For $-1 < \omega < -1/3$, the expansion is accelerated and falls under the quintessence regime, where a dynamical scalar field drives the acceleration. For $\omega < -1$, the Universe enters the phantom regime, in which the energy density grows with time, potentially culminating in a "Big Rip" future singularity.

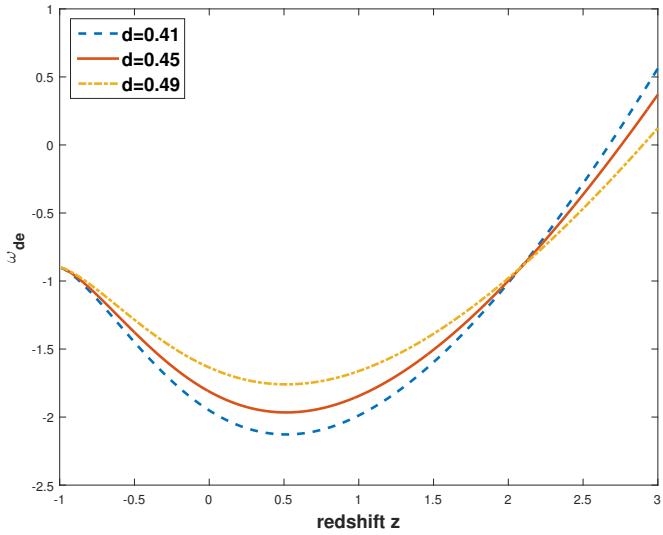

Figure 7. Plot of EoS parameter versus redshift z.

The EoS parameter (ω_{de}) of our model is obtained as

$$\omega_{de} = \frac{1}{3\left(\frac{4}{3}n+\frac{1}{3}\right)^2\beta_2^2\beta_3^2\coth^2(\beta_2 t+b_2)\,d^2}\Bigg[\frac{2n\beta_2^2\beta_3\,csch^2(\beta_2 t+b_2)-n^2\beta_2^2\beta_3^2\,\coth^2(\beta_2 t+b_2)}{\left(\beta_1\sinh(\beta_2 t+b_2)\right)^{2n\beta_3}}$$

$$-\frac{2n\beta_2^2\beta_3^2\,\coth^2(\beta_2 t+b_2)-\beta_2^2\beta_3\,csch^2(\beta_2 t+b_2)+\beta_2^2\beta_3^2\,\coth^2(\beta_2 t+b_2)}{\left(\beta_1\sinh(\beta_2 t+b_2)\right)^{2n\beta_3}}$$

$$+\tfrac{1}{2}M^2\phi_0^2\left(\beta_1\sinh(\beta_2 t+b_2)\right)^{\frac{2}{3}k\beta_3(4n+1)}$$

$$-\frac{\phi_0^2\left(\beta_1\sinh(\beta_2 t+b_2)\right)^{\frac{2}{3}k\beta_3(4n+1)}k^2\beta_3^2(4n+1)^2\beta_2^2\cosh^2(\beta_2 t+b_2)}{18\sinh^2(\beta_2 t+b_2)}\Bigg]$$

$$\times\left(1+\frac{\pi\delta}{\left(\frac{4}{3}n+\frac{1}{3}\right)^2\beta_2^2\beta_3^2\coth^2(\beta_2 t+b_2)}\right). \tag{27}$$

From Fig. 7, it is observed that at very high redshifts ($z \gtrsim 2$), the model effectively behaves close to the matter-dominated regime, ensuring consistency with the standard cosmological scenario. As the Universe evolves toward lower redshifts, the dark energy component becomes dynamically significant and the EoS parameter gradually shifts into the phantom region ($\omega_{de} < -1$), driving accelerated expansion. At the present epoch ($z = 0$), ω_{de} remains close to the cosmological constant boundary, in agreement with observational bounds. In the future evolution ($z < 0$), ω_{de} exhibits transitions between the quintessence ($-1 < \omega_{de} < -1/3$) and phantom regimes. This crossing of the phantom divide line characterizes a quintom-like behaviour, allowing a smooth transition between different acceleration phases while avoiding phantom domination.

Squared sound speed: An important diagnostic for testing the viability of DE models is the analysis of the squared sound speed $v_s^2 = \frac{\dot{p}_{de}}{\dot{\rho}_{de}} = \omega_{de} + \frac{\rho_{de}}{\dot{\rho}_{de}}\,\dot{\omega}_{de}$. The sign of v_s^2 plays a crucial role in determining the classical stability of perturbations. $v_s^2 > 0$ corresponds to a stable model where perturbations propagate without growing uncontrollably. $v_s^2 < 0$ indicates an unstable configuration, since perturbations tend to grow exponentially, leading to instabilities at the perturbative level.

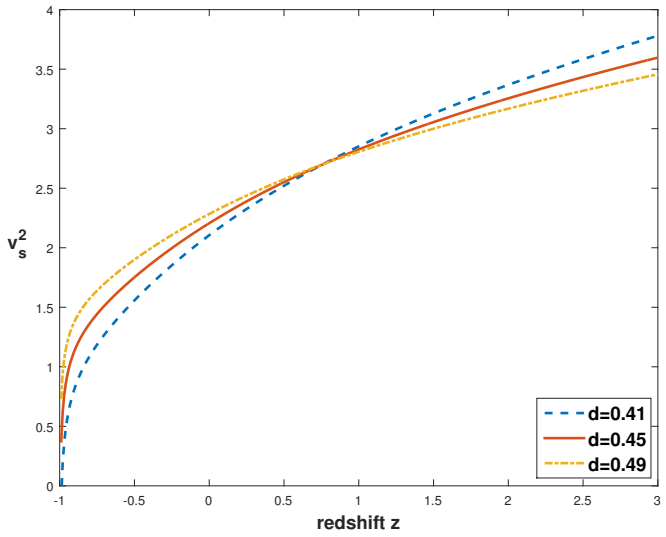

Figure 8. Plot of squared speed of sound versus redshift z.

In Fig. 8, the evolution of v_s^2 with redshift z is displayed for different values of the parameter d. It is evident that the squared speed of sound remains positive throughout the cosmic evolution for all considered parameter choices. In the early epochs ($z > 0$), particularly for $z \gtrsim 2$ corresponding to the matter-dominated era, v_s^2 maintains positive values, confirming that the model is dynamically stable during the decelerated expansion phase. At the present epoch ($z = 0$),

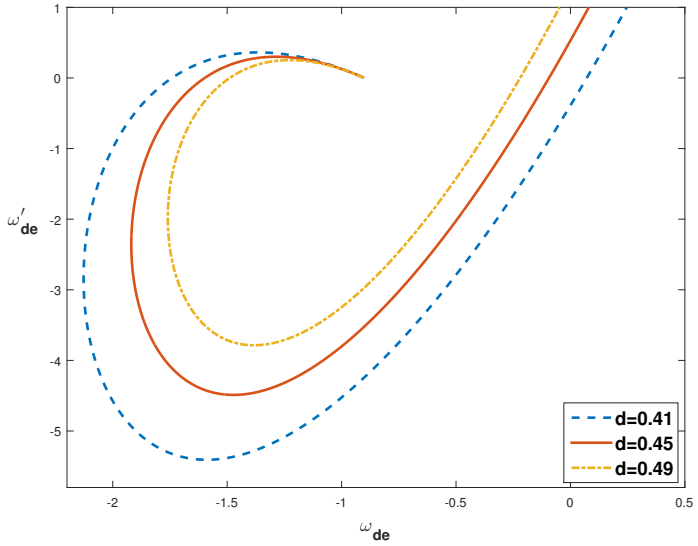

Figure 9. Plot of $\omega_{de} - \omega'_{de}$ plane.

v_s^2 continues to be positive, indicating that the current accelerated expansion driven by dark energy is free from classical instabilities. In the future evolution ($z < 0$), the squared sound speed remains positive and increases smoothly, suggesting that the dark energy fluid preserves its stability even in the late-time accelerated regime. Overall, the positivity of v_s^2 across all epochs demonstrates that the proposed model is classically stable and physically viable throughout the entire evolution of the Universe.

$\omega_{de} - \omega'_{de}$ **plane:** The dynamical nature of DE can be effectively studied through the $\omega_{de} - \omega'_{de}$ plane (Caldwell and Linder [90]), where ω_{de} is the equation of state (EoS) parameter and $\omega'_{de} = d\omega_{de}/d\ln a$ denotes its evolution with respect to the scale factor. This diagnostic is useful in distinguishing between different classes of DE models and their evolutionary behaviors. It is well established that the $\omega_{de} - \omega'_{de}$ plane can be divided into two distinct regions. Thawing region is characterized by ($\omega_{de} < 0,\ \omega'_{de} > 0$). In this regime, the DE equation of state parameter begins close to the cosmological constant value $\omega_{de} \simeq -1$ in the past and gradually increases towards higher values as the Universe evolves. Thawing models typically imply a slower rate of cosmic acceleration compared to freezing models, as the DE component evolves away from the cosmological constant behavior. Freezing region is characterized by ($\omega_{de} < 0,\ \omega'_{de} < 0$). In this regime, ω_{de} starts at values greater than -1 and gradually decreases towards -1 as the Universe evolves. Freezing models indicate a stronger acceleration rate, since the DE component asymptotically approaches a cosmological constant–like behavior in the far future.

From Fig. 9, it is observed that during the early epochs ($z > 0$), the trajectories of the model lie predominantly in the freezing region, characterized by $\omega_{de} < 0$ and $\omega'_{de} < 0$. This indicates that the dark energy component was dynamically evolving and contributed to a decelerated or mildly accelerated expansion while approaching a cosmological constant–like behavior. As the Universe evolves toward the present epoch ($z = 0$), the trajectories move closer to the boundary $\omega'_{de} = 0$, signifying a slowdown in the evolution of the equation of state parameter. In the future evolution ($z < 0$), the trajectories remain within the freezing region, implying that the dark energy gradually settles toward a stable attractor, typically associated with a de Sitter–like phase. This behavior corresponds to faster and sustained cosmic acceleration compared to thawing models. Hence, the $\omega_{de} - \omega'_{de}$ plane analysis confirms that the present model belongs to the freezing class of dark energy models, which is consistent with observational evidence of late-time accelerated expansion.

Statefinder parameters: The statefinder diagnostic, introduced by Sahni et al. [91] employs the pair of parameters (r, s) as a geometric tool to characterize and distinguish various DE models. These parameters are defined in terms of higher derivatives of the scale factor and provide a deeper insight into the cosmic expansion beyond the Hubble parameter and the deceleration parameter. They described as follows:

$$r = \frac{\dddot{a}}{aH^3}, \quad s = \frac{r-1}{3(q-\frac{1}{2})}. \tag{28}$$

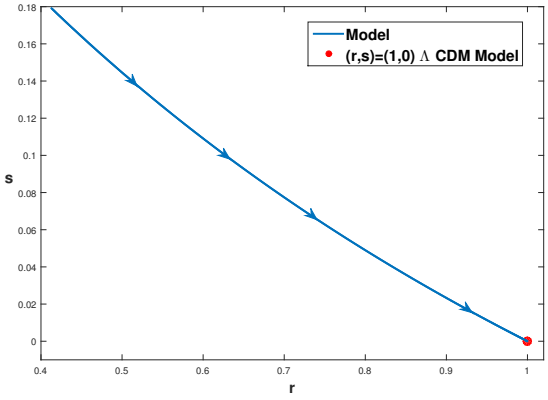

Figure 10. Plot of statefinder plane.

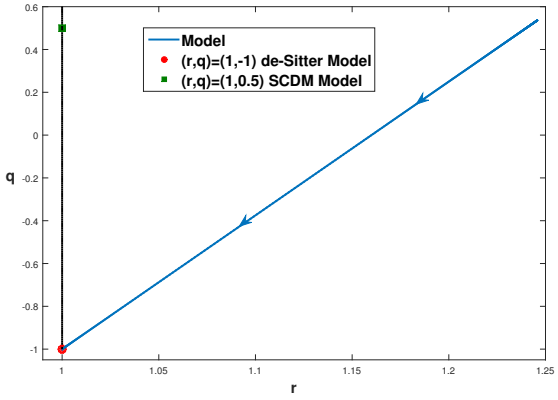

Figure 11. Plot of $r-q$ plane.

For our model statefinder parameters (r, s) are defined as

$$r = \frac{\left(\beta_1 \sinh(\beta_2 t + b_2)\right)^{\frac{1}{3}\beta_3(4n+1)}}{\left(\frac{4}{3}n + \frac{1}{3}\right)^3 \beta_2^3 \beta_3^3 \coth^3(\beta_2 t + b_2)} \left[\frac{1}{27} \frac{(4n+1)^3 \beta_2^3 \cosh^3(\beta_2 t + b_2)}{\beta_3^3 \sinh^3(\beta_2 t + b_2)}\right.$$
$$+ \frac{1}{3} \frac{(4n+1)^2 \beta_2^3 \cosh(\beta_2 t + b_2)}{\beta_3^2 \sinh(\beta_2 t + b_2)} - \frac{1}{3} \frac{(4n+1)^2 \beta_2^3 \cosh^3(\beta_2 t + b_2)}{\beta_3^2 \sinh^3(\beta_2 t + b_2)}$$
$$\left. - \frac{2}{3} \frac{\beta_3 (4n+1) \beta_2^3 \cosh(\beta_2 t + b_2)}{\sinh(\beta_2 t + b_2)} + \frac{2}{3} \frac{\beta_3 (4n+1) \beta_2^3 \cosh^3(\beta_2 t + b_2)}{\sinh^3(\beta_2 t + b_2)}\right]. \tag{29}$$

$$s = \left\{ \frac{\left(\beta_1 \sinh(\beta_2 t + b_2)\right)^{\frac{1}{3}\beta_3(4n+1)}}{\left(\frac{4}{3}n + \frac{1}{3}\right)^3 \beta_2^3 \beta_3^3 \coth^3(\beta_2 t + b_2)} \left[\frac{1}{27} \frac{(4n+1)^3 \beta_2^3 \cosh^3(\beta_2 t + b_2)}{\beta_3^3 \sinh^3(\beta_2 t + b_2)}\right.\right.$$
$$+ \frac{1}{3} \frac{(4n+1)^2 \beta_2^3 \cosh(\beta_2 t + b_2)}{\beta_3^2 \sinh(\beta_2 t + b_2)} - \frac{1}{3} \frac{(4n+1)^2 \beta_2^3 \cosh^3(\beta_2 t + b_2)}{\beta_3^2 \sinh^3(\beta_2 t + b_2)}$$
$$\left.\left. - \frac{2}{3} \frac{\beta_3 (4n+1) \beta_2^3 \cosh(\beta_2 t + b_2)}{\sinh(\beta_2 t + b_2)} + \frac{2}{3} \frac{\beta_3 (4n+1) \beta_2^3 \cosh^3(\beta_2 t + b_2)}{\sinh^3(\beta_2 t + b_2)}\right] - 1 \right\}$$
$$\times \left\{ 3 \left(-\frac{3}{2} + \frac{3 \left(\operatorname{sech}(\beta_2 t + b_2)\right)^2}{\beta_3 (4n+1)} \right) \right\}. \tag{30}$$

Notably, for $(r, s) = (1, 0)$ the model corresponds to the ΛCDM model, $(r, s) = (1, 1)$ corresponds to the CDM model without a cosmological constant. If $s > 0$, the model resides in the phantom regime, while $r < 1$ places it in the quintessence region. Both these regions indicate DE dominance. If $s < 0$ and $r > 1$, the trajectory reflects Chaplygin gas behavior, which provides an effective unification of dark matter and DE. In the $r - s$ plane (see Fig. 10), the trajectory of the present model approaches to $(r, s) = (1, 0)$, indicating its close connection with the ΛCDM cosmology at late times. As the Universe evolves, the trajectory deviates from this fixed point and moves toward regions with $r > 1$ and $s < 0$, which are characteristic of Chaplygin gas-like behavior. This implies that the model accommodates a unifying picture of cosmic evolution, transitioning from a ΛCDM-like state to a regime reminiscent of generalized Chaplygin gas. The plotted trajectory shows that our model finally behaves like ΛCDM, then departs into the $(s < 0, r > 1)$ region, demonstrating Chaplygin gas–like characteristics. This transition highlights that the model does not remain locked into a pure ΛCDM phase but instead evolves dynamically, thereby offering a richer phenomenology that could address both the early decelerated phase and the late-time accelerated expansion.

$r - q$ plane: The $r - q$ plane provides a complementary diagnostic to probe the cosmic dynamics by combining the statefinder parameter r with the deceleration parameter q. This approach not only distinguishes between different

cosmological models but also highlights the dynamical evolution of the Universe across different epochs. In Fig. 11, two important fixed points are identified. $(r, q) = (1, 0.5)$ corresponds to the Standard Cold Dark Matter (SCDM) model without a cosmological constant. In this phase, the Universe is dominated by matter, and the positive value of q indicates a decelerating expansion. This fixed point characterizes the early-time behavior of the Universe where matter played the dominant role in governing the dynamics. $(r, q) = (1, -1)$ represents the de-Sitter model, which is a cosmological constant-dominated Universe. Here, $q = -1$ corresponds to an exponentially accelerating expansion, consistent with a late-time DE dominated phase.

The trajectory of the present model starts from the vicinity of the SCDM point $(r, q) = (1, 0.5)$, indicating that the early Universe underwent a decelerated matter-dominated phase. As cosmic time evolves, the trajectory moves downward along the $r - q$ plane and asymptotically approaches the de Sitter point $(r, q) = (1, -1)$. This evolution reflects a natural transition from the decelerating epoch of matter domination to the accelerating epoch driven by DE. Physically, this behavior is highly significant. The model not only replicates the expected decelerated expansion of the early Universe but also predicts the transition to an accelerated phase consistent with current observations of late-time cosmic acceleration. Moreover, the asymptotic approach to the de Sitter point suggests that the model tends toward a ΛCDM-like cosmology in the far future, where the expansion will be dominated by an effective cosmological constant.

5. RESULTS AND CONCLUSIONS

The accelerated expansion of the Universe has attracted considerable attention from researchers around the globe. Various approaches have been proposed to investigate this phenomenon, including modified theories of gravity and a wide range of dynamical DE models. In this work, we focus on a non-static plane symmetric cosmological model incorporating RHDE, an attractive MSF, and CS within the framework of Einstein's theory of gravity. Furthermore, we examine the behavior of well-known cosmological parameters and diagnostic planes in order to analyze the physical implications of the model. To assess the viability of the proposed DE model, we have analyzed a wide range of cosmological diagnostics, including background evolution, stability, and consistency with general relativity through energy conditions. The collective discussion emerging from these diagnostics can be summarized as follows:

- At higher redshifts, λ is strongly negative, indicating a significant role of CS in early anisotropic phases. Toward the present epoch and in the future, λ approaches zero, implying that string effects dilute over time, leading to an effectively isotropic Universe. The analysis of $\phi(z)$ suggests that the scalar field has a dual role. It may have contributed significantly to the early anisotropic expansion and structure formation, and later evolved into a subdominant but still relevant component in the present epoch. This behaviour supports the viability of MSFs as effective candidates for modeling both early and late-time cosmic acceleration.

- The model exhibits a transition from a decelerated phase ($q > 0$) at high redshifts, corresponding to matter domination, to an accelerated phase ($q < 0$) at low redshifts. The transition occurs around $z \sim 1$, in agreement with observational constraints from supernovae and CMB data. In the far future ($z < 0$), q asymptotically approaches -1, signaling a de Sitter-like accelerating state. The statefinder parameters (r, s) and (r, q) serve as higher-order diagnostics to distinguish our model from ΛCDM and other DE candidates. In the (r, s) plane, the trajectory approaches to $(1, 0)$ (the ΛCDM point) and moves into the $(s < 0, r > 1)$ region, characteristic of Chaplygin gas behavior. This indicates a dynamical evolution beyond the simple ΛCDM picture. In the (r, q) plane, the model interpolates between the SCDM fixed point $(1, 0.5)$, representing a decelerating matter-dominated phase, and the de-Sitter point $(1, -1)$, representing a DE-dominated accelerated phase. This confirms that the model captures the expected cosmic history.

- The analysis of the cosmological parameters demonstrates that the proposed model provides a consistent and physically viable description of the cosmic evolution. The equation of state parameter exhibits quintom-like behavior, allowing a smooth transition across the phantom divide and supporting late-time acceleration. The deceleration parameter confirms the transition from an early matter-dominated decelerated phase to the present accelerated epoch. Stability analysis based on the squared speed of sound shows that the model remains classically stable throughout the evolution. The energy condition analysis reveals a necessary violation of the strong energy condition at late times, while the weak and null energy conditions are largely satisfied, ensuring physical plausibility. Furthermore, the $\omega_{de} - \omega'_{de}$ plane places the model in the freezing region, indicating a stable approach toward a de Sitter–like accelerated phase. Overall, these results collectively confirm that the model successfully captures the essential features of cosmic acceleration and remains compatible with observational and theoretical expectations.

Finally, the model originates in a matter-dominated, decelerating phase, subsequently undergoes a quintom-like evolution, and asymptotically approaches a de Sitter–like state in the far future. The late-time violation of the strong and null energy conditions provides the necessary mechanism for accelerated expansion, while the progressive decay of string tension facilitates the isotropization of the Universe. Altogether, the proposed framework successfully reproduces the essential features of cosmic evolution and offers a rich phenomenology that extends beyond the standard ΛCDM paradigm.

Acknowledgments

Y. Aditya is thankful to the National Board for Higher Mathematics, Department of Atomic Energy, Govt. of India for its financial support under the grant No: 02011/8/2023 NBHM(R.P.)/R & D II/3073. The authors sincerely thank the anonymous reviewer for their constructive comments and valuable suggestions, which have significantly improved the quality and presentation of this work.

ORCID

U.Y. Divya Prasanthi, https://orcid.org/0009-0004-5397-050X; **D. Tejeswararao**, https://orcid.org/0000-0003-3508-346X; **Mummidivarapu Nagaraju**, https://orcid.org/0009-0008-7272-0169; **Y. Aditya**, https://orcid.org/0000-0002-5468-9697; **G. Suryanarayana**, https://orcid.org/0000-0002-4866-4020

REFERENCES

[1] M.S. Berman, Il Nuovo Cimento B, **74**, 182 (1983). https://doi.org/10.1007/bf02721676

[2] D. Saez, V.J. Ballester, Phys. Lett. A, **113**, 467 (1986). https://doi.org/10.1016/0375-9601(86)90121-0

[3] A.G. Riess, et al., Astron. J. **116**, 1009 (1998). https://doi.org/10.1086/300499

[4] M. Tegmark, et al., Phys. Rev. D, **69**, 103501 (2004). https://doi.org/10.1103/PhysRevD.69.103501

[5] U. Seljak, et al., Phys. Rev. D, **71**, 103515 (2005). https://doi.org/10.1103/PhysRevD.71.103515

[6] E. Komatsu, et al., Astrophys. J. Suppl. **180**, 330 (2009). https://doi.org/10.1088/0067-0049/180/2/330

[7] P. Ade, et al., Astron. Astrophys. **594**, A28 (2016). http://dx.doi.org/10.1051/0004-6361/201525819

[8] N. Aghanim, et al., Astron. Astrophys. **596**, A105 (2016). https://doi.org/10.1051/0004-6361/201628636

[9] M. Li, Phys. Lett. B, **603**, 1 (2004). https://doi.org/10.1016/j.physletb.2004.10.014

[10] H. Wei, Class. Quantum Grav. **29**, 175008 (2012). https://doi.org/10.1088/0264-9381/29/17/175008

[11] M. Sharif, and A.A. Jawad, Eur. Phys. J. C, **73**, 2382 (2013). https://doi.org/10.1140/epjc/s10052-013-2382-1

[12] M. Sharif, and S. Rani, J. Exp. Theor. Phys. **119**, 75 (2014). https://doi.org/10.1134/S1063776114070152

[13] M. Tavayef, et al., Phys. Lett. B, **781**, 195 (2018). https://doi.org/10.1016/j.physletb.2018.04.001

[14] C. Tsallis, and L.J.L. Cirto, Eur. Phys. J. C, **73**, 2487 (2013). https://doi.org/10.1140/epjc/s10052-013-2487-6

[15] A.S. Jahromi, et al., Phys. Lett. B, **780**, 21 (2018). https://doi.org/10.1016/j.physletb.2018.02.052

[16] H. Moradpour, et al., Eur. Phys. J. C, **78**, 829 (2018). https://doi.org/10.1140/epjc/s10052-018-6309-8

[17] S. Nojiri, et al., Phys. Rev. D, **105**, 044042 (2022). https://doi.org/10.1103/PhysRevD.105.044042

[18] S. Maity, and U. Debnath, Eur. Phys. J. Plus, **134**, 514 (2019). https://doi.org/10.1140/epjp/i2019-12884-6

[19] Y. Aditya, et al., East European Journal of Physics, **1**, 85 (2024). https://doi.org/10.26565/2312-4334-2024-1-06

[20] B.G. Rao, et al., East European Journal of Physics, **1**, 43 (2024). https://doi.org/10.26565/2312-4334-2024-1-03

[21] Y. Aditya, and U.Y.D. Prasanthi, Bulg. Astron. J. **38**, 52 (2023). https://astro.bas.bg/AIJ/issues/n38/YAditya.pdf

[22] U.Y. Divya Prasanthi, and Y. Aditya, Results Phys. **17**, 103101 (2021). https://doi.org/10.1016/j.rinp.2020.103101

[23] U.Y. Divya Prasanthi, and Y. Aditya, Phys. Dark Univ. **31**, 100782 (2021). https://doi.org/10.1016/j.dark.2021.100782

[24] Y. Aditya,, et al., Eur. Phys. J. C, **79(12)**, 1020 (2019). https://doi.org/10.1140/epjc/s10052-019-7534-5L

[25] U.K. Sharma, and V.Ch. Dubey, Int. J. Geom. Theor. Mod. Phys. **19(1)**, 2250010 (2022). https://doi.org/10.1142/S0219887822500104

[26] S. Chunlen, and P. Rangdee, Phayao Res. Conf. **10**, 2413 (2021). https://doi.org/10.48550/arXiv.2008.13730

[27] M.V. Santhi, and T. Chinnappalanaidu, *New Astron.* **92**, 101725 (2022). https://doi.org/10.1016/j.newast.2021.101725

[28] G.E. Rao, et al., Int. J. Math. Phys. **16**, 4 (2025). https://doi.org/10.26577/ijmph.20251611

[29] Y. Aditya, Bulg. Astron. J. **40**, 95 (2024). https://astro.bas.bg/AIJ/issues/n40/YAditya.pdf

[30] Y. Aditya, et al., AIP Conf. Proc. **3298**, 040005 (2025). https://doi.org/10.1063/5.0279440

[31] Y. Aditya, et al., Afrika Matematika, **36**, 120 (2025). https://doi.org/10.1007/s13370-025-01340-7

[32] A. Vilenkin, and E. P. S. Shellard, *Cosmic Strings and Other Topological Defects*, (Cambridge University Press, 2000).

[33] P.S. Letelier, Phys. Rev. D, **20**, 1294 (1979). https://doi.org/10.1103/PhysRevD.20.1294

[34] P.S. Letelier, Phys. Rev. D, **28**, 2414 (1983). ttps://doi.org/10.1103/PhysRevD.28.2414

[35] K.D. Naidu, et al., Astrophys. Space Sci. **363**, 158 (2018). https://doi.org/10.1007/s10509-018-3380-4

[36] S.H. Shekh, and V.R. Chirde, Astrophys. Space Sci. **365**, 60 (2020). https://doi.org/10.1007/s10509-020-03772-y

[37] Y. Aditya, and D.R.K. Reddy, Int. J. Geom. Theor. Mod. Phys. **15**, 1850156 (2020). https://doi.org/10.1142/S0219887818501566

[38] P. Sahoo, et al., Can. J. Phys. **98**, 109 (2020). https://doi.org/10.1139/cjp-2019-0494

[39] U.Y.D. Prasanthi, and Y. Aditya, Results Phys. **17**, 103101 (2020). https://doi.org/10.1016/j.rinp.2020.103101
[40] U.Y.D. Prasanthi, and Y. Aditya, Phys. Dark Univ. **31**, 100782 (2021). https://doi.org/10.1016/j.dark.2021.100782
[41] M.V. Santhi, et al., Can. J. Phys. **95**, 381 (2017). https://doi.org/10.1139/cjp-2016-0781
[42] M.V. Santhi, et al., Astrophys. Space Sci. **361**, 142 (2016). https://doi.org/10.1007/s10509-016-2731-2
[43] Y. Aditya, et al., Eur. Phys. J. C, **79**, 1020 (2019). https://doi.org/10.1140/epjc/s10052-019-7534-5
[44] Y. Aditya, and D.R.K. Reddy, Astrophys. Space Sci. **364**, 3 (2019). https://doi.org/10.1007/s10509-018-3491-y
[45] Y. Aditya, and D.R.K. Reddy, Eur. Phys. J. C, **78**, 619 (2018). https://doi.org/10.1140/epjc/s10052-018-6074-8
[46] K.D. Naidu, et al., Eur. Phys. J. Plus, **133**, 303 (2018). https://doi.org/10.1140/epjp/i2018-12139-2
[47] M.V. Santhi, et al., Int. J. Geom. Methods Mod. Phys. **15**, 1850161 (2018). https://doi.org/10.1142/S021988781850161X
[48] M.V. Santhi, et al., Int. J. Theor. Phys. **56**, 362 (2017). https://doi.org/10.1007/s10773-016-3175-8
[49] M.V. Santhi, et al., Can. J. Phys. **94**, 578 (2016). https://doi.org/10.1139/cjp-2016-0099
[50] R.L. Naidu, et al., Heliyon, **5**, e01645 (2019). https://doi.org/10.1016/j.heliyon.2019.e01645
[51] D.R.K. Reddy, et al., J. Dyn. Syst. Geom. Theor. **17**, 1 (2019). https://doi.org/10.1080/1726037X.2018.1551291
[52] Y. Aditya, et al., Astrophys. Space Sci. **364**, 190 (2019). https://doi.org/10.1007/s10509-019-3681-2
[53] Y. Aditya, and D.R.K. Reddy, Astrophys. Space Sci. **364**, 3 (2019). https://doi.org/10.1007/s10509-018-3491-y
[54] K. Deniel Raju, et al., Astrophys. Space Sci. **365**, 28 (2020). https://doi.org/10.1007/s10509-020-3729-3
[55] K. Deniel Raju, et al., Astrophys. Space Sci. **365**, 45 (2020). https://doi.org/10.1007/s10509-020-03753-1
[56] K. Deniel Raju, et al., Can. J. Phys. **98**, 993 (2020). https://doi.org/10.1139/cjp-2019-0563
[57] Y. Aditya, et al., Indian J. Phys. **95**, 383 (2021). https://doi.org/10.1007/s12648-020-01722-6
[58] K.D. Naidu, et al., Int. J. Mod. Phys. A, **36**(8), 2150054 (2021). https://doi.org/10.1142/S0217732321500541
[59] R.L. Naidu, et al., New Astron. **85**, 101564 (2021). https://doi.org/10.1016/j.newast.2020.101564
[60] M.P.V.V. Bhaskara Rao, et al., New Astron. **92**, 101733 (2022). https://doi.org/10.1016/j.newast.2021.101733
[61] M.P.V.V. Bhaskara Rao, et al., Int. J. Mod. Phys. A, **36**(36), 2150260 (2021). https://doi.org/10.1142/S0217751X21502602
[62] Y. Aditya, et al., Int. J. Mod. Phys. A, **37**(16), 2250107 (2022). https://doi.org/10.1142/S0217751X2250107X
[63] Y. Aditya, Bulg. Astron. J. **39**, 12 (2023). https://astro.bas.bg/AIJ/issues/n39/YAditya.pdf
[64] V.U.M. Rao, et al., Results Phys. **10**, 469 (2018). https://doi.org/10.1016/j.rinp.2018.06.027
[65] Y. Aditya, et al., Results Phys. **12**, 339 (2019). https://doi.org/10.1016/j.rinp.2018.11.074
[66] Y. Aditya, et al., New Astron. **84**, 101504 (2021). https://doi.org/10.1016/j.newast.2020.101504
[67] K.S. Thorne, Astrophys. J. **148**, 51 (1967). https://ui.adsabs.harvard.edu/link_gateway/1967ApJ...148...51T/doi:10.1086/149127
[68] R. Kantowski, and R.K. Sachs, J. Math. Phys. **7**, 433 (1966). https://doi.org/10.1063/1.1704952
[69] J. Kristian, and R.K. Sachs, Astrophys. J. **143**, 379 (1966). https://doi.org/10.1086/148522
[70] C.B. Collins, et al., Gen. Relativ. Gravit. **12**, 805 (1980). https://doi.org/10.1007/BF00763057
[71] V.B. Johri, and K. Desikan, Gen. Relativ. Gravit. **26**, 1217 (1994). https://doi.org/10.1007/BF02106714
[72] V.B. Johri, and R. Sudharsan, Aust. J. Phys. **42**, 215 (1989). https://doi.org/10.1071/PH890215
[73] A. Pradhan, et al., Astrophys. Space Sci. **337**, 401 (2012). https://doi.org/10.1007/s10509-011-0835-2
[74] R.K. Mishra, et al., Int. J. Theor. Phys. **52**, 2546 (2013). https://doi.org/10.1007/s10773-013-1540-4
[75] V.U.M. Rao, and U.Y. Divya Prasanthi, Eur. Phys. J. Plus, **132**, 64 (2017). https://doi.org/10.1140/epjp/i2017-11328-9
[76] H. Amirhashchi, et al., Int. J. Theor. Phys. **50**, 3529 (2011). https://doi.org/10.1007/s10773-011-0861-4
[77] R.K. Mishra, et al., Int. J. Theor. Phys. **55**, 1241 (2016). https://doi.org/10.1007/s10773-015-2766-0
[78] J. Simon, L. Verde, and R. Jimenez, Phys. Rev. D, **71**, 123001 (2005). https://doi.org/10.1103/PhysRevD.71.123001
[79] G.S. Sharov, and V.O. Vasiliev, Math. Model. Geom. **6**, 1 (2018). https://doi.org/10.26456/mmg/2018-611
[80] C. Brans, and R. H. Dicke, Phys. Rev. **124**, 925 (1961). https://doi.org/10.1103/PhysRev.124.925
[81] V. Faraoni, Cosmology in Scalar-Tensor Gravity, (Springer, 2004).
[82] R. R. Caldwell, et al., Phys. Rev. Lett. **80**, 1582 (1998). https://doi.org/10.1103/PhysRevLett.80.1582
[83] B. Feng, et al., Phys. Lett. B, **607**, 35 (2005). https://doi.org/10.1016/j.physletb.2004.12.071
[84] N. Aghanim, et al., Astron. Astrophys. **641**, A6 (2020). https://doi.org/10.1051/0004-6361/201833910
[85] M. Moresco, et al., JCAP, **05**, 014 (2016). https://doi.org/10.1088/1475-7516/2016/05/014
[86] J.V. Cunha, Phys. Rev. D, **79**, 047301 (2009). https://doi.org/10.1103/PhysRevD.79.047301
[87] Z. Li, et al., Phys. Lett. B, **695**, 1 (2011). https://doi.org/10.1016/j.physletb.2010.10.044

[88] H. Amirhashchi, and S. Amirhashchi, Phys. Rev. D, **99**, 023516 (2019). https://doi.org/10.1103/PhysRevD.99.023516

[89] S. Capozziello, et al., Mon. Not. R. Astron. Soc. **484**, 4484 (2019). https://doi.org/10.1093/mnras/stz176

[90] R.R. Caldwell, and E.V. Linder, Phys. Rev. Lett. **95**, 141301 (2005). https://doi.org/10.1103/PhysRevLett.95.141301

[91] V. Sahni, et al., J. Exp. Theor. Phys. Lett. **77**, 201 (2003). https://doi.org/10.1134/1.1574831

ОБМЕЖЕННЯ СПОСТЕРЕЖЕНЬ НА ПЛОСКОМУ СИМЕТРИЧНОМУ ГОЛОГРАФІЧНОМУ ВСЕСВІТІ ТЕМНОЇ ЕНЕРГІЇ РЕНЫ ЗІ СКАЛЯРНИМИ ПОЛЯМИ ТА КОСМІЧНИМИ СТРУНАМИ

У.Й. Дів'я Прасанті[1], **Д. Техесварарао**[2], **Муммідіварапу Нагараджу**[3], **Ю. Адітья**[4], **Г. Сурьянарараяна**[5]

[1]*Департамент статистики & математики, коледж садівництва, Dr. Y.S.R. Садівничий університет, Парватіпурам-535502, Індія*

[2]*Кафедра фундаментальних та гуманітарних наук, Технологічний інститут GMR (GMRIT) – вважається університетом, Раджам-532127, Індія*

[3]*Кафедра математики, Університет Адітья, Сурампалем-533437, Індія*

[4]*Кафедра математики, Технологічний інститут GMR (GMRIT) – вважається університетом, Раджам-532127, Індія*

[5]*Кафедра математики, ANITS, Вішакхапатнам-533003, Індія*

У цій роботі ми досліджуємо космологічну модель, засновану на плоскому симетричному просторі-часі, де вміст речовини у Всесвіті описується голографічною темною енергією Реньї в рамках теорії гравітації Ейнштейна за наявності масивних скалярних полів та космічних струн. Точні розв'язки рівнянь поля отримуються, припускаючи певне співвідношення між метричними потенціалами. Спостережувальні обмеження на параметри моделі отримані з використанням найновіших даних космічного хронометра Хаббла за допомогою аналізу Монте-Карло методом ланцюгів Маркова. Отримані контурні графіки забезпечують чіткі межі для вільних параметрів, а реконструйований параметр Хаббла демонструє чудову узгодженість з моделлю ΛCDM у всьому діапазоні червоного зміщення. Детальне дослідження космологічних параметрів показує, що модель успішно відтворює стандартну космічну еволюцію. Параметр уповільнення вказує на фазу уповільнення з домінуванням матерії на ранніх епохах ($z \gtrsim 2$), після чого відбувається плавний перехід до поточної прискореної фази та асимптотичний наближення до розширення, подібного до де Ситтера, у майбутньому. Параметр рівняння стану темної енергії динамічно еволюціонує та перетинає фантомний вододіл, демонструючи поведінку, подібну до квінтома. Аналіз площини ω_{de}–ω'_{de} розміщує модель переважно в області замерзання, що вказує на стабільну та швидко прискорюючу фазу темної енергії. Діагностика Statefinder показує узгодженість з ΛCDM у сучасну епоху, з відхиленнями в бік поведінки, подібної до газоподібної Чаплигіна, на пізніх етапах часу. Крім того, аналіз енергетичних умов підтримує прискорене розширення через порушення сильного енергетичного стану на пізніх етапах часу. Загалом, модель забезпечує фізично життєздатний та спостережливо узгоджений опис космічної еволюції поза стандартним сценарієм ΛCDM.

Ключові слова: *нестатична модель; голографічна темна енергія Реньї; масивне скалярне поле; космічні струни; космологія*

East European Journal of Physics. 1. 45–59 (2026)
DOI: 10.26565/2312-4334-2026-1-04 ISSN 2312-4334

COSMOLOGICAL DYNAMICS OF TSALLIS HOLOGRAPHIC DARK ENERGY IN SAEZ-BALLESTER GRAVITY

P.E. Satyanarayana, K.V.S. Sireesha*, K.P.S. Suryanarayana, R. Sathibabu
Department of Mathematics, GSS, GITAM Deemed to be University, Visakhapatnam, India
Corresponding Author e-mail: sireeshakuppili@gmail.com
Received December 19, 2025; revised February 3, 2026; accepted February 10, 2026

- The cosmological models of Tsallis holographic dark energy (THDE) are examined within the framework of Sáez–Ballester (SB) gravity.
- Bianchi type II, VIII, and IX anisotropic universes with the Hubble horizon cutoff were analysed.
- Models extend beyond ΛCDM, predicting continuous acceleration and phantom-like behaviour ($w < -1$)
- he natural transition from the dominance of early matter to the dominance of late dark energy is reconstructed.
- Anisotropy diminishes over time, facilitating isotropization in accordance with CMB findings.
- Entropy modifications are more important than geometric differences, which shows that THDE is strong across anisotropic backgrounds.

We investigate interacting and non-interacting Tsallis Holographic Dark Energy (THDE) models within the framework of Sáez–Ballester (SB) scalar–tensor gravity for anisotropic Bianchi type(BT) II, VIII, and IX Universes. Employing the Hubble horizon as the infrared cutoff, we examine the models without assuming a particular scale factor law. The analysis covers key cosmological parameters, including the deceleration parameter, Hubble parameter, energy densities, skewness, the Equation of State (EoS), and the Squared sound speed. Our findings indicate a continuous phantom-like acceleration ($w < -1$) with transition redshift $z_t \approx 0.67$ and negligible late-time anisotropy, consistent with cosmic microwave background (CMB) bounds. Compared to ΛCDM, the THDE models predict an earlier onset of acceleration and a more negative present-day EoS. However, the presence of negative squared sound speed at higher redshifts signals a classical instability of the dark energy fluid. These results highlight THDE as a viable alternative to ΛCDM in anisotropic cosmologies, while motivating further work with alternative cutoffs or stabilising mechanisms to overcome the instability issue.

Keywords: *BT-II; VIII & IX models; Tsallis Holographic Dark Energy; Saez-Ballester theory of gravity; Cosmic acceleration; Anisotropic cosmology*

PACS: 95:30.sf, 95.35+d ,95.36+x
MSC: 85-xx, 85-08, 85A40, 85A99

1. INTRODUCTION

The understanding of the Universe has expanded significantly in recent years. It is widely assumed that around 95% of our Universe is made up of two unknown components known as dark matter (DM) and dark energy (DE). These two components generate fundamental issues and imply that fundamentally new physics should be investigated. DM constitutes approximately 25% of the Universe's total energy density (ED). While astrophysical studies on various scales have established the presence of DM, its nature remains unclear.DE is an unexplored component of our cosmos. Dark energy, distinct from ordinary baryonic matter due to its strong negative pressure, drives the Universe's expansion and constitutes over 70% of its energy density. While Einstein's cosmological constant could represent the dark energy model, its required magnitude challenges our understanding of its quantum characteristics. Unknown changes in dynamical fields or changes in General Relativity might induce DE. Cosmic microwave background (CMB) anisotropies, large-scale structure, and type-Ia supernovae are some of the cosmological advancements that allow the cosmos to expand more quickly. DE, an unexpected fluid with negative pressure, is the source of this accelerated phase. There are two explanations for the Universe's late-time acceleration. Einstein's field equations may be modified to generate dynamic DE models by modifying the matter component. Despite issues with cosmic coincidence and fine-tuning, the cosmological constant remains the most viable candidate for explaining DE. Numerous dark energy (DE) theories have been formulated to address these issues, including quintessence [1],tachyon[2],ghost [3], k-essence[4], f-essence [5, 6], phantom [7], Chaplygin gas[8], holographic dark energy (HDE) [9, 10, 11], and new-age graphic dark energy (NADE)[12, 13]. Integrating Dark Energy with Dark Matter may alleviate the cosmic coincidence problem. On the other hand, many modified gravity theories, such as f (R) theory[14],

Cite as: P.E. Satyanarayana, K.V.S. Sireesha, K.P.S. Suryanarayana, R. Sathibabu, East Eur. J. Phys. 1, 45 (2026), https://doi.org/10.26565/2312-4334-2026-1-04

f (T) theory[15], Horava-Lifshitz gravity [16, 17, 18, 19], Brans-Dicke theory [20], Gauss-Bonnet theory[21] , and f (R, T) theory [22], have been created by modifying the geometric component of the Einstein gravitational field equations. SB[23] scalar–tensor theory is a well-studied alternative to general relativity in which gravity is mediated by both the metric and a dimensionless scalar field ϕ. In this theory, the scalar field couples nontrivially to geometry while remaining dimensionless — a feature that allows for novel cosmological dynamics without the introduction of an explicit potential term. The theory has been widely applied to homogeneous and anisotropic cosmologies and has proved useful in modelling late-time acceleration, viscous fluids, and higher-dimensional cosmologies. In parallel, HDE models based on generalized (non-additive) entropy formalisms — in particular THDE have attracted attention as phenomenological alternatives to the standard cosmological constant, since the Tsallis entropy introduces a parameter that effectively modifies the DE equation of state and the cosmic evolution. Recently, several authors have combined THDE with SB gravity and investigated the cosmological consequences in FRW, Kaluza–Klein and anisotropic Bianchi backgrounds, deriving reconstruction schemes, stability/thermodynamic analyses, and interacting/non-interacting scenarios; these studies indicate that THDE in the SB framework can produce viable late-time acceleration and a rich dynamical behaviour that depends sensitively on the Tsallis parameter and the SB scalar-field coupling. For instance, Santhi and Babu[24] studied a BT-III THDE model in SB theory, showing its consistency with an accelerating universe. Dheepika and Mathew[25] reconsidered THDE models in SB gravity with improved stability analysis. Dasunaidu et al.[26] examined the Kaluza–Klein FRW THDE model and discussed the role of higher dimensions in cosmic evolution. Rao et al. [27] investigated anisotropic Sharma–Mittal HDE in SB theory, while Murali et al. [28] employed a cosmographic analysis of an anisotropic Kaniadakis HDE model, demonstrating the versatility of generalized holographic dark energy models in the SB framework. Collectively, these works highlight that SB theory, when combined with entropy-based dark energy formalisms, can successfully reproduce the evolution from slowdown to rapid acceleration, offering viable alternatives to ΛCDM. In parallel, anisotropic cosmological models, particularly BT spacetimes, provide a natural generalization of the standard FLRW universe and are especially relevant for probing the early universe, where isotropy may not yet have been established. Bianchi cosmologies are spatially homogeneous but anisotropic models classified into nine types (I–IX) according to the structure of their three-dimensional Lie groups of isometries. By allowing distinct scale factors in different spatial directions, they extend the isotropic FRW framework and offer a useful platform for studying the role of anisotropies in cosmic evolution, structure formation, and modified gravity theories. Among these, BT-II, VIII, and IX are of particular interest because they admit richer geometric structures and more complex dynamical anisotropy evolution. Embedding DE models in such anisotropic backgrounds has been shown to produce distinctive signatures in cosmic expansion, thereby providing a means to probe the role of anisotropies in the early universe. Santhi et al. [29] analysed viscous HDE theories of cosmology within the Brans–Dicke framework, whereas in SB gravity, bulk viscous string cosmological models were discussed by Rao et al. [30]. Sireesha and Rao [31, 32] contributed further by analyzing BT-II, VIII, and IX holographic dark energy models in Brans–Dicke theory, as well as modified holographic Ricci dark energy scenarios in f (R,T) gravity.More recently, Wath & Nimkar [33] investigated BT-VIII configurations in the SB framework, incorporating anisotropic dark matter and analyzing their stability and energy conditions. In order to prevent black hole creation in quantum field theory, the vacuum energy of a system of size 'L' must not be more than the mass of a black hole of the same size. This principle is used to develop the HDE model within quantum gravity. In the holographic dark energy framework, the energy density is expressed in terms of the infrared (IR) cutoff scale as

$$\rho_t = 3c^2 m_p^2 L^{-2} \tag{1}$$

Where m_p^2 represents the reduced Planck mass, the quantum field's vacuum energy density is measured against several kinds of cutoffs, including ultraviolet and infrared. Granda and Oliveros [34] introduced an infrared (IR) cutoff based on local Hubble quantities and their time derivatives. The advantages of this new HDE model, using the Granda and Oliveros cutoff, include its reliance on local quantities, avoidance of causality issues associated with the event horizon infrared cutoff, and its ability to describe the Universe's accelerated expansion. Additionally, it confirms that the evolution from a decelerating period to an accelerating period is consistent with existing data from observations [34]. Recently, the HDE model has gained interest for its ability to explain the constant ratio between DM and DE densities in the present Universe. Studies also suggest that the HDE model aligns well with observational data. Recent studies have employed various entropy formalisms to investigate gravitational and cosmological phenomena. Notably, HDE models have been examined through frameworks like THDE [35], RHDE [36], and SMHDE [37] . Sharif and Jawad [38] examined the cosmic development of interacting non-flat NHDE. Li et al. [39] employed Planck data to explore the cosmic implications of the HDE scenario. The cosmology and thermodynamics of the HDE model were examined by Praseetha and Mathew [40], who analysed the generalised second law of thermodynamics in a flat universe with interactions between DE and DM. Jawad et al.[41] conducted a study on the thermodynamic consequences of a modified HRDE model, focusing on the interaction between its energy density and that of CDM is examined under the context of Chameleon Brans-Dicke gravity. For this study, we use the HDE model with a modified entropy formalism, which is called Tsallis HDE, to reach the objective. Dubey et al. [42] examined THDE models within axially symmetric BT-I space-time, utilising the Hubble horizon as the infrared cutoff. In contrast, Dubey et al.[43] investigated THDE within a BT-I Universe, employing a hybrid expansion law in conjunction with k-essence. To date, no studies have explored the THDE model with an anisotropic background in the SB scalar-tensor theory of gravity. As a result, we investigated the dynamics of THDE in BT-II, VIII, and IX space-times using the Hubble horizon as the infrared cutoff and the SB gravity theory. Without assuming anything about the average

scale factor's expansion rule, By calculating the field equations of our proposed THDE model, we found an exact and suitable response. Aditya and Reddy suggested an anisotropic new HDE model inside the SB theory of gravity [44] . Prasanthi and Aditya[45] studied anisotropic RHDE models using general relativity as a framework. Gravitational and cosmic events have been studied using several entropy formalisms in the last few years. Tsallis generalised entropy-based THDE is intrinsically unstable at the classical level [46, 47]. Within the logarithmic Brans-Dicke (BD) theory framework, Aditya et al. [48] investigated observational limitations on interacting THDE. Two recent studies have investigated several models of THDE: Pandey et al. [49] and Kumar et al. [50], which focused on the quintessence model.

The combination of THDE, SB theory, and anisotropic Bianchi space-times thus provides a well-motivated framework to address outstanding questions about cosmic acceleration, the role of anisotropies, and deviations from Λ CDM. In particular, it enables the investigation of how generalized entropy corrections and scalar–tensor couplings influence the stability, energy conditions, and observational viability of anisotropic cosmological models. In BT-II, VIII, and IX space-times under SB gravity, with the Hubble horizon as the infrared cutoff, this study gives the field equations for interacting and non-interacting THDE models, as well as their solutions. We study the time-dependent changes in important physical characteristics and evaluate their stability in terms of the squared speed of sound, drawing qualitative comparisons to the expected general behaviour in classic Λ CDM cosmology. The study aims to evaluate whether THDE in SB theory can serve as a viable alternative to Λ CDM in anisotropic cosmologies and to explore the cosmic evolution in the initial and late universes as a result of anisotropies. Here, we take a look at the THDE models via an understanding of SB theory.

THDE is based on the non-extensive entropy formalism and provides a standard structure in which the infrared cutoff and the non-extensive parameter determine how dark energy evolves, allowing it to behave like a phantom or quintessence. The SB theory, although mathematically equivalent to general relativity with a minimally associated scalar field resulting in a field reorganization, has been extensively utilized in anisotropic contexts due to its straightforward scalar–tensor configuration and analytical manageability. In this study, THDE serves as the dynamic control of late-time acceleration, whereas the SB scalar primarily impacts early-time dynamics. This combination allows us to observe how generalised holographic dark energy evolves in anisotropic configurations and how quickly these kinds of universes become isotropic, which is the conventional ΛCDM limit.

This study is organised as follows. Section 2 formulates the field equations of SB theory, incorporating THDE and pressureless DM. Section 3 develops both non-interacting and interacting THDE cosmological models and presents their physical analysis. Section 4 outlines the key findings, observational consistency, and comparisons with the standard ΛCDM scenario. Finally, Section 5 provides a detailed discussion and conclusion, highlighting the model's implications, limitations, and prospects.

2. FIELD EQUATIONS IN SAEZ-BALLESTER'S THEORY OF GRAVITY

There have been studies of THDE in other Bianchi and scalar–tensor frameworks before, but this is the first time that the combined study of interacting and non-interacting THDE in SB gravity for the BT-II, VIII, and IX geometries with accurate analytical solutions has been addressed in depth. Previous studies predominantly concentrated on Bianchi I or III backgrounds, or on specific selections of scale components. Conversely, this study establishes the complete field equations for these three anisotropic categories, derives exact solutions based on consistent parameter relations, and examines the dynamical quantities, including the equation of state, deceleration parameter, evolution of anisotropy, and stability. This offers a more integrated and methodical analysis of THDE conduct across various anisotropic geometries. We take into account the spatially homogenous BT-II, VIII and IX metrics of the form.

$$ds^2 = dt^2 - R^2\left[d\theta^2 + f^2(\theta)\, d\phi^2\right] - S^2\left[d\psi + h(\theta)\, d\phi\right]^2 \tag{2}$$

This is when the Eulerian angles (θ, ϕ, ψ) and the functions R and S are defined exclusively with respect to 't'. When the values of $f(\theta) = 1, Cosh\theta$ & $Sin\theta$ and $h(\theta) = \theta, Sinh\theta$ & $Cos\theta$, then it represents BT -II, VIII & IX respectively.
It is essential to make clear that, employing the field modification, the SB theory under consideration is dynamically equivalent to general relativity with a minimally coupled massless scalar field $\phi = \frac{2}{n+2}\sqrt{\omega}\,\phi^{\frac{n+2}{2}}$. The scalar field effectively behaves as a stiff fluid with $\rho_\phi \propto a^{-6}$ under this mapping, and the SB action corresponds to that of an Einstein–massless–scalar (EMS) system. As a result, late-time acceleration is not possible with the SB scalar, since it disintegrates significantly more rapidly than radiation. The SB field primarily contributes to early-epoch dynamics in our model, whereas the Tsallis holographic dark energy component is the only source of the rapid expansion. By addressing the SB framework's fundamental shortcomings, this clarification strengthens the theoretical foundation for our findings. In place of Einstein's general theory of gravity, a number of gravitational theories have been proposed. Despite this, BD scalar-tensor theory is still regarded as the best substitute for the theory of Einstein. This study investigates a Universe characterised by pressure-less dark matter, with energy density ρ_m, and dark energy with density ρ_t. Consequently, utilising geometrised units 8πG =C= 1, the SB field equations for the combined scalar and tenor fields are given here by

$$G_{ij} - \omega\phi^m\left(\phi_{,i}\phi_{,j} - \frac{1}{2}g_{ij}\,\phi_{,k}\phi^{'k}\right) = -\left(T_{ij} + \bar{T}_{ij}\right) \tag{3}$$

When the scalar field meets the requirements of the equation

$$2\phi^m \phi^i{}_{,j} + m\phi^{m-1}\phi_{,k}\phi'^k = 0 \tag{4}$$

Where $G_{ij} = R_{ij} - \frac{1}{2}Rg_{ij}$ is an Einstein tensor, R is the scalar curvature, ω and m are constants, and $T_{ij} + \bar{T}_{ij}$ represents the stress-energy tensor associated with the matter and DE. We have an energy conservation equation as

$$\left(T_{ij} + \bar{T}_{ij}\right)_{;j} = 0 \tag{5}$$

The THDE energy-momentum tensor $\bar{T}_{ij}$ is structured here:

$$\bar{T}_{ij} = (\rho_t + p_t)u_i u_j - p_t g_{ij} = \text{diag}\left[1, -w_t, -w_t, -w_t\right]\rho_t \tag{6}$$

It can be parameterized as

$$\bar{T}_{ij} = \text{diag}\left[1, -w_t, -w_t, -(w_t + \gamma)\right]\rho_t \tag{7}$$

In this context, ρ_t, ρ_m represent the energy densities of THDE and matter, respectively, while p_t denotes the pressure of THDE. The equation of state (EoS) parameter is defined as $w_t = \frac{p_t}{\rho_t}$. Here, γ represents the deviation from the EoS parameter in the ψ-direction, referred to as the skewness parameter. Using Equations (6)-(7), the SB field equations for BT-II, VIII and IX Universes (2) can be expressed as follows.

$$\frac{\ddot{R}}{R} + \frac{\ddot{S}}{S} + \frac{\dot{R}\dot{S}}{RS} + \frac{S^2}{4R^4} - \frac{\omega}{2}\phi^m\dot{\phi}^2 = -w_t\rho_t \tag{8}$$

$$2\frac{\ddot{R}}{R} + \frac{\dot{R}^2 + \vartheta}{R^2} - \frac{3S^2}{4R^4} - \frac{\omega}{2}\phi^m\dot{\phi}^2 = -(w_t + \gamma)\rho_t \tag{9}$$

$$2\frac{\dot{R}\dot{S}}{RS} + \frac{\dot{R}^2 + \vartheta}{R^2} - \frac{S^2}{4R^4} + \frac{\omega}{2}\phi^m\dot{\phi}^2 = \rho_m + \rho_t \tag{10}$$

$$\ddot{\phi} + \dot{\phi}\left(2\frac{\dot{R}}{R} + \frac{\dot{S}}{S}\right) + \frac{m\dot{\phi}^2}{2\phi} = 0 \tag{11}$$

$$\dot{\rho}_m + \dot{\rho}_t + \left(2\frac{\dot{R}}{R} + \frac{\dot{S}}{S}\right)(\rho_m + (1 + w_t)\rho_t) + \gamma\frac{\dot{S}}{S}\rho_t = 0 \tag{12}$$

When $\vartheta = 0, -1\ \&1$, the cosmological models correspond to BT-II, VIII and IX, respectively.

3. THDE COSMOLOGICAL MODELS

The standard cosmological model depends on isotropy; however, anisotropic Bianchi universes function as significant theoretical frameworks for examining the durability of dark-energy models, the methodology for achieving isotropy, and initial departures from the FLRW baseline. Current Planck CMB observations only limit the present-day shear to be very minimal; they do not rule out the existence of anisotropies in older epochs. Bianchi models enable the investigation of whether THDE dynamics fundamentally accelerate the Universe towards isotropy in later epochs, a crucial criterion for alignment with observations.

By addressing the nonlinear field equations with certain physically reasonable assumptions, we develop THDE cosmological models. To achieve a deterministic solution, we rely on the following physically plausible condition:

- The shear scalar σ^2 is proportional to the scalar expansion θ, establishing a relationship between the metric potentials.

$$S = R^n \tag{13}$$

From equations (8),(9)and (13), we get

$$\frac{\ddot{R}}{R} + (1 + n)\frac{\dot{R}^2}{R^2} + \frac{\vartheta}{(1 - n)R^2} - \frac{R^{2n-4}}{1 - n} = \frac{\gamma\rho_t}{n - 1}, \qquad n \neq 1 \tag{14}$$

To solve Equation (14) , we adopt the following physically reasonable assumption.

$$\gamma = \frac{\gamma_0(n - 1)}{\rho_t} \text{ for BT-II model} \tag{15}$$

$$\gamma = \frac{\gamma_0(n - 1)R^2 + 1}{\rho_t R^2} \text{ for BT-VIII model} \tag{16}$$

$$\gamma = \frac{\gamma_0(n - 1)R^2 - 1}{\rho_t R^2} \text{ for BT-IX model} \tag{17}$$

Where γ_0 is an arbitrary constant. from equations (14) & (15), we get the metric potentials

$$R = \left[\frac{C_1}{C_2}\,\mathrm{sech}(C_1(2-n)t)\right]^{\frac{1}{n-2}} \tag{18}$$

$$S = \left[\frac{C_1}{C_2}\,\mathrm{sech}(C_1(2-n)t)\right]^{\frac{n}{n-2}} \tag{19}$$

Where $C_1^2 = \frac{\gamma_0}{2(n+2)}$ and $C_2^2 = \frac{1}{4n(n-1)}$. Substituting the values of R and S in Equations (18)and (19), we find that the scalar field.

$$\phi^{\frac{m+2}{2}} = \left(\frac{m+2}{2}\right)\left\{C\left(\frac{C_2}{C_1}\right)^{\frac{n+2}{n-2}}\int\left[\cosh\left(C_1(2-n)t\right)\right]^{\frac{n+2}{n-2}}\,dt\right\} \tag{20}$$

Where C is constant. Using the metric potentials (18) and (19) in the metric (2), we can write

$$\begin{aligned} ds^2 = dt^2 &- \left[\frac{C_1}{C_2}\,\mathrm{sech}(C_1(2-n)t)\right]^{\frac{2}{n-2}}\left[d\theta^2 + f^2(\theta)\,d\phi^2\right] \\ &- \left[\frac{C_1}{C_2}\,\mathrm{sech}(C_1(2-n)t)\right]^{\frac{2n}{n-2}}\left[d\psi + h(\theta)\,d\phi\right]^2 \end{aligned} \tag{21}$$

Equation (20) specifies the BT-II, VIII and IX THDE cosmological models in the SB scalar-tensor theory of gravity, as well as the following properties:

1. In anisotropic geometries, different spatial directions expand at distinct rates, which may lead to direction-dependent observational effects such as anisotropic redshifts.
2. The global expansion of the universe is characterized by the average scale factor $a(t) = (ABC)^{\frac{1}{3}}$, which allows us to derive analytical expressions and investigate the overall dynamical behavior of the model.
3. A detailed confrontation with observational data would require a direction-dependent analysis of luminosity distance and Hubble flow, which lies beyond the scope of the present work and is left for future investigation.

With the anisotropic framework and average expansion established, we now investigate the physical properties of the model, including the spatial volume, expansion scalar, shear scalar, anisotropy parameter, Hubble parameters, and the deceleration parameter, which together characterize the dynamical behavior of the universe.
The volume of space is

$$V = R^2S = \left[\frac{C_1}{C_2}\,\mathrm{sech}\big(C_1(2-n)t\big)\right]^{\frac{n+2}{n-2}} \tag{22}$$

The scale factor, on average, is

$$a(t) = V^{\frac{1}{3}} = \left[\frac{C_1}{C_2}\,\mathrm{sech}\big(C_1(2-n)t\big)\right]^{\frac{n+2}{3(n-2)}} \tag{23}$$

The scalar equations for expansion and shear are

$$\begin{aligned} \theta = 3H &= (n+2)C_1\tanh\left(C_1(2-n)t\right) \\ \sigma^2 &= \frac{7}{18}\theta^2 = \frac{7}{18}\left[(n+2)C_1\tanh\left(C_1(2-n)t\right)\right]^2 \end{aligned} \tag{24}$$

The deceleration parameter for our model is provided by

$$q = -\frac{3\dot{\theta}}{\theta^2} - 1 = \frac{n-2}{n+2}cosech^2\big(C_1(2-n)t\big) - 1 \tag{25}$$

The graph presents the deceleration parameter versus redshift in the framework of THDE, showcasing a persistent and intensifying cosmic acceleration. Covering a redshift range of $z = 2.5$ to $z = -1$, the curve remains negative throughout, indicating that the Universe is in a continuous accelerated expansion phase. Notably, as z increases beyond approximately 2, the deceleration parameter sharply drops to tremendous negative values, reflecting an intense acceleration in the early Universe. As a result, the THDE framework predicts a dominant and phantom-like DE influence even in the early Universe. The absence of any transition to a decelerating phase, as seen in standard models like Λ CDM, underlines the non-trivial role of THDE in cosmic dynamics and establishes it as a compelling candidate to explain the Universe's super-accelerated expansion throughout its history, especially within anisotropic cosmological backgrounds. However, the super-exponential expansion ($q < -1$) would indicate that the rate of acceleration in the Tsallis model is more rapid or intense than the Λ CDM model.

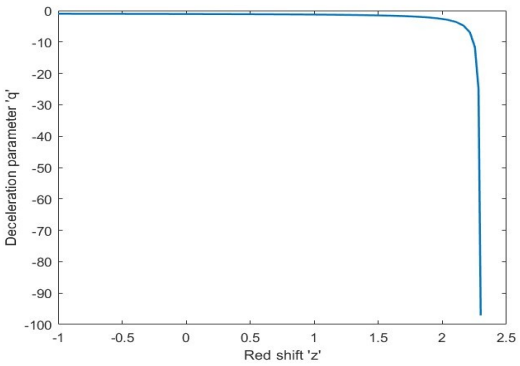

Figure 1. Deceleration parameter plotted against redshift for the SB cosmology for $\gamma_0 = 6.5$ & $n = 1.5$.

For our model, the Hubble parameter(H) can be obtained as

$$H = \frac{(n+2)C_1}{3} \tanh\left(C_1(2-n)t\right) \tag{26}$$

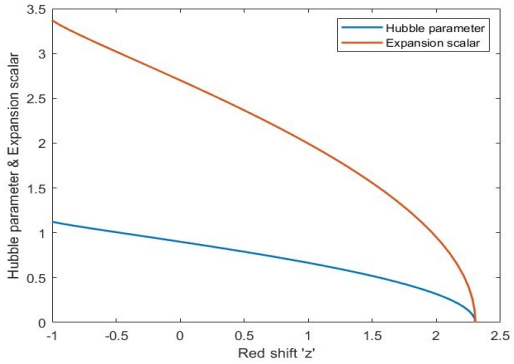

Figure 2. Hubble parameter and the Expansion scalar are plotted against redshift for the SB cosmology for $\gamma_0 = 6.5$ & $n = 1.5$.

The graph depicting the Hubble parameter and expansion scalar versus redshift in the THDE framework reveals crucial insights into the Universe's dynamic evolution. These two critical observable cosmological elements are essential to the Universe's expansion rate. The Hubble parameter and the expansion scalar graphs demonstrate that they are positive-valued accelerating cosmic time functions over extended periods. As redshift increases, both the Hubble parameter (H) and expansion scalar (θ) exhibit a monotonically decreasing trend, indicating that the Universe expanded rapidly in the future and slowed down in the past. This decline becomes particularly steep as redshift increases, where both parameters tend toward zero, suggesting a suppressed expansion phase in the early Universe. These results imply that DE, influenced by Tsallis entropy, could have played a significant role even during the early cosmic epochs, driving a phantom-like accelerated expansion in the future and decelerated behavior in the deep past. The combined analysis of H and θ confirms the robustness of THDE in explaining the Universe's expansion history beyond conventional ΛCDM scenarios.
The following relationship gives THDE energy density.

$$\rho_t = \alpha L^{2\delta-4} \tag{27}$$

In this context, α is a constant, L represents the current size of the Universe, such as the Hubble scale or the future event horizon, and δ is a free parameter. It can be demonstrated that when $\delta = 1$, the energy density ρ_t the THDE model reduces to that of the standard holographic dark energy (HDE) model. The Hubble horizon, defined as $L = H^{-1}$, where H is the Hubble parameter of the model, serves as the system's infrared (IR) cutoff. As a result, the energy density (27) has the form of the SB theory.

$$\rho_t = \alpha H^{4-2\delta} \tag{28}$$

From Equations (26) and (28), we get the energy density of the THDE as

$$\rho_t = \alpha \left[\frac{(n+2)C_1}{3} \tanh\left(C_1(2-n)t\right) \right]^{4-2\delta} \tag{29}$$

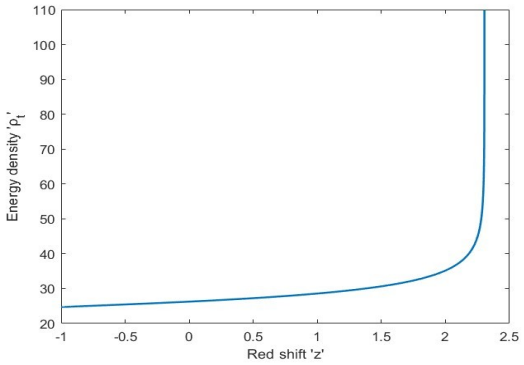

Figure 3. Energy density plotted against redshift for the SB cosmology for $\gamma_0 = 6.5$, $n = 1.5$, $\alpha = 25.5$, & $\delta = 2.14$

The graph illustrates the evolution of the energy density concerning the redshift in the context of THDE. Here, the redshift axis spans from 2.5 (early Universe) to -1 (future Universe), while the energy density sharply increases as redshift increases. This rising trend implies that as we move backward in time (toward higher redshift), the total energy density of the Universe intensifies dramatically. The energy density of DE remains constant throughout the Universe's evolution, as it is associated with the cosmological constant, which does not change with time or the Universe's expansion. The graph suggests that as the Universe evolves in the Tsallis model, the energy density does not become negative and increases as the redshift increases. Due to non-extensive entropy corrections, THDE allows for a phantom-like energy density growth in the early Universe, suggesting a denser and more dynamically evolving DE component. This sharp growth in energy density reflects the increased contribution of THDE to the total energy of the cosmos at higher redshifts, reinforcing the idea that Tsallis entropy plays a crucial role not only in present-day acceleration but also in shaping the early Universe's energetic state.
Using equations (10),(18),(19)& (26), we get the energy density of matter as

$$\begin{aligned}\rho_m =& (2n+1)C_1^2 \tanh^2\left(C_1(2-n)t\right) - \frac{1}{4}\left[\frac{C_1}{C_2}\operatorname{sech}\left(C_1(2-n)t\right)\right]^2 \\ &+ \frac{\omega}{2}C_3^2\left[\frac{C_1}{C_2}\operatorname{sech}\left(C_1(2-n)t\right)\right]^{\frac{2(n+2)}{2-n}} - \alpha\left[\frac{(n+2)C_1}{3}\tanh\left(C_1(2-n)t\right)\right]^{4-2\delta}\end{aligned} \tag{30}$$

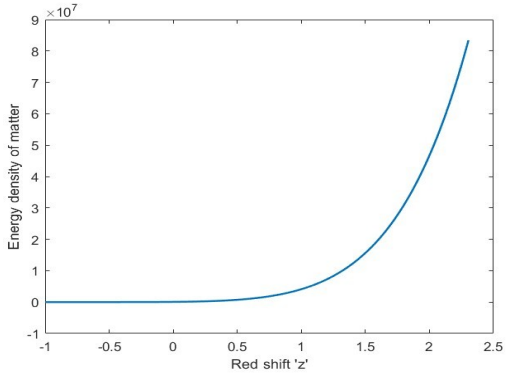

Figure 4. Energy density of matter plotted against redshift for the SB cosmology for $\gamma_0 = 6.5$, $n = 1.5$, $\alpha = 25.5$, & $\delta = 2.14$

The graph depicts the energy density of matter as a function of redshift (z) in the context of THDE. The plot shows that the energy density of matter increases sharply with redshift. This is consistent with cosmological expectations: in the

earlier Universe (corresponding to higher z), the energy density of matter was significantly higher. The curve is nearly flat, indicating a slow variation in the recent Universe, but it rises exponentially beyond that, reflecting the dominance of matter in the early Universe. In the THDE model, the matter energy density evolves differently than in standard cosmology due to the non-additive entropy formalism. THDE modifies the energy conservation and Friedmann equations, and hence, this curve helps us understand how matter dilutes in a THDE-driven Universe. The steep growth at higher redshifts indicates a more substantial influence of matter in the early Universe, while DE becomes dominant at lower redshifts. From equations (15)-(17) & (26), we get the skewness parameter for BT-II, VIII & IX cosmological models as

$$\gamma = \frac{\gamma_0(n-1)}{\alpha\left[\frac{(n+2)C_1}{3}\tanh(C_1(2-n)t)\right]^{4-2\delta}} \quad \text{For BT-II model} \tag{31}$$

$$\gamma = \frac{\gamma_0(n-1)\left[\left(\frac{C_1}{C_2}\right)\mathrm{sech}(C_1(2-n)t)\right]^{\frac{2}{n-2}}+1}{\alpha\left[\frac{(n+2)C_1}{3}\tanh(C_1(2-n)t)\right]^{4-2\delta}\left[\left(\frac{C_1}{C_2}\right)\mathrm{sech}(C_1(2-n)t)\right]^{\frac{2}{n-2}}} \quad \text{for BT-VIII model} \tag{32}$$

$$\gamma = \frac{\gamma_0(n-1)\left[\left(\frac{C_1}{C_2}\right)\mathrm{sech}(C_1(2-n)t)\right]^{\frac{2}{n-2}}-1}{\alpha\left[\frac{(n+2)C_1}{3}\tanh(C_1(2-n)t)\right]^{4-2\delta}\left[\left(\frac{C_1}{C_2}\right)\mathrm{sech}(C_1(2-n)t)\right]^{\frac{2}{n-2}}} \quad \text{for BT-IX model} \tag{33}$$

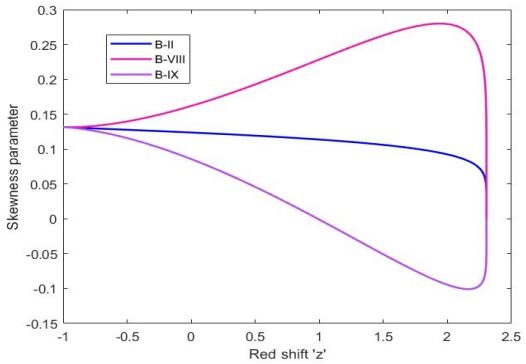

Figure 5. Skewness parameter plotted against redshift for the SB cosmology for $\gamma_0 = 6.5$, $n = 1.5$, $\alpha = 25.5$, & $\delta = 2.14$

The anisotropy parameters always go down as the universe expands. For the parameter choices we looked at, the current value of the dimensionless shear $\frac{\sigma}{H}$ is considerably below the Planck limit. This indicates that the model isotropies are established quickly enough and align with the observationally inferred near-isotropy of the cosmic microwave background.

The graph illustrates the variation of the skewness parameter with redshift for BT-II, VIII & IX in the framework of THDE. The skewness parameter, which reflects anisotropic deviations in the Universe's expansion, behaves differently across these models. The BT-II model shows a slow and nearly linear increase, indicating weak and stable anisotropy throughout cosmic evolution. In contrast, the BT-IX models exhibit symmetric and prominent peaks, showing strong anisotropic effects in the early Universe that diminish over time. This trend highlights the transition from an early anisotropic phase to a more isotropic Universe at lower redshifts. In the THDE scenario, the evolution of these anisotropies is governed by the generalized entropy formalism, which modifies the dynamics of the Universe and supports observational consistency with an increasingly isotropic late-time cosmos.

3.1. Non-Interacting THDE Scenario

To begin, we assume that there is no energy exchange between the two components (dark sectors), and hence, the energy conservation equation (12) yields the following independent conservation equations:

$$\dot{\rho}_m + 3H\rho_m = 0 \tag{34}$$

$$\dot{\rho}_t + 3H(1+w_t)\rho_t + \gamma\frac{\dot{S}}{S}\rho_t = 0 \tag{35}$$

We can determine the EoS parameter of THDE for the BT-II, VIII and IX models using the previously mentioned equations.

$$w_t = -1 - \frac{1}{(n+2)C_1}\coth(C_1(2-n)t) \left\{ \frac{\gamma_0 n(n-1)C_1}{\alpha}\left[\frac{(n+2)C_1}{3}\tanh(C_1(2-n)t)\right]^{2\delta-4} \times \right. \left. \tanh(C_1(2-n)t) + 4C_1(2-\delta)(2-n)\ \mathrm{cosech}(2C_1(2-n)t) \right\}. \tag{36}$$

$$w_t = -1 - \frac{1}{(n+2)C_1}\coth(C_1(2-n)t) \left\{ \frac{\gamma_0(n-1)\left[\frac{C_1}{C_2}\,\mathrm{sech}(C_1(2-n)t)\right]^{\frac{2}{n-2}}+1}{\alpha\left(\frac{(n+2)C_1}{3}\tanh(C_1(2-n)t)\right)^{4-2\delta}\left(\frac{C_1}{C_2}\,\mathrm{sech}(C_1(2-n)t)\right)^{\frac{2}{n-2}}} \times \right. \left. \tanh(C_1(2-n)t) + 4C_1(2-\delta)(2-n)\,\mathrm{cosech}(2C_1(2-n)t) \right\} \tag{37}$$

$$w_t = -1 - \frac{1}{(n+2)C_1}\coth(C_1(2-n)t) \left\{ \frac{\gamma_0(n-1)\left[\frac{C_1}{C_2}\,\mathrm{sech}(C_1(2-n)t)\right]^{\frac{2}{n-2}}-1}{\alpha\left(\frac{(n+2)C_1}{3}\tanh(C_1(2-n)t)\right)^{4-2\delta}\left(\frac{C_1}{C_2}\,\mathrm{sech}(C_1(2-n)t)\right)^{\frac{2}{n-2}}} \times \right. \left. \tanh(C_1(2-n)t) + 4C_1(2-\delta)(2-n)\,\mathrm{cosech}(2C_1(2-n)t) \right\} \tag{38}$$

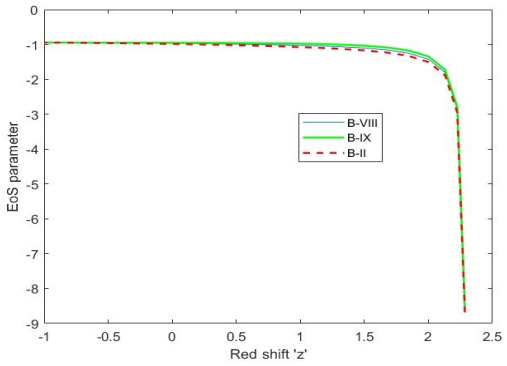

Figure 6. EoS parameter plotted against redshift for the SB cosmology for $\gamma_0 = 6.5$, $n = 1.5$, $\alpha = 25.5$, & $\delta = 2.14$

The graph illustrates the evolution of the EoS parameter with respect to redshift z for the non-interacting BT-II, VIII & IX cosmological models within the framework of THDE. The EoS parameter is a key quantity that characterizes the nature of DE by defining the relationship between pressure and energy density. In this plot, all three Bianchi models show EoS values very close to -1 across a wide range of redshift, indicating that the THDE behaves similarly to the cosmological constant (ΛCDM). As redshift increases, the EoS parameter drops sharply, suggesting a phantom-like behavior ($w_t < -1$) in the early Universe. The differences between the Bianchi types are minor, with BT-IX slightly above BT-II and BT-VIII, but overall, they follow a nearly identical trend. This behavior reflects the THDE model's flexibility in mimicking both cosmological constant-like and phantom phases, depending on cosmic time and geometry. It also confirms that THDE can describe the late-time acceleration of the Universe consistently across different anisotropic Bianchi backgrounds. The squared speed of sound is used to test the stability of our non-interacting THDE model against moderate disturbances in this situation. It can be defined as follows :

$$v_s^2 = \frac{\dot{p}_t}{\dot{\rho}_t} \tag{39}$$

By differentiating the relation $w_t = \frac{p_t}{\rho_t}$ with respect to time t, and dividing by $\dot{\rho}_t$, we obtain

$$v_s^2 = w_t + \frac{\rho_t}{\dot{\rho}_t}\dot{w}_t \tag{40}$$

$$v_s^2 = w_t + \frac{\dot{w}_t}{4C_1(2-\delta)(2-n)\ \mathrm{cosech}(2C_1(2-n)t)} \tag{41}$$

The sign of the square of the speed of sound is essential since its negative ($v_s^2 < 0$), denotes instability and vice versa.

Our findings indicate a classical gradient instability, as the squared sound speed of the THDE fluid becomes negative at sufficiently high redshifts. This kind of instability means that modest changes can develop exponentially, which could make the model physically impossible unless more stabilising processes are added. Possible improvements include using different infrared cutoffs, such as the Granda-Oliveros scale, adding a weak self-interaction potential for the SB scalar, or allowing non-minimal interactions between the matter and dark energy sectors. In future studies, we will do a more thorough perturbation analysis.

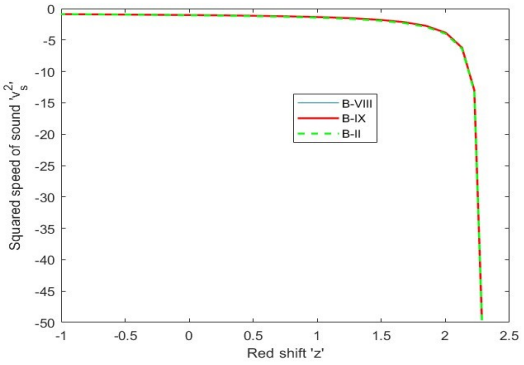

Figure 7. Squared sound speed plotted against redshift for the SB cosmology for $\gamma_0 = 6.5$, $n = 1.5$, $\alpha = 25.5$, & $\delta = 2.14$

The figure demonstrates a consistent and concerning behaviour across the BT-II, VIII & IX configurations of the THDE model. While these models exhibit a near-zero or slightly negative squared speed of sound at recent and moderate redshifts, they universally predict a sharp and significant drop into strongly negative values of v_s^2 at higher redshifts. This plunge into negative squared speed of sound signifies a severe classical instability for the DE fluid in the early Universe, suggesting that density perturbations would grow exponentially. Such pronounced instabilities at relatively observable redshifts present a major obstacle for these THDE models to be considered physically realistic candidates for DE, as a smooth and stable DE component is generally required to explain the observed large-scale homogeneity of the Universe and its accelerated expansion.

3.2. Interacting THDE Scenario

The interaction of the two fluids is considered here. Because the nature of DE and DM is yet unclear, there is no physical reason to rule out the possibility of interaction. Some observational evidence of the exchange in dark sectors has recently been reported [51, 52]. Abdalla et al. [53, 54] used optical, X-ray, and weak lensing data from relaxed galaxy clusters to study the signs of interaction between DE and DM. Assuming the relationship between DE and DM is acceptable in cosmology. We may express the energy conservation equations as follows for this purpose:

$$\dot{\rho}_t + 3H(1+\omega_t)\rho_t + \gamma\frac{\dot{S}}{S}\rho_t = -Q \tag{42}$$

$$\dot{\rho}_m + 3H\rho_m = Q \tag{43}$$

Where Q indicates the relationship between DE components. Equations (42) and (43) show that total energy is conserved. Because fundamental physics provides no natural information on the interaction term Q, it can only be studied phenomenologically. Among the many types of interaction terms extensively discussed in the literature are: $Q = 3cH\rho_m$, $Q = 3cH\rho_t$ and $Q = 3cH(\rho_m + \rho_t)$. Here c is a coupling constant; positive c indicates that DE decays into DM, while negative c indicates that DM decays into DE. We assume $Q = 3\beta H\rho_t$ as the interaction term with the coupling parameter β in this case. We may calculate the EoS parameter using the previous equations.

$$w_t = -1 - \beta - \frac{1}{(n+2)C_1}\coth(C_1(2-n)t) \left\{ \begin{array}{c} \frac{\gamma_0 n(n-1)C_1}{\alpha}\left[\frac{(n+2)C_1}{3}\tanh(C_1(2-n)t)\right]^{2\delta-4}\times \\ \tanh(C_1(2-n)t) + 4C_1(2-\delta)(2-n)\,\mathrm{cosech}(2C_1(2-n)t) \end{array} \right\} \tag{44}$$

$$w_t = -1 - \beta - \frac{1}{(n+2)C_1}\coth\left(C_1(2-n)t\right)$$

$$\left\{ \begin{array}{c} \frac{\gamma_0(n-1)\left(\frac{C_1}{C_2}\,\mathrm{sech}\left(C_1(2-n)t\right)\right)^{\frac{2}{n-2}}+1}{\alpha\left(\frac{(n+2)C_1}{3}\tanh\left(C_1(2-n)t\right)\right)^{4-2\delta}\left(\frac{C_1}{C_2}\,\mathrm{sech}\left(C_1(2-n)t\right)\right)^{\frac{2}{n-2}}}\times \\ \tanh\left(C_1(2-n)t\right)+4C_1(2-\delta)(2-n)\,\mathrm{cosech}\left(2C_1(2-n)t\right) \end{array} \right\} \tag{45}$$

$$w_t = -1-\beta-\frac{1}{(n+2)C_1}\coth\left(C_1(2-n)t\right)$$

$$\left\{ \begin{array}{c} \frac{\gamma_0(n-1)\left(\frac{C_1}{C_2}\,\mathrm{sech}\left(C_1(2-n)t\right)\right)^{\frac{2}{n-2}}-1}{\alpha\left(\frac{(n+2)C_1}{3}\tanh\left(C_1(2-n)t\right)\right)^{4-2\delta}\left(\frac{C_1}{C_2}\,\mathrm{sech}\left(C_1(2-n)t\right)\right)^{\frac{2}{n-2}}}\times \\ \tanh\left(C_1(2-n)t\right)+4C_1(2-\delta)(2-n)\,\mathrm{cosech}\left(2C_1(2-n)t\right) \end{array} \right\} \tag{46}$$

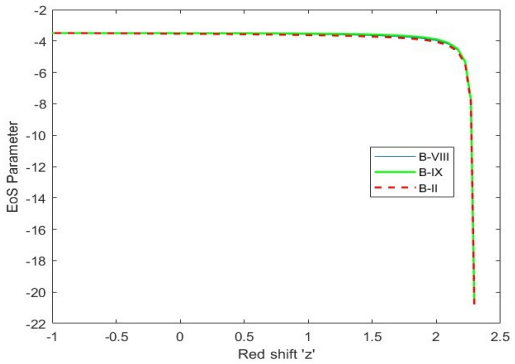

Figure 8. EoS parameter plotted against redshift for the SB cosmology for $\gamma_0 = 6.5$, $n = 1.5$, $\alpha = 25.5$, and $\delta = 2.14$ $\beta = 2.55$

Figure 8 illustrates the evolution of the Equation of State (EoS) parameter with respect to redshift 'z' for BT-II, VIII & IX cosmological models under the framework of THDE. The graph shows that the EoS parameter remains nearly constant from the future epoch ($z < 0$) , indicating a persistent phantom-like DE behaviour across these periods. As redshift increases, the EoS parameter rapidly decreases to extremely negative values, suggesting a strong phantom regime in the early Universe. Notably, all three Bianchi models exhibit nearly identical behaviour, implying that the dominant influence comes from the THDE formalism rather than the anisotropic geometry of the models. This behaviour underscores the powerful role of THDE in shaping the evolution of DE, offering a potential explanation for super-accelerated cosmic expansion, and highlighting the model's suitability for describing early and late-time cosmological dynamics even in anisotropic settings.

4. COMPARISON OF OUR RESULTS

To clearly contrast our findings with the concordance model, we provide in Table a comparative summary between the THDE models in SB gravity for BT-II, VIII, and IX Space-times, and the standard flat Λ CDM model constrained by Planck 2018 data. All three THDE models yield a transition redshift of approximately $z_t \backsimeq 0.67$, which is slightly higher than the Λ CDM prediction ($z_t \backsimeq 0.632$). The present-day equation of state lies in the phantom regime ($w_0 \approx -1.1$ to -1.2) , whereas Λ CDM fixes $w = -1$ identically. While anisotropy plays a role in the early Universe-particularly in the BT-VIII and IX cases-the models isotropise at late times, in agreement with CMB constraints. A persistent drawback of bare THDE with the Hubble cutoff is the appearance of negative squared sound speed ($v_s^2 < 0$) at higher redshifts, indicating classical instability, whereas Λ CDM remains stable. Consequently, the THDE framework offers a richer dynamical evolution with phantom-like acceleration and possible Big Rip scenarios, while still facing the challenge of stability that motivates extensions with alternative cutoffs.

In summary, the comparative analysis demonstrates that THDE in SB gravity can reproduce a transition redshift close to the observationally favoured value and yields a present-day EoS parameter in the phantom regime $w_0 \approx -1.1$ While this behaviour offers a richer dynamical evolution than Λ CDM, it also predicts a possible Big Rip–like fate. The transition redshift is obtained as $z_t \approx 0.67$, which lies well within the range inferred from Planck 2018, BAO, and Pantheon+ supernovae datasets $z_t \approx 0.65 - 0.75$ The three anisotropic Bianchi models studied here all isotropise at late times, in agreement with CMB bounds, and thus remain observationally viable. However, the persistent issue of negative squared sound speed ($v_s^2 < 0$) at higher redshift points to an inherent instability of the bare THDE fluid, distinguishing it from the

Model	Transition $z(z_t)$	Present EoS (w_0)	Stability (v_s^2)	Late-time anisotropy	Observational consistency
THDE (BT-II)	0.67	-1.15 (phantom-like,possible Big Rip)	≈ 0 today; < 0 at high z	negligible	z_t consistent; $w_0 < -1$ marginally allowed by Planck+SNe
THDE (BT-VIII)	0.67	-1.12 (phantom -like)	≈ 0 today; < 0 at high z	early anisotropy $\rightarrow$ isotropic	Consistent with SNe+BAO within errors; instability issue remains
THDE (BT-IX)	0.67	-1.13 (phantom -like)	≈ 0 today; < 0 at high z	early anisotropy $\rightarrow$ isotropic	Similar to VIII; agrees with q_0, but unstable at high z
Flat ΛCDM (Planck 2018)	0.632	-1.0 (cosmological constant, de Sitter fate)	stable	isotropic	Fully consistent with Planck + Pantheon + BAO

stable cosmological constant. Overall, THDE models in SB gravity provide a compelling alternative to Λ CDM with strong phenomenological motivation, but their long-term viability depends on introducing stabilising mechanisms or modified cutoffs to reconcile the theoretical predictions with observational robustness. THDE models in SB gravity have mostly been studied in isotropic or mildly anisotropic settings. Dubey et al.analyzed a BT-III Universe with the Hubble cutoff and found late-time acceleration consistent with de Sitter expansion, but also persistent instability due to negative squared sound speed ($v_s^2 < 0$). Our present BT- II, VIII, and IX results confirm this issue, showing that the phantom-like behaviour ($w < -1$) is robust and largely geometry-insensitive. In contrast, Chokyi et al. [55] showed that combining Tsallis and Kaniadakis HDE with viscous Van der Waals fluids and alternative cutoffs can restore stability ($v_s^2 > 0$). Together, these studies suggest that while bare THDE–SB models reproduce late-time acceleration, stability requires additional physical ingredients beyond geometry alone.

5. DISCUSSION AND CONCLUSIONS

We have analysed interacting and non-interacting THDE cosmological models in SB scalar–tensor gravity for anisotropic BT-II, VIII, and IX universes, using the Hubble horizon as the infrared cutoff. The deceleration parameter remains negative over the redshift range $-1 \leq z \leq 2.5$, implying a sustained, accelerated expansion that is sharper and more phantom-like than in Λ CDM. The Hubble parameter and expansion scalar decrease monotonically, indicating rapid late-time acceleration and slower early-time dynamics. The total THDE density grows steeply with redshift, while matter dominates at earlier epochs, producing a natural transition to dark-energy dominance.

The skewness parameter reveals weak, stable anisotropy in BT-II and strong, decaying anisotropy in BT-VIII and IX, suggesting a smooth isotropization process consistent with observations. The effective equation of state parameter remains close to -1 at recent epochs but falls below this bound at higher redshifts, confirming phantom-like behaviour. Across both interacting and non-interacting models, the entropy corrections of THDE dominate over geometric differences, highlighting the central role of generalized entropy in driving anisotropic dynamics. Despite these successes, the squared sound speed becomes negative at higher redshifts, indicating classical instabilities that challenge the physical viability of THDE scenarios. Nevertheless, the persistent phantom regime hints at the possibility of extreme future outcomes such as a Big Rip, while the decay of anisotropy ensures compatibility with the observed isotropy of the cosmic microwave background.

In summary, THDE within SB gravity provides a promising alternative to Λ CDM by combining late-time acceleration, phantom dynamics, and isotropization in anisotropic universes. Future work should focus on confronting the models with observational datasets (Planck 2018, BAO, Pantheon+), exploring alternative cutoffs or entropy generalizations to alleviate instability, and employing dynamical system analyses to rigorously assess their viability as cosmological scenarios.

Author contributions

P.E. Satyanarayana: conceptualisation, theoretical formulation, and supervision of the research work.
K.V.S. Sireesh: (Corresponding Author): Methodology, validation, manuscript review and editing, project administration, and correspondence with the journal.
K.P.S. Suryanarayana: Analytical calculations,data analysis, preparation of figures,and drafting of initial sections of the manuscript.
R. Sathibabu: literature survey,compilation of related works,and assistance in interpretation and discussion of physical results

Funding information No funding was received for conducting this study.

Data availability No new data were created or analysed during this study.Data sharing is not applicable to this article.

Declarations
Ethical statement There is no ethical issue,presently,the manuscript is submitted in this journal.
Competing interests The authors declare no competing interests.

Acknowledgements

The authors are grateful to the anonymous reviewers for their careful reading of the manuscript and for their constructive comments, which helped to improve the quality and clarity of this work.

ORCID

P.E. Satyanarayana, https://orcid.org/0000-0001-5461-8306; **K.V.S. Sireesha**, https://orcid.org/0000-0002-9751-2787; **K.P.S. Suryanarayana**, https://orcid.org/0000-0002-8793-3588; **R. Sathibabu**, https://orcid.org/0009-0007-4043-4750

REFERENCES

[1] A. Sen, "Tachyon matter," Journal of High Energy Physics, **2002**(07), 065 (2002). https://doi.org/10.48550/arXiv.hep-th/0203265

[2] M. Malekjani, T. Naderi, & F. Pace, "Effects of ghost dark energy perturbations on the evolution of spherical overdensities," Monthly Notices of the Royal Astronomical Society, **453**(4), 4148-4158 (2015). https://doi.org/10.1140/epjp/i2019-12884-6

[3] T. Chiba, T. Okabe, & M. Yamaguchi, "Kinetically driven quintessence," Physical Review D, **62**(2), 023511 (2000). https://doi.org/10.48550/arXiv.astro-ph/9912463

[4] R. Myrzakulov, "Cosmological models with non-canonical scalar and fermion fields: k-essence, f-essence and g-essence." arXiv preprint arXiv:1011.4337 (2010). https://doi.org/10.48550/arXiv.1011.4337

[5] S. Maity, & U. Debnath, "Correspondence between fermionic field and other dark energies," Astrophysics and Space Science, **345**(2), 399-403 (2013). https://doi.org/10.1007/s10509-013-1395-4

[6] U. Debnath, & S. Maity, "Correspondence of F-essence with Chaplygin gas cosmology," The European Physical Journal Plus, **129**(1), 14 (2014). https://doi.org/10.1140/epjp/i2014-14014-6

[7] S.I. Nojiri, & S. D. Odintsov, "de Sitter brane universe induced by phantom and quantum effects," Physics Letters B, **565**, 1-9 (2003). https://doi.org/10.1016/S0370-2693(03)00753-6

[8] A. Kamenshchik, U. Moschella, & V. Pasquier, "An alternative to quintessence," Physics Letters B, 511(2-4), 265-268 (2001). https://doi.org/10.1016/S0370-2693(01)00571-8

[9] S. Weinberg, "The cosmological constant problem," Reviews of Modern Physics, **61**(1), 1–23 (1989). https://doi.org/10.1103/RevModPhys.61.1

[10] E. J. Copeland, M. Sami, & S. Tsujikawa, "Dynamics of dark energy," International Journal of Modern Physics D, **15**(11), 1753-1935 (2006). https://doi.org/10.1142/S021827180600942X

[11] T. Padmanabhan, "Cosmological constant—the weight of the vacuum," Physics reports, **380**(5-6), 235-320 (2003). https://doi.org/10.1016/S0370-1573(03)00120-0

[12] H. Wei, & R. G. Cai, "A new model of agegraphic dark energy," Physics Letters B, **660**(3), 113-117 (2008). https://doi.org/10.1016/j.physletb.2007.12.030

[13] S. Maity, & U. Debnath, "Co-existence of modified Chaplygin gas and other dark energies in the framework of fractal universe," International Journal of Theoretical Physics, **55**(5), 2668-2681 (2016). https://doi.org/10.1007/s10773-015-2901-y

[14] M. R. Setare, "The holographic dark energy in non-flat Brans–Dicke cosmology," Physics Letters B, **644**(2-3), 99-103 (2007). https://doi.org/10.1016/j.physletb.2006.11.033

[15] A. De Felice, & S. Tsujikawa, "f (R) theories," Living Reviews in Relativity, **13**(1), 1-161 (2010). https://doi.org/10.12942/lrr-2010-3

[16] R. Ferraro, & F. Fiorini, "Non-trivial frames for f (T) theories of gravity and beyond," Physics Letters B, **702**(1), 75-80 (2011). https://doi.org/10.1016/j.physletb.2011.06.049

[17] P. Hořava, "Quantum gravity at a Lifshitz point," Physical Review D—Particles, Fields, Gravitation, and Cosmology, **79**(8), 084008 (2009). https://doi.org/10.1103/PhysRevD.79.084008

[18] P. Hořava, "Membranes at quantum criticality," Journal of High Energy Physics, **2009**(03), 020 (2009). https://doi.org/10.1088/1126-6708/2009/03/020

[19] P. Hořava, "Quantum gravity at a Lifshitz point," Physical Review D—Particles, Fields, Gravitation, and Cosmology, **79**(8), 084008 (2009). https://doi.org/10.1103/PhysRevD.79.084008

[20] C. Brans, & R. H. Dicke, "Mach's principle and a relativistic theory of gravitation," Physical review, **124**(3), 925 (1961). https://doi.org/10.1103/PhysRev.124.925

[21] G. Cognola, E. Elizalde, S. I. Nojiri, S. D. Odintsov, & S. Zerbini, "Dark energy in modified Gauss-Bonnet gravity: Late-time acceleration and¡? format?¿ the hierarchy problem," Physical Review D—Particles, Fields, Gravitation, and Cosmology, **73**(8), 084007 (2006). https://doi.org/10.1103/PhysRevD.73.084007

[22] T. Harko, F. S. Lobo, S. I. Nojiri, & S. D. Odintsov, "f (R, T) gravity," Physical Review D—Particles, Fields, Gravitation, and Cosmology, **84**(2), 024020 (2011). https://doi.org/10.1103/PhysRevD.84.024020

[23] D. Saez, & V. J. Ballester, "A simple coupling with cosmological implications," Physics Letters A, **113**(9), 467-470 (1986). https://doi.org/10.1016/0375-9601(86)90121-0

[24] M. V. Santhi, & Y. Sobhanbabu, "Bianchi type-III Tsallis holographic dark energy model in Saez–Ballester theory of gravitation," The European Physical Journal C, **80**(12), 1198 (2020). https://doi.org/10.1140/epjc/s10052-020-08743-9

[25] M. Dheepika, & T. K. Mathew, "Tsallis holographic dark energy reconsidered," The European Physical Journal C, **82**(5), 399 (2022). https://doi.org/10.1140/epjc/s10052-022-10365-2

[26] K. Dasunaidu, Y. Aditya, & V. S. Rao, "Kaluza-Klein FRW Tsallis holographic dark energy model in scalar-tensor theory of gravitation," Bulgarian Astronomical Journal, **39**, 72-86 (2023). https://astro.bas.bg/AIJ/issues/n39/KDasunaidu.pdf

[27] V. S. Rao, V. Ganesh, K. Dasunaidu, & Y. Aditya, "Anisotropic Sharma-Mittal holographic dark energy model in a scalar-tensor theory of gravitation," AIP Conference Proceedings, **3298**(1), 040052 (2025). https://doi.org/10.1063/5.0279450

[28] K. Murali, Y. Aditya, & S.K. Vali, "Cosmographic analysis of anisotropic Kaniadakis holographic dark energy model," Modern Physics Letters A, **39**(23n24), 2450106 (2024). https://doi.org/10.1142/S0217732324501062

[29] M. V. Santhi, T. Chinnappalanaidu, S. S. Madhu, & D. M. Gusu, "Some Bianchi type viscous holographic dark energy cosmological models in the Brans–Dicke theory," Advances in Astronomy, **2022**(1), 5364541 (2022). https://doi.org/10.1155/2022/5364541

[30] V. U. M. Rao, M.V. Santhi, K. V. S. Sireesha, & N.S. Rani, "Bulk viscous string cosmological models in Saez â Ballester theory of gravitation," Iranian Journal of Physics Research, **18**(3), 497-497 (2019). https://doi.org/10.29252/ijpr.18.3.497

[31] K. V. S. Sireesha, and V. U. M. Rao. "Bianchi type-II, VIII & IX holographic dark energy cosmological models in brans-dicke theory of gravitation." The African Review of Physics, **14**, (2019).

[32] K. V. S. Sireesha, & V. U. M. Rao, "Modified holographic Ricci dark energy cosmological models in f (R, T) gravity," In Journal of Physics: Conference Series **1344**(1), 012028 (2019). https://doi.org/10.1088/1742-6596/1344/1/012028

[33] J. S. Wath, & A. S. Nimkar, "Cosmological Parameters and Stability of Bianchi Type-VIII in Sáez-Ballester Theory of Gravitation," Bulgarian Journal of Physics, **50**(3) (2023). https://doi.org/10.55318/bgjp.2023.50.3.255

[34] L. N. Granda, & A. Oliveros, "Infrared cut-off proposal for the holographic density," Physics Letters B, **669**(5), 275-277 (2008). https://doi.org/10.1016/j.physletb.2008.10.017

[35] C. Tsallis, "Possible generalization of Boltzmann-Gibbs statistics," Journal of statistical physics, 52(1), 479-487 (1988). https://doi.org/10.1007/BF01016429

[36] U. K. Sharma, & V. C. Dubey, "Exploring the Sharma–Mittal HDE models with different diagnostic tools," The European Physical Journal Plus, 135(5), 391 (2020). https://doi.org/10.1140/epjp/s13360-020-00411-x

[37] B. D. Sharma, & D. P. Mittal, "New non-additive measures of entropy for discrete probability distributions," J. Math. Sci, **10**(75), 28-40 (1975). https://doi.org/10.1016/S0019-9958(79)90581-3

[38] M. Sharif, & A. Jawad, "Cosmological evolution of interacting new holographic dark energy in non-flat universe," The European Physical Journal C, **72**(8), 2097 (2012). https://doi.org/10.1140/epjc/s10052-012-2097-8

[39] M. Li, "Note on the production of scale-invariant entropy perturbation in the Ekpyrotic universe," Physics Letters B, **724**(4-5), 192-197 (2013). https://doi.org/10.1016/j.physletb.2013.06.035

[40] P. Praseetha, & T. K. Mathew, "Entropy of holographic dark energy and the generalized second law," Classical and Quantum Gravity, **31**(18), 185012 (2014). https://doi.org/10.1088/0264-9381/31/18/185012

[41] A. Jawad, S. Chattopadhyay, S. Bhattacharya, & A. Pasqua, "Modified holographic Ricci dark energy in chameleon Brans–Dicke cosmology and its thermodynamic consequence," Communications in Theoretical Physics, **63**(4), 453 (2015). https://doi.org/10.1088/0253-6102/63/4/453

[42] V.C. Dubey, A.K. Mishra, S. Srivastava, & U.K. Sharma, "Tsallis holographic dark energy models in axially symmetric space time," International Journal of Geometric Methods in Modern Physics, **17**(01), 2050011 (2020). https://doi.org/10.1142/S0219887820500115

[43] V. C. Dubey, S. Srivastava, U. K. Sharma, & A. Pradhan, "Tsallis holographic dark energy in Bianchi-I Universe using hybrid expansion law with k-essence," Pramana, **93**(5), 78 (2019). https://doi.org/10.1007/s12043-019-1843-y

[44] Y. Aditya, & D. R. K. Reddy, "Anisotropic new holographic dark energy model in Saez–Ballester theory of gravitation," Astrophysics and Space Science, **363**(10), 207 (2018). https://doi.org/10.1007/s10509-018-3429-4

[45] U. D. Prasanthi, & Y. Aditya, "Anisotropic Renyi holographic dark energy models in general relativity," Results in Physics, **17**, 103101 (2020). https://doi.org/10.1016/j.rinp.2020.103101

[46] M. Tavayef, A. Sheykhi, K. Bamba, & H. Moradpour, "Tsallis holographic dark energy," Physics Letters B, **781**, 195-200 (2018). https://doi.org/10.1016/j.physletb.2018.04.001

[47] C. Tsallis, & L. J. Cirto, "Black hole thermodynamical entropy," The European Physical Journal C, **73**(7), 2487 (2013). https://doi.org/10.1140/epjc/s10052-013-2487-6

[48] Y. Aditya, S. Mandal, P. K. Sahoo, & D. R. K. Reddy, "Observational constraint on interacting Tsallis holographic dark energy in logarithmic Brans–Dicke theory," The European Physical Journal C, **79**(12), 1020 (2019). https://doi.org/10.1140/epjc/s10052-019-7534-5

[49] B. D. Pandey, P. S. Kumar, Pankaj, & U. K. Sharma, "New Tsallis holographic dark energy," The European Physical Journal C, **82**(3), 233 (2022). https://doi.org/10.1140/epjc/s10052-022-10171-w

[50] P. S. Kumar, & U. K. Sharma, Quintessence model of Tsallis holographic dark energy. New Astronomy, **96**, 101829 (2022). https://doi.org/10.1016/j.newast.2022.101833

[51] O. Bertolami, F. G. Pedro, & M. Le Delliou, "Dark energy–dark matter interaction and putative violation of the equivalence principle from the Abell cluster A586," Physics Letters B, **654**(5-6), 165-169 (2007). https://doi.org/10.1016/j.physletb.2007.08.046

[52] O. Bertolami, F. Gil Pedro, & M. Le Delliou, "The Abell cluster A586 and the detection of violation of the equivalence principle," General Relativity and Gravitation, **41**(12), 2839-2846 (2009). https://doi.org/10.1007/s10714-009-0810-1

[53] E. Abdalla, L. R. Abramo, L. Sodré Jr, & B. Wang, "Signature of the interaction between dark energy and dark matter in galaxy clusters," Physics Letters B, **673**(2), 107-110 (2009). https://doi.org/10.1016/j.jet.2015.11.006

[54] E. Abdalla, L. R. Abramo, & J. C. de Souza, "Signature of the interaction between dark energy and dark matter in observations," Physical Review D—Particles, Fields, Gravitation, and Cosmology, **82**(2), 023508 (2010). https://doi.org/10.1103/PhysRevD.82.023508

[55] K. K. Chokyi, & S. Chattopadhyay, "Cosmological Models within f (T, B) Gravity in a Holographic Framework," Particles, **7**(3), 856-878 (2024). https://doi.org/10.3390/particles7030051

КОСМОЛОГІЧНА ДИНАМІКА ГОЛОГРАФІЧНОЇ ТЕМНОЇ ЕНЕРГІЇ ЦАЛЛІСА В ГРАВІТАЦІЇ САЕЗА-БАЛЛЕСТЕРА

П.Е. Сатьянарараяна, **К.В.С. Сіріша**, **К.П.С. Сурьянарараяна**, **Р. Сатібабу**

Кафедра математики, GSS, GITAM, вважається Університетом, Вішакхапатнам, Індія

Ми досліджуємо взаємодіючі та невзаємодіючі моделі голографічної темної енергії Цалліса (THDE) в рамках скалярно-тензорної гравітації Саеса-Баллестера (SB) для анізотропних Всесвітів типу Біанкі (BT) II, VIII та IX. Використовуючи горизонт Хаббла як інфрачервоний обріз, ми розглядаємо моделі, не припускаючи певного закону масштабного коефіцієнта. Аналіз охоплює ключові космологічні параметри, включаючи параметр уповільнення, параметр Хаббла, густину енергії, асиметрію, рівняння стану (EoS) та квадрат швидкості звуку. Наші результати вказують на безперервне фантомоподібне прискорення ($w < -1$) з червоним зміщенням переходу $z_t \approx 0.67$ та незначною анізотропією пізнього часу, що узгоджується з межами космічного мікрохвильового фону (CMB). Порівняно з ΛCDM, моделі THDE передбачають більш ранній початок прискорення та більш негативний сучасний EoS. Однак наявність негативного квадрата швидкості звуку при вищих червоних зміщеннях сигналізує про класичну нестабільність рідини темної енергії. Ці результати підкреслюють THDE як життєздатну альтернативу ΛCDM в анізотропних космологіях, водночас мотивуючи подальшу роботу з альтернативними обрізаннями або стабілізуючими механізмами для подолання проблеми нестабільності.

Ключові слова: *моделі BT-II; VIII & IX; голографічна темна енергія Цалліса; теорія гравітації Саеза-Баллестера; космічне прискорення; анізотропна космологія*

East European Journal of Physics. 1. 60–75 (2026)
DOI: 10.26565/2312-4334-2026-1-05 ISSN 2312-4334

COSMOLOGICAL DIAGNOSTICS OF BIANCHI TYPE-*II* BARROW HOLOGRAPHIC DARK ENERGY UNIVERSE

U.Y. Divya Prasanthi[1], **D. Tejeswararao**[2,*], **Diddi Srinivasa Rao**[3], **Y. Aditya**[4,*], **D. Ram Babu**[4]
[1]*Department of Statistics & Mathematics, College of Horticulture, Dr. Y.S.R. Horticultural University, Parvathipuram-535502, India*
[2]*Department of Basic Sciences and Humanities, GMR Institute of Technology (GMRIT) – Deemed to be University, Rajam-532127, India*
[3]*Department of Mathematics, Aditya University, Surampalem-533437, India*
[4]*Department of Mathematics, GMR Institute of Technology (GMRIT) – Deemed to be University, Rajam-532127, India*
[*]*Corresponding Author e-mail: yaditya2@gmail.com; aditya.y@gmail.com*
[*]*Corresponding Author e-mail: teja.iict@gmail.com*
Received September 26, 2025; revised January 2, 2026; in final form January 27, 2026; accepted January 29, 2026

In this paper, we investigate a Bianchi type-*II* anisotropic cosmological model in the framework of Barrow holographic dark energy, considering both the Hubble horizon and Granda–Oliveros scale as infrared cutoffs. To obtain exact solutions of the Einstein field equations, we assume a suitable relation between the metric potentials. Using Hubble cosmic chronometer data, we constrain the model parameters and obtain the best-fit values $b_4 = -0.091^{+0.013}_{-0.012}$ and $H_0 = 72.3 \pm 2.7$ km s^{-1}Mpc^{-1}. The $H(z)$ fit shows excellent agreement with observational data and overlaps with ΛCDM at low redshifts, with mild deviations at higher z. The physical behaviour of the model is examined through a detailed analysis of cosmological parameters. The deceleration parameter $q(z)$ reveals a smooth transition from an early decelerating phase to the present accelerating epoch. The equation of state parameter ω_{de} shows quintom-like dynamics, evolving across the cosmological constant boundary and entering the phantom regime, consistent with late-time acceleration. Stability is tested using the squared sound speed v_s^2, which remains positive in the recent Universe, ensuring classical stability. The $\omega_{de} - \omega'_{de}$ phase plane indicates that both models lie in the freezing region, corresponding to faster acceleration. The statefinder diagnostics (r, s) and (r, q) further confirm the transition from the standard cold dark matter dominated phase to a de Sitter-like attractor, with trajectories showing clear deviations from ΛCDM.

Keywords: *Bianchi type-II model; Barrow holographic dark energy; Dark energy; Cosmology; Modified theory of gravity*

PACS: 98.80.-k, 04.50.+h, 95.30.Sf

1. INTRODUCTION

One of the most fascinating topics in theoretical and experimental cosmology is the enigma of dark energy (DE), feature of the universe that propels cosmic acceleration [1]-[3]. Among the more attractive DE model candidates put forth in the literature is the holographic DE (HDE) idea. The origin of the connection between a quantum theory's IR cut-off and ultraviolet cut-off, which is the greatest distance at a cosmological scale, is the holographic principle [4, 5]. This principle states that the two-dimensional bounding area of the universe horizon entropy is similar to the Benkenstein-Hawking law of Black hole entropy area. The age of cosmic acceleration could not be described by the initial HDE model, which was proposed with the Hubble horizon as the IR cut-off [6]. To achieve this, physicists made various assumptions about horizon entropy and IR cut-off sizes, which resulted in a number of distinct HDE modes. A different DE model that exhibits a time-varying dynamic equation of state (EoS) and is in accordance with the quantum principle that obeys the Heisenberg type uncertainty principle is the HDE model. In issues that described the inflationary era and the bounce scenario, HDE models also saw significant success. Over recent decades, various entropy formulations have been applied to develop and examine cosmological models. This has led to several innovative HDE models, such as the Tsallis HDE [7, 8], Sharma-Mittal HDE (SMHDE) [9], and Renyi HDE model [10]. Numerous researchers have evaluated cosmological models based on these new HDE concepts [11] - [21]. Recently, Kaniadakis statistics have been utilized as a generalized measure of entropy [22] - [24] to investigate various gravitational and cosmological phenomena. Kaniadakis entropy modifies the standard thermodynamics, allowing for non-linearities that account for a broader range of behaviors in DE. It provides a more generalized EoS, enabling flexibility in describing the evolution of DE over cosmic time. Barrow [25] introduced a generalized entropy–area relation that accounts for quantum gravitational effects through a fractal deformation of the horizon surface. This leads to the concept of Barrow entropy, characterized by the deformation parameter δ, which quantifies deviations from the standard entropy law. When applied to the holographic framework, this correction yields the Barrow HDE (BHDE) model. The inclusion of Barrow entropy enriches the thermodynamic foundation of DE, linking quantum gravitational effects with cosmic expansion and offering a broader understanding of the universe's late-time acceleration. It should be noted that in [26, 27], cosmological limitations on parameter δ have been inferred. Oliveros et al. [28] studied the BHDE model using the Granda–Oliveros IR cutoff and provided a detailed account

Cite as: U.Y.D. Prasanthi, D. Tejeswararao, Diddi Srinivasa Rao, Y. Aditya, D. Ram Babu, East Eur. J. Phys. 1, 60 (2026), https://doi.org/10.26565/2312-4334-2026-1-05

of its cosmic evolution. Remya et al. [29] analyzed the cosmological behavior of BHDE incorporating a time-varying deceleration parameter, while Koussour et al. [30] explored the BT-I spacetime influenced by BHDE using the Hubble horizon as the IR cutoff within the context of symmetric teleparallel gravity. Recently, Aditya et al. [31] examined the BT-I BHDE model in the framework of logarithmic BD gravity.

Most cosmological analyses are based on the Friedmann–Robertson–Walker (FRW) line element, which assumes perfect spatial isotropy. However, several physical processes—such as primordial anisotropies, relics of early phase transitions, or anisotropic stresses arising from dark sector physics—motivate the investigation of more general anisotropic cosmological models. Among these, the Bianchi type (BT) models represent spatially homogeneous but anisotropic cosmologies. In particular, the BT-II model is of special interest, as it is one of the simplest non-flat models that admits shear and anisotropic expansion modes while retaining analytical tractability in many scenarios. Studies of BT models are valuable for assessing the robustness of isotropization mechanisms and for identifying possible observational imprints—such as those in the cosmic microwave background (CMB) anisotropies or large-scale structure—that may provide constraints on exotic dark sector physics. The combination of anisotropic backgrounds with modified entropy or dark energy (DE) models is, therefore, well motivated, as it allows one to explore potential couplings among geometry, thermodynamics, and late-time cosmic acceleration. Alternative theories of gravity offer a complementary framework for addressing outstanding cosmological puzzles. Barber [32] introduced two continuous creation theories: one formulated as a variant of the Brans–Dicke (BD) theory, and the other as a modification of general theory of relativity (GTR) that incorporates continuous matter creation consistent with observational evidence. These models posit a universe that arises from self-contained gravitational and matter fields. Barber's second self-creation theory has inspired numerous studies of cosmological models (Refs. [33]–[37]), providing a setting in which the cosmological constant can emerge dynamically from the interaction between matter and the gravitational field. This approach offers an alternative explanation for cosmic acceleration and dark energy without invoking a constant vacuum energy density. Essentially, the theory introduces a mechanism of self-creation of gravity, which modifies both the gravitational field equations and the overall evolution of the universe. For a comprehensive treatment of dark energy and modified gravity frameworks, the reader is referred to Refs. [38]–[51]. The Self-Creation Theory (SCT), originally formulated by Barber and subsequently extended by various authors, modifies scalar–tensor gravity in such a way that matter can be created from the interplay between geometry and scalar fields, while simultaneously altering the effective gravitational coupling. SCT has been extensively investigated in the context of cosmological solutions, including Bianchi space-times, as it provides a versatile theoretical framework to study the interaction between modified gravitational dynamics and non-standard dark energy models. Combining SCT with Barrow Holographic Dark Energy (BHDE) within an anisotropic BT-*II* background allows for a unified investigation, anisotropic geometric effects, and scalar–tensor gravitational dynamics. Such an integrated approach enables the study of how these factors may influence structure formation, isotropization, and the observed late-time cosmic acceleration.

With this motivation, in this paper, we construct and analyze a spatially homogeneous BT-*II* cosmological model within the framework of SCT, where the DE sector is modelled by BHDE. We derive the modified field equations appropriate to the Self creation theory of gravity. The work is organized as follows: Section-2 contains field equations and BHDE models. Section-3 consists of observational constraints on model parameters. In section-4, we include physical discussion of our dynamical parameters. Section-5 deals with final remarks and conclusions.

2. FIELD EQUATIONS AND MODEL

We begin with the BT-II line element, which in comoving coordinates is given by

$$ds^2 = -dt^2 + \mathcal{R}(t)^2\,dx^2 + \mathcal{S}(t)^2\,dy^2 + 2\mathcal{S}(t)^2 x\,dy\,dz + \left(\mathcal{S}(t)^2x^2 + \mathcal{R}(t)^2\right)dz^2, \tag{1}$$

where $\mathcal{R}(t)$ and $\mathcal{S}(t)$ denote the directional scale factors along the x, z- and y-axes, respectively. In the framework of self-creation theory, the gravitational field equations take the form

$$R_{ij} - \tfrac{1}{2}Rg_{ij} = -\frac{8\pi}{\phi}\left(T_{ij} + \overline{T}_{ij}\right), \tag{2}$$

together with the scalar field equation

$$\Box\phi \equiv \phi^{;v}_{;v} = \frac{8\pi\mu}{3}\left(T + \overline{T}\right), \tag{3}$$

where ϕ represents the scalar field of self-creation theory, and μ is a coupling constant. The total energy-momentum distribution is split into two components: the standard matter contribution and the anisotropic DE contribution. We define the matter and DE tensors as diagonal tensors in the comoving frame (i.e., $u^i = (1,0,0,0)$, $u_i = (-1,0,0,0)$ and $u^i u_i = -1$), namely

$$T^j_i = \mathrm{diag}(-\rho_m,\,0,\,0,\,0)\,, \qquad \overline{T}^j_i = \mathrm{diag}\big(-\rho_{de},\,p_x,\,p_y,\,p_z\big)\,, \tag{4}$$

with the anisotropic EoS

$$p_x = \omega_{de}\rho_{de}, \qquad p_y = (\omega_{de} + \gamma)\rho_{de}, \qquad p_z = \omega_{de}\rho_{de}, \tag{5}$$

where ρ_m and ρ_{de} denote the energy densities of matter and DE, respectively. The parameter ω_{de} is the equation-of-state parameter of DE, while γ characterizes its anisotropic deviation along the y-direction. We stress that the skewness parameter γ introduces anisotropic diagonal pressures and does not generate shear stresses. A non-zero expression for $T^y{}_z$ would necessarily originate from a non-diagonal energy-momentum tensor (e.g. shear/tilted fluid/heat flow) which is not assumed in our formulation (since, we have a non-zero component of Einstein tensor G^y_z). In our framework, the dark-energy skewness parameter γ modifies only the diagonal pressure component p_y.

Substituting the BT-II metric (1) and the above energy-momentum components into the field equations (2)–(3) (using mixed form of these field equations), we obtain the dynamical equations governing the evolution of the anisotropic universe in self-creation theory. The mixed form is often preferred in cosmological and anisotropic models because it allows a direct physical interpretation of the energy density and directional pressures. These equations explicitly couple the scale factors $\mathcal{R}(t)$, $\mathcal{S}(t)$, and the scalar field $\phi(t)$, thereby allowing us to study the impact of anisotropic DE on the cosmological dynamics.

$$\frac{\ddot{\mathcal{S}}}{\mathcal{S}} + \frac{\dot{\mathcal{R}}}{\mathcal{R}}\frac{\dot{\mathcal{S}}}{\mathcal{S}} + \frac{\ddot{\mathcal{R}}}{\mathcal{R}} + \frac{\mathcal{S}^2}{4\mathcal{R}^4} = \frac{-8\pi\omega_{de}\rho_{de}}{\phi} \tag{6}$$

$$\frac{2\ddot{\mathcal{R}}}{\mathcal{R}} + \frac{\dot{\mathcal{R}}^2}{\mathcal{R}^2} - \frac{3\mathcal{S}^2}{4\mathcal{R}^4} = \frac{-8\pi(\omega_{de}+\gamma)\rho_{de}}{\phi} \tag{7}$$

$$\frac{2\dot{\mathcal{R}}\dot{\mathcal{S}}}{\mathcal{R}\mathcal{S}} + \frac{\dot{\mathcal{R}}^2}{\mathcal{R}^2} - \frac{\mathcal{S}^2}{4\mathcal{R}^4} = \frac{8\pi[\rho_m+\rho_{de}]}{\phi} \tag{8}$$

$$\dot{\phi}\left(\frac{2\dot{\mathcal{R}}}{\mathcal{R}} + \frac{\dot{\mathcal{S}}}{\mathcal{S}}\right) + \ddot{\phi} = \frac{8\pi\mu(T+\overline{T})}{3}. \tag{9}$$

Differentiation with respect to time t is represented by a dot above a variable in this notation. The non-diagonal Einstein tensor satisfies the geometric identity

$$G^y{}_z = -x\left(-\frac{\ddot{\mathcal{S}}}{\mathcal{S}} + \frac{\ddot{\mathcal{R}}}{\mathcal{R}} + \frac{\dot{\mathcal{R}}^2}{\mathcal{R}^2} - \frac{\mathcal{S}^2}{\mathcal{R}^4} - \frac{\dot{\mathcal{R}}\dot{\mathcal{S}}}{\mathcal{R}\mathcal{S}}\right) = x\left(G^y_y - G^x_x\right), \tag{10}$$

which follows from the specific non-diagonal structure of the metric. Hence, the mixed Einstein equation is not independent and can be obtained from the difference of the diagonal field equations. The total energy–momentum tensor employed in Eq. (4) which represents an anisotropic dark energy component together with pressureless matter. Using field equations (expressed in mixed form by raising the indices in Eq. (2)),

$$G^j{}_i = -\frac{8\pi}{\phi}T^j{}_i, \tag{11}$$

the difference of the yy and xx components yields

$$G^y{}_y - G^x{}_x = -\frac{8\pi}{\phi}\left(T^y{}_y - T^x{}_x\right) = -\frac{8\pi}{\phi}\,\gamma\,\rho_{de}. \tag{12}$$

Therefore, the off-diagonal field equation $G^y{}_z = -\frac{8\pi}{\phi}T^y{}_z$ is automatically satisfied and does not introduce an additional independent constraint. We can solve the system of equations (6)-(8) appropriately with the use of assumptions which connects unknowns in the field equations. Because of this, we take into account the following physically plausible circumstances:

$$\mathcal{R} = \mathcal{S}^k. \tag{13}$$

In this framework, k represents a constant (Collins et al. [52]). Observational studies of velocity–redshift relations from extragalactic sources reveal that the present cosmic expansion is isotropic to within nearly 30% [53, 54, 55]. Complementary redshift surveys further constrain the shear-to-expansion ratio, yielding $\frac{\sigma}{H} \leq 0.3$ within our Galaxy at the current epoch. A widely employed approach in scalar–tensor cosmologies is to relate the scalar field ϕ to the average scale factor $a(t)$ through a simple power-law ansatz [56, 57]:

$$\phi \propto a(t)^n,$$

where n is a dimensionless index. This relation has been extensively investigated in the literature, as it captures a range of possible scalar-field behaviors with remarkable simplicity [58]-[63]. Motivated by both its mathematical tractability and its physical plausibility, we adopt the following specific assumption in our analysis:

$$\phi(t) = \phi_0[a(t)]^n. \tag{14}$$

Using the relations (13) and (14) in Eqs. (6) and (7), we obtain the metric potentials as

$$\mathcal{R} = (b_3 e^{\gamma_0 t} + b_4)^{\frac{1}{k+2}} \tag{15}$$

and

$$\mathcal{S} = (b_3 e^{\gamma_0 t} + b_4)^{\frac{k}{k+2}} \tag{16}$$

where $b_3 = \frac{(k+2)b_1}{\gamma_0}$, $b_4 = (k+2)b_2$, b_1 and b_2 are integrating constants. The scalar field of the model is

$$\phi = \phi_0 \left(b_3 e^{\gamma_0 t} + b_4\right)^{\frac{n}{3}}. \tag{17}$$

Now metric (1), with the aid of Eqs. (15) and (16), can be written as

$$\begin{aligned} ds^2 = -dt^2 + (b_3 e^{\gamma_0 t} + b_4)^{\frac{2}{k+2}} dx^2 + (b_3 e^{\gamma_0 t} + b_4)^{\frac{2k}{k+2}} dy^2 + 2(b_3 e^{\gamma_0 t} + b_4)^{\frac{2k}{k+2}} x dy dz \\ +((b_3 e^{\gamma_0 t} + b_4)^{\frac{2k}{k+2}} x^2 + (b_3 e^{\gamma_0 t} + b_4)^{\frac{2}{k+2}}) dz^2. \end{aligned} \tag{18}$$

Equation (18) describes a anisotropic BT-II BHDE model within the context of self-creation gravity theory, with the following physical parameters. The model's average scale factor $a(t)$ and volume $V(t)$ are defined as follows:

$$V(t) = a(t)^3 = (b_3 e^{\gamma_0 t} + b_4). \tag{19}$$

The expressions for the mean Hubble H and the expansion scalar θ parameters are derived as follows:

$$\begin{aligned} H = 3\theta &= \frac{b_3 \gamma_0 e^{\gamma_0 t}}{3\, b_3 e^{\gamma_0 t} + 3\, b_4} \\ &= \frac{\gamma_0}{3}\left[1 - b_4(1+z)^3\right] = \frac{H_0}{1-b_4}\left[1 - b_4(1+z)^3\right]. \end{aligned} \tag{20}$$

where $1 + z = \frac{1}{a(t)}$ and $a(t)$ is average scale factor. Here $\frac{H_0}{1-b_4} = \frac{\gamma_0}{3}$. We will constrain following parameters H_0 and b_4 with observational datasets in section-3. We will evaluate the parameters γ_0 and k from the expression $\gamma_0 = \frac{3H_0}{1-b_4}$, and $k = \frac{b_4}{b_2} - 2$ for appropriate choice of arbitrary integrating constant b_2 and observationally constrained values of H_0 and b_4. The average anisotropic parameter A_h and shear scalar σ^2 are given by

$$\sigma^2 = \frac{(k-1)^2 b_3^2 \gamma_0^2 e^{2\gamma_0 t}}{(k+2)^2 (b_3 e^{\gamma_0 t} + b_4)^2}\ ;\ \ A_h = \frac{2(k-1)^2}{(k+2)^2}. \tag{21}$$

From the obtained solutions, it is clear that the spatial volume of the universe undergoes an exponential increase, which reflects the accelerated expansion characteristic of the present cosmic epoch. During the initial stages of cosmic evolution, all dynamical quantities such as the scale factors, expansion scalar, and energy densities remain finite, thereby avoiding any initial singularity. As cosmic time progresses, i.e., in the limit $t \to \infty$, these quantities diverge, indicating the unbounded growth of the universe in accordance with an accelerated expansion scenario. A particularly interesting case emerges when $k = 1$. In this situation, the model becomes shear-free and isotropic, as demonstrated by the vanishing conditions $\sigma^2 = 0$ and $A_h = 0$. This implies that the anisotropic contributions completely disappear, and the model smoothly reduces to the isotropic case, which is consistent with the standard FLRW cosmology. Such a limiting behavior is significant, since it shows that the present anisotropic model can naturally accommodate isotropy under specific parameter choices, in agreement with observational evidence from CMB measurements and large-scale structure surveys that strongly favor an isotropic universe on large scales.

BHDE: The conventional formulation of HDE employs the Hubble horizon as the IR cutoff and makes use of the Bekenstein–Hawking area law to determine the horizon of the Universe. However, this framework falls short in reproducing the full cosmic evolution, which has motivated several modifications. These adjustments typically involve either adopting alternative IR cutoffs or modifying the entropy–area relation. In this context, an HDE model inspired by Barrow entropy has attracted considerable attention in recent years. Barrow proposed that quantum gravity effects may alter the

geometry of black hole horizons, imparting them with intricate, fractal-like features. Such corrections render the entropy formula more general, leading to the expression

$$S \sim \mathcal{A}^{1+\delta/2}, \tag{22}$$

where $0 \leq \delta \leq 1$. The cases $\delta = 0$ and $\delta = 1$ correspond to the standard entropy–area law and the maximal deviation from it, respectively. Notably, observational bounds on δ have already been obtained. Building on Eq. (22) and the profound link between gravity and thermodynamics, Barrow's framework has been extended to cosmology. In particular, the DE density in the Barrow HDE scenario is given by

$$\rho_{de} = C\,\mathcal{L}^{\delta-2}, \tag{23}$$

where the constant $C = 3c^2M_p^2$ has dimensions $[\mathcal{L}]^{2-\delta}$. Here, c is a numerical parameter and $M_p^2 = \frac{1}{8\pi G}$ denotes the reduced Planck mass. Within the framework of self creation theory of gravity, since $\frac{1}{G} = \phi$, one obtains $C = \frac{3c^2\phi}{8\pi}$.

Model-1: BHDE model with Hubble horizon

The IR cutoff determines the largest scale that contributes to the energy density in HDE. In the standard HDE framework, the choice of IR cutoff (such as the event horizon, particle horizon, or Hubble horizon) significantly influences the cosmic dynamics. Unlike the event horizon, which depends on the future evolution of the scale factor, the Hubble horizon is locally defined. This feature allows it to avoid the causality problem, thereby making it a more physically consistent choice in certain cosmological scenarios. In the BHDE model, adopting the Hubble radius as the IR cutoff provides a local, causal, and observationally viable description of DE. By setting the IR cutoff as $\mathcal{L} = \frac{1}{H}$, we obtain

$$\rho_{de} = CH^{2-\delta} \tag{24}$$

where Hubble parameter H is given by Eq. (20). Using Hubble parameter (20) in Eq. (24), we obtain the energy density of BHDE with Hubble horizon as IR cutoff as

$$\rho_{de} = \frac{3c^2\phi_0\,(b_3e^{\gamma_0 t}+b_4)^{\frac{n}{3}}}{8\pi}\left[\frac{\gamma_0}{3}\left[1-b_4(1+z)^3\right]\right]^{2-\delta}. \tag{25}$$

The BT-II universe with BHDE with Hubble horizon inside the framework of self-creation theory of gravity is shown by Eq. (18), the scalar field (17), and the energy density (25). Using Eqs. (6), (15)-(17) and (25), we get EoS parameter as

$$\begin{aligned}\omega_{de} = -\frac{1}{3c^2}\Bigg(&\frac{b_3^2\gamma_0^2\,e^{2\gamma_0 t}}{(k+2)^2\,(b_3e^{\gamma_0 t}+b_4)^2}+\frac{b_3b_4\gamma_0^2\,e^{\gamma_0 t}}{(k+2)\,(b_3e^{\gamma_0 t}+b_4)^2}+\frac{k^2b_3^2\gamma_0^2\,e^{2\gamma_0 t}}{(k+2)^2\,(b_3e^{\gamma_0 t}+b_4)^2}+\frac{k\,b_3b_4\gamma_0^2\,e^{\gamma_0 t}}{(k+2)\,(b_3e^{\gamma_0 t}+b_4)^2}\\&+\frac{k\,b_3^2\gamma_0^2\,e^{2\gamma_0 t}}{(k+2)^2\,(b_3e^{\gamma_0 t}+b_4)^2}+\frac{1}{4}\,\frac{\left((b_3e^{\gamma_0 t}+b_4)^{\frac{k}{k+2}}\right)^2}{\left((b_3e^{\gamma_0 t}+b_4)^{(k+2)^{-1}}\right)^4}\Bigg)\times\left(\left(\frac{b_3\gamma_0e^{\gamma_0 t}}{3\,(b_3e^{\gamma_0 t}+b_4)}\right)^{2-\delta}\right)^{-1}.\end{aligned} \tag{26}$$

and we find the skewness parameter as

$$\gamma = \frac{1}{3c^2}\left(\left((b_3e^{\gamma_0 t}+b_4)^{\frac{1}{k+2}}\right)^{2k-4}+\frac{(k-1)\,\gamma_0^2\,b_3e^{\gamma_0 t}}{(k+2)\,(b_3e^{\gamma_0 t}+b_4)}\right)\left(\left(\frac{b_3\gamma_0e^{\gamma_0 t}}{3(b_3e^{\gamma_0 t}+b_4)}\right)^{2-\delta}\right)^{-1}. \tag{27}$$

Model-2: BHDE model with Granda–Oliveros horizon

The Granda–Oliveros (GO) cutoff is determined by the present value of the Hubble parameter H and its time derivative $\dot{H}$. Unlike the event horizon cutoff, it avoids issues of non-locality and causality, since the presence of $\dot{H}$ introduces a dynamical component that allows the DE density to evolve naturally. Moreover, because it does not involve integration over the future cosmic time, the GO cutoff is regarded as physically more realistic and more consistent with both thermodynamics and causality. In this framework, we consider the BHDE model with the GO horizon cutoff defined as $\mathcal{L} = \left(\alpha_1H^2+\alpha_2\dot{H}\right)^{-\frac{1}{2}}$, (Granda and Oliveros [64, 65]), and hence we obtain

$$\rho_{de} = \frac{3}{8}\,\frac{c^2\phi_0\left(b_3e^{\gamma_0 t}+b_4\right)^{\frac{n}{3}}}{\pi}\left(\frac{\alpha_1\,b_3^2\gamma_0^2\,e^{2\gamma_0 t}}{\left(3b_3e^{\gamma_0 t}+3b_4\right)^2}+\frac{1}{3}\,\frac{\alpha_2\,b_3b_4\gamma_0^2\,e^{\gamma_0 t}}{\left(b_3e^{\gamma_0 t}+b_4\right)^2}\right)^{1-\frac{\delta}{2}} \tag{28}$$

The BT-II universe with BHDE with GO horizon inside the framework of self-creation theory of gravity is shown by Eq. (18), the scalar field (17), and the energy density (28). Using Eqs. (6), (15)-(17) and (28), we get EoS parameter as

$$\omega_{de} = -\frac{1}{3c^2}\left[\frac{b_3^2\gamma_0^2e^{2\gamma_0 t}}{(k+2)^2(b_3e^{\gamma_0 t}+b_4)^2}+\frac{(k+1)b_3b_4\gamma_0^2e^{\gamma_0 t}}{(k+2)(b_3e^{\gamma_0 t}+b_4)^2}+\frac{(k^2+k)b_3^2\gamma_0^2e^{2\gamma_0 t}}{(k+2)^2(b_3e^{\gamma_0 t}+b_4)^2}\right.$$

$$+\frac{1}{4}\frac{\left((b_3e^{\gamma_0 t}+b_4)^{\frac{k}{k+2}}\right)^2}{\left((b_3e^{\gamma_0 t}+b_4)^{\frac{1}{k+2}}\right)^4}\Bigg]\times\left(\frac{\alpha_1 b_3^2\gamma_0^2e^{2\gamma_0 t}}{(3b_3e^{\gamma_0 t}+3b_4)^2}+\frac{1}{3}\frac{\alpha_2 b_3 b_4\gamma_0^2e^{\gamma_0 t}}{(b_3e^{\gamma_0 t}+b_4)^2}\right)^{\frac{\delta}{2}-1} \tag{29}$$

we find the skewness parameter as

$$\gamma=\frac{1}{3c^2}\left[\left((b_3e^{\gamma_0 t}+b_4)^{\frac{1}{k+2}}\right)^{2k-4}+\frac{(k-1)\gamma_0^2b_3e^{\gamma_0 t}}{(k+2)(b_3e^{\gamma_0 t}+b_4)}\right]\left(\frac{\alpha_1 b_3^2\gamma_0^2e^{2\gamma_0 t}}{(3b_3e^{\gamma_0 t}+3b_4)^2}+\frac{1}{3}\frac{\alpha_2 b_3 b_4\gamma_0^2e^{\gamma_0 t}}{(b_3e^{\gamma_0 t}+b_4)^2}\right)^{\frac{\delta}{2}-1}. \tag{30}$$

3. OBSERVATIONAL CONSTRAINTS

The field equations with anisotropic DE in the framework of self-creation theory of gravity have been solved in closed form, leading to a cosmological model in which the Hubble parameter depends explicitly on the parameters (H_0, b_4). To test the viability of this solution in describing the present Universe, we employ observational Hubble datasets to constrain the model parameters. For this purpose, we use a joint compilation of 31 Hubble parameter measurements obtained from cosmic chronometer (CC) observations [66, 67]. To explore the parameter space around the local minima, we carry out a numerical analysis with the `emcee` package in Python, adopting Gaussian priors centered on the initial estimates with a fixed standard deviation of $\sigma = 1.0$. The statistical analysis is based on the chi-square estimator, defined as

$$\chi^2_H(H_0,b_4)=\sum_{i=1}^{31}\frac{[H_{\rm th}(z_i;H_0,b_4)-H_{\rm obs}(z_i)]^2}{\sigma^2_{H(z_i)}}, \tag{31}$$

where $H_{\rm obs}(z_i)$ denotes the observed Hubble parameter at redshift z_i, $H_{\rm th}(z_i;H_0,b_4)$ is the theoretical prediction of the model, and $\sigma_{H(z_i)}$ represents the corresponding observational uncertainty. Using this dataset, we obtain the best-fit values of the parameters H_0 and b_4. The constraints are derived through a Markov Chain Monte Carlo (MCMC) analysis, ensuring a robust estimation of the model parameters in light of current observational data.

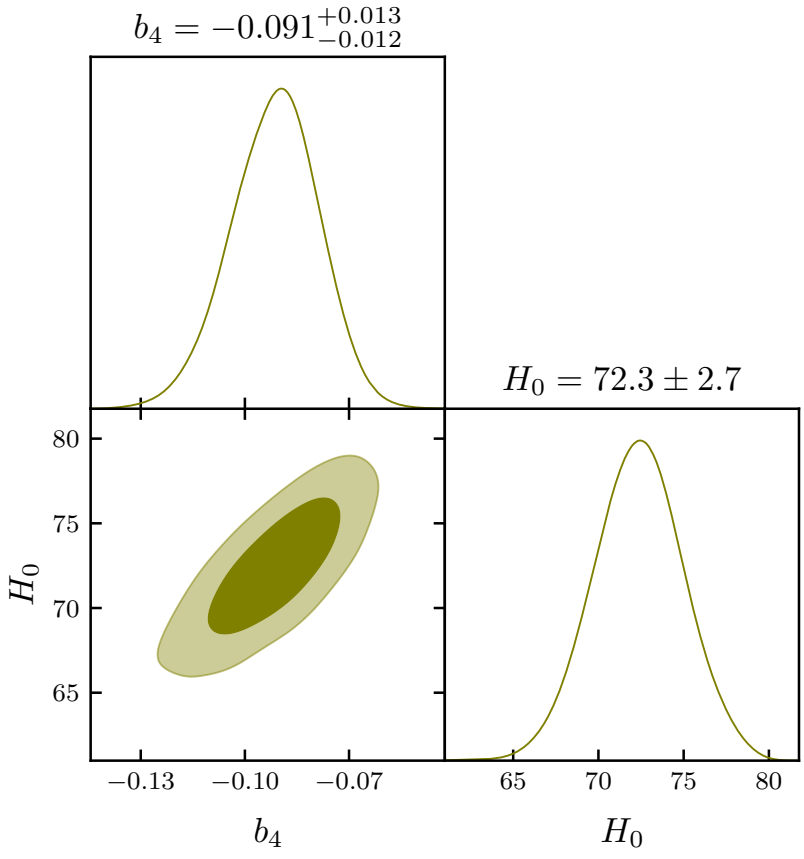

Figure 1. The plot displays the 2D contour plots of the model parameters.

In order to test the validity of the proposed BHDE models, we have constrained the free parameters using Hubble cosmic chronometer (CC) data. The joint analysis provides best-fit values for the model parameter and the present Hubble

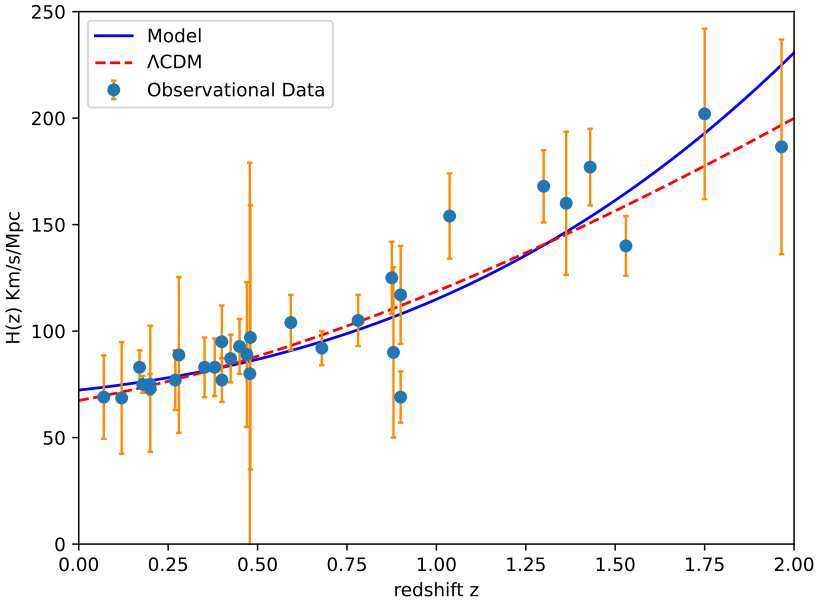

Figure 2. Evolution of Hubble parameter $H(z)$ versus redshift z. The solid line represents our model and dotted-line indicates the ΛCDM model with $\Omega_{m0} = 0.3$ and $\Omega_{\Lambda 0} = 0.7$. The dots are shown the Hubble dataset with error bar.

constant as

$$b_4 = -0.091^{+0.013}_{-0.012}, \qquad H_0 = 72.3 \pm 2.7 \text{ km s}^{-1}\text{Mpc}^{-1}.$$

Fig. 1 displays the contour plots in the b_4–H_0 parameter space. The contours show a well-defined and narrow confidence region, implying that both b_4 and H_0 are tightly constrained by the CC dataset. Fig. 2 illustrates the theoretical prediction of the Hubble parameter $H(z)$ for the best-fit model, along with the observational Hubble data points and the standard ΛCDM curve for comparison. The model curve exhibits excellent agreement with the observational Hubble data across the redshift range $0 < z < 2$, confirming its consistency with the observed expansion history. The combination of low-z ΛCDM-like behaviour and high-z deviations highlights the dynamical nature of BHDE, which interpolates between standard expansion and phantom-like regimes.

4. COSMOLOGICAL PARAMETERS

In this section, we analyze the expansion behavior of the universe for the constructed BHDE models (Model-1 and Model-2) using well-established cosmological diagnostics, including the EoS parameter ω_{de}, the squared sound speed v_s^2, the deceleration parameter q. Additionally, we employ cosmological diagnostic planes such as $\omega_{de} - \omega'_{de}$, the statefinder pair (r, s), and the $r - q$ plane. Here, we have used the parameter values as $\gamma_0 = 0.62$, $n = -0.964$, $b_1 = 0.3$, $b_2 = -0.03063$, $b_4 = -0.091^{+0.013}_{-0.012}$, $H_0 = 72.3 \pm 2.7$, $\lambda = 10.02$, $\phi_0 = 40.021$, $w = 60.1$, $k = 0.98$, $c = 0.65$, $\delta = 0.66$, $\alpha_1 = 0.98$, $\alpha_2 = 0.01$ for graphical representation of the dynamical parameters of the models.

Scalar field: Fig. 3 shows the evolution of the scalar field $\phi(z)$ as a function of redshift z, where the shaded region represents the 1σ confidence interval obtained for the parameter $b_4 = -0.091^{+0.013}_{-0.012}$. The scalar field increases monotonically with redshift, starting from small values at $z < 0$ (future epoch) and attaining progressively larger values at higher redshifts ($z > 1$). This trend indicates that the scalar field was dynamically significant in the early Universe and gradually decreased in relative strength toward the present epoch. The shaded area in the plot quantifies the effect of uncertainties in b_4. Near the present epoch ($z \approx 0$), the uncertainty is minimal, indicating that the scalar field behaviour is well constrained by observations. At higher redshifts ($z > 2$), the spread grows wider, reflecting the cumulative impact of parameter uncertainties on the early-time evolution of $\phi(z)$. The increasing scalar field amplitude in the past suggests its dominance during the anisotropic early Universe, possibly contributing to structure formation or stiff-fluid–like dynamics. Toward late times, the reduction in $\phi(z)$ signifies its transition to a subdominant role. The constrained negative value of b_4 ensures consistency with this transition while still allowing for a dynamical scalar field contribution.

Deceleration parameter: The deceleration parameter

$$q(z) = -\frac{\ddot{a}\,a}{\dot{a}^2} = -1 - \frac{3b_4}{b_3 e^{\gamma_0 t}} \tag{32}$$

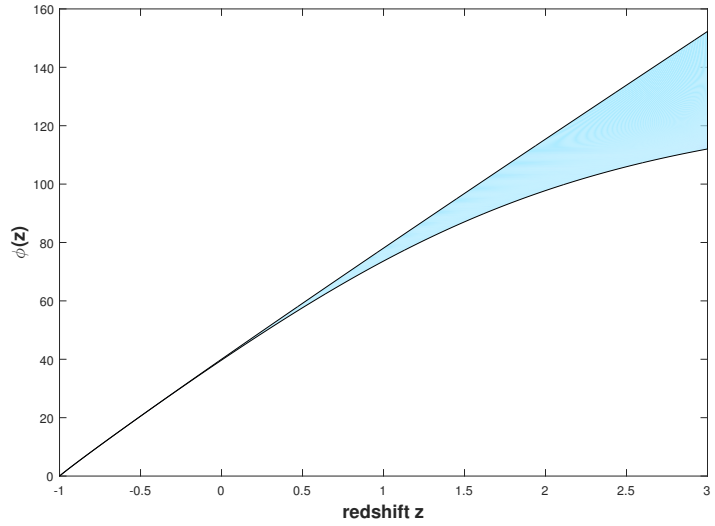

Figure 3. Plot of scalar field versus redshift.

encodes the kinematic state of cosmic expansion: $q > 0$ denotes a decelerating universe, $q = 0$ a uniform expansion rate, and $q < 0$ an accelerating expansion.

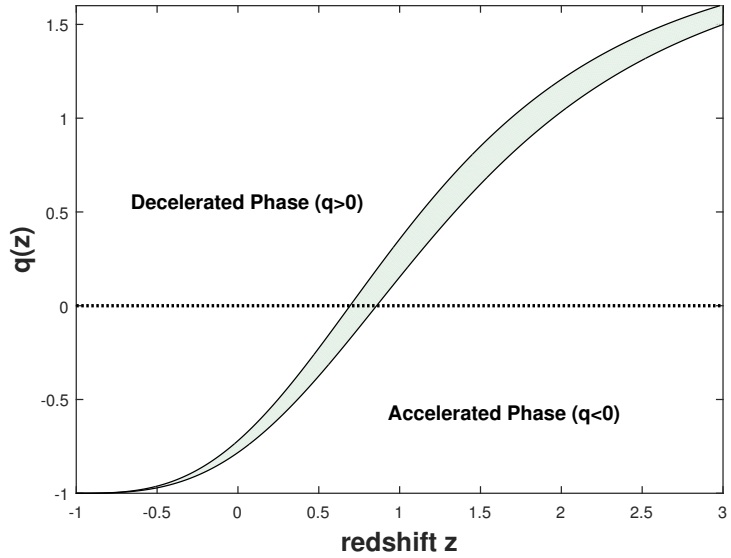

Figure 4. Deceleration parameter versus redshift.

The plotted curve of $q(z)$ with the shaded band in Fig. 4 shows both the best–fit evolution and the 1σ uncertainty corresponding to the fitted parameter $b_4 = -0.091^{+0.013}_{-0.012}$. The small uncertainty on b_4 indicates that the data set used for the fit tightly constrains the model direction controlled by this parameter. The narrow shaded region around the central curve implies that the inferred shape of $q(z)$ is robust against modest changes in model parameters. The curve clearly shows $q(z) > 0$ at sufficiently large redshift, signaling the expected decelerated expansion in the matter (and earlier radiation) dominated epochs. At lower redshifts the curve crosses $q = 0$ and becomes negative, indicating a transition to accelerated expansion. The transition (or transition redshift z_t) lies in the intermediate redshift range (roughly of order unity), marking the epoch when the dark–energy–like component began to dominate the expansion dynamics. At the present epoch ($z \approx 0$) the curve lies in the $q < 0$ region, consistent with a presently accelerating Universe. The shaded band shows that the sign and magnitude of q_0 are determined with good precision. It can be seen that our models decelerates at high z, a transition at $z \sim 1$, and acceleration at low z which is in agreement with independent probes such as SNe Ia, BAO and CC measurements.

Statefinder parameters: Various DE models have emerged in recent years, aiming to elucidate the accelerating ex-

pansion of the universe. Interestingly, these models often yield identical values for the current Hubble and deceleration parameters, making them practically indistinguishable from one another. Sahni et al. [68] proposed a merger of the deceleration and Hubble parameters, expressed as:

$$r=\frac{\dddot{a}}{aH^3}, \quad s=\frac{r-1}{3(q-1/2)}. \tag{33}$$

The statefinder parameters for our model are

$$r = 1+\frac{9{b_4}^2}{{b_3}^2\left(e^{\gamma_0 t}\right)^2} \tag{34}$$

$$s = \frac{{b_4}^2}{{b_3}^2\left(e^{\gamma_0 t}\right)^2}\left(-\frac{1}{2}-\frac{b_4}{b_3 e^{\gamma_0 t}}\right)^{-1} \tag{35}$$

Fig. 5 displays the trajectories of the models in the (r, s) diagnostic plane, which provide powerful geometrical tools to distinguish different DE scenarios from one another and from the concordance ΛCDM model. The statefinder pair (r, s) is defined in terms of higher derivatives of the scale factor and is particularly effective in discriminating among DE models. The ΛCDM model corresponds to the fixed point $(r, s) = (1, 0)$, while the CDM model lies at $(r, s) = (1, 1)$. The trajectories in the figure show that the model under consideration evolves away from the ΛCDM fixed point, moving through different evolutionary regimes. The sign of s carries important physical meaning. For $s > 0$, the trajectory indicates a phantom-like behaviour of DE, whereas $r < 1$ corresponds to the quintessence regime. The region $s < 0$ with $r > 1$ is characteristic of the Chaplygin gas model, representing a unified description of dark matter and DE. The trajectory's excursion into this domain indicates that the model mimics Chaplygin-like behaviour during certain epochs.

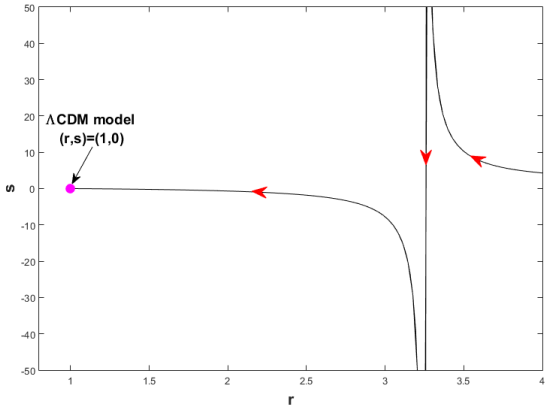

Figure 5. Plot of $r - s$ plane.

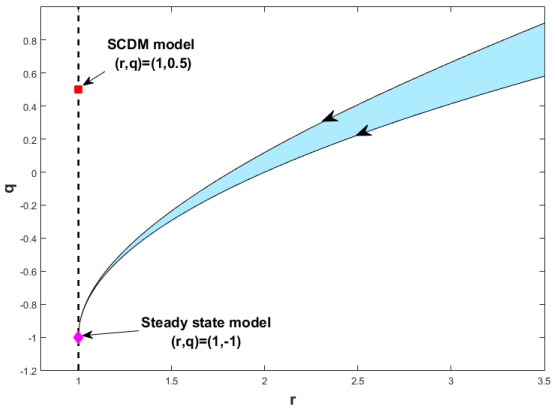

Figure 6. Plot of $r - q$ plane.

(r, q) **plane:** The (r, q) diagnostic provides another valuable tool for testing the dynamical behaviour of cosmological models, particularly in distinguishing between decelerating and accelerating phases. Fig. 6 gives the behavior of our model in $r - q$ plane. Two fixed points are of particular interest: $(r, q) = (1, 0.5)$, corresponding to the standard cold dark matter (SCDM) model without a cosmological constant, and $(r, q) = (1, -1)$, corresponding to the de Sitter model. The trajectories in the (r, q) plane clearly illustrate the transition from the decelerating matter-dominated epoch to the accelerating DE-dominated epoch. The shaded region corresponds to the uncertainty arising from the fitted model parameters and highlights the robustness of this transition. The arrows on the curves indicate the evolutionary direction, showing that the Universe starts near the SCDM point at high redshift and evolves towards the de Sitter attractor at late times.

Skewness parameter: Figs. 7 and 8 illustrate the behaviour of the skewness (or deviation) parameter γ as a function of redshift for both model-1 and model-2. The parameter γ quantifies the deviation of the DE EoS from its isotropic counterpart and therefore serves as a diagnostic tool for identifying anisotropies, departures from ΛCDM, and higher-order dynamical corrections. In both models, γ increases with redshift, reaches a peak around $z \sim 1$–2, and then saturates or decreases at higher redshift. This peak corresponds to the transition epoch from deceleration to acceleration, indicating that anisotropic effects and deviations from the canonical EoS are most pronounced during this phase. In the late Universe, $\gamma \to 0$, implying that the DE component behaves isotropically and resembles the standard ΛCDM model. This result is consistent with present observational constraints that strongly favour isotropy and $\omega_{de} \approx -1$ in the current epoch. At early times, the value of γ decreases again, reflecting the dominance of the matter component over DE. This indicates

that anisotropic deviations become less significant when the Universe approaches the standard matter-dominated evolution. Both models exhibit similar qualitative trends, but subtle differences are evident. Model-1 produces slightly larger uncertainty bands and stronger anisotropic deviations at higher z, whereas model-2 yields a narrower confidence region and smoother evolution of γ. This suggests that the model-2 provides a more stable description of anisotropic departures from ΛCDM and is therefore better aligned with current observational data.

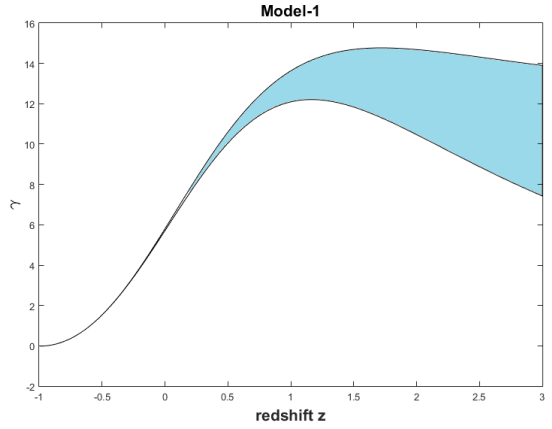

Figure 7. Plot of skewness parameter versus redshift for model-1.

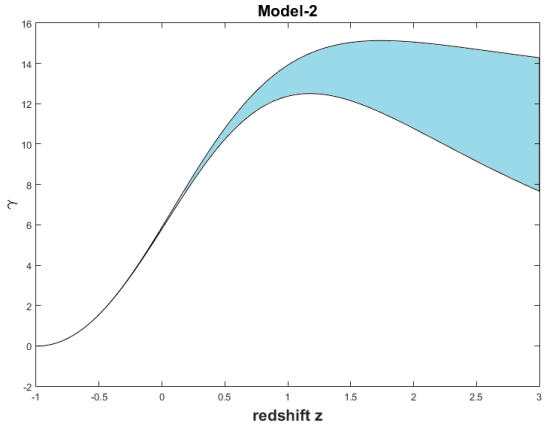

Figure 8. Plot of skewness parameter versus redshift for model-2.

Energy conditions: The Raychaudhuri equations initiated the exploration of energy conditions, playing a crucial role in analyzing the alignment of null and time-like geodesics. The energy conditions are used to illustrate other universal principles about the dynamics of intense gravitational fields. The often observed energy conditions are as follows:

Dominant energy condition (DEC): $\rho_{de} \geq 0$, $\rho_{de} \pm p_{de} \geq 0$.
Strong energy conditions (SEC) : $\rho_{de} + p_{de} \geq 0$, $\rho_{de} + 3p_{de} \geq 0$,
Null energy conditions (NEC): $\rho_{de} + p_{de} \geq 0$,
Weak energy conditions (WEC): $\rho_{de} \geq 0$, $\rho_{de} + p_{de} \geq 0$,

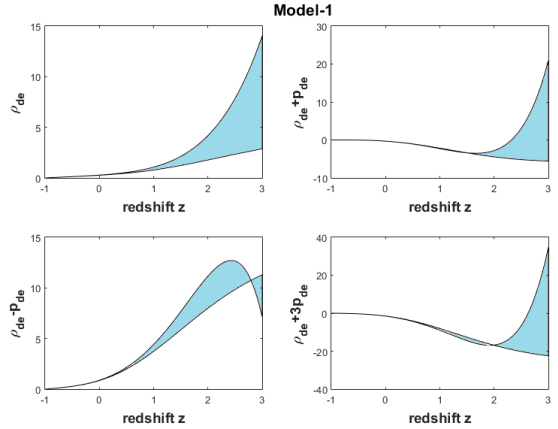

Figure 9. Plot of energy conditions versus redshift for model-1.

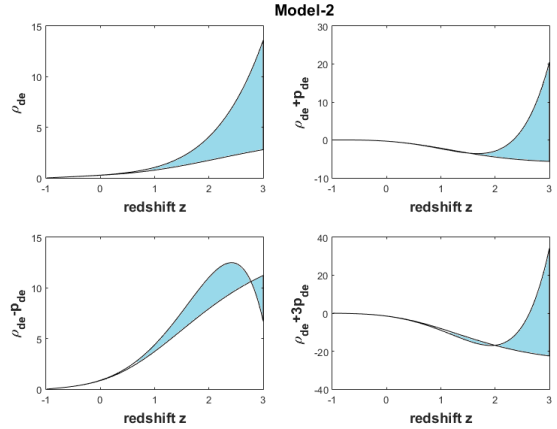

Figure 10. Plot of energy conditions versus redshift for model-2.

Figs. 9 and 10 show the behaviour of various combinations of the DE density and pressure that are directly related to the classical energy conditions. The shaded regions correspond to the 1σ confidence interval due to the constraint $b_4 = -0.091^{+0.013}_{-0.012}$. The following points are the implications for the dominant, strong, null, and weak energy conditions in both model-1 and model-2. The WEC requires $\rho_{de} \geq 0$ and $\rho_{de} + p_{de} \geq 0$. From the plots, ρ_{de} remains strictly positive throughout the redshift range for both models, ensuring that the first part of the WEC is always satisfied. However, the condition $\rho_{de} + p_{de} \geq 0$ shows periods of violation at intermediate and high redshifts, particularly in model-1, reflecting the phantom-like behaviour of DE in those epochs. The NEC has the same requirement as the second part of the WEC, i.e. $\rho_{de} + p_{de} \geq 0$. In both models, NEC is violated when the evolution of ω_{de} dips into the phantom regime ($\omega_{de} < -1$). The DEC requires $\rho_{de} \geq 0$ and $\rho_{de} \pm p_{de} \geq 0$. As noted, $\rho_{de} \geq 0$ is always satisfied. However, $\rho_{de} - p_{de}$ (not explicitly

plotted) is easily satisfied since p_{de} is negative in most of the evolution. The critical test is $\rho_{de} + p_{de} \geq 0$, which, as discussed, is violated in the phantom era. Therefore, DEC is violated in epochs where the models enter deep phantom behaviour, more prominently in model-1. The SEC requires $\rho_{de} + p_{de} \geq 0$ and $\rho_{de} + 3p_{de} \geq 0$. The plots clearly show that $\rho_{de} + 3p_{de}$ becomes negative at low redshift in both models, indicating a violation of SEC in the late-time Universe. This violation is essential to drive accelerated expansion, consistent with the requirement for a negative effective pressure. In the high-redshift regime, the SEC can be partially restored, though the uncertainty bands suggest that the violation remains robust across most of the evolution. Both models share the same qualitative features with respect to the energy conditions, but the strength of violation differs. Model-1 shows stronger and more prolonged violations of NEC, WEC, and SEC, consistent with its deeper phantom excursions. Model-2, by contrast, exhibits milder violations and tends to stay closer to the boundary of the conditions.

EoS parameter (ω_{de}): It serves as a crucial tool for categorizing the various phases in the expanding universe. It is expressed as $\omega = \frac{p}{\rho}$, representing the relationship between pressure (p) and energy density (ρ) within a given matter distribution. Different phases, characterized by deceleration or acceleration, correspond to specific ranges of ω. Deceleration phases encompass intervals such as those involving cold dark matter or dust fluid (ω equals zero), indicating the radiation era when ω lies between 0 and $1/3$, and the fluid is classified as stiff for $\omega = 1$. The accelerating phase, akin to the cosmic constant/vacuum period (ω equals -1), corresponds to the quintessence period when $-1 < \omega < -1/3$, and it's known as the phantom era when $\omega < -1$. This signifies a quintom period characterized by a combination of both quintessence and phantom components.

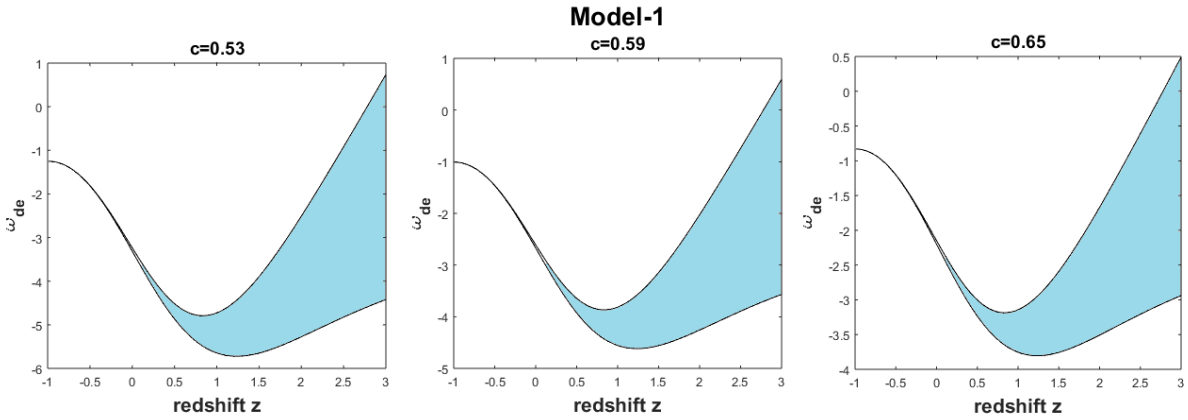

Figure 11. Plot of EoS parameter versus redshift for model-1.

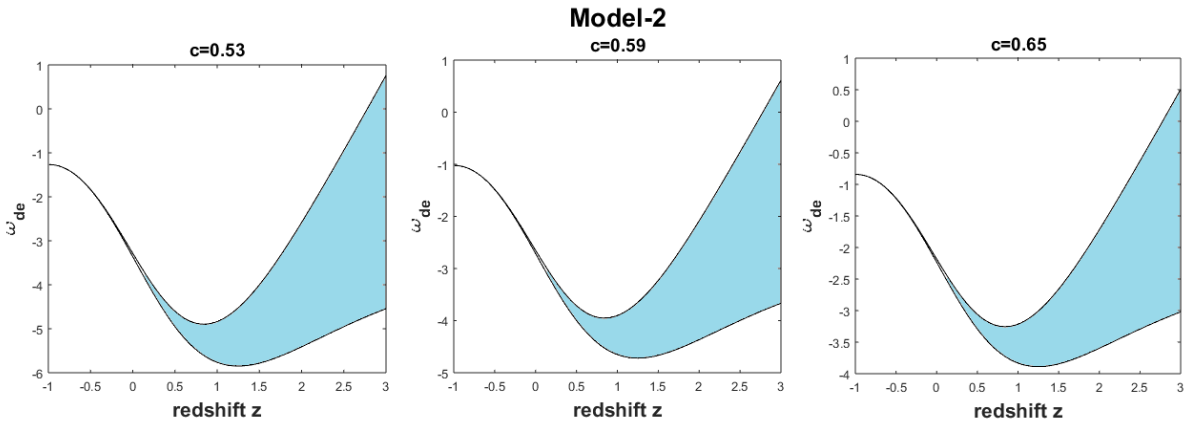

Figure 12. Plot of EoS parameter versus redshift for model-2.

Figs. 11 and 12 display the redshift evolution of the BHDE EoS parameter $\omega_{de}(z)$ for two models-1 & 2. Each panel shows the best–fit curve (solid line) and the 1σ uncertainty band for three representative values of the BHDE parameter c (here $c = 0.53, 0.59, 0.65$). Both models exhibit a strongly dynamical $\omega_{de}(z)$: the EoS begins near $\omega_{de} \simeq -1$ at very low redshift, steepens into a pronounced phantom regime ($\omega_{de} < -1$) at intermediate redshifts, reaches a minimum value typically around $z \sim 1$, and then turns upward at higher redshift. This nontrivial evolution indicates that the BHDE scenarios considered are dynamical DE models rather than simple cosmological constant models. Although the two model

types share the same qualitative trend, model-2 generally produces milder phantom regime than model-1 for the same values of c. Increasing c (from 0.53 to 0.65 in the panels) systematically shifts $\omega_{de}(z)$ upward, i.e. towards less phantom (closer to -1) behaviour. For each model the smallest c gives the deepest phantom dip, whereas larger c softens the deviation. This monotonic dependence highlights that the BHDE parameter controls the strength of dynamical effects: larger c weakens the departure from a cosmological constant. At low redshift the models are close to the cosmological constant ($\omega \approx -1$); at intermediate redshift they enter the phantom domain ($\omega < -1$); and at sufficiently high redshift they approach less negative values. Because ω_{de} can cross the phantom divide ($\omega = -1$) during evolution, the model naturally realizes a quintom-like behaviour (i.e., a combination of quintessence and phantom characteristics over cosmic history).

$\omega_{de}-\omega'_{de}$ plane: We examine the $\omega_{de} - \omega'_{de}$ plane, where ω'_{de} represents the rate of change of the EoS parameter ω_{de} with respect to $\ln(a(t))$ [69]. It has also been found that the $\omega_{de} - \omega'_{de}$ plane can be split into two regions: thawing ($\omega_{de} < 0$, $\omega'_{de} > 0$) and freezing ($\omega_{de} < 0$, $\omega'_{de} < 0$). The freezing region corresponds to a phase of faster cosmic acceleration compared to the thawing region.

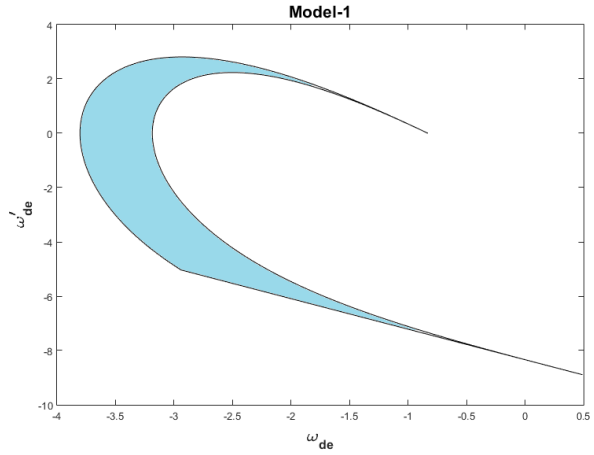

Figure 13. Plot of $\omega_{de} - \omega'_{de}$ plane for model-1.

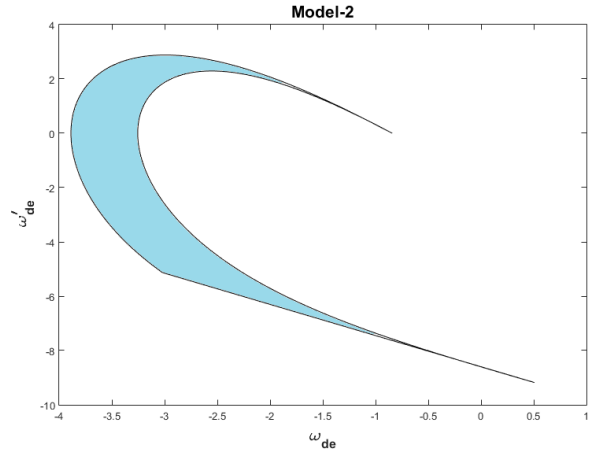

Figure 14. Plot of $\omega_{de} - \omega'_{de}$ plane for model-2.

Figs. 13 and 14 illustrate the trajectories of the BHDE models in the $\omega_{de} - \omega'_{de}$ phase plane. The shaded regions correspond to the 1σ confidence band for the parameter $b_4 = -0.091^{+0.013}_{-0.012}$. This diagnostic plane is especially useful in classifying DE models into thawing and freezing behaviours. Thawing region is defined by ($\omega_{de} < 0$, $\omega'_{de} > 0$), thawing models describe DE that was initially frozen at $\omega_{de} \simeq -1$ (cosmological constant–like) and then evolves towards less negative values. This regime typically corresponds to slower acceleration and a late-time deviation from ΛCDM. Freezing region is defined by ($\omega_{de} < 0$, $\omega'_{de} < 0$), freezing models evolve towards $\omega_{de} \to -1$, indicating a stronger tendency towards accelerated expansion. In this case, DE dynamics slow down asymptotically, producing a phase of more rapid cosmic acceleration compared to thawing models. Both model-1 (Hubble cutoff) and model-2 (GO cutoff) predominantly lie in the freezing region, as indicated by $\omega_{de} < 0$ and $\omega'_{de} < 0$ over most of the evolution. This suggests that the BHDE framework naturally drives the Universe towards a phase of faster acceleration at late times. The parameter $b_4 < 0$ ensures that ω_{de} remains deeply in the phantom regime ($\omega_{de} < -1$) for substantial intervals, while ω'_{de} is negative, reinforcing the freezing behaviour. The narrow shaded band implies that this classification is stable against 1σ variations in b_4. Both models show a qualitatively similar trajectory in the $\omega_{de} - \omega'_{de}$ plane. However, Model-2 (GO cutoff) produces a slightly less steep descent in ω'_{de}, which suggests a milder approach to the freezing regime compared to Model-1. This aligns with earlier findings that the GO cutoff yields more moderate dynamical behaviour and is closer to observationally preferred values. The freezing behaviour in both models is consistent with a late-time Universe dominated by a phantom-like DE component, driving accelerated expansion more efficiently than ΛCDM.

Squared sound speed: The squared sound speed

$$v_s^2 = \frac{\dot{p}_{de}}{\dot{\rho}_{de}} = \omega_{de} + \frac{\rho_{de}}{\dot{\rho}_{de}}\,\dot{\omega}_{de}. \tag{36}$$

is a primary diagnostic for the classical (linear) stability of cosmic fluids and effective DE components. If $v_s^2 > 0$ small perturbations oscillate (or propagate), and the background is classically stable at the linear level. Conversely, $v_s^2 < 0$ implies exponentially growing modes and a classical instability of the effective fluid, signalling that the background solution is not robust under perturbations.

Figs. 15 and 16 show the behavior of $v_s^2(z)$ for model-1 and model-2. The shaded band corresponds to the 1σ variation induced by the parameter $b_4 = -0.091^{+0.013}_{-0.012}$, so the blue region indicates the uncertainty in the predicted v_s^2

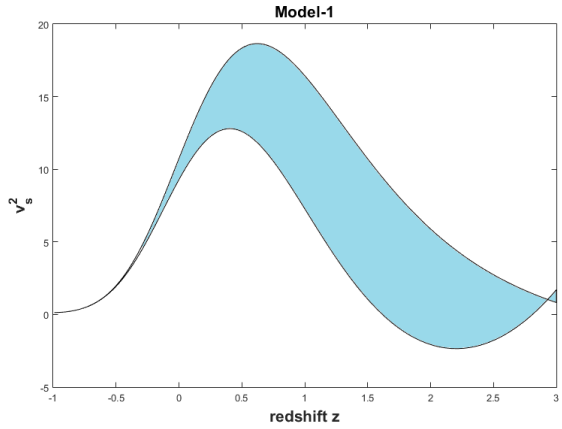

Figure 15. Plot of v_s^2 versus redshift for model-1.

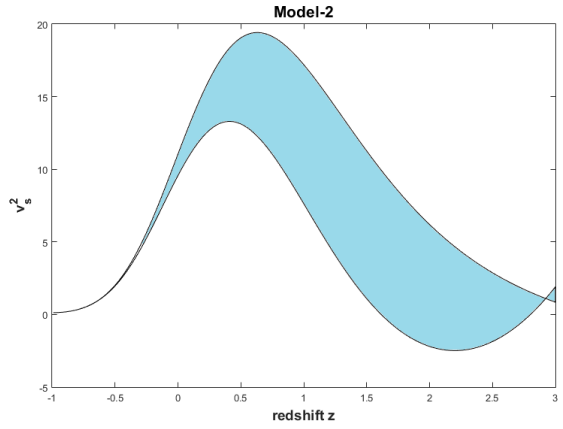

Figure 16. Plot of v_s^2 versus redshift for model-2.

due to the allowed range of b_4. For both models v_s^2 is positive over a substantial redshift interval (approximately around $0 \lesssim z \lesssim 2$ in the plots). This positive region indicates that — at least at the linear perturbation level — the models are classically stable during the recent cosmic history and around the epoch where DE dynamics is most relevant. At larger redshift (or at the far end of the plotted range) v_s^2 declines and in the displayed examples it approaches or crosses slightly below zero. Where v_s^2 becomes negative, the model develops a classical instability for perturbations in that epoch. The two models show qualitatively similar $v_s^2(z)$ shapes and uncertainty bands for the given b_4 range, although small quantitative differences are present in the peak height and the redshift where v_s^2 declines. Model-2 (GO cutoff) tends to produce a slightly more moderate peak and a somewhat narrower band at intermediate z, consistent with earlier findings that the GO cutoff yields milder departures from ΛCDM for comparable parameters. Both models, however, share the same qualitative features: a stable positive region followed by a decline and potential instability at larger $|z|$.

5. CONCLUSIONS

In this work, we have constructed anisotropic BT-*II* cosmological models within the framework of Self-creation theory of gravitation, considering BHDE with two different IR cutoffs: the Hubble horizon and the GO cutoff. By assuming a suitable relation between metric potentials, we obtained exact solutions of the field equations and explored the dynamical and observational features of the models. The main conclusions can be summarized as follows:

- The contour plot obtained from Hubble CC data, which provides joint constraints on the model parameter b_4 and the present Hubble constant H_0. The analysis yields the best-fit values $b_4 = -0.091^{+0.013}_{-0.012}$, $H_0 = 72.3 \pm 2.7$ km s^{-1}Mpc^{-1}. The contour plots confirm the robustness of these constraints, while the $H(z)$ fit demonstrates consistency with the observed expansion history and mild deviations from ΛCDM at high redshifts.

- The scalar field $\phi(z)$ decreases monotonically with evolution of the models, with larger values at higher redshift indicating its strong dynamical contribution in the early Universe. At low z, the scalar field contribution diminishes, consistent with a DE-dominated accelerated phase. The models successfully reproduce the transition from a past decelerated epoch ($q > 0$) to the present accelerating epoch ($q < 0$). The transition redshift lies in the interval $z_{tr} \sim$ 0.6–0.8, which is in excellent agreement with observational estimates from SNeIa and BAO data [70, 71]. In the (r, s) plane, both models evolve away from the ΛCDM fixed point $(r, s) = (1, 0)$, entering regions corresponding to quintessence and phantom behaviour depending on epoch. In the (r, q) plane, the trajectories clearly demonstrate the transition from the SCDM point $(1, 0.5)$ (matter-dominated decelerated era) to the de-Sitter model $(1, -1)$ (cosmological constant-dominated accelerated era).

- The deviation parameter γ shows strong growth around the transition epoch ($z \sim$ 1–2), signaling maximum deviations from isotropy and enhanced dynamical effects of DE. At late times, $\gamma \to 0$, restoring isotropy and a ΛCDM-like state. Model-2 again demonstrates a more stable and narrower evolution of γ compared to model-1, suggesting that anisotropic effects are better regulated under the GO cutoff. The WEC and NEC are largely satisfied in both models. However, the SEC is violated in the low-redshift regime, which is consistent with the requirement for cosmic acceleration. The DEC is upheld in most cases, validating the physical viability of the models.

- Both models exhibit a quintom-like behaviour, evolving across the cosmological constant boundary $\omega_{de} = -1$. At low redshift, ω_{de} remains close to -1, consistent with current Planck 2018 bounds [72] ($\omega_{de} = -1.03 \pm 0.03$), while at higher redshifts both models transition into the phantom regime ($\omega_{de} < -1$). The shaded regions confirm that this transition is robust under observational uncertainties. Both models lie predominantly in the freezing region ($\omega_{de} <$

Table 1. Comparison of cosmological behaviour between Model-1 (Barrow HDE with Hubble cutoff) and Model-2 (Barrow HDE with GO cutoff).

Diagnostic	**Model-1 (Hubble cutoff)**	**Model-2 (GO cutoff)**
Scalar field $\phi(z)$	Monotonically increasing with redshift and slightly stronger growth	Same behavior as model-1
Deceleration parameter $q(z)$	Clear transition at $z_{tr} \sim 0.6$–0.8 consistent with data	Same behavior as model-1
Statefinder (r, s) **plane**	Model finally approaches to ΛCDM $(1, 0)$ model and also shows quintessence and phantom phases	Same behavior as model-1
(r, q) **plane**	Transition from SCDM $(1, 0.5)$ to de-Sitter $(1, -1)$ and larger spread	Same transition as model-1
Energy conditions	WEC and NEC satisfied, SEC violated at late times (required for acceleration) and DEC valid mostly	Similar behaviour but with fewer violations and more consistent with cosmic acceleration
Skewness parameter γ	Peaks strongly around $z \sim 1-2$, larger deviations from isotropy and broader band	Similar peak but narrower confidence region and anisotropy effects better controlled
Equation of state parameter ω_{de}	Shows quintom behaviour, crosses $\omega = -1$ and broader uncertainty band	Similar quintom behaviour, smoother trajectory and closer to Planck constraints
$\omega_{de} - \omega'_{de}$ **plane**	Mostly in freezing region and strong acceleration phase	Also in freezing region and smoother evolution but closer to de-Sitter attractor
Squared sound speed v_s^2	Stability at intermediate z, instabilities at certain epochs and wider uncertainty	More stable evolution, reduced instabilities and narrower uncertainty band

$0, \omega'_{de} < 0$), corresponding to stronger cosmic acceleration compared to thawing models. This indicates that the DE dynamics in these models naturally drive a future de Sitter-like phase. The squared sound speed v_s^2 exhibits both positive and negative values. In the intermediate redshift regime, $v_s^2 > 0$ confirms stability, while instabilities ($v_s^2 < 0$) arise at certain epochs. Model-2 provides a smoother and more stable profile compared to model-1, with narrower uncertainty bands, suggesting that the GO cutoff yields a more observationally consistent description.

Finally, both BHDE models (Hubble and GO cutoffs) are consistent with observational constraints and reproduce the main features of cosmic evolution, including the transition from deceleration to acceleration, quintom behaviour of DE, and late-time convergence to ΛCDM-like dynamics. Model-1 (Hubble cutoff) shows slightly stronger deviations and broader uncertainty bands, while model-2 (GO cutoff) provides smoother trajectories, reduced anisotropies, and better stability properties. This suggests that the GO cutoff may represent a more robust framework for describing the late-time dynamics of the Universe.

Acknowledgment: We thank the reviewers/editor for their constructive comments which have considerably improved the presentation of our work. Y. Aditya expresses gratitude to the National Board for Higher Mathematics, Department of Atomic Energy, Government of India, for their financial support under grant No: 02011/8/2023 NBHM(R.P.)/R & D II/3073.

ORCID

U.Y. Divya Prasanthi, https://orcid.org/0009-0004-5397-050X; **D. Tejeswararao**, https://orcid.org/0000-0003-3508-346X; **Diddi Srinivasa Rao**, https://orcid.org/0009-0001-6890-9603; **Y. Aditya**, https://orcid.org/0000-0002-5468-9697; **D. Ram Babu**, https://orcid.org/0009-0008-7791-5977

REFERENCES

[1] S. Perlmutter, et al., Astrophys. J. **517**, 565 (1999). https://doi.org/10.1086/307221

[2] A. G. Riess, et al., Astron. Soc. Pac. **112**, 1284 (2000). https://doi.org/10.1086/316624

[3] M. Tegmark, et al., Phys. Rev. D, **69**, 103501 (2004). https://doi.org/10.1103/PhysRevD.69.103501
[4] L. Susskind, J. Math. Phys. **36**, 6377 (1994). http://dx.doi.org/10.1063/1.531249
[5] R. Bousso, JHEP, **07**, 004 (1999). https://doi.org/10.1088/1126-6708/1999/07/004
[6] A. Cohen, et al., Phys. Rev. Lett. **82**, 4971 (1999). https://doi.org/10.1103/PhysRevLett.82.4971
[7] M. Tavayef, et al., Phys. Lett. B, **781**, 195 (2018). https://doi.org/10.1016/j.physletb.2018.04.001
[8] C. Tsallis, and L.J.L. Cirto, Eur. Phys. J. C, **73**, 2487 (2013). https://doi.org/10.1140/epjc/s10052-013-2487-6
[9] A.S. Jahromi et al., Phys. Lett. B, **780**, 21 (2018). https://doi.org/10.1016/j.physletb.2018.02.052
[10] H. Moradpour et al., Eur. Phys. J. C, **78**, 829 (2018). https://doi.org/10.1140/epjc/s10052-018-6309-8
[11] Y. Aditya, and D.R.K. Reddy, Eur. Phys. J. C, **78**, 619 (2018). https://doi.org/10.1140/epjc/s10052-018-6074-8
[12] Y. Aditya, and D.R.K. Reddy, Astrophys. Space Sci. **363**, 207 (2018). https://doi.org/10.1007/s10509-018-3429-4
[13] U.Y. Divya Prasanthi, and Y. Aditya, Results Phys. **17**, 103101 (2020). https://doi.org/10.1016/j.rinp.2020.103101
[14] Y. Aditya, Bulgarian Astronomical Journal **40**, 95 (2024). https://astro.bas.bg/AIJ/issues/n40/YAditya.pdf
[15] Y. Aditya, and U.Y.D. Prasanthi, Bulgarian Astronomical Journal **38**, 52 (2023). https://astro.bas.bg/AIJ/issues/n38/YAditya.pdf
[16] Y. Aditya, et al., East Eur. J. Phys. **1**, 85 (2024). https://doi.org/10.26565/2312-4334-2024-1-06
[17] A. V. Prasanthi, et al., East Eur. J. Phys. **2**, 10 (2024). https://doi.org/10.26565/2312-4334-2024-2-01
[18] V.U.M. Rao, et al., Results in Physics, **10**, 469 (2018). https://doi.org/10.1016/j.rinp.2018.06.027
[19] M.V. Santhi, et al., Int. J. Theor. Phys. **56**, 362 (2017). https://doi.org/10.1007/s10773-016-3175-8
[20] Y. Aditya, et al., Eur. Phys. J. C, **79**, 1020 (2019). https://doi.org/10.1140/epjc/s10052-019-7534-5
[21] A. Iqbal, and A. Jawad, Physics of the Dark Universe, **26**, 100349 (2019). https://doi.org/10.1016/j.dark.2019.100349
[22] G. Kaniadakis, Physica A: Stat. Mech. and its Appl. **296**(3-4), 405 (2001). https://doi.org/10.1016/S0378-4371(01)00184-4
[23] M. Masi, Phys. Lett. A, **338**, 217 (2005). https://doi.org/10.1016/j.physleta.2005.01.094
[24] E.M. Abreu, et al., EPL (Europhysics Letters), **124**, 30003 (2018). https://doi.org/10.1209/0295-5075/124/30003
[25] J. D. Barrow, S. Basilakos, and E. N. Saridakis, Phys. Lett. B, **815**, 136134 (2021). https://doi.org/10.1016/j.physletb.2021.136134
[26] G. G. Luciano, and E. N. Saridakis, Eur. Phys. J. C, **82**, 558 (2022). https://doi.org/10.1140/epjc/s10052-022-10530-7
[27] G. G. Luciano, Phys. Rev. D, **106**, 083530 (2022). https://doi.org/10.1103/PhysRevD.106.083530
[28] A. Oliveros, et al., Eur. Phys. J. Plus. **137**, 783 (2022). https://doi.org/10.1140/epjp/s13360-022-02994-z
[29] A. Remya, et al., Int. J. Geom. Methods Mod. Phys. **19**, 2250082 (2022). https://doi.org/10.1142/S0219887822500827
[30] M. Koussour, et al., Int. J. Mod. Phys. A, **37**, 2250184 (2022). https://doi.org/10.1142/S0217751X22501846
[31] Y. Aditya, et al., Afrika Matematika, **36**, 120 (2025). https://doi.org/10.1007/s13370-025-01340-7
[32] G.A. Barber, Gen. Relativ. Gravit. **14**, 117 (1982). https://doi.org/10.1007/BF00756918
[33] T. Singh, Astrophys. Space Sci. **102**, 67 (1984). https://doi.org/10.1007/BF00651062
[34] D.R.K. Reddy, Astrophys. Space Sci. **133**, 389 (1987). https://doi.org/10.1007/BF00642496
[35] V.U.M. Rao, et al., Astrophys Space Sci. **317**, 83 (2008). https://doi.org/10.1007/s10509-008-9859-7
[36] R.L. Naidu, et al., Astrophys Space Sci. **358**, 23 (2015). https://doi.org/10.1007/s10509-015-2421-5
[37] V.U.M. Rao, and U.Y.D. Prasanthi, Can. J. Phys. **95(6)**, 554 (2017). https://doi.org/10.1139/cjp-2017-0014
[38] R.R. Caldwell, and M. Kamionkowski, Ann. Rev. Nucl. Part. Sci. **59**, 397 (2009). https://doi.org/10.1146/annurev-nucl-010709-151330
[39] K. Bamba, et al., Astrophys. Space Sci. **342**, 155 (2012). https://doi.org/10.1007/s10509-012-1181-8
[40] S. Nojiri, et al., Phys. Rept. **692**, 1 (2017). https://doi.org/10.1016/j.physrep.2017.06.001
[41] Y. Aditya, D.R.K. Reddy, Eur. Phys. J. C, **78**, 619 (2018). https://doi.org/10.1140/epjc/s10052-018-6074-8
[42] V.U.M. Rao, et al., Results in Physics, **10**, 469 (2018). https://doi.org/10.1016/j.rinp.2018.06.027
[43] Y. Aditya, et al., Eur. Phys. J. C, **79**, 1020 (2019). vhttps://doi.org/10.1140/epjc/s10052-019-7534-5
[44] U.K. Sharma, et al., IJMPD, **31**, 2250013 (2022). https://doi.org/10.1142/S0218271822500134
[45] U.Y.D. Prasanthi, and Y. Aditya, Results of Physics, **17**, 103101 (2020). https://doi.org/10.1016/j.rinp.2020.103101
[46] U.Y.D. Prasanthi, and Y. Aditya, Physics of the dark universe, **31**, 100782 (2021). https://doi.org/10.1016/j.dark.2021.100782
[47] Y. Aditya, D.R.K. Reddy, Astrophys. Space Sci, **363**, 207 (2018). https://doi.org/10.1007/s10509-018-3429-4
[48] Y Aditya, et al., Results in Physics, **12**, 339 (2019). https://doi.org/10.1016/j.rinp.2018.11.074
[49] Y. Aditya, et al. Astrophys. Space Sci. **364**, 190 (2019). https://doi.org/10.1007/s10509-019-3681-2
[50] Y. Aditya, et al., Int. J. Mod. Phys. A, **37**, 2250107 (2022). https://doi.org/10.1142/S0217751X2250107X

[51] A. Jawad, et al. Symmetry, **10**, 635 (2018). https://doi.org/10.3390/sym10110635
[52] C.B. Collins, et al., Gen. Relativ. Gravit. **12**, 805 (1980). https://doi.org/10.1007/BF00763057
[53] K.S. Thorne, Astrophys. J. **148**, 51 (1967). https://doi.org/10.1086/149127
[54] R. Kantowski, and R.K. Sachs, J. Math. Phys. **7**, 433 (1966). https://doi.org/10.1063/1.1704952
[55] J. Kristian, and R.K. Sachs, Astrophys. J. **143**, 379 (1966). http://dx.doi.org/10.1086/148522
[56] V.B. Johri, and R. Sudharsan, Australian Journal of Physics, **42(2)**, 215 (1989). https://doi.org/10.1071/PH890215
[57] V.B. Johri, and K. Desikan, Gen. Relat. Gravit. **26**, 1217 (1994). https://doi.org/10.1007/BF02106714
[58] K. D. Raju, et al., Astrophys. Space Sci. **365**, 28 (2020). https://doi.org/10.1007/s10509-020-3729-3
[59] K. D. Raju, et al., Astrophys. Space Sci. **365**, 45 (2020). https://doi.org/10.1007/s10509-020-03753-1
[60] Y. Aditya, et al., Indian J. Phys. **95**, 383 (2021). https://doi.org/10.1007/s12648-020-01722-6
[61] K.D. Naidu, et al., Int. J. Mod. Phys. A, **36**(8), 2150054 (2021). https://doi.org/10.1142/S0217732321500541
[62] R.L. Naidu, et al., New Astron. **85**, 101564 (2021). https://doi.org/10.1016/j.newast.2020.101564
[63] Y. Aditya, Bulg. Astron. J. **39**, 12 (2023). https://astro.bas.bg/AIJ/issues/n39/YAditya.pdf
[64] L. N. Granda, and A. Oliveros, Phys. Lett. B, **669**, 275 (2008). https://doi.org/10.1016/j.physletb.2008.10.017
[65] L. N. Granda, and A. Oliveros, Phys. Lett. B, **671**, 199 (2009). https://doi.org/10.1016/j.physletb.2008.12.025
[66] J. Simon, L. Verde, and R. Jimenez, Phys. Rev. D, **71**, 123001 (2005). https://doi.org/10.1103/PhysRevD.71.123001
[67] G.S. Sharov, and V.O. Vasiliev, Math. Model. Geom. **6**, 1-20 (2018).
[68] V. Sahni, et al. J. Exp. Theor. Phys. Lett. **77**, 201 (2003). https://doi.org/10.1134/1.1574831
[69] R. Caldwell, and E.V. Linder, Phys. Rev. Lett. **95**, 141301 (2005). https://doi.org/10.1103/PhysRevLett.95.141301
[70] S. Capozziello, et al., MNRAS, **484**, 4484 (2019). https://doi.org/10.1093/mnras/stz176
[71] G. F. Hinshaw, et al., Astrophys. J. Suppl. **208**, 19 (2018). https://doi.org/10.1088/0067-0049/208/2/19
[72] N. Aghanim, et al., A&A **641**, A6 (2020). https://doi.org/10.1051/0004-6361/201833910

КОСМОЛОГІЧНА ДІАГНОСТИКА ГОЛОГРАФІЧНОЇ ТЕМНОЇ ЕНЕРГІЇ ВСЕСВІТУ БАРРОУ ТИПУ БІАНКІ-II

У.Й. Дів'я Прасанті[1], **Д. Техесварарао**[2], **Дідді Шрініваса Рао**[3], **Ю. Адітья**[4], **Д. Рам Бабу**[4]

[1]*Департамент статистики & математики Коледж садівництва, доктор Y.S.R. Садівничий університет, Парватіпурам-535502, Індія*

[2]*Кафедра фундаментальних та гуманітарних наук, Технологічний інститут GMR (GMRIT) – вважається університетом, Раджам-532127, Індія*

[3]*Кафедра математики, Університет Адітья, Сурампалем-533437, Індія*

[4]*Кафедра математики, Технологічний інститут GMR (GMRIT) – вважається університетом, Раджам-532127, Індія*

У цій статті ми досліджуємо анізотропну космологічну модель типу *II* Біанкі в рамках голографічної темної енергії Барроу, розглядаючи як горизонт Хаббла, так і шкалу Гранда–Оліверoса як інфрачервоні обрізання. Щоб отримати точні розв'язки рівнянь поля Ейнштейна, ми припускаємо відповідне співвідношення між метричними потенціалами. Використовуючи дані космічного хронометра Хаббла, ми обмежуємо параметри моделі та отримуємо значення найкращого наближення $b_4 = -0,091^{+0,013}_{-0,012}$ та $H_0 = 72,3 \pm 2,7$ км с$^{-1}$Мпк$^{-1}$. $H(z)$ апроксимація демонструє чудову відповідність з даними спостережень та перекриття з ΛCDM при низьких червоних зміщеннях, з незначними відхиленнями при вищих z. Фізичну поведінку моделі досліджують за допомогою детального аналізу космологічних параметрів. Параметр уповільнення $q(z)$ демонструє плавний перехід від ранньої фази уповільнення до сучасної епохи прискорення. Параметр рівняння стану ω_{de} демонструє квінтомоподібну динаміку, розвиваючись через межу космологічної константи та входячи у фантомний режим, що узгоджується з прискоренням наприкінці часу. Стабільність перевіряється за допомогою квадрата швидкості звуку v_s^2, який залишається додатним у нещодавньому Всесвіті, що забезпечує класичну стабільність. Фазова площина $\omega_{de} - \omega'_{de}$ вказує на те, що обидві моделі лежать в області замерзання, що відповідає швидшому прискоренню. Діагностика стану (r, s) та (r, q) додатково підтверджує перехід від стандартної фази, де домінує холодна темна матерія, до атрактора, подібного до де Ситтера, з траєкторіями, що показують чіткі відхилення від ΛCDM.

Ключові слова: *модель Біанкі типу II; голографічна темна енергія Барроу; темна енергія; космологія; модифікована теорія гравітації*

East European Journal of Physics. 1. 76-87 (2026)
DOI:10.26565/2312-4334-2026-1-06 ISSN 2312-4334

CONCEPTUAL VIOLATION OF ENERGY CONDITIONS IN BOUNCING COSMOLOGY

A.Y. Shaikh[1#], S.M. Shingne[2]*, A.P. Jenekar[3†]
[1]*Department of Mathematics, Indira Gandhi Kala Mahavidyalaya, Ralegaon-445402. (M.S.) India.*
[2]*Department of Mathematics, G. S. Science, Arts and Commerce College, Khamgaon-444312. (M.S.) India.*
[3]*Department of Mathematics, Arts, Commerce and Science College, Maregaon-445303. (M.S.) India.*
**Corresponding Author Email: smshingne131@gmail.com; [#]Email: shaikh_2324ay@yahoo.com; [†]Email: apjenekar@gmail.com*
Received November 5, 2025; revised January 23, 2026. accepted January 27, 2026

This paper focuses on examining the bouncing model within a flat Friedmann–Robertson–Walker (FRW) Universe. The equation of state (EoS) parameter pertaining to the considered model under consideration specifies the Universe's peculiar functioning. The kinematics along with the physical attributes of the model's dynamic parameters are investigated comprehensively. We explored several energy conditions (ECs) in this scenario. The diagnostic pair $\{r,s\}$ of statefinder and the jerk parameter $j(t)$ are investigated to identify significantly different cosmic phases. We used the squared sound speed parameter C_s^2, designed to meet the needs of our model's stability analysis. Our analysis revealed that outcomes of our study are in accordance with patterns observed in the bouncing scenarios, offering a method to explain the cosmic acceleration as well as the singularity problem in our Universe.
Keywords: *Bouncing scenario; FRW metric;* $f(R,T)$ gravity; *Cosmic acceleration*
PACS: 98.80.-k, 04.20.-q, 04.50.Kd, 98.80.Cq

1. INTRODUCTION

In pursuance of an intuitive essence of the Universe and astrophysical mechanisms, General Relativity (GR), pioneered by Einstein, is widely considered the most significant theory offering explanations for many mysterious factors of gravitational dynamics. According to observational cosmic evidence, our Universe came across an early inflation accompanied by late-time expansion, which is presently occurring more rapidly [1–4]. It is believed that the force propelling the expanding cosmos appears to be dark energy (DE), characterized by its negative pressure, thereby allocating 68.3% of the peculiar ingredient of the Universe, with an additional 25% being dark matter (DM) [5–10]. Modified gravity (MG) represents a method that alters the action principle GR and serves as an alternative approach to remedying DE, whereas the other method introduces a number of dynamical DE candidates, such as the cosmological constant [11], Chaplygin gas (CG) [12], X-matter [13,14], and quintessence [15,16] for better comprehension of the nature of DE. In GR, the accelerating cosmos is typically ascribed to a cosmological constant, leading to the standard ΛCDM model. Notwithstanding its observable success, ΛCDM encounters fine-tuning and cosmic coincidence issues [17,18]. Numerous researchers have investigated MG in diverse cosmological frameworks; for a comprehensive survey, see ref. [19,20]. Several kinds of MG theories, starting with $f(R)$ gravity, $f(T)$ gravity, $f(G)$ gravity, and $f(Q)$ gravity, are being put forward in this setting. Out of the many MG theories, $f(R)$ gravity is believed to be the best fit for cosmologically useful models, though it faces considerable problems [19,20]. The $f(R,T)$ gravity was presented as an extension, wherein the gravitational Lagrangian is contingent upon the Ricci scalar (R) along with the trace (T) of the matter energy–momentum tensor. In recent decades, much research has been undertaken in a promising category of $f(R,T)$ gravity, with numerous functional expressions being extensively investigated to explain late-time acceleration [21–27]. Even while certain models raise questions about their cosmic viability [28,29], $f(R,T)$ gravity is still a major way to bring together matter and geometry in cosmological dynamics.

The important issue of initial singularity was encountered by GR, among other issues, during the early Universe. In an attempt to tackle the concern of initial singularity, bouncing cosmological models are currently being studied, which prescribe that the cosmos initially contracted leading up to expanding, shorn of coming across a singularity [30]. For a smooth bouncing approach, Steinhardt and Ijjas [31] put together a wedge diagram to gain insight into the detrimental impacts of certain cosmological challenges. Nonetheless, the non-singular bounce might not be able to meet the null energy condition (NEC) within the system associated with a flat Universe. Moreover, the widely accepted Galileon theories [32] addressed non-singular cosmology, which fails to uphold the NEC. In recent years, bouncing cosmology has become more prevalent because it presents a distinct speculative framework compared to other common cosmic theories. For the systematic review regarding conventional bouncing cosmologies, see ref. [33]. Brandenberger and Peter [34] have looked into the current circumstances of bouncing cosmologies as possible alternatives to cosmic inflation to offer an explanation of the very early cosmos. Relevant bounce arrangements founded on the concept of GR are examined in [35-40], while the appropriate bouncing scenarios integrated within MG are analyzed in [41–50]; interestingly, in $f(R,T)$

Cite as: A.Y. Shaikh, S.M. Shingne, A.P. Jenekar, East Eur. J. Phys. 1, 76 (2026), https://doi.org/10.26565/2312-4334-2026-1-06

gravity [51–56], featuring the role of the big bang singularity. The main motivations for this study on the bouncing model within in the light of the GR and $f(R,T)$ gravity are to examine the cosmic speed singularity over a prolonged phase along with exploration of the bouncing conduction appearing in its earliest stages. The structure of the paper follows this approach. Sec. 2 contains the cosmological framework of the FRW world and its associated field equations, whereas its solution via the bouncing scenario is established in sec. 3. The dynamic parameters of our model with the inclusion of DE are analyzed in sec. 4. Sec. 5 covers the exploration of various energy conditions (ECs) of the model. The statefinder diagnostics and jerk parameter, along with the stability of our model, are investigated in secs. 6 and 7, respectively, and at last, the conclusions together with discussion are covered in sec. 8.

2. THE FRW UNIVERSE AND FIELD EQUATIONS

The majority of cosmological models within the confines of contemporary cosmology are predicated on the most underlying aspects of the cosmological principle, claiming that the cosmos is homogeneous as well as isotropic over the cosmological extent. It is widely accepted that the observable cosmos is nearly isotropic and homogeneous. Consequently, cosmologists have focused a considerable amount of emphasis on a flat FRW model, which is articulated as

$$ds^2 = dt^2 - a^2(t)(dx^2 + dy^2 + dz^2), \tag{1}$$

with $a(t)$ representing the scaling factor, a function that depends only on t. The Ricci scalar R for the metric (1) arrives to be $R = -6\left(\dot{H} + 2H^2\right)$, with $H = \dot{a}/a$ means the Hubble parameter, while ' · ' reflects the conventional time derivative.

2.1. FIELD EQUATIONS IN GR

The Einstein's field equations in GR are expressed as

$$R_{ij} - \frac{1}{2} g_{ij} R = -T_{ij} \tag{2}$$

where T_{ij} stands for the standard matter energy momentum tensor, which is defined as $T_{ij} = (\rho + p)u_i u_j - g_{ij} p$ with ρ representing energy density, and p is the pressure.
The metric (1) yields the field equations in the form:

$$2\dot{H} + 3H^2 = -p\,, \tag{3}$$

and

$$3H^2 = \rho\,. \tag{4}$$

2.2. FIELD EQUATIONS IN $f(R,T)$ GRAVITY

The action of $f(R,T)$ gravity has the form [57],

$$S = \int \left[\frac{f(R,T)}{16\pi} + L_m \right] \sqrt{-g}\, d^4x\,, \tag{5}$$

with L_m accounting the matter Lagrangian and the stress- energy tensor of matter is specified as

$$T_{ij} = -\frac{2}{\sqrt{-g}} \frac{\delta(\sqrt{-g}\, L_m)}{\delta g^{ij}}\,. \tag{6}$$

Following the work of Agrawal et al.[55] in $f(R,T)$ gravity for the bouncing scenario,

We looked into the non-minimal dependence on matter and geometry as, $f(R,T) = f_1(R) + f_2(T)$. The field equations of $f(R,T)$ gravity concerning non-minimal matter interaction can be acquired by tailoring the action pertaining the metric tensor g_{ij} as,

$$f_R(R) R_{ij} - \frac{1}{2} f(R) g_{ij} - (\nabla_i \nabla_j - g_{ij}) f_R(R) = 8\pi T_{ij} + f_T(T) T_{ij} + [f_T(T) p + \frac{1}{2} f(T)] g_{ij}, \tag{7}$$

In Eq. (7), we denote $f_R(R) = \partial f_1(R)/\partial R$ and $f_T(T) = \partial f_2(T)/\partial T$, while p reflects the pressure of the matter.

Based on the three options of $f(R,T)$ provided by Harko et. al. [57], we have selected $f(R,T)=R+2f(T)$. A substantial assortment of cosmological scenarios is described in the field, with $f_1(R)=R$ and $f_2(T)=\beta T$, β as coupling constant. We intend to embrace the timeless cosmological constant Λ_0 here in a way that $f(R,T)=R+2\beta T+2\Lambda_0$. Consequently, the field equations (7) become

$$G_{ij}=(8\pi+2\beta)T_{ij}+\Lambda(T)\ g_{ij}\ , \tag{8}$$

with $\Lambda(T)=(2p+T)\beta+\Lambda_0$ specifying effective cosmological constant.

The discovery of supernovae has significantly enhanced the relevance of the cosmological constant Λ, previously considered negligible, in the examination of accelerating cosmological models. As the Universe evolves, this changes too. The current extended gravity hypothesis that it happens over cosmic time. It turns out that Λ becomes a pure constant Λ_0 for a vanishing β. Moreover, the field equations (8) are simplified to

$$G_{ij}=(8\pi+2\beta)T_{ij}+[(2\rho+T)\beta+\Lambda_0]\ g_{ij}\ . \tag{9}$$

And then the field equations of $f(R,T)$ gravity arrive at

$$2\dot{H}+3H^2=-\eta\ p+\beta\rho+\Lambda_0\ , \tag{10}$$

and

$$3H^2=\eta\rho-\beta\ p+\Lambda_0\ , \tag{11}$$

with $\eta=8\pi+3\beta$. The above field equations reduce to GR case for a vanishing β. Performing some algebraic manipulations among eqns. (10) and (11), we can derive the pressure p, energy density ρ and equation of state (EoS) parameter in terms of Hubble parameter as,

By executing algebraic modifications on Eqs. (10) and (11) as it relates to the Hubble parameter, we can formulate pressure p, energy density ρ, and EoS parameter ω as

$$p=-\frac{1}{(\eta^2-\beta^2)}[2\eta\dot{H}+3(\eta-\beta)H^2-(\eta-\beta)\Lambda_0] \tag{12}$$

$$\rho=\frac{1}{(\eta^2-\beta^2)}[-2\beta\dot{H}+3(\eta-\beta)H^2-(\eta-\beta)\Lambda_0] \tag{13}$$

and

$$\omega=-1+\left[\frac{2(\eta+\beta)\dot{H}}{2\beta\dot{H}-3(\eta-\beta)H^2+(\eta-\beta)\Lambda_0}\right] \tag{14}$$

Given the present circumstances, including yet another constraint equation is absolutely necessary in fully resolving the set of field equations (3)-(4) and (12)-(14) that are formulated with the Hubble term. We want to examine the model's bouncing behavior using an established bouncing scale factor, thus explaining why we're presenting its settings in Hubble terms. It is necessary to prefigure a particular form for the Hubble parameter to acquire the expressions for the dynamical components. Given that bouncing cosmology, an adversary substitute for the inflationary paradigm [58], is being vigorously researched to solve the singularity problem, we are brought about to look into the model within the matter bounce context. Consequently, our next step involves establishing an appropriate bouncing model to explore a particular cosmological solution to the system of field equations.

3. BOUNCING COSMOLOGICAL SOLUTIONS

This section intends to examine a cosmological solution that ultimately results in a bouncing scenario. The cosmos undergoes a non-singular bounce during its initial matter-dominated segregation phase in the bouncing state, as explained in [34,52,54,59–63]. An investigation conducted in [64] suggests that the Universe, which expands following a minimal collapse, represents the bouncing Universe. In bouncing cosmology, the scale factor declines $(\dot{a}<0)$ in the negative time region, indicating the contracting era, and then again it elevates $(\dot{a}>0)$ in the positive time region, representing the expanding era, whereas it vanishes $(\dot{a}=0)$ close to the point $t=0$ where the bounce occurs. The Hubble parameter's positive value $(H>0)$ signifies the expanding period of the cosmos and it is negative $(H<0)$ during the contracting period of the cosmos, as investigated in [65]. At the site of the bounce, the scale factor must attain a minimal, non-zero value, whereas the Hubble parameter must vanish for the effective functioning of the bouncing model without

encountering singularity [66]. Additional requirements at the bouncing point consist of violating NEC and transitioning the EoS parameter across the phantom split line $(\omega = -1)$ as discussed in [67]. In order to satisfy these conditions and to have a congruous bounce over the scale factor, we consider $a(t) = \sqrt{1+\gamma^2 t^2}$ with $\gamma > 0$ representing a constant parameter that regulates the cosmic expansion, adhering to the scale factor specified in [56]. Consequently, the Hubble parameter $H(t)$ becomes

$$H = \frac{\dot{a}}{a} = \frac{\gamma^2 t}{1+\gamma^2 t^2} \tag{15}$$

The deviations of the scale factor $a(t)$ and how the Hubble parameter $H(t)$ has evolved across cosmic time (t) are illustrated in Figs. 1 and 2, respectively, which specify the orientation of its curvature for three assigned values of the parameter $\gamma = 0.7, 0.8, 0.9$. As demonstrated in Fig. 1, the scale factor $a(t)$ experiences symmetrical progression from the contracting era of the cosmos towards the expanding Universe and stays finite with a non-zero value, $a(0) = 1$ at the bouncing spot $t = 0$, enabling the Hubble parameter $H(t)$ to potentially be zero during this epoch as shown in Fig. 2, thereby satisfying the bouncing conditions [67]. To visualize a bounce, one can envision the cosmos contracting and then expanding, with this behavior being evident at and near the bounce point. Eventually, the Hubble parameter evolves rectilinearly from the contracting to the expanding era with the assistance of a bounce by passing through zero as depicted in Fig. 2, thereby constituting the bouncing model.

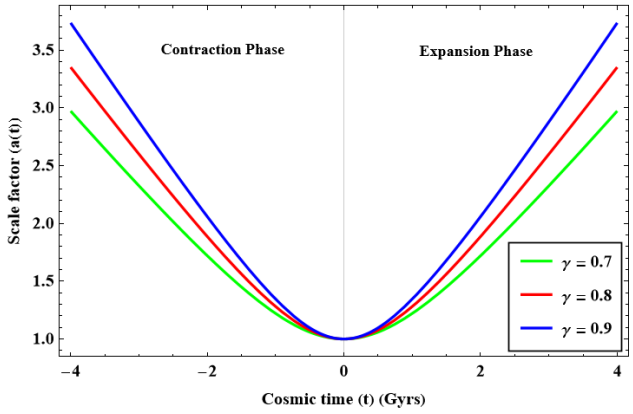

Figure 1. Inspection of the scale factor $a(t)$ versus cosmic time (t).

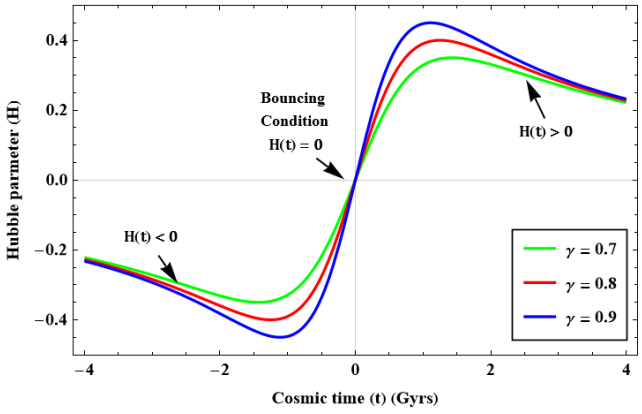

Figure 2. Displays the approach of the Hubble parameter $H(t)$ against cosmic time (t).

The deceleration parameter (q) elucidates the evolution of the Universe's expansion and is found to be

$$q = -1 - \frac{\dot{H}}{H^2} = -\frac{1}{\gamma^2 t^2}. \tag{16}$$

In scenarios in which the Universe experiences deceleration throughout its existence, the deceleration parameter remains positive $(q > 0)$; whereas, it becomes negative $(q < 0)$ as the cosmos expands rapidly. Fig. 3 outlines the way the deceleration parameter behaves symmetrically over the bouncing point. It's noteworthy that the deceleration parameter encounters a negative trend $(q < -1)$ with regard to both contracting and expanding Universe, indicating super

exponential expansion, and showcases a large negative value in close proximity to the bouncing point. Consequently, the estimated deceleration parameter's value lined up with topical cosmological inspection associated with Type Ia Supernovae [68–70], emphasizing that our cosmos continues to expand at an accelerating pace throughout its evolution. Based on the classification of cosmos explored in [65], our model exhibits a contracting and accelerating phase $(H<0, q<0)$ followed by an expanding and accelerating stage $(H>0, q<0)$, as illustrated in Figs. 2 and 3.

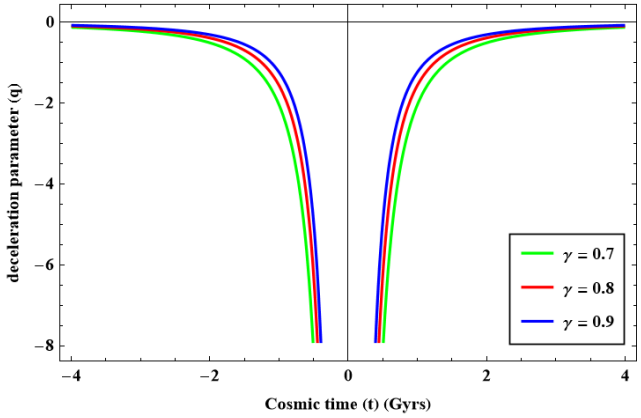

Figure 3. Displays the approach of the deceleration parameter (q) against cosmic time (t).

4. ANALYSIS OF MODEL'S DYNAMICAL PARAMETERS

The appropriate functioning of the dynamical parameters is essential for the sustainability of any cosmological model, and its results ought to align with an equitable agreement. Disparities point to systemic errors arising from varying analytical methods or cosmological observations. The expression's free parameters and the selected representative values for the model might also be linked with its origin. Recent findings of cosmic acceleration reveal that the EoS parameter and pressure must be negative, preferably in both the immediate and distant future. Moreover, a non-singular bounce requires both a positive energy density and negative pressure. Due to this, we now examine the model's dynamic features concerning the patterns of behavior exhibited during bouncing in the light of the scale factor that is taken into account in the present investigation. From field equations (3)-(4), the energy density and pressure for GR are expressed as

$$\rho=\frac{3\gamma^4t^2}{\left(1+\gamma^2t^2\right)^2} \tag{17}$$

and

$$p=-\frac{\left(2+t^2\gamma^2\right)\gamma^2}{\left(1+t^2\gamma^2\right)^2}. \tag{18}$$

Using barotropic EoS, $p=\omega\rho$, the EoS parameter (ω) can be obtained as

$$\omega=-\frac{1}{3}-\frac{2}{3\gamma^2t^2}. \tag{19}$$

From the field equations (12)-(14), the pressure, the energy density and the EoS parameter for $f(R,T)$ gravity are expressed as

$$p=\frac{1}{\left(\beta^2-\eta^2\right)\left(1+t^2\gamma^2\right)^2}[2\eta\gamma^2+(\eta-3\beta)\gamma^4t^2+\left(1+\gamma^2t^2\right)^2(\beta-\eta)\Lambda_0], \tag{20}$$

$$\rho=\frac{1}{(\beta^2-\eta^2)\left(1+\gamma^2t^2\right)^2}[\beta\gamma^2\left(2+\gamma^2t^2\right)-3\eta\gamma^4t^2-\left(1+\gamma^2t^2\right)^2(\beta-\eta)\Lambda_0], \tag{21}$$

and

$$\omega=-1+\frac{2\gamma^2(\beta+\eta)\left(\gamma^2t^2-1\right)}{3\eta\gamma^4t^2-\left(2+\gamma^2t^2\right)\beta\gamma^2+\left(1+\gamma^2t^2\right)^2(\beta-\eta)\Lambda_0}. \tag{22}$$

For graphical illustration, we have used the considered values of the parameter $\gamma=0.7,0.8,0.9$ with $\beta=-5.8$ and $\Lambda_0=0.001$[55]. The progression of energy density across cosmic time for both cases of GR and $f(R,T)$ gravity is depicted in Fig. 4 for three assigned values of parameters γ.The graphical representations in Fig. 4 illustrate the energy density over cosmic time related to the bouncing model. It shows a downward trajectory (indicating contraction) before

the bounce and a subsequent rising tendency (indicating expansion) after the bounce, with a minimum occurring at the bounce point. Throughout cosmic time, both the contracting and expanding models maintain positive energy density, although there is a negative trend that culminates at the bounce site. The behavior of pressure (p) up against cosmic time is illustrated in Fig. 5, which validates an assertion that the pressure continues to be negative in both the temporal realms of the contracting as well as the expanding Universe, thereby providing additional backing for the Universe's cosmic acceleration.

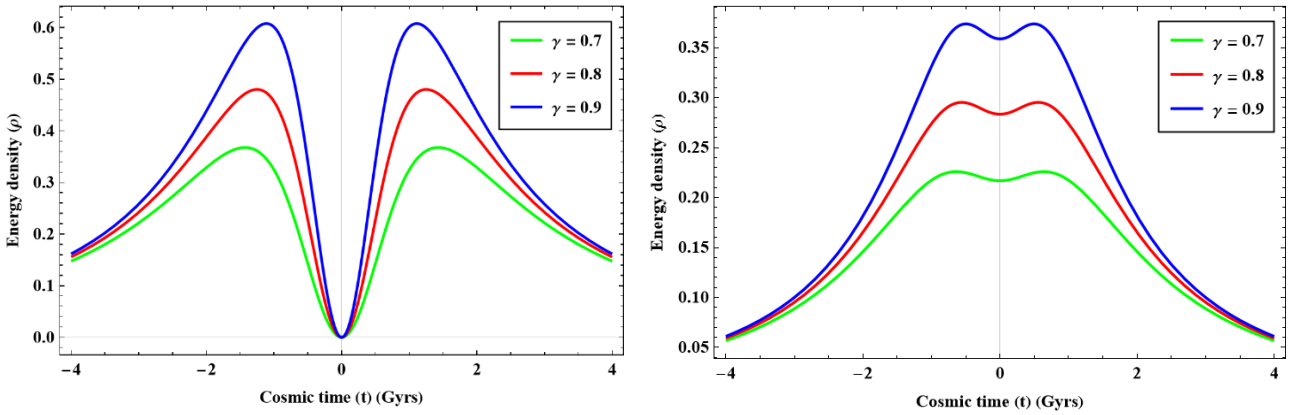

(a) For GR (b) For $f(R,T)$ gravity

Figure 4. Displays the energy density (ρ) for three assigned values of γ.

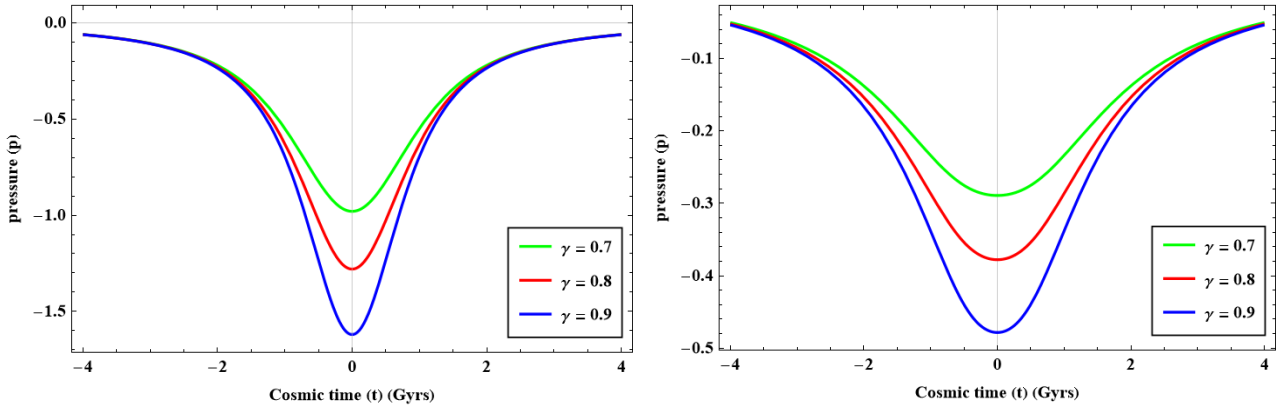

(a) For GR (b) For $f(R,T)$ gravity

Figure 5. Displays the pressure (p) for three assigned values of γ.

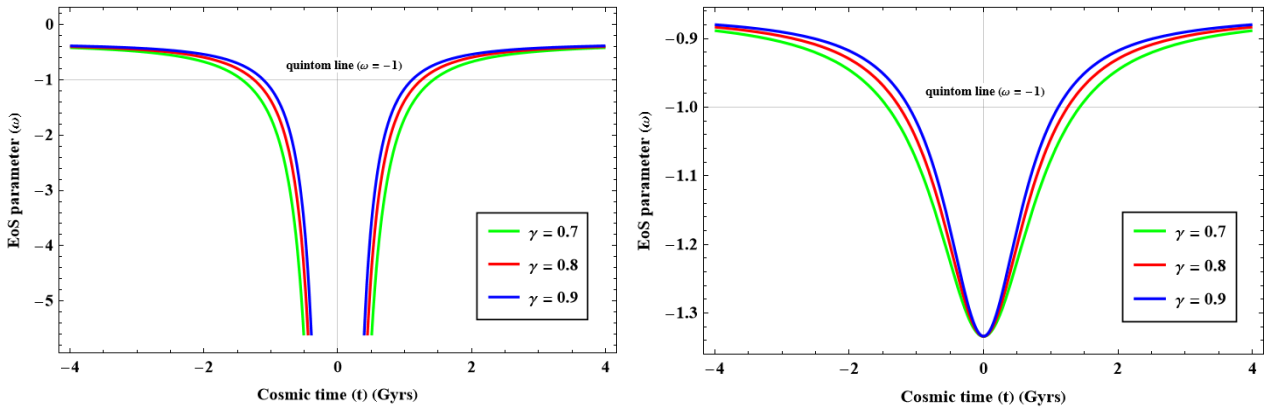

(a) For GR (b) For $f(R,T)$ gravity

Figure 6. The advancement of the EoS parameter (ω) for three assigned values of γ.

Fig. 6 demonstrates the aspects of the EoS parameter's advancement associated with the bouncing model for both the cases of GR and $f(R,T)$ gravity. The EoS parameter downscales all via the phantom divide line $(\omega=-1)$ to the underlying negative value in each respective temporal realm of the contracting and expanding Universe, thereby entering

the phantom region $(\omega < -1)$, and it showcases a symmetric trend over the two faces of the bouncing epoch. This indicates that the cosmos is presently undergoing a phantom DE phase in symmetric bouncing cosmology. Moreover, the intriguing traversal of the EoS parameter along the quintom line close to the bouncing spot, as illustrated in Fig. 6, for three conceivable values of these model parameters γ, provides additional supporting evidence for the efficiency and credibility of the suggested bouncing model [71,72].

5. ENERGY CONDITIONS

A system of linear equations incorporating density along with pressure referred to as energy conditions (ECs), which points out that gravity remains constantly repulsive; additionally, the energy density is unlikely to be negative. Building feasible bouncing models and investigating the kind of dark energy that sustains them depend on insights from ECs. Each of these ECs which are assimilated into GR and $f(R,T)$ gravity as follows:

(1) Null Energy condition (NEC) $\Leftrightarrow$ $\rho + p \geq 0$

(2) Strong Energy Condition (SEC) $\Leftrightarrow$ $\rho + 3p \geq 0$

(3) Dominant Energy Condition (DEC) $\Leftrightarrow$ $\rho_{de} \geq |p_{de}|$

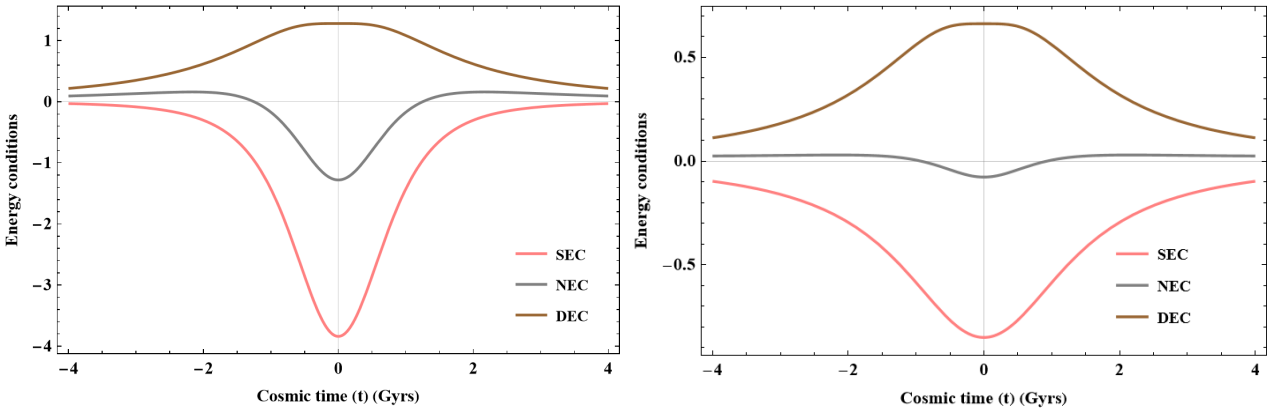

(a) For GR (b) For $f(R,T)$ gravity

Figure 7. Approach of ECs varying over the cosmic time.

For the present bouncing scenario, the graphical representations of NEC, DEC, and SEC of our model varying with the passage of cosmic time for both the cases of GR and $f(R,T)$ gravity are demonstrated in Fig. 7. An essential aspect of the bouncing situation is non-compliance with the ECs. It is abundantly clear from an investigation conducted in [59] that one must account for the violation of NEC and SEC while attempting to accomplish non-singular bouncing solutions within GR. Astrophysical observations [69, 70] must go against the SEC while complying with the persisting statistics of the speeding cosmos. It is noteworthy that an outbreak of dark energy is initiated by an invalidation of the SEC, which thereby validates the Universe's fast expansion. Furthermore, the spatially flat setting that we focused on herein demands NEC violation at the bouncing point for a successful bounce to occur [67]. As per the illustration in Fig. 7, we noticed the overall validation of DEC, whereas SEC is violated for intermediate values of γ. Consequently, our model meets the necessary criteria of NEC violation with constant negative value to enable a successful bouncing mechanism, while averting singularities, and the violation of SEC culminates in the Universe's accelerating expansion, which is in concurrence with the current scenario of the cosmos.

6. STATEFINDER DIAGNOSTIC

The statefinder diagnostic assists in the investigation of bouncing model, as their time-dependent behavior close to the bounce indicates departures from conventional expansion and aids in finding the consequences of the DE model. These are therefore critically essential for grasping the dynamics of a non-singular, bounce-driven Universe. Sahni et al. [73] accompanied by Alam et al. [74] established the statefinder diagnostic pair $\{r,s\}$ by exploiting the derivatives of the scaling factor with r as the jerk parameter whereas s represents the physical entities of DE, which are described by $r \equiv \frac{\dddot{a}}{aH^3}$ and $s \equiv \frac{r-1}{3(q-1/2)}$. For $(r,s) = (1,1)$, the model reflects the cold dark matter (CDM) limit, while $(r,s) = (1,0)$ belongs to the ΛCDM limit. When $r < 1$, it contributes to the quintessence DE era, the phantom DE region for $s > 0$

while the trajectory for the Chaplygin Gas (CG) model arrives for $r>1$ with $s<0$. These two statefinder settings turn out to be $r=-\frac{3}{\gamma^2 t^2}$ with $s=\frac{2}{3}\left(1+\frac{1}{2+\gamma^2 t^2}\right)$ and their relation is expressed as

$$r=\frac{3s-2}{2(s-1)} \tag{23}$$

The deviation of r against s is depicted in Fig. 8 which signifies that our model approaches the ΛCDM model as it crosses the point $(r,s)=(1,0)$, while serving variations thereafter by covering the DE regions, including CG, quintessence, and phantom over the course of the Universe's development, which further supports the model's consistency with our earlier studies [75–77].

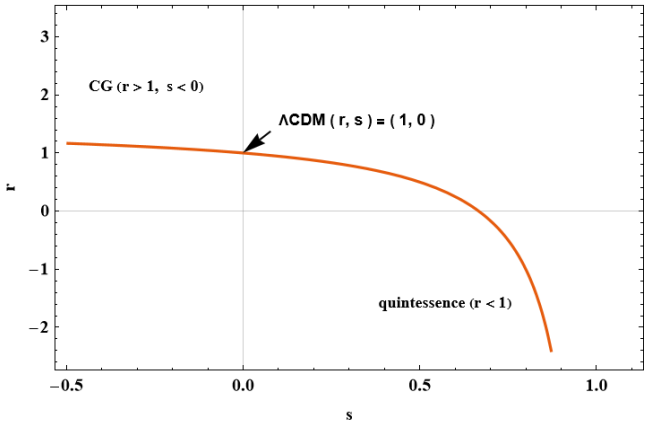

Figure 8. The deviations of r against s.

7. STABILITY OF THE UNIVERSE

Figuring out the stability of an observatory model is crucial for examining distorting behavior while forecasting the progression of the cosmos. The worthwhile indicator for assessing a dark energy model's stability in opposition to perturbations is the square of sound speed v_s^2 as studied in [49] which is prescribed by $v_s^2=dp/d\rho$. The model's stability is specified by the sign of v_s^2. If v_s^2 is positive, the model is rendered stable; otherwise, it grows into unstable. The expressions for v_s^2 for our GR and $f(R,T)$ gravity framework are obtained, respectively, as

$$v_s^2=\frac{3+\gamma^2 t^2}{3(1-\gamma^2 t^2)} \text{ and } v_s^2=\frac{3\beta(1-\gamma^2 t^2)+\eta(3+\gamma^2 t)}{\beta(3+\gamma^2 t^2)+3\eta(1-\gamma^2 t^2)}. \tag{24}$$

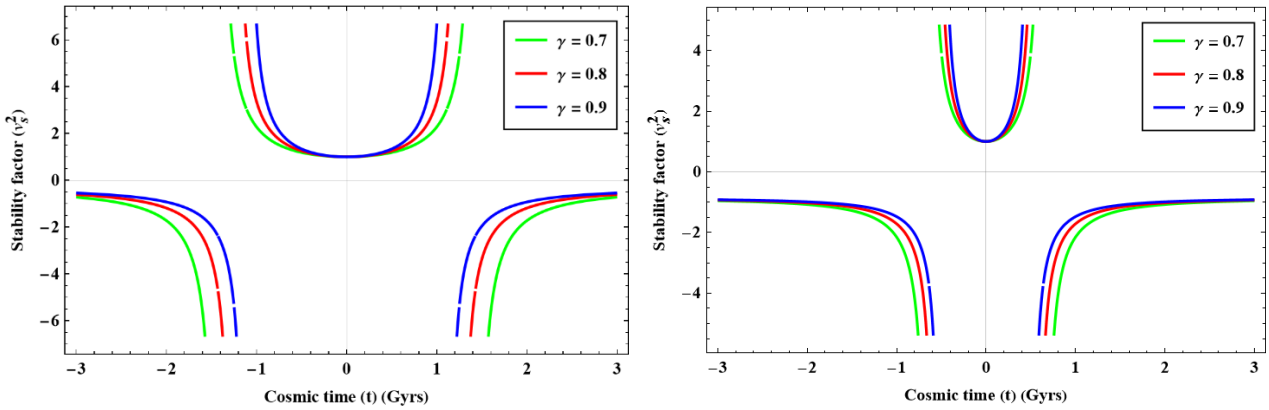

(a) For GR

(b) For $f(R,T)$ gravity

Figure 9. Approach of stability factor v_s^2 varying over the cosmic time.

For three specified values of γ, Fig. 9 displays the variations of the stability factor C_s^2 over the cosmic time. At the bouncing site and its neighbourhood, the stability factor $C_s^2>0$ which foresees stable behaviour for the bouncing period,

while the stability factor $C_s^2 < 0$ thereafter indicates instability over a prolonged time frame. Our model showcases bouncing conduct near $t = 0$, we draw the inference that our model is stable in the close proximity of the bouncing point.

8. CONCLUSIONS

In this study on the bouncing model within the light of the GR and $f(R,T)$ gravity, we examined the cosmic speed singularity over a prolonged phase along with the exploration of the bouncing conduction. The incorporation of our model aims to elucidate the dynamics of the early Universe, particularly through the bounce, as well as the current era of accelerated expansion. Our approach was to prevent singularities and facilitate a smooth progression from contraction to expansion. We consider three conceivable values of model parameters as $\gamma = 0.7, 0.8, 0.9$ for obtaining the graphical presentations of various dynamic parameters of our model in accordance with the patterns of behavior observed during bouncing. The illustrations in the Figs. 1 and 2 display that the scale factor and Hubble parameter are respectively certain to be constrained by an essential condition of minimum non-zero scale factor $a(t)$ and Hubble parameter H being zero at the bouncing point owing to its symmetrical trajectory that transitions from contraction to expansion through a process of bounce whereas Fig. 3 shows that the deceleration parameter propels from $q = -1$ to significant negative value while approaching to the point where the bounce occurs. The following presents a snapshot of the findings we observed for both the cases of the GR and $f(R,T)$ gravity:

- Our bouncing model has effectively shown an identifiable phase change from contraction to expansion, as evidenced by the graphical representations of both the energy density (ρ) over cosmic time for all assigned values of model parameters γ (see Fig. 4). The model's effectiveness in illustrating this pivotal shift is highlighted by the consistent downward trajectory leading up to the bounce, followed by a rising trend post-bounce. Additionally, the behavior of pressure (p) throughout the cosmic timeline as reflected in the Fig. 5 reinforces the model's viability, as it remains negative during both the Universe's temporal regions which makes up an additional foundation for the Universe's rapid expansion. This combination of positive energy density along with negative pressure is crucial for achieving a non-singular bounce, further underscoring the attainment of our model.
- The intriguing traversal of the EoS parameter along the quintom line $(\omega = -1)$, close to the bouncing spot, thereby entering the phantom region $(\omega < -1)$ and a symmetric trend over the two faces of the bouncing epoch, as illustrated in Fig. 6 for all assigned values of model parameters γ, provides additional supporting evidence for the efficiency and credibility of the suggested bouncing model [71,72].
- Our study points out how important the violations of energy condition are in establishing a non-singular bouncing model that takes cosmic acceleration into account, especially the NEC near the bouncing spot and SEC thoroughly as displayed in Fig. 7. The SEC breach offers reliable evidence of the rapid expansion of the cosmos. Our model accomplishes the required criteria of the NEC violation near the bouncing spot, thereby enabling an efficient bounce mechanism that refrains from singularities.
- The statefinder diagnostic suggests that our model covers the DE components such as quintessence, phantom, and Chaplygin gas, thereby approaching subsequently to the ΛCDM model during cosmic progression as demonstrated in Fig. 8. At the bouncing spot, the stability factor C_s^2 supports the model's requirements for a bounce, as shown in Fig. 9.

ORCID

A.Y. Shaikh, https://orcid.org/0000-0001-5315-559X; **A.P. Jenekar**, https://orcid.org/0009-0005-8928-3725

REFERENCES

[1] A.G. Riess, et al., "Observational Evidence from Supernovae for an Accelerating Universe and a Cosmological Constant," Astron. J. **116**, 1009–1038 (1998). https://doi.org/10.1086/300499
[2] S. Perlmutter, *et al*., "Measurements of Ω and Λ from 42 High-Redshift Supernovae," Astrophys. J. **517**, 565–586 (1999). https://doi.org/10.1086/307221
[3] M. Tegmark, *et al*., "Cosmological parameters from SDSS and WMAP," Phys. Rev. D, **69**, 103501 (2004). https://doi.org/10.1103/PhysRevD.69.103501
[4] E. Komatsu, *et al*., "Seven-Year Wilkinson Microwave Anisotropy Probe (WMAP) Observations: Cosmological Interpretation," Astrophys. J. Suppl. Ser. **192**, 18 (2011). https://doi.org/10.1088/0067-0049/192/2/18
[5] S. Nojiri, and S.D. Odintsov, "The new form of the equation of state for dark energy fluid and accelerating universe," Phys. Lett. B, **639**, 144–150 (2006). https://doi.org/10.1016/j.physletb.2006.06.065
[6] S. Nojiri, and S.D. Odintsov, "Introduction to modified gravity and gravitational alternative for dark energy," Int. J. Geom. Methods Mod. Phys. **04**, 115–145 (2007). https://doi.org/10.1142/S0219887807001928
[7] A. Silvestri, and M. Trodden, "Approaches to understanding cosmic acceleration," Rep. Prog. Phys. **72**, 096901 (2009). https://doi.org/10.1088/0034-4885/72/9/096901

[8] R.R. Caldwell, and M. Kamionkowski, "The Physics of Cosmic Acceleration," Annu. Rev. Nucl. Part. Sci. **59**, 397–429 (2009). https://doi.org/10.1146/annurev-nucl-010709-151330
[9] P. Astier, and R. Pain, "Observational evidence of the accelerated expansion of the universe," Comptes Rendus Phys. **13**, 521-538 (2012). https://doi.org/10.1016/j.crhy.2012.04.009
[10] K. Bamba, *et al*., "Dark energy cosmology: the equivalent description via different theoretical models and cosmography tests," Astrophys. Space Sci. **342**, 155–228 (2012). https://doi.org/10.1007/s10509-012-1181-8
[11] S.M. Carroll, W.H. Press, and E.L. Turner, "The Cosmological Constant," Annu. Rev. Astron. Astrophys. **30**, 499–542 (1992). https://doi.org/10.1146/annurev.aa.30.090192.002435
[12] V. Gorini, A. Kamenshchik, U. Moschella, and V. Pasquier, "The Chaplygin gas as a model for dark energy," arXiv:gr-qc/0403062 (2004). https://doi.org/10.48550/ARXIV.GR-QC/0403062
[13] M.S. Turner, and M. White, "CDM models with a smooth component," Phys. Rev. D, **56**, R4439–R4443 (1997). https://doi.org/10.1103/PhysRevD.56.R4439
[14] Z.-H. Zhu, M.-K. Fujimoto, and D. Tatsumi, "Determining the cosmic equation of state using future gravitational wave detectors," Astron. Astrophys. **372**, 377–380 (2001). https://doi.org/10.1051/0004-6361:20010458
[15] B. Ratra, and P.J.E. Peebles, "Cosmological consequences of a rolling homogeneous scalar field," Phys. Rev. D, **37**, 3406–3427 (1988). https://doi.org/10.1103/PhysRevD.37.3406
[16] V. Sahni, and L. Wang, "New cosmological model of quintessence and dark matter," Phys. Rev. D, **62**, 103517 (2000). https://doi.org/10.1103/PhysRevD.62.103517
[17] S. Weinberg, "The cosmological constant problem," Rev. Mod. Phys. **61**, 1–23 (1989). https://doi.org/10.1103/RevModPhys.61.1
[18] P.J.E. Peebles, and B. Ratra, "The cosmological constant and dark energy," Rev. Mod. Phys. **75**, 559–606 (2003). https://doi.org/10.1103/RevModPhys.75.559
[19] A. De Felice, and S. Tsujikawa, "f(R) Theories," Living Rev. Relativ. **13**, 3 (2010). https://doi.org/10.12942/lrr-2010-3
[20] V. Faraoni, "f(R) gravity: successes and challenges," (2008). https://doi.org/10.48550/ARXIV.0810.2602
[21] K.R. Mule, S.P. Gaikwad, and V.G. Mete, "Bianchi type-III holographic dark energy cosmological model in f (R , T) theory of gravitation," New Astron. **105**, 102087 (2024). https://doi.org/10.1016/j.newast.2023.102087
[22] P.K. Sahoo, B. Mishra, and S.K. Tripathy, "Kaluza–Klein cosmological model in f(R, T) gravity with Λ(T)," Indian J. Phys. **90**, 485–493 (2016). https://doi.org/10.1007/s12648-015-0759-8
[23] M.J.S. Houndjo, "Reconstruction of f(R, T) Gravity Describing Matter Dominated and Accelerated Phases," Int. J. Mod. Phys. D, **21**, 1250003 (2012). https://doi.org/10.1142/S0218271812500034
[24] R. Zaregonbadi, M. Farhoudi, and N. Riazi, "Dark matter from f (R, T) gravity," Phys. Rev. D, **94**, 084052 (2016). https://doi.org/10.1103/PhysRevD.94.084052
[25] S.B. Fisher, and E.D. Carlson, "Reexamining f (R, T) gravity," Phys. Rev. D, **100**, 064059 (2019). https://doi.org/10.1103/PhysRevD.100.064059
[26] H. Shabani, and M. Farhoudi, "f(R,T) cosmological models in phase space," Phys. Rev. D, **88**, 044048 (2013). https://doi.org/10.1103/PhysRevD.88.044048
[27] P. Sarmah, and U.D. Goswami, "Observational constraints on cosmological parameters in the Bianchi type III Universe with f(R,T) gravity theory," Phys. Dark Universe, **48**, 101932 (2025). https://doi.org/10.1016/j.dark.2025.101932
[28] E. Barrientos, *et al*., "Metric-affine f(R,T) theories of gravity and their applications," Phys. Rev. D, **97**, 104041 (2018). https://doi.org/10.1103/PhysRevD.97.104041
[29] H. Velten, and T.R.P. Caramês, "Cosmological inviability of f(R,T) gravity," Phys. Rev. D, **95**, 123536 (2017). https://doi.org/10.1103/PhysRevD.95.123536
[30] P.J. Steinhardt, and N. Turok, "Cosmic evolution in a cyclic universe," Phys. Rev. D, **65**, (2002). https://doi.org/10.1103/physrevd.65.126003
[31] A. Ijjas, and P.J. Steinhardt, "Fully stable cosmological solutions with a non-singular classical bounce," Phys. Lett. B, **764**, 289-294 (2017). https://doi.org/10.1016/j.physletb.2016.11.047
[32] T. Kobayashi, "Generic instabilities of nonsingular cosmologies in Horndeski theory: A no-go theorem," Phys. Rev. D, **94**, (2016). https://doi.org/10.1103/physrevd.94.043511
[33] D. Battefeld, and P. Peter, "A critical review of classical bouncing cosmologies," Phys. Rep. **571**, 1–66 (2015). https://doi.org/10.1016/j.physrep.2014.12.004
[34] R. Brandenberger, and P. Peter, "Bouncing Cosmologies: Progress and Problems," Found. Phys. **47**, 797–850 (2017). https://doi.org/10.1007/s10701-016-0057-0
[35] J. Martin, and P. Peter, "Parametric amplification of metric fluctuations through a bouncing phase," Phys. Rev. D, **68**, 103517 (2003). https://doi.org/10.1103/PhysRevD.68.103517
[36] T. Singh, R. Chaubey, and A. Singh, "Bouncing cosmologies with viscous fluids," Astrophys. Space Sci. **361**, 106 (2016). https://doi.org/10.1007/s10509-016-2696-1
[37] F.R. Klinkhamer, and Z.L. Wang, "Nonsingular bouncing cosmology from general relativity," Phys. Rev. D, **100**, 083534 (2019). https://doi.org/10.1103/PhysRevD.100.083534
[38] E. Battista, "Nonsingular bouncing cosmology in general relativity: physical analysis of the spacetime defect," Class. Quantum Gravity, **38**, 195007 (2021). https://doi.org/10.1088/1361-6382/ac1900
[39] A.S. Agrawal, *et al*., "Global phase space analysis for a class of single scalar field bouncing solutions in general relativity," Eur. Phys. J. C, **84**, (2024). https://doi.org/10.1140/epjc/s10052-023-12377-y
[40] S. Chakraborty, S. Mishra, and S. Chakraborty, "A dynamical system analysis of bouncing cosmology with spatial curvature," Gen. Relativ. Gravit. **56**, 83 (2024). https://doi.org/10.1007/s10714-024-03265-1
[41] A.Y. Shaikh, and B. Mishra, "Bouncing scenario of general relativistic hydrodynamics in extended gravity," Commun. Theor. Phys. **73**, 025401 (2021). https://doi.org/10.1088/1572-9494/abcfb2
[42] A.S. Agrawal, L. Pati, S.K. Tripathy, and B. Mishra, "Matter bounce scenario and the dynamical aspects in f(Q,T) gravity," Phys. Dark Universe, **33**, 100863 (2021). https://doi.org/10.1016/j.dark.2021.100863

[43] A. S Agrawal, S.K. Tripathy, S. Pal, and B. Mishra, "Role of extended gravity theory in matter bounce dynamics," Phys. Scr. **97**, 025002 (2022). https://doi.org/10.1088/1402-4896/ac49b2
[44] A.Y. Shaikh, "Exploring the bouncing cosmological models in symmetric teleparallel gravity," Int. J. Geom. Methods Mod. Phys. **20**, 2350220 (2023). https://doi.org/10.1142/S0219887823502201
[45] M. Zubair, *et al*., "Bouncing universe scenarios in an extended gravitational framework involving curvature-matter coupling," J. High Energy Astrophys. **44**, 243–265 (2024). https://doi.org/10.1016/j.jheap.2024.10.005
[46] L.V. Jaybhaye, R. Solanki, and P.K. Sahoo, "Bouncing cosmological models in f(R,Lm) gravity," Phys. Scr. **99**, 065031 (2024). https://doi.org/10.1088/1402-4896/ad4838
[47] M. Sharif, M.Z. Gul, and I. Hashim, "Theoretical insights and implications of bouncing cosmology in f(R,T^2) theory," Eur. Phys. J. C, **84**, 1094 (2024). https://doi.org/10.1140/epjc/s10052-024-13473-3
[48] M. Koussour, *et al*., "Bouncing behavior in f(R, Lm) gravity: Phantom crossing and energy conditions," Int. J. Geom. Methods Mod. Phys. **21**, 2450184 (2024). https://doi.org/10.1142/S0219887824501846
[49] Shaily, J.K. Singh, D. Sethi, R. Rani, and K. Bamba, "Bouncing cosmology and the dynamical stability analysis in f(R,Lm) gravity," Nucl. Phys. B, **1013**, 116854 (2025). https://doi.org/10.1016/j.nuclphysb.2025.116854
[50] A.Y. Shaikh, and A.P. Jenekar, "Cosmological implications of dark energy with bouncing scenario in f(R,Lm) gravity," Int. J. Geom. Methods Mod. Phys. S0219887826500222 (2025). https://doi.org/10.1142/S0219887826500222
[51] S.K. Tripathy, R.K. Khuntia, and P. Parida, "Bouncing cosmology in an extended theory of gravity," Eur. Phys. J. Plus, **134**, 504 (2019). https://doi.org/10.1140/epjp/i2019-12879-3
[52] S.K. Tripathy, B. Mishra, S. Ray, and R. Sengupta, "Bouncing universe models in an extended gravity theory," Chin. J. Phys. **71**, 610–622 (2021). https://doi.org/10.1016/j.cjph.2021.03.026
[53] S. Bhattacharjee, and P.K. Sahoo, "Comprehensive analysis of a non-singular bounce in f(R,T) gravitation," Phys. Dark Universe, **28**, 100537 (2020). https://doi.org/10.1016/j.dark.2020.100537
[54] P. Sahoo, S. Bhattacharjee, S.K. Tripathy, and P.K. Sahoo, "Bouncing scenario in f(R,T) gravity," Mod. Phys. Lett. A, **35**, 2050095 (2020). https://doi.org/10.1142/S0217732320500959
[55] A.S. Agrawal, *et al*., "Bouncing Cosmology in Extended Gravity and Its Reconstruction as Dark Energy Model," Fortschritte Phys. **70**, 2100065 (2022). https://doi.org/10.1002/prop.202100065
[56] A.Y. Shaikh, *et al*., "Bouncing cosmological model with general relativistic hydrodynamics in extended gravity," Int. J. Geom. Methods Mod. Phys. **19**, 2250193 (2022). https://doi.org/10.1142/S0219887822501936
[57] T. Harko, F.S.N. Lobo, S. Nojiri, and S.D. Odintsov, "f(R,T) gravity," Phys. Rev. D, **84**, 024020 (2011). https://doi.org/10.1103/PhysRevD.84.024020
[58] R.H. Brandenberger, "The Matter Bounce Alternative to Inflationary Cosmology," arXiv:1206.4196 [astro-ph.CO] (2012). https://doi.org/10.48550/arXiv.1206.4196
[59] M. Novello, and S. Bergliaffa, "Bouncing cosmologies," Phys. Rep. **463**, 127–213 (2008). https://doi.org/10.1016/j.physrep.2008.04.006
[60] C. Barragán, G.J. Olmo, and H. Sanchis-Alepuz, "Bouncing cosmologies in Palatini f(R) gravity," Phys. Rev. D, **80**, 024016 (2009). https://doi.org/10.1103/PhysRevD.80.024016
[61] K. Bamba, *et al*., "Bounce cosmology from $F(R)$ gravity and $F(R)$ bigravity," J. Cosmol. Astropart. Phys. **2014**, 008–008 (2014). https://doi.org/10.1088/1475-7516/2014/01/008
[62] S.K. Tripathy, and B. Mishra, "Phantom cosmology in an extended theory of gravity," Chin. J. Phys. **63**, 448–458 (2020). https://doi.org/10.1016/j.cjph.2019.12.022
[63] B. Mishra, S.K. Tripathy, and S. Tarai, "Accelerating models with a hybrid scale factor in extended gravity," J. Astrophys. Astron. **42**, 2 (2021). https://doi.org/10.1007/s12036-020-09655-6
[64] Yu.L. Bolotin, *et al*., "Cosmology In Terms Of The Deceleration Parameter. Part I," arXiv:1502.00811 [gr-qc] (2015). https://doi.org/10.48550/ARXIV.1502.00811
[65] G.P. Singh, and B.K. Bishi, "Bulk Viscous Cosmological Model in Brans-Dicke Theory with New Form of Time Varying Deceleration Parameter," Adv. High Energy Phys. **2017**, 1–24 (2017). https://doi.org/10.1155/2017/1390572
[66] H. Matsui, F. Takahashi, and T. Terada, "Non-singular bouncing cosmology with positive spatial curvature and flat scalar potential," Phys. Lett. B, **795**, 152–159 (2019). https://doi.org/10.1016/j.physletb.2019.06.013
[67] M. Koussour, and N. Myrzakulov, "Bouncing cosmologies and stability analysis in symmetric teleparallel f(Q) gravity," Eur. Phys. J. Plus, **139**, 799 (2024). https://doi.org/10.1140/epjp/s13360-024-05574-5
[68] B.P. Schmidt, *et al*., "The High-Z Supernova Search: Measuring Cosmic Deceleration and Global Curvature of the Universe Using Type Ia Supernovae," Astrophys. J. **507**, 46 (1998). https://doi.org/10.1086/306308
[69] J.L. Tonry, *et al*., "Cosmological Results from High-z Supernovae," Astrophys. J. **594**, 1 (2003). https://doi.org/10.1086/376865
[70] A.G. Riess, *et al*., "Type Ia Supernova Discoveries at z > 1 from the Hubble Space Telescope: Evidence for Past Deceleration and Constraints on Dark Energy Evolution," Astrophys. J. **607**, 665 (2004). https://doi.org/10.1086/383612
[71] Y.-F. Cai, and X. Zhang, "Evolution of metric perturbations in a model of nonsingular inflationary cosmology," J. Cosmol. Astropart. Phys. **2009**, 003 (2009). https://doi.org/10.1088/1475-7516/2009/06/003
[72] Y.-F. Cai, R. Brandenberger, and X. Zhang, "The matter bounce curvaton scenario," J. Cosmol. Astropart. Phys. **2011**, 003 (2011). https://doi.org/10.1088/1475-7516/2011/03/003
[73] V. Sahni, *et al*., "Statefinder—A new geometrical diagnostic of dark energy," J. Exp. Theor. Phys. Lett. **77**, 201–206 (2003). https://doi.org/10.1134/1.1574831
[74] U. Alam, *et al*., "Exploring the expanding Universe and dark energy using the statefinder diagnostic," Mon. Not. R. Astron. Soc. **344**, 1057–1074 (2003). https://doi.org/10.1046/j.1365-8711.2003.06871.x
[75] A.Y. Shaikh, and A.P. Jenekar, "Cosmological Dynamics of Barrow Holographic Dark Energy in f(G) gravity: An Analytical and Observational Approach," New Astron. 102497 (2025). https://doi.org/10.1016/j.newast.2025.102497
[76] A.Y. Shaikh, and A.P. Jenekar, "Constraining the Hybrid Model for Investigating Holographic Dark Energy in Modified Gravity," East Eur. J. Phys. (3), 26–40 (2025). https://doi.org/10.26565/2312-4334-2025-3-03

[77] A.Y. Shaikh, A.P. Jenekar, and S.M. Shingne, "Constrained Dynamics of Holographic Dark Energy in Modified f (R) Gravity," East Eur. J. Phys. (3), 4–16 (2025). https://doi.org/10.26565/2312-4334-2025-3-01

КОНЦЕПТУАЛЬНЕ ПОРУШЕННЯ ЕНЕРГЕТИЧНИХ УМОВ У КОСМОЛОГІЇ ВІДСКОКУ

А.Й. Шайх[1], С.М. Шінгне[2], А.П. Дженекар[3]

[1]Кафедра математики, Індіра Ганді Кала Махавідьялая, Ралегаон-445402. (M.S.) Індія

[2]Кафедра математики, Коледж наук, мистецтв та комерції ім. Г.С., Кхамгаон-444312. (M.S.) Індія

[3]Кафедра математики, мистецтв, комерції та науки, Коледж Марегаон-445303. (M.S.) Індія

Ця стаття зосереджена на дослідженні моделі відскоку в плоскому Всесвіті Фрідмана-Робертсона-Вокера (FRW). Параметр рівняння стану (EoS), що стосується розглянутої моделі, визначає особливості функціонування Всесвіту. Кінематику разом із фізичними атрибутами динамічних параметрів моделі всебічно досліджують. У цьому сценарії ми дослідили кілька енергетичних умов (ЕУ). Діагностична пара, що складається з методу визначення стану та параметра ривка, досліджується для ідентифікації суттєво різних космічних фаз. Ми використовували параметр квадрата швидкості звуку , розроблений для задоволення потреб аналізу стійкості нашої моделі. Наш аналіз показав, що результати нашого дослідження відповідають закономірностям, що спостерігаються у сценаріях відскоків, пропонуючи метод пояснення космічного прискорення, а також проблеми сингулярності у нашому Всесвіті.

Ключові слова: *сценарій відскоків; метрика FRW; гравітація; космічне прискорення*

East European Journal of Physics. 1. 88–104 (2026)
DOI: 10.26565/2312-4334-2026-1-07 ISSN 2312-4334

HYBRID SOLITARY WAVES AND SHOCK WAVES FOR DOUBLE–LAYERED FLUID FLOW WITH DISPERSION TRIPLET: ZAREMAOGHADDAM AND GEAR–GRIMSHAW MODELS (mKdV EQUATION)

Lakhveer Kaur[1], **O. González–Gaxiola**[2*], **Ahmed H. Arnous**[3,4], **Husham M. Ahmed**[5], **Haitham Alqahtani**[5], **Anjan Biswas**[6,7,8,9]

[1]*Department of Mathematics, Jaypee Institute of Information Technology, Noida–201304, India*
[2]*Applied Mathematics and Systems Department, Universidad Autónoma Metropolitana–Cuajimalpa, Vasco de Quiroga 4871, 05348, Mexico City, Mexico*
[3]*Department of Mathematical Sciences, Saveetha School of Engineering, SIMATS, Chennai - 602105, Tamilnadu, India*
[4]*Research Center of Applied Mathematics, Khazar University, Baku, AZ 1096, Azerbaijan*
[5]*College of Engineering, University of Technology Bahrain, Kingdom of Bahrain*
[6]*Department of Mathematics & Physics, Grambling State University, Grambling, LA 71245—2715, USA*
[7]*Department of Physics and Electronics, Khazar University, Baku, AZ—1096, Azerbaijan*
[8]*Department of Mathematics and Applied Mathematics, Sefako Makgatho Health Sciences University, Medunsa—0204, Pretoria, South Africa*
[9]*Applied Science Research Center, Applied Science Private University, Amman—11937, Jordan*
[*]*Corresponding Author e-mail: ogonzalez@cua.uam.mx*

Received November 11, 2025; revised February 4, 2025; accepted February 14, 2026

The current paper recovers hybrid solitary waves for double–layered shallow water waves with the basic platform being the mKdV equation. The selected models are the Zaremaoghaddam equation and the Gear–Grimshaw equation. The integration algorithm adopted is the generalized exponential differential function method. This yields hybrid waves that emerge from solitary waves, shock waves and the singular solitary waves. The existence criteria for such waves are also presented as parameter constraints.

Keywords: *mKdV equation; Hybrid; Integrability; Parameter constraints; Gear–Grimshaw equation*

PACS: 04.50.Kd, 04.20.Jb
AMS: 35Q51

1. INTRODUCTION

The concept of double–layered shallow water waves existed in the literature of Fluid Dynamics for a few decades. There are several aspects to this that has been successfully addressed and reported in the past. The current paper revisits the double–layered shallow water wave dynamics but from a fresher perspective. The concept of dispersion triplet was first introduced in 1977 and was later implemented during 2022 to study the standard fundamental models from shallow water wave dynamics [1, 2]. After a long hiatus, the 2022 implementation incorporated dispersion–triplet into KdV and mKdV–type settings and, within the traveling–wave framework, retrieved solitary and shock structures together with the associated conservation laws [1]. The current paper recovers the hybrid of solitary waves and shock waves for double–layered fluid flow with modified Korteweg–de Vries equation (mKdV) equation as its platform. The two governing models that were considered in this paper were Zaremaoghaddam model and the Gear–Grimshaw model. It must be noted that the same study has been previously carried out with KdV equation as its platform [3]. Thus, the present contribution constitutes the first dispersion–triplet double–layered revisit in which mKdV (rather than KdV) serves as the platform, thereby extending the double–layered dispersion–triplet framework to cubic nonlinearity. Meanwhile, double–layered flow itself remains a steady research theme; see, e.g., layered shallow-water approximations and stable or energy-consistent schemes [4, 5], and related solitary-wave dynamics in near-integrable regimes [6], alongside coupled-model developments such as Zaremaoghaddam–type formulations [7]. There are several additional double–layered models that exist in the literature such as the Bona–Chen equation, the current paper focuses on the aforementioned couple of models only. Additional models (e.g., Bona–Chen [8]) will be pursued in forthcoming work.

The adopted integration algorithm in this work is the generalized exponential differential rational function method which is an efficient one as compared to the pre–existing similar such schemes [9–14]. This integration scheme retrieves hybrid solitary waves and shock waves to the two models that were constructed with mKdV equation as their platform. One of the several shortcomings of this adopted integration approach is its failure to recover the solitary wave radiation as well as the phonons' component of shock waves. Such are only recoverable with the usage of inverse scattering transform

Cite as: L. Kaur, O. González–Gaxiola, A.H. Arnous, H.M. Ahmed, H. Alqahtani, A. Biswas, East Eur. J. Phys. 1, 88 (2026), https://doi.org/10.26565/2312-4334-2026-1-07

that is outside the scope of this paper. The details are exhibited in the rest of the paper after a quick display of the two governing models.

From the modeling perspective, modern two-layer shallow-water theory is often developed as a systematic long-wave reduction of the full water-wave problem, with the Green–Naghdi framework providing a canonical fully nonlinear, weakly dispersive baseline [15,16]. In particular, refined two-layer Green–Naghdi and Boussinesq-type closures have been constructed to improve frequency-dispersion properties and to better represent interfacial mode interactions [17,18]. Such formulations connect naturally with classical internal-wave models in two-fluid systems and support coherent interfacial structures of practical interest [19,20]. In parallel, the coupling between surface and internal modes, including barotropic–baroclinic transfer and resonance mechanisms, has been studied in several contexts, ranging from analytical mode-coupling descriptions to topographically mediated resonant exchange [21, 22].

At the level of reduced evolution equations, modified Korteweg–de Vries (mKdV) dynamics occupy a central role in nonlinear dispersive-wave theory, with a well-developed analytical foundation for well-posedness and global dynamics in both the line and periodic settings [23]. Beyond the classical scalar model, integrable and near-integrable generalizations continue to be developed, providing structured coupled dynamics and enlarged families of coherent waves [24]. Moreover, coupled and multi-component mKdV systems exhibit rich asymptotic behavior and long-time dynamics, complementing the study of higher-order coherent structures such as breather families in higher-order mKdV settings [25, 26]. These advances motivate revisiting double-layered hydrodynamic models on an mKdV platform, where coupling and dispersive extensions may yield hybrid morphologies beyond the classical single-field picture.

Alongside these modeling developments, there has been sustained progress in constructive methods for obtaining exact solutions of nonlinear evolution equations. Representative strands include the extended F-expansion methodology [27], transformed rational-function approaches capable of generating complexiton-type structures [28], and rational-exponential constructions for fractional or generalized equal-width models [29]. More recently, generalized Exp-function frameworks have been successfully applied to dispersive hydrodynamic equations motivated by wave phenomena, illustrating the flexibility of exponential-ansatz technology in producing closed-form wave families [30].

1.1. Governing Models

There are several models to address double-layered shallow water waves. With the basic platform at mKdV equation, the two models that ate commonly addressed are going to be taken uop in this paper. They are the Zaremaoghaddam model and the Gear-Grimshaw equation. One model that has been tacitly omitted is the Bona—Chen equation. These two models are first introduced in the next subsection.

1.1.1. Zaremaoghaddam Model. The interesting dynamics of two-layered water waves are described by Zareomaghoddam mKdV model, in which $q(x,t)$ and $r(x,t)$ represent the wave variables of the two layers. This study consist of examination of the following structure of Zareomaghoddam mKdV model, in order to provide exact solutions for the very first and foremost time in the literature:

$$\begin{aligned} q_t + a_1 q^2 q_x + a_2 r^2 q_x + a_3 q_{xxx} + a_4 q_{xxt} + a_5 q_{xtt} = 0, \\ r_t + b_1 r^2 r_x + b_2 q^2 r_x + b_3 r_{xxx} + b_4 r_{xxt} + b_5 r_{xtt} = 0, \end{aligned} \tag{1}$$

such that $a_i,\ b_i,\ i = 1, 2, 3, 4, 5$ display the physical parameters related to model (1).

1.1.2. Gear–Grimshaw Model. Gear-Grimshaw (GG) mKdV model, with spatial and time variables x and t, and dependent variables as $q(x,t)$ and $r(x,t)$, is mentioned as below:

$$\begin{aligned} q_t + a_1 q^2 q_x + a_2 q_{xxx} + a_3 q_{xxt} + a_4 q_{xtt} = a_5 r r_x + a_{10}\left(q^2 r\right)_x + a_6\left(q r^2\right)_x + a_7 r_{xxx} + a_8 r_{xxt} + a_9 r_{xtt}, \\ r_t + b_1 r^2 r_x + b_2 r_{xxx} + b_3 r_{xxt} + b_4 r_{xtt} = b_5 q q_x + b_6 (r^2 q)_x + b_{10}\left(r q^2\right)_x + b_7 q_{xxx} + b_8 q_{xxt} + b_9 q_{xtt}. \end{aligned} \tag{2}$$

The first term in (2) represents the temporal evolution, and $a_1,\ a_2,\ a_3,\ a_4$ represents the coefficients of dispersion terms, with similar while the coefficients of $b_1,\ b_2,\ b_3,\ b_4$ accountfor nonlinearity. For $j = 5,\ 6,\ 7,\ 8,\ 9,\ 10$, the coupling terms are represented by the coefficients $a_j,\ b_j$. This model provides a good description of a resonant interaction between traverse internal gravity wave modes in a stratified liquid.

The structure of this study is described as: An overview of the employed technique, referred as generalized exponential differential rational function technique, is given in Section 2. A variety of exact solutions are found in Section 3, respectively, by applying the stated procedure to the models (1) and (2). Finally, a thorough, succinct words of conclusion is appended to complement a few simulations of these research findings.

2. THE GENERALIZED EXPONENTIAL DIFFERENTIAL RATIONAL FUNCTION METHOD (GEDRF): AN OVERVIEW

The algorithmic perspective of the generalized exponential rational function (GEDRF) technique is presented in this section, and we have briefly described each stage in this procedure. It offers a variety of analytical solutions for various physical phenomena, being expressed in terms of NLPDEs, by combining exponential and rational functions. The following detailed explanations can be used to develop a number of exact solutions for nonlinear evolution equations (NLEEs):

Step–1: The general form of NLEE with variable $\Lambda(x,t)$ is considered as follows:

$$\rho(\Lambda, \Lambda_x, \Lambda_t, \Lambda_{xx}, \Lambda_{tt}, \Lambda_{xt}, \Lambda_{xxt}, \ldots) = 0. \tag{3}$$

The subsequent transformation is applied to (3) for seeking reduced ordinary differential equation (ODE) in terms of new variables as $\sigma,\ \tau$:

$$\Lambda(x,t) = \sigma(\tau), \quad \text{with} \quad \tau = x - p_1 t. \tag{4}$$

The expression (4) is plugged into equation (3) and hence resulting ODE is produced as follows:

$$\mathcal{M}(\sigma, \sigma', \sigma'', \sigma''' \ldots) = 0. \tag{5}$$

Step–2: Then after, ODE (5) is assumed to have following solution structure in terms of new dependent variable $\mathcal{T}(\tau)$ as:

$$\mathcal{M}(\zeta) = A_0 + \sum_{j=1}^{N} A_j \left(\frac{d^j}{d\tau^j}\mathcal{T}(\tau)\right)^j + \sum_{i=1}^{N} B_i \left(\frac{d^i}{d\tau^i}\mathcal{T}(\tau)\right)^{-i}, \tag{6}$$

also, $\mathcal{T}(\tau)$ is characterized as:

$$\mathcal{T}(\tau) = \frac{R_1 \exp(S_1\tau) + R_2 \exp(S_2\tau)}{R_3 \exp(S_3\tau) + R_4 \exp(S_4\tau)}. \tag{7}$$

Step–3: Balancing principle is used in ODE (5) for calculating the corresponding value of N for expression (6). One can choose the parameters $R_1, R_2, R_3, R_4, S_1, S_2, S_3$, and S_4 so that the function $\mathcal{T}(\tau)$ can be well described in terms of hyperbolic functions for seeking new exact solutions for considered model. Additionally, A_0, A_j, and B_i, $1 \le i, j \le N$ are determined in main procedure of computations.

Step–4: In this step, equation (6) is clubbed with equation (5), resulting into polynomial equation and then all of the coefficients in this polynomial are set to zero, creating a system of algebraic equations.

Step–5: In order to determine exact solutions for equation (3), the system of equations produced in the previous stage is investigated to explore the appropriate values of the involved parameters. These parameter values are then inserted into equations (6) and (7), for procuring the final closed form solutions of considered model.

The GEDRF scheme used here can be viewed as an ansatz-based traveling-wave approach. In this sense, it is related in spirit to classical methods such as the tanh-method, F-expansion, and exp-function approaches. The distinguishing feature is the choice of generating function $\mathcal{T}(\tau)$ as a rational combination of exponentials and the resulting solution structure, which admits both "direct" and "inverse/reciprocal" derivative contributions (cf. the trial form and the rational-exponential definition of $\mathcal{T}(\tau)$). By suitable selections of parameters in the rational-exponential representation, $\mathcal{T}(\tau)$ reduces to standard hyperbolic building blocks (e.g., tanh, coth, sech, csch), so many individual solutions can, in principle, be reproduced using traditional ansätze.

However, the practical advantage of GEDRF is that it provides a single unified template from which multiple waveform families—regular solitary profiles as well as singular/hybrid profiles—are generated by parameter choices within the same algebraic framework, together with the corresponding parameter constraints ("existence conditions"). In contrast, reproducing the entire catalogue typically requires multiple standard ansätze (polynomial-in-tanh, polynomial-in-exp, singular coth/csch ansätze, etc.), each treated separately with its own balancing and coefficient matching. The contribution of this work is therefore not to claim that ansatz methods are new, but to provide a systematic, family-wise construction of exact solutions and parameter regimes for the considered coupled mKdV-based double-layer models using this unified rational-exponential ansatz.

3. APPLICATION TO DOUBLE–LAYERED FLUID FLOW

3.1. Zaremaoghaddam Model

Generalized exponential differential function (GEDRF) method has been implemented to system of NLEEs, termed as Zareomaghoddam mKdV model (1) in this phase of the study. The primary objective is to investigate multiple novel exact soliton solutions to the governing model (1), which could greatly progress pertinent physical circumstances related to two layer liquid waves dynamics.

In accordance with GEDRF method, we have rewritten equation (1) in the form of an ordinary differential equation by using the wave translation

$$q(x,t) = K(\tau), \;\; r(x,t) = L(\tau) \quad \text{where} \quad \tau = x - p_1 t, \tag{8}$$

with p_1 as free parameter, representing wave velocity, which could be evaluated in mean implementation procedure.

Then, the resultant ODEs are procured as follows, utilizing (8) in equation (1) :

$$\begin{aligned} \left(a_5 {p_1}^2 - a_4 p_1 + a_3\right) K'''(\tau) + \left((K(\tau))^2 a_1 + (L(\tau))^2 a_2 - p_1\right) K'(\tau) = 0, \\ \left(b_5 {p_1}^2 - b_4 p_1 + b_3\right) L'''(\tau) + \left((K(\tau))^2 b_2 + (L(\tau))^2 b_1 - p_1\right) L'(\tau) = 0. \end{aligned} \tag{9}$$

After applying the balancing principle on the highest order derivative terms and a nonlinear term of equation (9), we have obtained that $N = 1$. Thus, from equation (6), the following trial solution structure for equation (9) is proposed:

$$\begin{aligned} K(\tau) &= \theta_1 \mathcal{T}'(\tau) + \frac{\omega_1}{\mathcal{T}'(\tau)} + \theta_0, \\ L(\tau) &= \theta_2 \mathcal{T}'(\tau) + \frac{\omega_2}{\mathcal{T}'(\tau)} + \theta_3, \end{aligned} \tag{10}$$

Here, the parameters $\theta_i, i = 0, 1, 2, 3,$ and $\omega_j, j = 1, 2$ are to be assessed in all calculation process. Next, using (10), the system (9) is converted into another system of ODEs with the new dependent variable $\mathcal{T}(\tau)$. Following that, work is being carried out to obtain exact solitary wave solutions for the system of ODEs provided in equation (9), as follows:

Family–I:

Putting up $[R_1, R_2, R_3, R_4] = [1, -1, 1, 1]$ and $[S_1, S_2, S_3, S_4] = [1, -1, 0, 0]$ in equation (7), we have retrieved hyperbolic function as follows:

$$\mathcal{T}(\tau) = \sinh(\tau). \tag{11}$$

Setting equation (11) in equation (10) for equation (9), the following coefficient values are acquired:

$$\begin{aligned} &a_1 = b_2, \; a_2 = -\frac{b_2 {\theta_1}^2}{{\theta_2}^2}, \; a_3 = -16\, a_5 {b_2}^2 {\omega_1}^2 {\theta_1}^2 + 4\, a_4 b_2 \omega_1 \theta_1, \\ &b_1 = -\frac{b_2 {\theta_1}^2}{{\theta_2}^2}, \; b_3 = -4\, b_2 \omega_1 \theta_1 \left(4\, b_2 b_5 \omega_1 \theta_1 - b_4\right), \\ &\omega_2 = -\frac{\omega_1 \theta_2}{\theta_1}, p_1 = 4\, b_2 \omega_1 \theta_1, \; \theta_0 = 0, \; \theta_3 = 0, \end{aligned} \tag{12}$$

along with $a_4, \; a_5, \; b_4, \; b_5, \; b_2, \; \omega_1, \; \theta_2, \; \theta_1$ as free parameters.

Hence, the solution of system (9) is represented with help of parameter values (12) as

$$\begin{aligned} K(\tau) &= \theta_1 \cosh(\tau) + \frac{\omega_1}{\cosh(\tau)}, \\ L(\tau) &= \theta_2 \cosh(\tau) - \frac{\omega_1 \theta_2}{\theta_1 \cosh(\tau)}. \end{aligned} \tag{13}$$

Finally, the newly constructed solution of model (1) is depicted in terms of original variables $x, \; t$ as

$$\begin{aligned} q(x,t) &= \theta_1 \cosh(x - p_1 t) + \frac{\omega_1}{\cosh(x - p_1 t)}, \\ r(x,t) &= \theta_2 \cosh(x - p_1 t) - \frac{\omega_1 \theta_2}{\theta_1 \cosh(x - p_1 t)}. \end{aligned} \tag{14}$$

Family–II:
Letting $[R_1, R_2, R_3, R_4] = [1, 1, 1, 1]$ and $[S_1, S_2, S_3, S_4] = [1, -1, 0, 0]$ in equation (7), leads to subsequent function:

$$\mathcal{T}(\tau) = \cosh(\tau). \tag{15}$$

The following coefficient values are generated after setting equation (15) in equation (10) for equation (9):

$$\begin{aligned} &a_1 = b_2,\ a_2 = -\frac{b_2{\theta_1}^2}{{\theta_2}^2}, a_3 = -\frac{4b_2\omega_2{\theta_1}^2\left(4\,a_5b_2\omega_2{\theta_1}^2 + a_4\theta_2\right)}{{\theta_2}^2},\ b_1 = -\frac{b_2{\theta_1}^2}{{\theta_2}^2},\\ &b_3 = -\frac{4b_2\omega_2{\theta_1}^2\left(4\,b_2b_5\omega_2{\theta_1}^2 + b_4\theta_2\right)}{{\theta_2}^2},\ \omega_1 = -\frac{\omega_2\theta_1}{\theta_2},\\ &p_1 = -\frac{4b_2\omega_2{\theta_1}^2}{\theta_2},\ \theta_0 = 0,\ \theta_3 = 0, \end{aligned} \tag{16}$$

along with $a_4,\ a_5,\ b_4,\ b_5,\ b_2,\ \omega_2,\ \theta_2,\ \theta_1$ as free parameters.

Consequently, exact solution of system (1) is depicted with the help of (16) and (15) and reverting back into original variables $x,\ t$ as follows:

$$\begin{aligned} q(x,t) &= \theta_1\sinh\left(x - p_1t\right) - \frac{\omega_2\theta_1}{\theta_2\sinh\left(x - p_1t\right)},\\ r(x,t) &= \theta_2\sinh\left(x - p_1t\right) + \frac{\omega_2}{\sinh\left(x - p_1t\right)}. \end{aligned} \tag{17}$$

Family–III:
Regarding $[R_1, R_2, R_3, R_4] = [1, -1, 1, 1]$ and $[S_1, S_2, S_3, S_4] = [1, -1, 1, -1]$ in equation (7), we have found

$$\mathcal{T}(\tau) = \tanh(\tau). \tag{18}$$

The following set of coefficients are obtained from equation (9) by substituting (10) and (18):

$$\begin{aligned} &a_1 = b_2,\ a_2 = -\frac{b_2{\theta_1}^2}{{\theta_2}^2},\ a_3 = 4\,b_2\omega_1\theta_1\left(-4\,a_5b_2\omega_1\theta_1 + a_4\right),\\ &b_1 = -\frac{b_2{\theta_1}^2}{{\theta_2}^2},\ b_3 = -4\,b_2\omega_1\theta_1\left(4\,b_2b_5\omega_1\theta_1 - b_4\right),\ \omega_2 = -\frac{\omega_1\theta_2}{\theta_1},\\ &p_1 = 4\,b_2\omega_1\theta_1,\ \theta_0 = 0,\ \theta_3 = 0, \end{aligned} \tag{19}$$

with $a_4,\ a_5,\ b_4,\ b_5,\ b_2,\ \omega_1,\ \theta_2,\ \theta_1$ as free parameters.

Thus, utilizing (19) and (18) in equation (10), the following solution of equation (9) is found:

$$\begin{aligned} K(\tau) &= \theta_1\left(\operatorname{sech}\left(\tau\right)\right)^2 + \frac{\omega_1}{\left(\operatorname{sech}\left(\tau\right)\right)^2},\\ L(\tau) &= \theta_2\left(\operatorname{sech}\left(\tau\right)\right)^2 - \frac{\omega_1\theta_2}{\theta_1\left(\operatorname{sech}\left(\tau\right)\right)^2}. \end{aligned} \tag{20}$$

Then after the exact solution of equation (1) is written in terms of original independent and dependent variables $x,\ t$ with the assistance of equation (20) and equation (19) as follows:

$$\begin{aligned} q\left(x,t\right) &= \theta_1\left(\operatorname{sech}\left(x - p_1t\right)\right)^2 + \frac{\omega_1}{\left(\operatorname{sech}\left(x - p_1t\right)\right)^2},\\ r\left(x,t\right) &= \theta_2\left(\operatorname{sech}\left(x - p_1t\right)\right)^2 - \frac{\omega_1\theta_2}{\theta_1\left(\operatorname{sech}\left(x - p_1t\right)\right)^2}. \end{aligned} \tag{21}$$

3.2. Gear–Grimshaw Model

This portion of current study involves the execution of GEDRF method to the system of NLEEs (2), describing the dynamics of resonant interaction between the internal gravity wave modes in a thin stratified liquid. It lead to curation of several novel soliton solutions to the governing model (2), equipped with a number of free parameters, which have considerable ability to illustrate crucial physical situations.

The subsequent variable transformation is executed to reduce equations (2) to system of ODEs:

$$q(x,t) = U(\tau), \;\; r(x,t) = V(\tau) \quad \text{where} \quad \tau = x - p_1 t, \tag{22}$$

with p_1 as free parameter, representing wave velocity, which is evaluated in computational procedure.
Then, resultant system of ODEs is obtained by considering (22) in (2) as follows:

$$\begin{aligned}
&\left(-a_{10}\left(U(\tau)\right)^2 - 2\,a_6 V(\tau)\,U(\tau) - a_5 V(\tau)\right)V'(\tau) + \left(a_1\left(U(\tau)\right)^2 - 2\,a_{10}U(\tau)\,V(\tau) - a_6\left(V(\tau)\right)^2 - p_1\right)U'(\tau)\\
&+ \left({p_1}^2 a_4 - p_1\,a_3 + a_2\right)U'''(\tau) + \left(-{p_1}^2 a_9 + p_1\,a_8 - a_7\right)V'''(\tau) = 0,\\
&\left(-b_{10}\left(U(\tau)\right)^2 - 2\,b_6 V(\tau)\,U(\tau) + b_1\left(V(\tau)\right)^2 - p_1\right)V'(\tau) + \left(-2\,b_{10}U(\tau)\,V(\tau) - b_6\left(V(\tau)\right)^2 - b_5 U(\tau)\right)U'(\tau)\\
&+ \left({p_1}^2 b_4 - p_1\,b_3 + b_2\right)V'''(\tau) + \left(-{p_1}^2 b_9 + p_1\,b_8 - b_7\right)U'''(\tau) = 0.
\end{aligned} \tag{23}$$

As stated in Step–3 of section 2, we have calculated $N = 1$ using the balancing principle in equation (23). Equation (23) yielded the following solution structure:

$$\begin{aligned}
U(\tau) &= \theta_1 \mathcal{T}'(\tau) + \frac{\omega_1}{\mathcal{T}'(\tau)} + \theta_0,\\
V(\tau) &= \theta_4 \mathcal{T}'(\tau) + \frac{\omega_4}{\mathcal{T}'(\tau)} + \theta_5,
\end{aligned} \tag{24}$$

The parameters $\theta_i, i = 0, 1, 4, 5$ and $\omega_j, j = 1, 4$ can be assessed in the mean way of the entire computations. Next, equation (24) is used to convert the system (23) into another system of ODEs, with a new dependent variable $\mathcal{T}(\tau)$. After then, investigation is being done to obtain exact solitary wave solutions for the system of ODEs provided in equation (23), as follows:

Family–I:

The equation (7) is appraised with $[R_1, R_2, R_3, R_4] = [1, -1, 1, 1]$ and $[S_1, S_2, S_3, S_4] = [1, -1, 0, 0]$ and its recovered that

$$\mathcal{T}(\tau) = \sinh(\tau). \tag{25}$$

Plugging this value in (24) for equation (23) along with substituting trail solution, we achieved the system of algebraic equations. By setting coefficients of each function to zero, the following coefficient values are recovered:

$$\begin{aligned}
a_1 &= \frac{a_{10}\omega_4 + 2\,b_6\omega_4 + 3\,b_{10}\omega_1}{\omega_1},\; a_2 = \frac{Z_1}{{\omega_4}^4{\omega_1}^3},\\
a_5 &= \frac{2}{3}\,\frac{\omega_1\left(a_{10}\omega_1\omega_4\theta_5 - a_{10}{\omega_4}^2\theta_0 - 4\,b_6\omega_1\omega_4\theta_5 + 4\,b_6{\omega_4}^2\theta_0 - 6\,b_{10}{\omega_1}^2\theta_5 + 6\,b_{10}\omega_1\omega_4\theta_0\right)}{{\omega_4}^3},\\
a_6 &= -\,\frac{\omega_1\left(2\,a_{10}\omega_4 - 2\,b_6\omega_4 - 3\,b_{10}\omega_1\right)}{3{\omega_4}^2},\\
b_1 &= \frac{3\omega_1\left(b_6\omega_4 + b_{10}\omega_1\right)}{{\omega_4}^2},\; b_5 = \frac{2\left(b_6\omega_1\omega_4\theta_5 - b_6{\omega_4}^2\theta_0 + 2\,b_{10}{\omega_1}^2\theta_5 - 2\,b_{10}\omega_1\omega_4\theta_0\right)}{{\omega_1}^2},\\
b_7 &= \frac{Z_2}{{\omega_4}^4{\omega_1}^3},\;\; \theta_1 = \frac{\omega_1\theta_4}{\omega_4}\\
p_1 &= \frac{2\,b_6{\omega_1}^2\omega_4{\theta_5}^2 - 4\,b_6\omega_1{\omega_4}^2\theta_0\theta_5 + 2\,b_6{\omega_4}^3{\theta_0}^2 + 3\,b_{10}{\omega_1}^3{\theta_5}^2 - 6\,b_{10}{\omega_1}^2\omega_4\theta_0\theta_5 + 3\,b_{10}\omega_1{\omega_4}^2{\theta_0}^2}{\omega_1{\omega_4}^2},
\end{aligned} \tag{26}$$

with

$Z_1 = -4\,a_4b_6{}^2\omega_1{}^5\omega_4{}^2\theta_5{}^4 + 16\,a_4b_6{}^2\omega_1{}^4\omega_4{}^3\theta_0\theta_5{}^3 - 24\,a_4b_6{}^2\omega_1{}^3\omega_4{}^4\theta_0{}^2\theta_5{}^2 + 16\,a_4b_6{}^2\omega_1{}^2\omega_4{}^5\theta_0{}^3\theta_5 - 4\,a_4b_6{}^2\omega_1\omega_4{}^6\theta_0{}^4 - 12\,a_4b_6b_{10}\omega_1{}^6\omega_4\theta_5{}^4 + 48\,a_4b_6b_{10}\omega_1{}^5\omega_4{}^2\theta_0\theta_5{}^3 - 72\,a_4b_6b_{10}\omega_1{}^4\omega_4{}^3\theta_0{}^2\theta_5{}^2 + 48\,a_4b_6b_{10}\omega_1{}^3\omega_4{}^4\theta_0{}^3\theta_5 - 12\,a_4b_6b_{10}\omega_1{}^2\omega_4{}^5\theta_0{}^4 - 9\,a_4b_{10}{}^2\omega_1{}^7\theta_5{}^4 + 36\,a_4b_{10}{}^2\omega_1{}^6\omega_4\theta_0\theta_5{}^3 - 54\,a_4b_{10}{}^2\omega_1{}^5\omega_4{}^2\theta_0{}^2\theta_5{}^2 + 36\,a_4b_{10}{}^2\omega_1{}^4\omega_4{}^3\theta_0{}^3\theta_5 - 9\,a_4b_{10}{}^2\omega_1{}^3\omega_4{}^4\theta_0{}^4 + 4\,a_9b_6{}^2\omega_1{}^4\omega_4{}^3\theta_5{}^4 - 16\,a_9b_6{}^2\omega_1{}^3\omega_4{}^4\theta_0\theta_5{}^3 + 24\,a_9b_6{}^2\omega_1{}^2\omega_4{}^5\theta_0{}^2\theta_5{}^2 - 16\,a_9b_6{}^2\omega_1\omega_4{}^6\theta_0{}^3\theta_5 + 4\,a_9b_6{}^2\omega_4{}^7\theta_0{}^4 + 12\,a_9b_6b_{10}\omega_1{}^5\omega_4{}^2\theta_5{}^4 - 48\,a_9b_6b_{10}\omega_1{}^4\omega_4{}^3\theta_0\theta_5{}^3 + 72\,a_9b_6b_{10}\omega_1{}^3\omega_4{}^4\theta_0{}^2\theta_5{}^2 - 48\,a_9b_6b_{10}\omega_1{}^2\omega_4{}^5\theta_0{}^3\theta_5 + 12\,a_9b_6b_{10}\omega_1\omega_4{}^6\theta_0{}^4 + 9\,a_9b_{10}{}^2\omega_1{}^6\omega_4\theta_5{}^4 - 36\,a_9b_{10}{}^2\omega_1{}^5\omega_4{}^2\theta_0\theta_5{}^3 + 54\,a_9b_{10}{}^2\omega_1{}^4\omega_4{}^3\theta_0{}^2\theta_5{}^2 - 36\,a_9b_{10}{}^2\omega_1{}^3\omega_4{}^4\theta_0{}^3\theta_5 + 9\,a_9b_{10}{}^2\omega_1{}^2\omega_4{}^5\theta_0{}^4 + 2\,a_3b_6\omega_1{}^4\omega_4{}^3\theta_5{}^2 - 4\,a_3b_6\omega_1{}^3\omega_4{}^4\theta_0\theta_5 + 2\,a_3b_6\omega_1{}^2\omega_4{}^5\theta_0{}^2 + 3\,a_3b_{10}\omega_1{}^5\omega_4{}^2\theta_5{}^2 - 6\,a_3b_{10}\omega_1{}^4\omega_4{}^3\theta_0\theta_5 + 3\,a_3b_{10}\omega_1{}^3\omega_4{}^4\theta_0{}^2 - 2\,a_8b_6\omega_1{}^3\omega_4{}^4\theta_5{}^2 + 4\,a_8b_6\omega_1{}^2\omega_4{}^5\theta_0\theta_5 - 2\,a_8b_6\omega_1\omega_4{}^6\theta_0{}^2 - 3\,a_8b_{10}\omega_1{}^4\omega_4{}^3\theta_5{}^2 + 6\,a_8b_{10}\omega_1{}^3\omega_4{}^4\theta_0\theta_5 - 3\,a_8b_{10}\omega_1{}^2\omega_4{}^5\theta_0{}^2 + a_7\omega_1{}^2\omega_4{}^5,$

$Z_2 = 4\,b_4b_6{}^2\omega_1{}^4\omega_4{}^3\theta_5{}^4 - 16\,b_4b_6{}^2\omega_1{}^3\omega_4{}^4\theta_0\theta_5{}^3 + 24\,b_4b_6{}^2\omega_1{}^2\omega_4{}^5\theta_0{}^2\theta_5{}^2 - 16\,b_4b_6{}^2\omega_1\omega_4{}^6\theta_0{}^3\theta_5 + 4\,b_4b_6{}^2\omega_4{}^7\theta_0{}^4 + 12\,b_4b_6b_{10}\omega_1{}^5\omega_4{}^2\theta_5{}^4 - 48\,b_4b_6b_{10}\omega_1{}^4\omega_4{}^3\theta_0\theta_5{}^3 + 72\,b_4b_6b_{10}\omega_1{}^3\omega_4{}^4\theta_0{}^2\theta_5{}^2 - 48\,b_4b_6b_{10}\omega_1{}^2\omega_4{}^5\theta_0{}^3\theta_5 + 12\,b_4b_6b_{10}\omega_1\omega_4{}^6\theta_0{}^4 + 9\,b_4b_{10}{}^2\omega_1{}^6\omega_4\theta_5{}^4 - 36\,b_4b_{10}{}^2\omega_1{}^5\omega_4{}^2\theta_0\theta_5{}^3 + 54\,b_4b_{10}{}^2\omega_1{}^4\omega_4{}^3\theta_0{}^2\theta_5{}^2 - 36\,b_4b_{10}{}^2\omega_1{}^3\omega_4{}^4\theta_0{}^3\theta_5 + 9\,b_4b_{10}{}^2\omega_1{}^2\omega_4{}^5\theta_0{}^4 - 4\,b_6{}^2b_9\omega_1{}^5\omega_4{}^2\theta_5{}^4 + 16\,b_6{}^2b_9\omega_1{}^4\omega_4{}^3\theta_0\theta_5{}^3 - 24\,b_6{}^2b_9\omega_1{}^3\omega_4{}^4\theta_0{}^2\theta_5{}^2 + 16\,b_6{}^2b_9\omega_1{}^2\omega_4{}^5\theta_0{}^3\theta_5 - 4\,b_6{}^2b_9\omega_1\omega_4{}^6\theta_0{}^4 - 12\,b_6b_9b_{10}\omega_1{}^6\omega_4\theta_5{}^4 + 48\,b_6b_9b_{10}\omega_1{}^5\omega_4{}^2\theta_0\theta_5{}^3 - 72\,b_6b_9b_{10}\omega_1{}^4\omega_4{}^3\theta_0{}^2\theta_5{}^2 + 48\,b_6b_9b_{10}\omega_1{}^3\omega_4{}^4\theta_0{}^3\theta_5 - 12\,b_6b_9b_{10}\omega_1{}^2\omega_4{}^5\theta_0{}^4 - 9\,b_9b_{10}{}^2\omega_1{}^7\theta_5{}^4 + 36\,b_9b_{10}{}^2\omega_1{}^6\omega_4\theta_0\theta_5{}^3 - 54\,b_9b_{10}{}^2\omega_1{}^5\omega_4{}^2\theta_0{}^2\theta_5{}^2 + 36\,b_9b_{10}{}^2\omega_1{}^4\omega_4{}^3\theta_0{}^3\theta_5 - 9\,b_9b_{10}{}^2\omega_1{}^3\omega_4{}^4\theta_0{}^4 - 2\,b_3b_6\omega_1{}^3\omega_4{}^4\theta_5{}^2 + 4\,b_3b_6\omega_1{}^2\omega_4{}^5\theta_0\theta_5 - 2\,b_3b_6\omega_1\omega_4{}^6\theta_0{}^2 - 3\,b_3b_{10}\omega_1{}^4\omega_4{}^3\theta_5{}^2 + 6\,b_3b_{10}\omega_1{}^3\omega_4{}^4\theta_0\theta_5 - 3\,b_3b_{10}\omega_1{}^2\omega_4{}^5\theta_0{}^2 + 2\,b_6b_8\omega_1{}^4\omega_4{}^3\theta_5{}^2 - 4\,b_6b_8\omega_1{}^3\omega_4{}^4\theta_0\theta_5 + 2\,b_6b_8\omega_1{}^2\omega_4{}^5\theta_0{}^2 + 3\,b_8b_{10}\omega_1{}^5\omega_4{}^2\theta_5{}^2 - 6\,b_8b_{10}\omega_1{}^4\omega_4{}^3\theta_0\theta_5 + 3\,b_8b_{10}\omega_1{}^3\omega_4{}^4\theta_0{}^2 + b_2\omega_1{}^2\omega_4{}^5,$
and equipped with $\theta_0, \theta_4, \theta_5, b_8, b_9, b_{10}, b_6, \omega_1, \omega_4, b_2, b_3, b_4, a_7, a_8, a_9, a_{10}, a_3, a_4$ as arbitrary parameters.

Hence, the solution of system (23) is represented as, with help of (26) in terms of parent variables $x,\ t$ as mentioned below:

$$\begin{aligned} U(\tau) &= \frac{\omega_1\theta_4\cosh(\tau)}{\omega_4} + \frac{\omega_1}{\cosh(\tau)} + \theta_0, \\ V(\tau) &= \theta_4\cosh(\tau) + \frac{\omega_4}{\cosh(\tau)} + \theta_5. \end{aligned} \tag{27}$$

Finally, the novel soliton solution for model (2) is formulated as

$$\begin{aligned} q(x,t) &= \frac{\omega_1\theta_4\cosh(x-p_1t)}{\omega_4} + \frac{\omega_1}{\cosh(x-p_1t)} + \theta_0, \\ r(x,t) &= \theta_4\cosh(x-p_1t) + \frac{\omega_4}{\cosh(x-p_1t)} + \theta_5. \end{aligned} \tag{28}$$

Family–II:

Letting $[R_1, R_2, R_3, R_4] = [1, 1, 1, 1]$ and $[S_1, S_2, S_3, S_4] = [1, -1, 0, 0]$ in equation (7), we found

$$\mathcal{T}(\tau) = \cosh(\tau). \tag{29}$$

The equation (24) is reformatted with (29) for equation (23), and then collecting the coefficients of like powers leads to subsequent coefficient values:

$$\begin{aligned} a_1 &= \frac{a_{10}\omega_4 + 2\,b_6\omega_4 + 3\,b_{10}\omega_1}{\omega_1},\ a_2 = \frac{Z_3}{\omega_4{}^4\omega_1{}^3}, \\ a_5 &= \frac{2}{3}\,\frac{\omega_1\left(a_{10}\omega_1\omega_4\theta_5 - a_{10}\omega_4{}^2\theta_0 - 4\,b_6\omega_1\omega_4\theta_5 + 4\,b_6\omega_4{}^2\theta_0 - 6\,b_{10}\omega_1{}^2\theta_5 + 6\,b_{10}\omega_1\omega_4\theta_0\right)}{\omega_4{}^3}, \\ a_6 &= -\frac{\omega_1\left(2\,a_{10}\omega_4 - 2\,b_6\omega_4 - 3\,b_{10}\omega_1\right)}{3\omega_4{}^2},\ b_1 = \frac{3\omega_1\left(b_6\omega_4 + b_{10}\omega_1\right)}{\omega_4{}^2}, \\ b_5 &= \frac{2\left(b_6\omega_1\omega_4\theta_5 - b_6\omega_4{}^2\theta_0 + 2\,b_{10}\omega_1{}^2\theta_5 - 2\,b_{10}\omega_1\omega_4\theta_0\right)}{\omega_1{}^2}, \\ b_7 &= \frac{Z_4}{\omega_4{}^4\omega_1{}^3},\ \theta_1 = \frac{\omega_1\theta_4}{\omega_4}, \\ p_1 &= \frac{2\,b_6\omega_1{}^2\omega_4\theta_5{}^2 - 4\,b_6\omega_1\omega_4{}^2\theta_0\theta_5 + 2\,b_6\omega_4{}^3\theta_0{}^2 + 3\,b_{10}\omega_1{}^3\theta_5{}^2 - 6\,b_{10}\omega_1{}^2\omega_4\theta_0\theta_5 + 3\,b_{10}\omega_1\omega_4{}^2\theta_0{}^2}{\omega_1\omega_4{}^2}, \end{aligned} \tag{30}$$

with
$Z_3 = -4\,a_4b_6{}^2\omega_1{}^5\omega_4{}^2\theta_5{}^4 + 16\,a_4b_6{}^2\omega_1{}^4\omega_4{}^3\theta_0\theta_5{}^3 - 24\,a_4b_6{}^2\omega_1{}^3\omega_4{}^4\theta_0{}^2\theta_5{}^2 + 16\,a_4b_6{}^2\omega_1{}^2\omega_4{}^5\theta_0{}^3\theta_5 - 4\,a_4b_6{}^2\omega_1\omega_4{}^6\theta_0{}^4 - 12\,a_4b_6b_{10}\omega_1{}^6\omega_4\theta_5{}^4 + 48\,a_4b_6b_{10}\omega_1{}^5\omega_4{}^2\theta_0\theta_5{}^3 - 72\,a_4b_6b_{10}\omega_1{}^4\omega_4{}^3\theta_0{}^2\theta_5{}^2 + 48\,a_4b_6b_{10}\omega_1{}^3\omega_4{}^4\theta_0{}^3\theta_5 - 12\,a_4b_6b_{10}\omega_1{}^2\omega_4{}^5\theta_0{}^4 - 9\,a_4b_{10}{}^2\omega_1{}^7\theta_5{}^4 + 36\,a_4b_{10}{}^2\omega_1{}^6\omega_4\theta_0\theta_5{}^3 - 54\,a_4b_{10}{}^2\omega_1{}^5\omega_4{}^2\theta_0{}^2\theta_5{}^2 + 36\,a_4b_{10}{}^2\omega_1{}^4\omega_4{}^3\theta_0{}^3\theta_5 - 9\,a_4b_{10}{}^2\omega_1{}^3\omega_4{}^4\theta_0{}^4 + 4\,a_9b_6{}^2\omega_1{}^4\omega_4{}^3\theta_5{}^4 - 16\,a_9b_6{}^2\omega_1{}^3\omega_4{}^4\theta_0\theta_5{}^3 + 24\,a_9b_6{}^2\omega_1{}^2\omega_4{}^5\theta_0{}^2\theta_5{}^2 - 16\,a_9b_6{}^2\omega_1\omega_4{}^6\theta_0{}^3\theta_5 + 4\,a_9b_6{}^2\omega_4{}^7\theta_0{}^4 + 12\,a_9b_6b_{10}\omega_1{}^5\omega_4{}^2\theta_5{}^4 - 48\,a_9b_6b_{10}\omega_1{}^4\omega_4{}^3\theta_0\theta_5{}^3 + 72\,a_9b_6b_{10}\omega_1{}^3\omega_4{}^4\theta_0{}^2\theta_5{}^2 - 48\,a_9b_6b_{10}\omega_1{}^2\omega_4{}^5\theta_0{}^3\theta_5 + 12\,a_9b_6b_{10}\omega_1\omega_4{}^6\theta_0{}^4 + 9\,a_9b_{10}{}^2\omega_1{}^6\omega_4\theta_5{}^4 - 36\,a_9b_{10}{}^2\omega_1{}^5\omega_4{}^2\theta_0\theta_5{}^3 + 54\,a_9b_{10}{}^2\omega_1{}^4\omega_4{}^3\theta_0{}^2\theta_5{}^2 - 36\,a_9b_{10}{}^2\omega_1{}^3\omega_4{}^4\theta_0{}^3\theta_5 + 9\,a_9b_{10}{}^2\omega_1{}^2\omega_4{}^5\theta_0{}^4 + 2\,a_3b_6\omega_1{}^4\omega_4{}^3\theta_5{}^2 - 4\,a_3b_6\omega_1{}^3\omega_4{}^4\theta_0\theta_5 + 2\,a_3b_6\omega_1{}^2\omega_4{}^5\theta_0{}^2 + 3\,a_3b_{10}\omega_1{}^5\omega_4{}^2\theta_5{}^2 - 6\,a_3b_{10}\omega_1{}^4\omega_4{}^3\theta_0\theta_5 + 3\,a_3b_{10}\omega_1{}^3\omega_4{}^4\theta_0{}^2 - 2\,a_8b_6\omega_1{}^3\omega_4{}^4\theta_5{}^2 + 4\,a_8b_6\omega_1{}^2\omega_4{}^5\theta_0\theta_5 - 2\,a_8b_6\omega_1\omega_4{}^6\theta_0{}^2 - 3\,a_8b_{10}\omega_1{}^4\omega_4{}^3\theta_5{}^2 + 6\,a_8b_{10}\omega_1{}^3\omega_4{}^4\theta_0\theta_5 - 3\,a_8b_{10}\omega_1{}^2\omega_4{}^5\theta_0{}^2 + a_7\omega_1{}^2\omega_4{}^5,$

$Z_4 = 4\,b_4b_6{}^2\omega_1{}^4\omega_4{}^3\theta_5{}^4 - 16\,b_4b_6{}^2\omega_1{}^3\omega_4{}^4\theta_0\theta_5{}^3 + 24\,b_4b_6{}^2\omega_1{}^2\omega_4{}^5\theta_0{}^2\theta_5{}^2 - 16\,b_4b_6{}^2\omega_1\omega_4{}^6\theta_0{}^3\theta_5 + 4\,b_4b_6{}^2\omega_4{}^7\theta_0{}^4 + 12\,b_4b_6b_{10}\omega_1{}^5\omega_4{}^2\theta_5{}^4 - 48\,b_4b_6b_{10}\omega_1{}^4\omega_4{}^3\theta_0\theta_5{}^3 + 72\,b_4b_6b_{10}\omega_1{}^3\omega_4{}^4\theta_0{}^2\theta_5{}^2 - 48\,b_4b_6b_{10}\omega_1{}^2\omega_4{}^5\theta_0{}^3\theta_5 + 12\,b_4b_6b_{10}\omega_1\omega_4{}^6\theta_0{}^4 +$

$9\,b_4b_{10}{}^2\omega_1{}^6\omega_4\theta_5{}^4 - 36\,b_4b_{10}{}^2\omega_1{}^5\omega_4{}^2\theta_0\theta_5{}^3 + 54\,b_4b_{10}{}^2\omega_1{}^4\omega_4{}^3\theta_0{}^2\theta_5{}^2 - 36\,b_4b_{10}{}^2\omega_1{}^3\omega_4{}^4\theta_0{}^3\theta_5 + 9\,b_4b_{10}{}^2\omega_1{}^2\omega_4{}^5\theta_0{}^4 - 4\,b_6{}^2b_9\omega_1{}^5\omega_4{}^2\theta_5{}^4 + 16\,b_6{}^2b_9\omega_1{}^4\omega_4{}^3\theta_0\theta_5{}^3 - 24\,b_6{}^2b_9\omega_1{}^3\omega_4{}^4\theta_0{}^2\theta_5{}^2 + 16\,b_6{}^2b_9\omega_1{}^2\omega_4{}^5\theta_0{}^3\theta_5 - 4\,b_6{}^2b_9\omega_1\omega_4{}^6\theta_0{}^4 - 12\,b_6b_9b_{10}\omega_1{}^6\omega_4\theta_5{}^4 + 48\,b_6b_9b_{10}\omega_1{}^5\omega_4{}^2\theta_0\theta_5{}^3 - 72\,b_6b_9b_{10}\omega_1{}^4\omega_4{}^3\theta_0{}^2\theta_5{}^2 + 48\,b_6b_9b_{10}\omega_1{}^3\omega_4{}^4\theta_0{}^3\theta_5 - 12\,b_6b_9b_{10}\omega_1{}^2\omega_4{}^5\theta_0{}^4 - 9\,b_9b_{10}{}^2\omega_1{}^7\theta_5{}^4 + 36\,b_9b_{10}{}^2\omega_1{}^6\omega_4\theta_0\theta_5{}^3 - 54\,b_9b_{10}{}^2\omega_1{}^5\omega_4{}^2\theta_0{}^2\theta_5{}^2 + 36\,b_9b_{10}{}^2\omega_1{}^4\omega_4{}^3\theta_0{}^3\theta_5 - 9\,b_9b_{10}{}^2\omega_1{}^3\omega_4{}^4\theta_0{}^4 - 2\,b_3b_6\omega_1{}^3\omega_4{}^4\theta_5{}^2 + 4\,b_3b_6\omega_1{}^2\omega_4{}^5\theta_0\theta_5 - 2\,b_3b_6\omega_1\omega_4{}^6\theta_0{}^2 - 3\,b_3b_{10}\omega_1{}^4\omega_4{}^3\theta_5{}^2 + 6\,b_3b_{10}\omega_1{}^3\omega_4{}^4\theta_0\theta_5 - 3\,b_3b_{10}\omega_1{}^2\omega_4{}^5\theta_0{}^2 + 2\,b_6b_8\omega_1{}^4\omega_4{}^3\theta_5{}^2 - 4\,b_6b_8\omega_1{}^3\omega_4{}^4\theta_0\theta_5 + 2\,b_6b_8\omega_1{}^2\omega_4{}^5\theta_0{}^2 + 3\,b_8b_{10}\omega_1{}^5\omega_4{}^2\theta_5{}^2 - 6\,b_8b_{10}\omega_1{}^4\omega_4{}^3\theta_0\theta_5 + 3\,b_8b_{10}\omega_1{}^3\omega_4{}^4\theta_0{}^2 + b_2\omega_1{}^2\omega_4{}^5,$
along with $\theta_0, \theta_4, \theta_5, b_8, b_9, b_{10}, b_6, \omega_1, \omega_4, b_2, b_3, b_4, a_7, a_8, a_9, a_{10}, a_3, a_4$ as free parameters.

Consequently, exact soliton solution for system (2) is depicted with the help of (30) and (29) and followed by reverting back into original variables $x,\ t$ as follows:

$$\begin{aligned} q(x,t) &= \frac{\omega_1\theta_4\sinh(x-p_1t)}{\omega_4} + \frac{\omega_1}{\sinh(x-p_1t)} + \theta_0, \\ r(x,t) &= \theta_4\sinh(x-p_1t) + \frac{\omega_4}{\sinh(x-p_1t)} + \theta_5. \end{aligned} \tag{31}$$

Important Remark:

Following the same procedure outlined in the previous sections, additional solutions of the considered model (2) can be derived with parameter values as (26). For brevity, the detailed computations are omitted, and hence resulting hybrid solitary waves are enlisted below for enhanced comprehension:

Family–III:

$$\begin{aligned} q(x,t) &= \frac{\omega_1\theta_4\left(\operatorname{sech}(x-p_1t)\right)^2}{\omega_4} + \frac{\omega_1}{\left(\operatorname{sech}(x-p_1t)\right)^2} + \theta_0, \\ r(x,t) &= \theta_4\left(\operatorname{sech}(x-p_1t)\right)^2 + \frac{\omega_4}{\left(\operatorname{sech}(x-p_1t)\right)^2} + \theta_5. \end{aligned} \tag{32}$$

Figure 1 shows the 3D and 2D profile of a traveling wave solution for the Gear–Grimshaw model which corresponds to the solutions given in equations (28) and for the parameters indicated in the same figure.

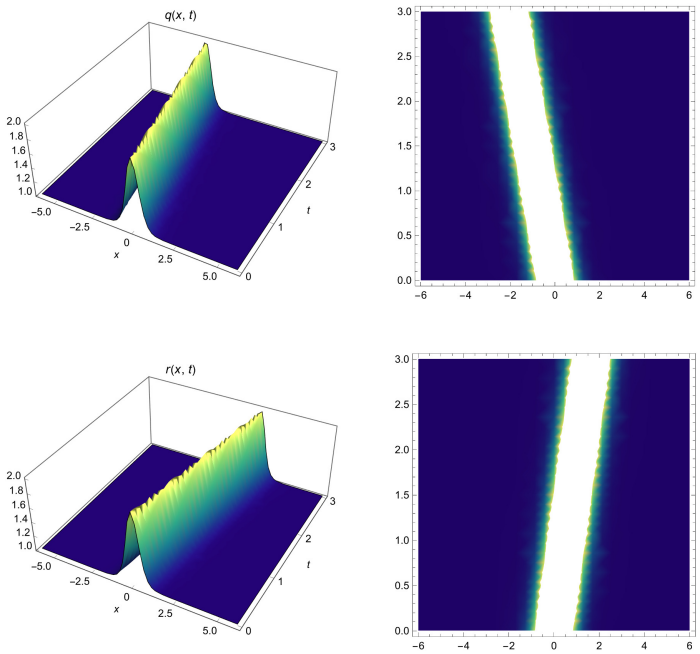

Figure 1. 3D and 2D profile of a traveling wave solution for the Gear–Grimshaw model which corresponds to the solutions given in equations (28). The parameter selection is: $a_1 = 2.12$, $a_2 = 0.78$, $a_3 = 0.95$, $a_4 = 3.22$, $a_5 = 2.45$, $a_6 = 1.67$, $a_7 = 2.66$, $a_8 = 0.55$, $a_9 = 0.33$, $b_1 = 1.88$, $b_2 = 0.45$, $b_3 = -5.22$, $b_4 = 0.68$, $b_5 = 6.04$, $b_6 = 3.76$, $b_7 = 1.88$, $b_8 = -3.50$ and $b_9 = 3.65$.

Figure 2 shows the 3D and 2D singular traveling wave solution for the Zaremaoghaddam model which corresponds to the solutions given in equations (53) and for the parameters indicated in the same figure. The left side of the waveform decreases abruptly, while the right side grows abruptly along a straight line.

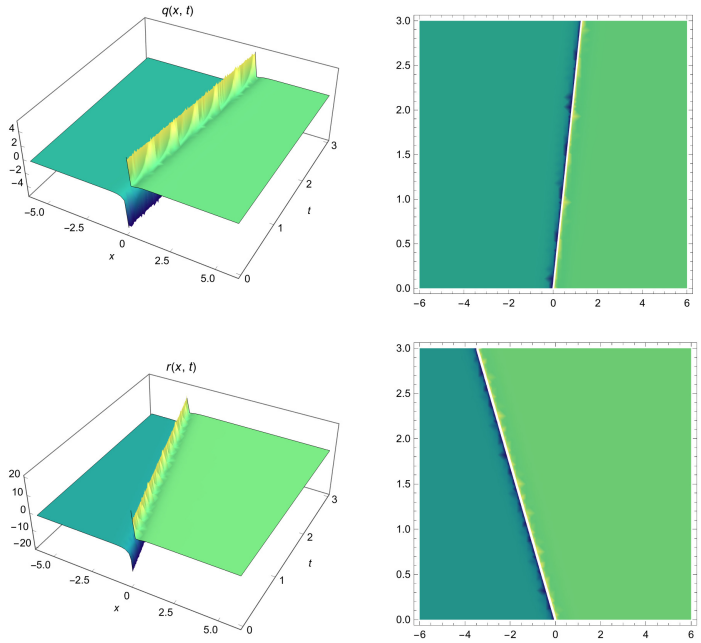

Figure 2. 3D and 2D singular traveling wave solution for the Zaremaoghaddam model which corresponds to the solutions given in equations (53). The parameter selection is: $a_1 = 0.50$, $a_2 = 2.18$, $a_3 = 2.05$, $a_4 = 1.05$, $a_5 = 0.55$, $b_1 = 1.05$, $b_2 = 0.65$, $b_3 = 5.05$, $b_4 = 5.12$, and $b_5 = 2.45$.

4. RESULTS AND DISCUSSION

The generalized exponential differential rational function (GEDRF) construction yields multiple closed-form traveling-wave families for the coupled double-layer models, including: (i) localized solitary profiles (e.g., sech^2-type), (ii) singular solitary profiles (e.g., csch^2-type and csch coth-type), and (iii) non-decaying hyperbolic growth profiles (e.g., cosh- and sinh-type). From a physical standpoint for stratified shallow-water internal modes, only the localized (finite-energy) profiles are directly compatible with the usual interpretation of solitary waves, whereas the singular and non-decaying profiles require additional discussion (Sections 4.2–4.4).

A key structural feature of several families is that the two layer variables share the *same* basic shape function of the comoving coordinate $\xi = x - p_1 t$ (up to amplitude scaling and possible additive offsets). This "shape locking" is consistent with a resonant two-mode interaction in which the interfacial displacement and the associated velocity potential components (or modal amplitudes) propagate coherently as a composite entity.

4.1. Dependence of wave shape on parameters

4.1.1. Amplitude, polarity, and background level. For each family, the solution can be written schematically as

$$q(x,t) = Q(\xi), \qquad r(x,t) = R(\xi), \qquad \xi = x - p_1 t,$$

where the *polarity* and *peak amplitude* are controlled by algebraic combinations of the free parameters appearing in the GEDRF ansatz.

Localized sech^2 family (prototype). For the Zaremaoghaddam model, a representative localized family has the form

$$q(x,t) = A_q \ \text{sech}^2(\xi), \qquad r(x,t) = A_r \ \text{sech}^2(\xi),$$

where A_q and A_r are explicit algebraic combinations of the free parameters (e.g., combinations of θ's and ω's in the reported families). In this case:

- **Amplitude scaling:** $|A_q|$ and $|A_r|$ scale linearly with the corresponding free amplitude parameters; changing the sign of A_q (resp. A_r) flips the polarity of the pulse in that layer.
- **Relative layer strength:** the ratio $\Gamma := A_r/A_q$ determines whether the two layers exhibit in-phase ($\Gamma > 0$) or out-of-phase ($\Gamma < 0$) excursions.

Offset solitary waves in the Gear–Grimshaw model. Some Gear–Grimshaw families include additive constants,

$$q(x,t) = \tilde{Q}(\xi) + q_\infty, \qquad r(x,t) = \tilde{R}(\xi) + r_\infty,$$

so that the traveling structure sits on a nonzero background state. In that setting, (q_∞, r_∞) controls the far-field equilibrium, while the localized part $(\tilde{Q}, \tilde{R})$ controls the pulse/shock component. This is important for stability because the continuous spectrum is determined by the linearization about the far-field state.

4.1.2. Width, steepness, and wave speed. In the explicit families presented, the basic width is set by the scaling chosen in the generating function (e.g., $\tanh(\xi)$, $\mathrm{sech}(\xi)$, $\mathrm{csch}(\xi)$). More generally, if one uses a scaled argument $\kappa\xi$ in the generating function, then $\kappa > 0$ controls the width: larger κ produces narrower (steeper) pulses.

The **speed** p_1 is not arbitrary; it is typically determined by the algebraic constraints that enforce exact solvability. Consequently:

- changing amplitude parameters can *also* change p_1;
- in many families, the speed is proportional to an amplitude product, producing an amplitude–velocity relation (qualitatively consistent with classical soliton theory).

This coupling between speed and amplitude is central in any stability discussion, since the derivative of an appropriate conserved quantity with respect to p_1 often enters stability criteria (see Section 4.4).

4.2. Physical realizability of singular solutions

4.2.1. Nature of the singularity. Singular families (e.g., $\mathrm{csch}^2(\xi)$, $\mathrm{csch}(\xi)\coth(\xi)$) blow up at $\xi = 0$, i.e., along the characteristic line $x = p_1 t$. In the context of two-layer shallow-water dynamics, such divergences correspond to an *unbounded* modal amplitude or slope at the interface, and therefore lie outside the strict validity range of weakly nonlinear, weakly dispersive asymptotic models. Practically, these solutions are best interpreted as:

1. **local asymptotics** describing the tendency toward gradient catastrophe (incipient breaking) in an unregularized model; or
2. **idealized limits** of sharply peaked structures that would be regularized by physics not included here (viscosity, higher-order dispersion, surface tension, finite-depth corrections, or nonhydrostatic effects).

4.2.2. Regularization viewpoints. There are three standard ways to give singular profiles a controlled physical meaning:

(i) Exclusion of the singular core: treat the solution as valid only for $|\xi| \geq \delta$ for some small $\delta > 0$, matching to a different inner solution near $\xi = 0$.

(ii) Weak/distributional interpretation: interpret the singular family as a weak solution capturing a steep-front/shock-like transition, with the understanding that additional entropy/selection mechanisms would be required to pick the physically relevant branch.

(iii) Model regularization: add physically motivated higher-order terms (e.g., fifth-order dispersion, dissipative terms) that smooth the singularity into a finite-amplitude sharply localized pulse.

In the reported numerical visualizations of singular profiles, one indeed observes extremely steep behavior near $x = p_1 t$, consistent with the above interpretation.

4.3. Comparison with classical mKdV solitons

4.3.1. Classical scalar mKdV solitary waves. Consider the classical scalar mKdV equation

$$u_t + \alpha u^2 u_x + \beta u_{xxx} = 0, \qquad \alpha\beta \neq 0, \tag{33}$$

which admits the well-known one-soliton

$$u(x,t) = \pm\sqrt{\frac{2c}{\alpha}}\ \mathrm{sech}\left(\sqrt{\frac{c}{\beta}}\,(x - ct - x_0)\right), \qquad c > 0 \text{ if } \beta > 0, \tag{34}$$

with amplitude proportional to $\sqrt{c}$ and width proportional to $1/\sqrt{c}$.

4.3.2. Differences induced by coupling and dispersion-triplet structure. The coupled double-layer models studied here extend the classical setting in two major ways:

1. **Two-component coupling:** energy can be exchanged between layers, producing locked two-field pulses (q, r) and allowing out-of-phase structures not present in scalar mKdV.
2. **Extended dispersive operator:** the mixed-derivative terms (e.g., q_{xxt} and q_{xtt}) modify the linear dispersion and may allow non-classical localized profiles (including hybrid and singular shapes) beyond the standard sech soliton in (34).

Therefore, while some families mimic classical solitons through a single-hump localized structure and amplitude–speed coupling, the catalog also contains non-classical profiles (e.g., sech^2-type or singular csch^2-type) that should be regarded as *hybrid solitary/shock-like* structures enabled by the extended ansatz and the higher-order dispersive framework.

4.4. Stability analysis

This subsection provides a linear (spectral) stability framework for the obtained traveling waves and derives explicit, checkable stability conditions for the far-field spectrum. The analysis is presented for the Zaremaoghaddam system; the Gear–Grimshaw system follows analogously.

4.4.1. Linear dispersion and well-posedness about a uniform state. Let (q_∞, r_∞) be a constant background. Linearizing the Zaremaoghaddam system about that state yields (to first order in perturbations) a pair of *uncoupled* linear dispersive equations because the nonlinear coupling terms are quadratic. In particular, about the rest state $(0, 0)$ one has

$$q_t + a_3 q_{xxx} + a_4 q_{xxt} + a_5 q_{xtt} = 0, \qquad r_t + b_3 r_{xxx} + b_4 r_{xxt} + b_5 r_{xtt} = 0.$$

Using plane waves $q \sim e^{i(kx-\omega t)}$ gives the quadratic dispersion relation

$$a_5 k\,\omega^2 + (1 - a_4 k^2)\omega - a_3 k^3 = 0, \tag{35}$$

and similarly

$$b_5 k\,\omega^2 + (1 - b_4 k^2)\omega - b_3 k^3 = 0. \tag{36}$$

A sufficient condition for *real* $\omega(k)$ for all $k \in \mathbb{R}$ (hence absence of exponential growth in the linearized constant-coefficient problem) is

$$a_3 a_5 \geq 0, \qquad b_3 b_5 \geq 0, \tag{37}$$

since then the discriminants

$$\Delta_q(k) = (1 - a_4 k^2)^2 + 4 a_3 a_5 k^4, \qquad \Delta_r(k) = (1 - b_4 k^2)^2 + 4 b_3 b_5 k^4$$

are nonnegative for all k. Condition (37) is a practical *baseline* requirement before discussing the stability of any nonlinear coherent structure.

4.4.2. Spectral problem for perturbations of a traveling wave. Let $(Q(\xi), R(\xi))$ be an exact traveling wave with $\xi = x - p_1 t$. Consider perturbed solutions

$$q(x,t) = Q(\xi) + \varepsilon u(\xi) e^{\lambda t}, \qquad r(x,t) = R(\xi) + \varepsilon v(\xi) e^{\lambda t}, \qquad 0 < \varepsilon \ll 1.$$

In the moving frame, the time derivative acts as $\partial_t \mapsto \lambda - p_1 \partial_\xi$, and one computes

$$q_t \mapsto (\lambda - p_1\partial_\xi)u, \quad q_{xxx} \mapsto \partial_\xi^3 u, \quad q_{xxt} \mapsto \partial_\xi^2(\lambda - p_1\partial_\xi)u, \quad q_{xtt} \mapsto \partial_\xi(\lambda - p_1\partial_\xi)^2 u,$$

and similarly for r.

Linearizing the nonlinear terms gives

$$q^2 q_x \mapsto Q^2 u' + 2QQ'u, \qquad r^2 q_x \mapsto R^2 u' + 2RR'v,$$
$$r^2 r_x \mapsto R^2 v' + 2RR'v, \qquad q^2 r_x \mapsto Q^2 v' + 2QQ'u,$$

where $' = \partial_\xi$. Thus the eigenvalue problem takes the compact quadratic-pencil form

$$\Big(\mathcal{A}_2\lambda^2 + \mathcal{A}_1\lambda + \mathcal{A}_0\Big)\begin{pmatrix} u \\ v \end{pmatrix} = 0, \tag{38}$$

where $\mathcal{A}_2, \mathcal{A}_1, \mathcal{A}_0$ are matrix differential operators in ξ determined by (Q, R) and the model coefficients. Explicitly, the q-equation component reads

$$0 = (\lambda - p_1\partial_\xi)u + a_3 u''' + a_4\partial_\xi^2(\lambda - p_1\partial_\xi)u + a_5\partial_\xi(\lambda - p_1\partial_\xi)^2 u$$

$$+ a_1\big(Q^2u' + 2QQ'u\big) + a_2\big(R^2u' + 2RR'v\big), \tag{39}$$

and the r-equation component is

$$\begin{aligned} 0 = {} & (\lambda - p_1\partial_\xi)v + b_3v''' + b_4\partial_\xi^2(\lambda - p_1\partial_\xi)v + b_5\partial_\xi(\lambda - p_1\partial_\xi)^2v \\ & + b_1\big(R^2v' + 2RR'v\big) + b_2\big(Q^2v' + 2QQ'u\big). \end{aligned} \tag{40}$$

A traveling wave is **spectrally stable** if the spectrum of (38) satisfies $\Re(\lambda) \le 0$.

Neutral translation mode. Because the governing PDEs are translation invariant in x, the derivative $(u, v) = (Q', R')$ always produces a neutral eigenfunction at $\lambda = 0$:

$$\Big(\mathcal{A}_0\Big)\begin{pmatrix} Q' \\ R' \end{pmatrix} = 0.$$

Hence $\lambda = 0$ is generically present in the point spectrum (simple under nondegeneracy conditions), and stability means there are *no* eigenvalues with $\Re(\lambda) > 0$.

4.4.3. Essential spectrum and a far-field stability criterion. Assume the traveling wave is localized about a constant state, i.e.,

$$(Q(\xi), R(\xi)) \to (q_\infty, r_\infty) \quad \text{as} \quad |\xi| \to \infty.$$

Then the coefficients in (39)–(40) tend to constants, and the far-field eigenvalue problem is diagonal to leading order. Substituting Fourier modes $(u, v) \sim e^{ik\xi}$ yields the far-field (essential-spectrum) relations

$$(\lambda + ip_1k)\,(1 + a_4k^2) + ia_3k^3 + ia_5k\,(\lambda + ip_1k)^2 = 0, \tag{41}$$

$$(\lambda + ip_1k)\,(1 + b_4k^2) + ib_3k^3 + ib_5k\,(\lambda + ip_1k)^2 = 0. \tag{42}$$

Equations (41)–(42) provide a *checkable* necessary condition for spectral stability: for each real k, all roots $\lambda(k)$ must satisfy $\Re(\lambda(k)) \le 0$. A sufficient practical condition ensuring that the essential spectrum remains on (or to the left of) the imaginary axis is:

$$a_3a_5 \ge 0, \quad b_3b_5 \ge 0, \quad 1 + a_4k^2 > 0, \quad 1 + b_4k^2 > 0 \quad \forall k \in \mathbb{R}, \tag{43}$$

which prevents ill-posedness and avoids sign changes in the effective far-field "mass" factors $(1 + a_4k^2)$ and $(1 + b_4k^2)$ that can trigger high-wavenumber instabilities.

4.4.4. Point spectrum and stability of localized pulses: energy-index viewpoint. The remaining (discrete) spectrum of (38) depends on the localized potentials QQ', RR', Q^2, R^2 and requires an index argument.

For coherent structures generated as solitary critical points of an augmented functional

$$\mathcal{F}[q, r] = \mathcal{H}[q, r] + p_1\,\mathcal{P}[q, r],$$

(where $\mathcal{H}$ is an energy/Hamiltonian and $\mathcal{P}$ is the momentum associated with translation invariance), the Grillakis–Shatah–Strauss philosophy predicts orbital stability when the second variation $\delta^2\mathcal{F}$ has exactly one negative direction and a simple kernel spanned by (Q', R'), together with a *slope condition* (a generalized Vakhitov–Kolokolov condition)

$$\frac{d}{dp_1}\mathcal{P}[Q_{p_1}, R_{p_1}] \ne 0, \qquad \text{with sign determining stability branch.} \tag{44}$$

In practice, for the present double-layer setting, (44) is evaluated on the explicit families by computing $\mathcal{P}$ as a function of the parameters through (Q, R) and p_1 (recall p_1 is itself constrained algebraically). This provides an analytically tractable stability diagnostic because the integrals of sech^m profiles are closed form.

Concrete diagnostic for sech^2-type localized pulses. For a representative localized pulse of the form

$$Q(\xi) = A_q\,\mathrm{sech}^2(\kappa\xi), \qquad R(\xi) = A_r\,\mathrm{sech}^2(\kappa\xi),$$

one may use the quadratic momentum proxy

$$\mathcal{P}_2 = \frac{1}{2}\int_{-\infty}^{\infty}\big(Q^2 + R^2\big)\,d\xi = \frac{1}{2}(A_q^2 + A_r^2)\int_{-\infty}^{\infty}\mathrm{sech}^4(\kappa\xi)\,d\xi = \frac{(A_q^2 + A_r^2)}{3\kappa}.$$

Thus, if κ is fixed by the family scaling, the monotonicity of $\mathcal{P}_2$ with respect to p_1 reduces to the monotonicity of $A_q^2 + A_r^2$ with respect to p_1 through the algebraic constraints. A positive slope $\frac{d}{dp_1}\mathcal{P}_2 > 0$ is typically associated with the stable branch in Hamiltonian dispersive systems, while a negative slope signals an instability exchange.

4.4.5. Instability mechanisms for singular and non-decaying families. Finally, two generic instability mechanisms are expected for the non-regular families:

- **Singular families:** the blow-up at $\xi = 0$ implies infinite L^2 norm and breakdown of standard energy methods; linearization about a singular profile typically yields non-self-adjoint operators with spectrum extending into $\Re(\lambda) > 0$, so these waves are best viewed as *nonlinearly unstable* idealizations unless regularized.
- **Non-decaying** cosh/sinh **families:** these do not approach a finite far-field equilibrium, so the essential spectrum is not defined in the usual solitary-wave sense; physically, such profiles correspond to nonlocalized excitations or boundary-driven responses rather than freely propagating solitary waves.

4.5. Summary of implications

Overall, the explicit solution catalog demonstrates that (i) coherent two-layer traveling structures exist in multiple morphologies, (ii) only the localized finite-energy families are directly consistent with solitary-wave propagation in stratified fluids, (iii) singular solutions should be interpreted as limiting/shock-like objects requiring regularization, and (iv) a rigorous stability assessment reduces to the spectral analysis of the quadratic pencil (38), with immediate far-field admissibility conditions given by (43) and point-spectrum diagnostics accessible via the explicit parameter dependence of integral invariants such as $\mathcal{P}_2$.

5. CONCLUSIONS

The paper recovered solitary waves, shock waves and their combination thereof for double layered shallow water flow. Two of the models out of very many such models, have been addressed in this paper. They are Zaremaoghaddam model and the Gear–Grimshaw model. The basic platform is the mKdV equation and therefore the current work is a continuation or a follow–up of the previously reported work that has KdV equation as its basic platform. The adopted integration algorithm was the generalized exponential differential rational function approach. This algorithm revealed various hybrid forms of solitary waves, shock waves and singular solitary waves. An obvious drawback is that the integration scheme failed to reveal single–standing waves such as solitary waves or singular solitary waves or shock waves. For retrieving such single–standing waves one must resort to additional integration approaches. The results from such research activities will be disseminated in future.

A. ADDITIONAL SOLUTION FAMILIES FOR MODEL (1)

Family–IV

Upon embedding $[R_1, R_2, R_3, R_4] = [1, 1, 1, -1]$ and $[S_1, S_2, S_3, S_4] = [1, -1, 1, -1]$ in equation (7), we obtain

$$\mathcal{T}(\tau) = \coth(\tau). \tag{45}$$

By making substitution of (45) in (10) for equation (9), coefficient values are procured as:

$$\begin{aligned} &a_1 = b_2,\ a_2 = -\frac{b_2{\theta_1}^2}{{\theta_2}^2}, a_3 = -\frac{4b_2{\theta_1}^2\omega_2\left(4\,a_5 b_2\omega_2{\theta_1}^2 + a_4\theta_2\right)}{{\theta_2}^2},\\ &b_1 = -\frac{b_2{\theta_1}^2}{{\theta_2}^2}, b_3 = -\frac{4b_2\omega_2{\theta_1}^2\left(4\,b_2 b_5\omega_2{\theta_1}^2 + b_4\theta_2\right)}{{\theta_2}^2},\\ &\omega_1 = -\frac{\theta_1\omega_2}{\theta_2},\ p_1 = -\frac{4b_2{\theta_1}^2\omega_2}{\theta_2},\ \theta_0 = 0,\ \theta_3 = 0. \end{aligned} \tag{46}$$

having $a_4,\ a_5,\ b_4,\ b_5,\ b_2,\ \omega_2,\ \theta_2,\ \theta_1$ as free parameters.

Accordingly, newly generated solution of equation (1) is presented with the help of equation (45) and (46) as follows:

$$\begin{aligned} q(x,t) &= -\theta_1\big(\operatorname{csch}(x - p_1 t)\big)^2 + \frac{\theta_1\omega_2}{\theta_2\big(\operatorname{csch}(x - p_1 t)\big)^2},\\ r(x,t) &= -\theta_2\big(\operatorname{csch}(x - p_1 t)\big)^2 - \frac{\omega_2}{\big(\operatorname{csch}(x - p_1 t)\big)^2}. \end{aligned} \tag{47}$$

Family–V

Upon embedding $[R_1, R_2, R_3, R_4] = [1, 1, 1, -1]$ and $[S_1, S_2, S_3, S_4] = [0, 0, 1, -1]$ in equation (7), we obtain

$$\mathcal{T}(\tau) = \operatorname{csch}(\tau). \tag{48}$$

Putting (48) in (10) for equation (9), following parameter values are obtained:

$$\begin{aligned} &a_1 = b_2,\ a_2 = -\frac{b_2{\theta_1}^2}{{\theta_2}^2}, a_3 = -\frac{4b_2\omega_2{\theta_1}^2\left(4\,a_5b_2\omega_2{\theta_1}^2 + a_4\theta_2\right)}{{\theta_2}^2},\\ &b_1 = -\frac{b_2{\theta_1}^2}{{\theta_2}^2},\ b_3 = -\frac{4b_2\omega_2{\theta_1}^2\left(4\,b_2b_5\omega_2{\theta_1}^2 + b_4\theta_2\right)}{{\theta_2}^2},\\ &\omega_1 = -\frac{\omega_2\theta_1}{\theta_2},\ p_1 = -\frac{4b_2\omega_2{\theta_1}^2}{\theta_2},\ \theta_0 = 0,\ \theta_3 = 0. \end{aligned} \tag{49}$$

having $a_4,\ a_5,\ b_4,\ b_5,\ b_2,\ \omega_2,\ \theta_2,\ \theta_1$ as arbitrary constants.

Thus, using equations (48) and (49), the newly generated solution of equation (1) is shown as follows:

$$\begin{aligned} q(x,t) &= -\theta_1\,\mathrm{csch}(x-p_1t)\coth(x-p_1t) + \frac{\omega_2\theta_1}{\theta_2\,\mathrm{csch}(x-p_1t)\coth(x-p_1t)},\\ r(x,t) &= -\theta_2\,\mathrm{csch}(x-p_1t)\coth(x-p_1t) - \frac{\omega_2}{\mathrm{csch}(x-p_1t)\coth(x-p_1t)}. \end{aligned} \tag{50}$$

Family–VI

Upon embedding $[R_1, R_2, R_3, R_4] = [1, 1, 1, 1]$ and $[S_1, S_2, S_3, S_4] = [0, 0, 1, -1]$ in equation (7), we obtain

$$\mathcal{T}(\tau) = \mathrm{sech}(\tau). \tag{51}$$

Putting (51) in (10) for equation (9), following parameter values are obtained:

$$\begin{aligned} &a_1 = b_2,\ a_2 = -\frac{b_2{\theta_1}^2}{{\theta_2}^2},\ a_3 = -\frac{4b_2\omega_2{\theta_1}^2\left(4\,a_5b_2\omega_2{\theta_1}^2 + a_4\theta_2\right)}{{\theta_2}^2},\\ &b_1 = -\frac{b_2{\theta_1}^2}{{\theta_2}^2},\ b_3 = -\frac{4b_2\omega_2{\theta_1}^2\left(4\,b_2b_5\omega_2{\theta_1}^2 + b_4\theta_2\right)}{{\theta_2}^2},\\ &\omega_1 = -\frac{\omega_2\theta_1}{\theta_2},\ p_1 = -\frac{4b_2\omega_2{\theta_1}^2}{\theta_2},\ \theta_0 = 0,\ \theta_3 = 0. \end{aligned} \tag{52}$$

having $a_4,\ a_5,\ b_4,\ b_5,\ b_2,\ \omega_2,\ \theta_2,\ \theta_1$ as arbitrary parameters.

As a result, using (51) and (52), the new soliton solution of equation (1) is written as:

$$\begin{aligned} q(x,t) &= -\theta_1\,\mathrm{sech}(x-p_1t)\tanh(x-p_1t) + \frac{\omega_2\theta_1}{\theta_2\,\mathrm{sech}(x-p_1t)\tanh(x-p_1t)},\\ r(x,t) &= -\theta_2\,\mathrm{sech}(x-p_1t)\tanh(x-p_1t) - \frac{\omega_2}{\mathrm{sech}(x-p_1t)\tanh(x-p_1t)}. \end{aligned} \tag{53}$$

A. ADDITIONAL SOLUTION FAMILIES FOR MODEL (2)

Family–IV

$$\begin{aligned} q(x,t) &= -\frac{\omega_1\theta_4\big(\mathrm{csch}(x-p_1t)\big)^2}{\omega_4} - \frac{\omega_1}{\big(\mathrm{csch}(x-p_1t)\big)^2} + \theta_0,\\ r(x,t) &= -\theta_4\big(\mathrm{csch}(x-p_1t)\big)^2 - \frac{\omega_4}{\big(\mathrm{csch}(x-p_1t)\big)^2} + \theta_5. \end{aligned} \tag{54}$$

Family–V

$$\begin{aligned} q(x,t) &= -\frac{\omega_1\theta_4\,\mathrm{csch}\,(x-p_1t)\coth\,(x-p_1t)}{\omega_4} - \frac{\omega_1}{\mathrm{csch}\,(x-p_1t)\coth\,(x-p_1t)} + \theta_0,\\ r(x,t) &= -\theta_4\,\mathrm{csch}\,(x-p_1t)\coth\,(x-p_1t) - \frac{\omega_4}{\mathrm{csch}\,(x-p_1t)\coth\,(x-p_1t)} + \theta_5. \end{aligned} \tag{55}$$

Family–VI

$$q(x,t) = -\frac{\omega_1\theta_4 \operatorname{sech}(x-p_1t)\tanh(x-p_1t)}{\omega_4} - \frac{\omega_1}{\operatorname{sech}(x-p_1t)\tanh(x-p_1t)} + \theta_0,$$
$$r(x,t) = -\theta_4 \operatorname{sech}(x-p_1t)\tanh(x-p_1t) - \frac{\omega_4}{\operatorname{sech}(x-p_1t)\tanh(x-p_1t)} + \theta_5. \tag{56}$$

Acknowledgements

This work of the last author (AB) was supported from the budget of Grambling State University for the Endowed Chair of Mathematics. The author thankfully acknowledges this support.

Author contributions

All authors contributed to the study conception and design. Material preparation, data collection, review & editing, analysis and result interpretation were performed by [O. González-Gaxiola], [Husham M. Ahmed], [Haitham Alqahtani], and [Ahmed H. Arnous]. The first draft of the manuscript was written by [Lakhveer Kaur] and [Anjan Biswas]. All authors commented on previous versions of the manuscript. The final manuscript was read and approved by all writers.

Funding

The authors confirm that they did not receive any financial, grant, or other forms of help during the preparation of this manuscript.

Data availability

The article contains all the information required to comprehend the results of this investigation.

Declarations

Conflict of interest

We are ignorant of any financial conflicts of interest or personal relationships that could have potentially impacted the research described in this article.

ORCID

Lakhveer Kaur, https://orcid.org/0000-0002-1936-474X; **O. González–Gaxiola**, https://orcid.org/0000-0003-3317-9820; **Ahmed H. Arnous**, https://orcid.org/0000-0002-7699-7068; **Husham M. Ahmed**, https://orcid.org/0009-0003-6093-2010; **Haitham Alqahtani**, https://orcid.org/0009-0009-0817-4746; **Anjan Biswas**, https://orcid.org/0000-0002-8131-6044

REFERENCES

[1] A. Biswas, N. Coleman, A. H. Kara, S. Khan, L. Moraru, S. Moldovanu, C. Iticescu & Y. Yıldırım, "Shallow water waves and conservation laws with dispersion triplet," Applied Sciences, **12**, 3647 (2022). https://doi.org/10.3390/app12073647

[2] R. I. Joseph & R. Egri, "Another possible model equation for long waves in nonlinear dispersive systems," Physics Letters A, **61**(7), 429–430 (1977). https://doi.org/10.1016/0375-9601(77)90739-3

[3] L. Kaur, O. M. K. Al–Dulaimi, F. M. Mohammed, A. J. M. Jawad, M. Abdelkawy, O. González–Gaxiola, A. H. Arnous & A. Biswas, "Solitary waves and shock waves for double–layered fluid flow with dispersion–triplet: Zaremaoghaddam and Gear–Grimshaw models (KdV equation)," Beni-Suef University Journal of Basic and Applied Sciences, **14**, 95 (2025). https://doi.org/10.1186/s43088-025-00679-x

[4] A. Chertock, A. Kurganov, Z. Qu & T. Wu, "Three-layer approximation of two-layer shallow water equations," Mathematical Modelling and Analysis, **18**(5), 675–693 (2013). https://doi.org/10.3846/13926292.2013.869269

[5] U. S. Fjordholm, "Energy conservative and stable schemes for the two-layer shallow water equations," in: *Hyperbolic Problems, Series in Contemporary Applied Mathematics*, (World Scientific, 2012), pp. 414–421. https://doi.org/10.1142/9789814417099_0039

[6] Y. S. Kivshar & B. A. Malomed, "Dynamics of solitons in nearly integrable systems," Reviews of Modern Physics, **61**(4), 763–915 (1989). https://doi.org/10.1103/RevModPhys.61.763

[7] H. Zaremaoghaddam, "Analytic study for solving coupled KdV equations," Middle-East Journal of Scientific Research, **7**(6), 1061–1064 (2011). https://idosi.org/mejsr/mejsr7(6)11/36.pdf

[8] A. Biswas, E. V. Krishnan, P. Suarez, A. H. Kara & S. Kumar, "Solitary waves and conservation laws of Bona–Chen equations," Indian Journal of Physics, **87**(2), 169–175 (2013). https://doi.org/10.1007/s12648-012-0208-x

[9] N. A. Kudryashov & D. I. Sinelshchikov, "A note on the Lie symmetry analysis and exact solutions for the extended mKdV equation," Acta Applicandae Mathematicae, **113**(1), 41–44 (2011). https://doi.org/10.1007/s10440-010-9582-6

[10] C. S. Liu, "Applications of complete discrimination system for polynomial for classifications of traveling wave solutions to nonlinear differential equations," Computer Physics Communications, **181**(2), 317–324 (2010). https://doi.org/10.1016/j.cpc.2009.10.006

[11] A. D. Polyanin & N. A. Kudryashov, "Nonlinear Schrödinger equations with delay: closed–form and generalized separable solutions," Contemporary Mathematics, **5**(4), 5783–5794 (2024).

[12] X. Y. Tang & S. Y. Lou, "Extended multilinear variable separation approach and multivalued localized excitations for some (2+1)–dimensional integrable systems," Journal of Mathematical Physics, **44**, 4000–4025 (2003). https://doi.org/10.1063/1.1598619

[13] H. Triki, A. H. Kara, A. Bhrawy & A. Biswas, "Soliton solution and conservation law of Gear–Grimshaw model for shallow water waves," Acta Physica Polonica A, **125**(5), 1099–1106 (2014). https://doi.org/10.12693/APhysPolA.125.1099

[14] A. M. Wazwaz, "Multiple soliton solutions and other scientific solutions for a new Painlevé integrable fifth–order equation," Chaos, Solitons & Fractals, **196**, 116307 (2025). https://doi.org/10.1016/j.chaos.2025.116307

[15] A. E. Green & P. M. Naghdi, "A derivation of equations for wave propagation in water of variable depth," Journal of Fluid Mechanics, **78**(2), 237–246 (1976). https://doi.org/10.1017/S0022112076002425

[16] D. Lannes, *The Water Waves Problem: Mathematical Analysis and Asymptotics*, Mathematical Surveys and Monographs, Vol. 188, (American Mathematical Society 2013).

[17] V. Duchêne, S. Israwi & R. Talhouk, "A new class of two-layer Green–Naghdi systems with improved frequency dispersion," Studies in Applied Mathematics, **137**(3), 356–415 (2016). https://doi.org/10.1111/sapm.12125

[18] V. Duchêne & S. Israwi, "Well-posedness of the Green–Naghdi and Boussinesq–Peregrine systems," Annales Mathématiques Blaise Pascal, **25**(1), 21–74 (2018). https://dx.doi.org/10.5802/ambp.372

[19] W. Choi & R. Camassa, "Fully nonlinear internal waves in a two-fluid system," Journal of Fluid Mechanics, **396**, 1–36 (1999). https://doi.org/10.1017/S0022112099005820

[20] R. Grimshaw, "Internal solitary waves," in: *Solitary Waves in Fluids* (Kluwer Academic Publishers, 2006), pp. 1–27.

[21] W. Craig, P. Guyenne & C. Sulem, "Coupling between internal and surface waves," Natural Hazards, **57**(3), 617–642 (2011). https://doi.org/10.1007/s11069-010-9535-4

[22] J. Boschan, M. Vincze, I. M. Jánosi & T. Tél, "Nonlinear resonance in barotropic–baroclinic transfer generated by bottom sills," Physics of Fluids, **24**(4), 046601 (2012). https://doi.org/10.1063/1.3699062

[23] J. Colliander, M. Keel, G. Staffilani, H. Takaoka & T. Tao, "Sharp global well-posedness for KdV and modified KdV on $\mathbb{R}$ and $\mathbb{T}$," Journal of the American Mathematical Society, **16**(3), 705–749 (2003). https://doi.org/10.1090/S0894-0347-03-00421-1

[24] A. Karasu-Kalkanlı, A. Karasu, A. Sakovich, S. Sakovich & R. Turhan, "A new integrable generalization of the Korteweg–de Vries equation," Journal of Mathematical Physics, **49**(7), 073516 (2008). https://doi.org/10.1063/1.2953474

[25] W. Ma, "Long-time asymptotics of a three-component coupled mKdV system," Mathematics, **7**(7), 573 (2019). https://doi.org/10.3390/math7070573

[26] M. A. Alejo, "Higher order mKdV breathers," Proyecciones (Antofagasta), **43**(2), 495–520 (2024). https://doi.org/10.22199/issn.0717-6279-6048

[27] M. Abdou, "The extended F-expansion method and its application for a class of nonlinear evolution equations," Chaos, Solitons & Fractals, **31**(1), 95–104 (2005). https://doi.org/10.1016/j.chaos.2005.09.030

[28] H. Zhang & W. Ma, "Extended transformed rational function method and applications to complexiton solutions," Applied Mathematics and Computation, **230**, 509–515 (2014). https://doi.org/10.1016/j.amc.2013.12.156

[29] A. Zafar, "Rational exponential solutions of conformable space-time fractional equal-width equations," Nonlinear Engineering, **8**(1), 350–355 (2018). https://doi.org/10.1515/nleng-2018-0076

[30] M. Shakeel, Attaullah, E. R. El-Zahar, N. A. Shah & J. D. Chung, "Generalized Exp-Function method to find closed form solutions of nonlinear dispersive modified Benjamin–Bona–Mahony equation defined by seismic sea waves," Mathematics, **10**(7), 1026 (2022). https://doi.org/10.3390/math10071026

ГІБРИДНІ ОДИНОКІ ХВИЛІ ТА УДАРНІ ХВИЛІ ДЛЯ ДВОСТАРОВОГО ПОТОКУ РІДИНИ З ТРИПЛЕТОМ ДИСПЕРСІЇ: МОДЕЛІ ЗАРЕМАОГАДДАМА ТА ГІРА-ГРІМШОУ (РІВНЯННЯ mKdV)

Лаквір Каур[1], **О. Гонзалес–Гаксіола**[2], **Ахмед Х. Арнус**[3,4], **Хушам М. Ахмед**[5], **Хайтам Алкахтані**[5], **Анджан Бісвас**[6,7,8,9]

[1]*Кафедра математики, Інститут інформаційних технологій Джайпі, Нойда–201304, Індія*

[2]*Кафедра прикладної математики та систем, Університет Аутонома Метрополіта–Куахімальпа, Васко де Кірога 4871, 05348, Мехіко, Мексика*

[3]*Кафедра математичних наук, Інженерна школа Саветха, SIMATS, Ченнаї - 602105, Тамілнад, Індія*

[4]*Дослідницький центр прикладної математики, Університет Хазар, Баку, Аризона 1096, Азербайджан*

[5]*Інженерний коледж, Технологічний університет Бахрейну, Королівство Бахрейн*

[6]*Кафедра математики та фізики, Державний університет Грамблінга, Грамблінг, Луїзіана 71245—2715, США*

[7]*Кафедра фізики та електроніки, Університет Хазар, Баку, Аризона—1096, Азербайджан*

[8]*Кафедра математики та прикладної математики, Університет медичних наук Сефако Макгатхо, Медунса—0204, Преторія, Південна Африка*

[9]*Науково-дослідний центр прикладних наук, Приватний університет прикладних наук, Амман—11937, Йорданія*

У цій статті відновлено гібридні поодинокі хвилі для двошарових хвиль на мілководді, базовою платформою яких є рівняння mKdV. Вибраними моделями є рівняння Заремаогаддама та рівняння Гіра-Грімшоу. Використаний алгоритм інтегрування — узагальнений метод експоненціальної диференціальної функції. Це призводить до гібридних хвиль, що виникають з одиночних хвиль, ударних хвиль та одиночних одиночних хвиль. Критерії існування таких хвиль також представлені як обмеження параметрів.
Ключові слова: *рівняння mKdV; гібрид; інтегрованість; обмеження параметрів; рівняння Гіра–Грімшоу*

EAST EUROPEAN JOURNAL OF PHYSICS. 1. 105-111 (2026)
DOI:10.26565/2312-4334-2026-1-08 ISSN 2312-4334

NONLINEAR SELF-FOCUSING OF q-GAUSSIAN LASER BEAMS IN PLASMA WITH RELATIVISTIC AND PONDEROMOTIVE EFFECTS UNDER LINEAR ABSORPTION

Keshav Walia[1‡], Nisha Singh Rathore[2], Vinit Kakkar[3], Deepak Tripathi[4*]
[1]*Department of Physics, DAV University Jalandhar, Punjab, India*
[2]*Department of Applied Sciences, KCC Institute of Technology and Management, Greater Noida, India*
[3]*Department of Physics, Lotus Valley International School, Sector-50, Gurgaon, India*
[4]*Physics Department, USAR/USBS, Guru Gobind Singh Indraprastha University, East Delhi Campus, Delhi, India-110032*
**Corresponding author e-mail: deepakkrt@gmail.com*; *[‡]keshavwalia86@gmail.com*
Received January 9, 2026; revised February 8, 2026; accepted February 15, 2026

The current study presents a theoretical analysis of the nonlinear self-focusing of a q-Gaussian laser beam propagating through an unmagnetized plasma, incorporating the simultaneous effects of relativistic mass variation and the ponderomotive mechanism. Linear absorption is also included to account for energy dissipation during beam propagation. By applying WKB and paraxial approximations, the problem is reduced to 2nd order differential equation that governs the evolution of the laser beam width as a function of the normalized propagation distance. The resulting equation is solved numerically using 4th order Runge-Kutta method. A systematic analysis is performed to examine the effect of laser intensity, plasma density, absorption coefficient, q-parameter, and initial beam radius on the self-focusing dynamics of a q-Gaussian laser beam. These findings indicate that laser-plasma parameters substantially affect beam dynamics and critically govern the self-focusing process.
Keywords: *Laser-plasma interaction; q-Gaussian beam; Nonlinear self-focusing; Absorption coefficient; Nonlinear dynamics*
PACS: 52.38.Hb, 52.35.Mw, 52.38.Dx

1. INTRODUCTION

The sustained interest has been attracted by laser-plasma interaction in view of its vital role in diverse range of applications including ionospheric modification, charged particle acceleration, laser-driven fusion and nonlinear radiation generation [1-10]. The ability of laser beams to transit through plasma decides efficiency of all these applications. Much deeper penetration of laser beams through plasma media causes beam narrowing, which further causes enhancement in energy confinement and improvement in transfer of laser energy to plasma. However, the natural beam's diffraction imposes fundamental limitation on their transition through plasma environment. Self-focusing provides an effective mechanism to counteract diffraction during laser beam transition through plasma. Under intense laser irradiation, there is excitation of several nonlinear phenomenon including self-focusing, filamentation, and parameteric instabilities [11-19]. Among these nonlinear effects, the central role is played by self-focusing as it directly governs beam confinement and greatly influences the growth of other nonlinear processes. The concept of nonlinear refraction and the possibility of self-focusing of an intense electromagnetic wave was provided by Askar'yan [20]. Since then, theoretical/experimental researchers have extensively explored this phenomenon in view of its importance in nonlinear optics and plasma dynamics [21-32]. It has been demonstrated from numerous investigations that self-focusing critically governs overall behavior of laser-plasma interaction [33-36]. Self-focusing causes contraction of laser beam's transverse dimensions, thereby causing strong localization of intensity. This enhanced localization may disrupt beam uniformity, which is undesirable in applications such as laser-driven fusion. Therefore, achieving effective control over beam transition through plasma is mandatory in order to optimize energy coupling and attaining high energy gain. The first experiment observation of self-focusing was reported by Akhmanov et al. [37], followed by comprehensive studies by Sodha et al. in plasmas, dielectrics, and semiconductors [38-39]. In plasmas, self-focusing occurs due to intensity dependent variations of effective dielectric permittivity, leading to significant changes in plasma optical properties. These changes mainly originate from three mechanisms: ponderomotive, thermal, and relativistic nonlinearities. The ponderomotive self-focusing was first time introduced by Hora [40], who successfully derived critical power condition by balancing ponderomotive and hydrostatic forces. The ponderomotive force expels electrons from high intensity regions, producing plasma density depressions and corresponding reduction in local plasma frequency [41]. The density redistribution alters the plasma dielectric function and leads to self-focusing. Relativistic self-focusing becomes significant at ultra-high laser intensities, where electrons attain relativistic velocities. The associated relativistic mass increase modifies plasma frequency and dielectric permittivity, resulting in intensity dependent refractive index and enhanced beam focusing. Despite extensive studies, relativistic and ponderomotive nonlinearities are often treated separately, although both may exist depending on laser pulse duration. Relativistic effects dominate for $\tau < \tau_e$, whereas for $\tau_e < \tau < \tau_i$, both mechanisms act simultaneously. Here, τ is time scale of laser-plasma interaction, τ_e and τ_i correspond to electron and ion response times. Ponderomotive nonlinearity complements relativistic effects, enhancing self-focusing and plasma density perturbations. Mostly earlier investigations

Cite as: K. Walia, N.S. Rathore, V. Kakkar, D. Tripathi, East Eur. J. Phys. 1, 105 (2026), https://doi.org/10.26565/2312-4334-2026-1-08

of laser-plasma interactions have employed conventional Gaussian beam profiles. The q-Gaussian laser beams form an important class characterized by the irradiance distribution $f(r) = f(0)\left(1 + \frac{r^2}{qr_0^2}\right)^{-q}$, which reduces to the standard Gaussian profile in the limit $q->\infty$. Here, $f(r)$ is radial profile of laser beam amplitude and $f(0)$ is beam's peak value at $r = 0$. The q-Gaussian beams possess lower total power then Gaussian beams and exhibit distinct propagation features, making them suitable for controlled nonlinear interaction studies. The main origin of q-Gaussian profile is from q-Gaussian distribution which was derived in non-extensive statistical mechanics by Tsallis [42]. In laser-plasma interaction, this form has been adopted by many authors for modeling high power beams transiting through nonlinear plasma media. Motivated by these considerations, the present research investigates nonlinear self-focusing of q-Gaussian laser beams propagating in unmagnetized plasma under the combined influence of relativistic and ponderomotive nonlinearities, with linear absorption included to account for energy dissipation. The organization of paper is as follows: Section 2 presents theoretical formulation, where the paraxial and WKB approximations are employed to derive 2nd order differential equation governing the beam width. Section 3 discusses numerical results and their physical implications; the main conclusions are summarized in Section 4.

2. NONLINEAR EVOLUTION OF BEAM SPOT SIZE

A laser beam with q-Gaussian intensity profile is assumed to be propagating along z-axis in unmagnetized plasma. One can describe the beam intensity at the initial plane $(z = 0)$ by

$$E_0 \cdot E_0^*|_{z=0} = E_{00}^2\left(1 + \frac{r^2}{qr_0^2}\right)^{-q} \tag{1}$$

Where, r_0 represents initial beam radius, E_0 is the complex field amplitude, and E_{00} denotes field amplitude along the beam axis. The beam profile and decay behavior of its tails are governed by the q-parameter. This q-parameter is helpful in distinguishing a q-Gaussian beam from conventional beams. During the transition of the beam through propagation axis $(z > 0)$, its intensity distribution behaves according to equation,

$$E_0 \cdot E_0^* = \frac{E_{00}^2}{f^2}\left(1 + \frac{r^2}{qr_0^2 f^2}\right)^{-q}. \tag{2}$$

Where f denotes beam waist evolution, describing focusing/defocusing of beam during its transition through plasma. Eq.(2) provides complete description of energy distribution of q-Gaussian beam along propagation axis. Maxwell's equation can be used to derive fundamental equation governing propagation of an electromagnetic wave in plasma medium. Faraday's law and Ampere's law can be combined to obtain following wave equation for electric field of laser beam as

$$\nabla^2 E - \nabla(\nabla \cdot E) + \frac{\omega^2}{c^2}\varepsilon E = 0. \tag{3}$$

In Eq.(3), ε represents the effective dielectric response of plasma, ω is angular frequency of incident radiation, and c is speed of light in vacuum. The second term on LHS, $\nabla(\nabla \cdot E)$ arises on account of possible spatial variation in dielectric function of plasma. However, for a slowly varying and weakly inhomogeneous medium, a negligible contribution is made by this term towards overall beam dynamics. This approximation remains valid provided $\frac{c^2}{\omega^2}\left|\frac{1}{\varepsilon}\nabla^2 \ln \varepsilon\right| \leq 1$ condition is satisfied. As a result, $\nabla(\nabla \cdot E)$ term can be safely neglected. So, Eq. (3) reduces to

$$\nabla^2 E + \frac{\omega^2}{c^2}\varepsilon E = 0. \tag{4}$$

The transition of high intensity electromagnetic wave through plasma medium causes strong nonlinear behavior of electron dynamics. In such regimes, electrons simultaneously experience relativistic mass enhancement, due to their large quiver velocities, and the ponderomotive force which arises from spatial gradient in electromagnetic field intensity. The combined action of these two mechanisms is referred to as relativistic ponderomotive force (RP force). The electrons are driven away from strong laser intensity regions due to this RP force, thereby causing redistribution of charge density and corresponding modification of optical properties of plasma. The RP force acting on an electron in an intense laser field is given by [43-45]

$$F_{pe} = -m_0 c^2 \nabla(\gamma - 1). \tag{5}$$

Where, m_0, c and γ correspond to electron rest mass, speed of light in vacuum and Lorentz relativistic factor respectively. At sufficiently high laser intensities, electron quiver motion becomes relativistic, resulting in a Lorentz factor that explicitly depends on local electromagnetic field amplitude. It may be expressed as $\gamma = \sqrt{1 + \alpha E E^*}$ with $\alpha = \frac{e^2}{m_0^2 c^2 \omega_0^2}$ representing the nonlinear coefficient. As a direct consequence of RP force, electrons are expelled from high intensity regions of the beam, resulting in a local depletion of electron density. This density modification plays a

crucial role in determining plasma's dielectric response. Accounting for both relativistic mass variation and ponderomotive density redistribution, the effective dielectric function of plasma can be written as [43-45]

$$\varepsilon = 1 - \frac{\omega_p^2}{\gamma\omega^2} exp\left(-\frac{m_0c^2}{T_e}(\gamma - 1)\right). \tag{6}$$

Where $\omega_p = \sqrt{\frac{4\pi N_0 e^2}{m_0}}$ is electron plasma frequency corresponding to unperturbed electron density N_0, and T_e denotes electron temperature. The RP force-induced modification of equilibrium electron density is correspondingly given by [45]

$$N_{0e} = \frac{N_0}{\gamma} exp\left(-\frac{m_0c^2}{T_e}(\gamma - 1)\right). \tag{7}$$

Accordingly, total plasma dielectric function may be decomposed in to linear and nonlinear components as

$$\varepsilon = \varepsilon_0 + \Phi(E \cdot E^*). \tag{8}$$

Where, $\varepsilon_0 = 1 - \frac{\omega_p^2}{\omega^2}$ represents the linear dielectric response of cold plasma in absence of RP force. The nonlinear contribution, $\frac{\omega_P^2}{\omega^2}\left[1 - \frac{N_{0e}}{N_0}\right]$, arises from the intensity dependent depletion of electron density and represents the nonlinear susceptibility induced by relativistic mass variation and ponderomotive expulsion of electrons.

Following [37-39], a suitable solution of wave Eq. (4) may be written in the form of a slowly varying envelope modulating a rapidly oscillating carrier wave, namely

$$E = E_0(r, z)\exp[i(\omega t - k(S + z))]. \tag{9}$$

The corresponding intensity distribution of the q-Gaussian beam during propagation is expressed as [38-39]

$$E_0 \cdot E_0^* = \frac{E_{00}^2}{f^2}\left(1 + \frac{r^2}{qr_0^2f^2}\right)^{-q} exp(-2k_iz). \tag{10}$$

Here, k_i accounts for absorption effects in plasma medium. The phase function $'S'$ which incorporates the effect of beam curvature and axial phase variation is given by

$$S = \frac{1}{2}r^2\frac{1}{f}\frac{df}{dz} + \Phi_0(z). \tag{11}$$

Where, $\Phi_0(z)$ denotes longitudinal phase shift accumulated during propagation. The wave number k in plasma is defined as

$$k = \frac{\omega}{c}\sqrt{\varepsilon_0} \tag{12}$$

The transverse evolution of laser beam is described by beam width function $'f(z)'$ whose variation along direction of propagation is governed by following 2nd order nonlinear ordinary differential equation [38-39];

$$\frac{d^2f}{d\eta^2} = \frac{q+4}{qf^3} - \left(\frac{\omega_p r_0}{c}\right)^2 exp(-2k_i\eta)\frac{\alpha E_{00}^2}{2f^3} exp\left[-\frac{mc^2}{T_e}\left\{\sqrt{1 + \frac{\alpha E_{00}^2 exp(-2k_i\eta)}{f^2}} - 1\right\}\right]\left(1 + \frac{\alpha E_{00}^2 exp(-2k_i\eta)}{f^2}\right)^{-3/2}\left[1 + \frac{mc^2}{T_e}\sqrt{1 + \frac{\alpha E_{00}^2 exp(-2k_i\eta)}{f^2}}\right] \tag{13}$$

Eq. (13) governs evolution of normalized beam waist f as a function of normalized distance η. The first term on right hand side represents diffraction induced beam spreading, which tends to increase the beam width as beam propagates. The second term arises from nonlinear RP force, which introduces an effective focusing mechanism by modifying the plasma dielectric response. The competition between these two opposing effects, diffraction-driven divergence and RP-induced nonlinear convergence dictates the overall propagation behavior of beam. Depending on relative strength of these mechanisms, the beam may undergo continuous expansion, strong self-focusing, or exhibit oscillatory evolution as it propagates through plasma medium.

The initial condition used is, $f = 1$ & $\frac{df}{d\eta} = 0$ at $\eta = 0$.

3. DISCUSSION

Eq. (13) can't be solved numerically; its solution is obtained through numerical technique using Runge-kutta 4th order method. The computations are carried out for a representative set of experimentally relevant laser-plasma parameters;

$$\alpha E_{00}^2 = 3.0, 4.0, 5.0; \frac{\omega_p^2}{\omega^2} = 0.4, 0.5, 0.6; k_i = 0, 0.3, 0.6\ ; q = 1, 2, 3; r_0 = 20\ \mu m, 25\ \mu m, 30\ \mu m$$

The evolution of beam width governed by Eq. (13) results from interplay of two distinct mechanisms appearing on right hand side. The first mechanism is connected with diffraction, which reflects beam's tendency to spread as it transits through plasma. The dominance of this mechanism causes beam's divergence, leading to an increase in transverse width. Mathematically, this regime is characterized by $\frac{d^2f}{d\eta^2} > 0$. The second mechanism arises from nonlinear modification plasma's refractive index caused by interaction of an intense laser field. The dominance of this mechanism causes beam's convergence, leading to decrease in transverse width. Mathematically, this regime is characterized by $\frac{d^2f}{d\eta^2} < 0$. A special situation arises, when both mechanisms exactly compensate each other. Under this balance, the beam transits in a steady state manner without any change in its transverse width. This stationary transition condition is characterized by $\frac{d^2f}{d\eta^2} = 0$.

Figure 1 shows evolution of beam width f as a function of normalized distance η for different laser intensities, $\alpha E_{00}^2 = 3.0, 4.0,$ and 5.0, represented by Black, Red, and Blue respectively. In all cases, the beam width exhibits oscillatory behavior due to saturating response of plasma dielectric function. These oscillations arise from continuous interplay between diffraction, which tends to broaden the beam, and nonlinear self-focusing, which acts to contract it. As the laser intensities increases, the diffraction term becomes increasingly dominant over nonlinear focusing term, thereby reducing beam's self-focusing tendency. Consequently, at higher laser intensities, the beam reaches its minimum width at larger propagation distances, clearly indicating diminished self-focusing effect.

Figure 2 shows evolution of beam width f as a function of normalized distance η for different plasma densities, $\frac{\omega_p^2}{\omega^2} = 0.4, 0.5,$ and 0.6, represented by Black, Red, and Blue respectively. In all cases, the beam width exhibits oscillatory behavior due to saturating response of plasma dielectric function. These oscillations arise from continuous interplay between diffraction, which tends to broaden the beam, and nonlinear self-focusing, which acts to contract it. As the plasma density increases, the nonlinear focusing term becomes increasingly dominant over diffraction term, thereby strengthening beam's self-focusing tendency. Consequently, at higher plasma densities, the beam reaches its minimum width at shorter propagation distances, clearly indicating enhanced self-focusing effect.

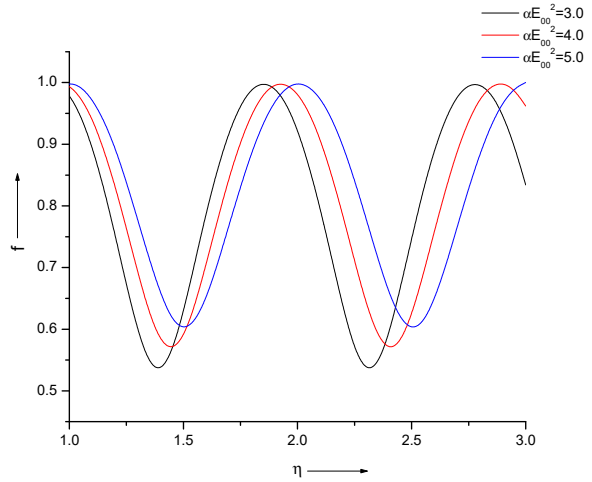

Figure 1. Evolution of beam width f as a function of normalized distance η for different laser intensities, $\alpha E_{00}^2 = 3.0, 4.0,$ and 5.0, represented by Black, Red, and Blue respectively

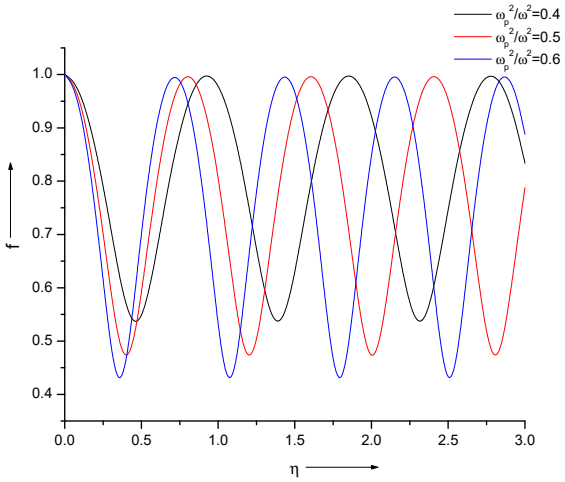

Figure 2. Evolution of beam width f as a function of normalized distance η for different plasma densities, $\omega_p^2/\omega^2 = 0.4, 0.5,$ and 0.6, represented by Black, Red, and Blue respectively

Figure 3 shows evolution of beam width f as a function of normalized distance η for different beam radii, $r_0 = 20\ \mu m, 25\ \mu m,$ and $30\ \mu m$, represented by Black, Red, and Blue respectively. In all cases, beam width exhibits an oscillatory behavior, which originates from saturating response of plasma dielectric function. As the beam radius increases, the contribution of nonlinear focusing term becomes increasingly dominant compared to diffraction term. This shift strengthens beam's tendency to self-focus. As a result, for larger beam radii, the beam reaches its minimum width at shorter propagation distances, clearly indicating an enhanced self-focusing effect.

Figure 4 shows evolution of beam width f as a function of normalized distance η for different q parameters, $q = 1,2,$ and 3, represented by Black, Red, and Blue respectively. In all cases, beam width exhibits an oscillatory nature, which arises from saturating response of plasma dielectric function. It is clearly observed that increasing the value of q markedly enhances focusing characteristics of beam. At higher q values, the nonlinear focusing contribution becomes stronger relative to diffraction, enabling the beam to converge more effectively. This leads to improved spatial localization of beam and corresponding increase in central field intensity. The enhanced intensity strengthens the nonlinear interaction beam and the plasma, which further reinforces self-focusing mechanism and results in deeper and more pronounced beam convergence.

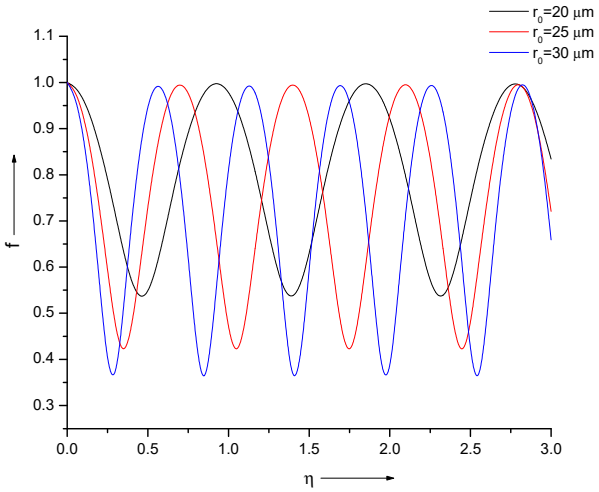

Figure 3. Evolution of beam width f as a function of normalized distance η for different beam radii, $r_0 = 20\ \mu m, 25\ \mu m,$ and $30\ \mu m$, represented by Black, Red, and Blue respectively

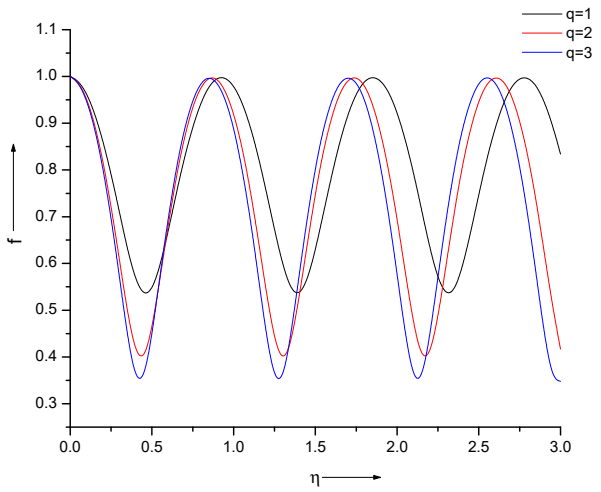

Figure 4. Evolution of beam width f as a function of normalized distance η for different q parameters, $q = 1,2,$ and 3, represented by Black, Red, and Blue respectively

Figure 5 shows evolution of beam width f as a function of normalized distance η for different k_i values, $k_i = 0, 0.3, 0.6$, represented by Black, Red, and Blue respectively. The figure shows that increasing k_i weakens beam's self-focusing due to energy loss through absorption. As absorption grows, the refractive index gradient decreases thereby reducing nonlinear convergence effect. Consequently, diffraction dominates and beam focuses less effectively.

Figure 6 shows evolution of beam width f as a function of normalized distance η for two different plasma regimes. The Black line shows the combined effect of relativistic mass variation and ponderomotive nonlinearities, while Red line represents relativistic nonlinearity alone. When both act together, the beam width f shifts to smaller η, indicating stronger self-focusing. Since, relativistic nonlinearity acts instantaneously, the ponderomotive contribution reinforces it, enhancing overall focusing effect.

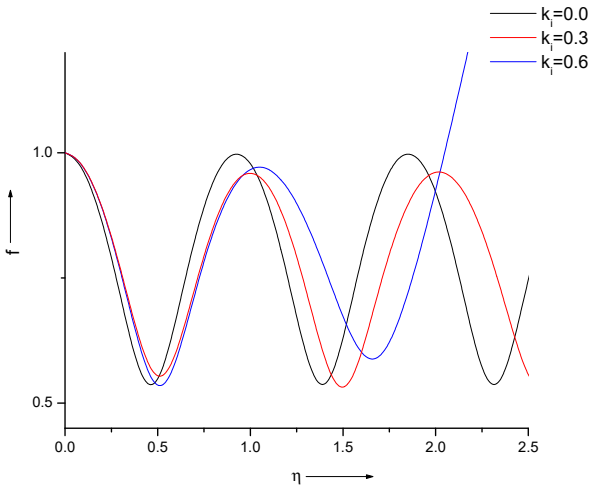

Figure 5. Evolution of beam width f as a function of normalized distance η for different k_i values, $k_i = 0, 0.3, 0.6$, represented by Black, Red, and Blue respectively

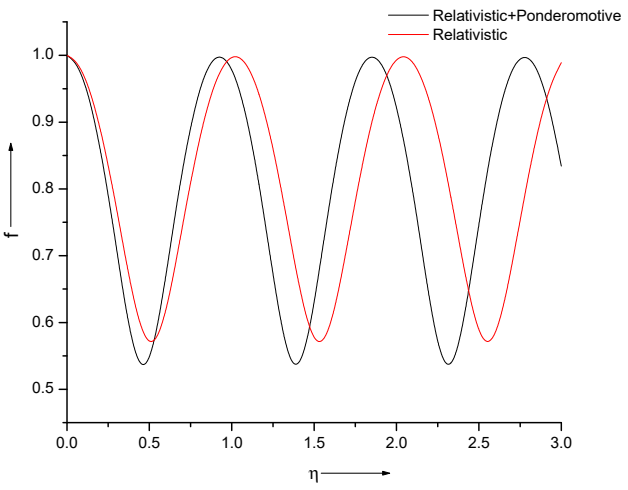

Figure 6. Evolution of beam width f as a function of normalized distance η for two different plasma regimes. The Black line shows the combined effect of relativistic mass variation and ponderomotive nonlinearities, while Red line represents relativistic nonlinearity alone

4. CONCLUSION

This study examines a detailed analysis of nonlinear self-focusing of q-Gaussian laser beams in plasma with relativistic and ponderomotive effects under linear absorption. Using WKB and paraxial approximations, self-focusing equation is derived, revealing that beam's focusing strengthens with higher plasma density, larger q-parameter, increased initial beam radius, combined action of RP force, while higher beam intensity and absorption weakens it. These results provide essential insights for controlling laser propagation in plasma, with direct implications for optimizing laser-driven fusion and other high intensity laser applications.

Funding
No funding was received for conducting this study.

Conflict of Interest
The authors declare that there are no conflicts of interest.

ORCID
Keshav Walia, https://orcid.org/0000-0001-9547-3027; **Deepak Tripathi,** https://orcid.org/0000-0001-9945-4069

REFERENCES

[1] S.C. Wilks, J.M. Dawson, W.B. Mori, T. Katsouleas, and M.E. Jones, "Photon accelerator," Phys. Rev. Lett. **62**, 2600 (1989). https://doi.org/10.1103/physrevlett.62.2600
[2] J. Faure, Y. Glinec, A. Pukhov, S. Kiselev, S. Gordienko, E. Lefebvre, J.P. Rousseau, *et al*., "A laser-plasma accelerator producing monoenergetic electron beams," Nature, **431**, 541 (2004). https://doi.org/10.1038/nature02963
[3] P.E. Young, H.A. Baldis, R.P. Drake, E.M. Campbell, and K.G. Estabrook, "Direct evidence of ponderomotive filamentation in a laser-produced plasma," Phys. Rev. Lett. **61**, 2336 (1988). https://doi.org/10.1103/physrevlett.61.2336
[4] A. Singh, K. Walia, "Relativistic self-focusing and self-channeling of Gaussian laser beam in plasma," Appl. Phys. B, **101**, 617 (2010). https://doi.org/10.1007/s00340-010-4230-4
[5] H. Hora, G. Korn, L. Giuffrida, D. Margarone, *et al*., "Fusion energy using avalanche increased boron reactions for block-ignition by ultrahigh power picosecond laser pulses," Laser Part. Beams, **33**, 607-619 (2015). https://doi.org/10.1017/S0263034615000634
[6] H. Hora, "Self-focusing of laser beams in a plasma by ponderomotive forces", Z. Phys. **226**, 156-159 (1969). https://doi.org/10.1007/BF01392018
[7] R. Sauerbrey, "Acceleration in femtosecond laser-produced plasmas," Phys. Plasmas, **3**, 4712 (1996). https://doi.org/10.1063/1.872038
[8] A. Bhatia, K. Walia, and A. Singh, "Second harmonic generation of intense Laguerre–Gaussian beam in relativistic plasma having an exponential density transition," Optik, **244**, 167608 (2021). https://doi.org/10.1016/j.ijleo.2021.167608
[9] D. Tripathi, S. Kaur, A. Vijay, and K. Walia, "Nonlinear dynamics of q-Gaussian laser beam in collisional plasma: Effect of linear absorption," J. Contemp. Phys. **60**, 16 (2025). https://doi.org/10.1134/s1068337225700409
[10] K. Walia, "Self-focusing of high power beam in unmagnetized plasma and its effect on stimulated Raman scattering process," Optik, **225**, 165592 (2021). https://doi.org/10.1016/j.ijleo.2020.165592
[11] K. Walia, N. Mehra, and S. Pandit, "Propagation characteristics of q-Gaussian laser beam in cold collisionless plasma", J. Contemp. Phys. **59**, 378 (2024). https://doi.org/10.1134/s1068337225700203
[12] T. Singh, and K. Walia, "Impact of high-power cosh-Gaussian beam on second harmonic generation in collisionless magnetoplasma," J. Contemp. Phys. **59**, 254 (2024). https://doi.org/10.1134/s106833722470049x
[13] K. Singh, and K. Walia, "Second harmonic generation of high power cosh-Gaussian beam in thermal quantum plasma: Effect of relativistic and ponderomotive nonlinearity," J. Contemp. Phys. **59**, 244 (2024). https://doi.org/10.1134/s1068337224700488
[14] K. Singh, and K. Walia, "Influence of self-focused elliptical laser beam on second harmonic generation in cold quantum plasma," J. Contemp. Phys. **59**, 154 (2024). https://doi.org/10.1134/s1068337224700300
[15] P. Sprangle, E. Esarey, and J. Krall, "Laser driven electron acceleration in vacuum, gases, and plasmas," Phys. Plasmas, **3**, 2183 (1996). https://doi.org/10.1063/1.871673
[16] B.E. Lemoff, G.Y. Yin, C.L. Gordon III, C.P.J. Barty, and S.E. Harris, "Demonstration of a 10-Hz femtosecond-pulse-driven XUV laser at 41.8 nm in Xe IX," Phys. Rev. Lett. **74**, 1574 (1995). https://doi.org/10.1103/physrevlett.74.1574
[17] C. Deutsch, A. Bret, M.C. Firpo, L. Gremillet, E. Lefebvre, and A. Lifschitz, "Onset of coherent electromagnetic structures in the relativistic electron beam–deuterium–tritium fuel interaction of fast ignition concern," Laser Part. Beams, **26**, 157 (2008). https://doi.org/10.1017/s0263034608000189
[18] X. Liu, D. Umstadter, E. Esarey, and A. Ting, "Harmonic generation by an intense laser pulse in neutral and ionized gases," IEEE Trans. Plasma Sci. **21**, 90 (1993). https://doi.org/10.1109/27.221106
[19] P. Kaw, G. Schmidt, and T. Wilcox, "Filamentation and trapping of electromagnetic radiation in plasmas," Phys. Fluids, **16**, 1522 (1973). https://doi.org/10.1063/1.1694552
[20] G.A. Askaryan, "Effects of the gradient of a strong electromagnetic beam on electrons and atoms," JETP, **15**, 1088 (1962).
[21] V.N. Ginzburg, V.V. Lozhkarev, S.Y. Mironov, A.K. Potemkin, and E.A. Khazanov, "Influence of small-scale self-focusing on second harmonic generation in an intense laser field," Quantum Electron. **40**, 503 (2010). https://doi.org/10.1070/QE2010v040n06ABEH014126
[22] D. Tripathi, T. Singh, A. Vijay, and K. Walia, "Nonlinear laser–plasma interaction under relativistic conditions," J. Contemp. Phys. **60**, 171-180 (2025). https://doi.org/10.1134/S1068337225700574
[23] A. Bhatia, K. Walia, and A. Singh, "Laguerre–Gaussian laser beam guiding and its second harmonics in plasma having density ramp," Phys. Plasmas, **29**, 092107 (2022). https://doi.org/10.1063/5.0103924
[24] A. Singh, and K. Walia, "Stimulated Raman scattering of Gaussian laser beam in relativistic plasma", Optik, **124**, 3470 (2013).
[25] K. Walia, "Effect of self-focusing of elliptical laser beam on second harmonic generation in collisionless plasma", Optik 127, 6618 (2016). https://doi.org/10.1016/j.ijleo.2012.10.031
[26] K. Walia, T. Singh, and A. Singh, "Effect of self-focused Cosh-Gaussian beam on second harmonic generation in collisional plasmas," Optik, **258**, 168894 (2022). https://doi.org/10.1016/j.ijleo.2022.168894
[27] W. Yu, M.Y. Yu, H. Xu, Y.W. Tian, J. Chen, and A.Y. Wong, "Intense local plasma heating by stopping of ultrashort ultraintense laser pulse in dense plasma," Laser Part. Beams, **25**, 631 (2007). https://doi.org/10.1017/s0263034607000742
[28] H.M. Milchberg, C.G. Durfee III, and T.J. McIlrath, "High-order frequency conversion in the plasma waveguide," Phys. Rev. Lett. **75**, 2494 (1995). https://doi.org/10.1103/physrevlett.75.2494

[29] V.T. Tikhonchuk, S. Hüller, and P. Mounaix, "Effect of speckle self-focusing on the stationary stimulated Brillouin scattering reflectivity from a randomized laser beam in an inhomogeneous plasma," Phys. Plasmas, **4**, 4369 (1997). https://doi.org/10.1063/1.872599
[30] J.L. Bobin, "High intensity laser–plasma interaction," Phys. Rep. **122**, 173 (1985). https://doi.org/10.1016/0370-1573(85)90077-8
[31] L.N. Glandorf, M. Scheer, D.A. Samuels, A.M. Mulhisen, E.R. Grant, X. Yang, V.M. Bierbaum, and S.R. Leone, "Ultrafast time-resolved soft X-ray photoelectron spectroscopy of dissociating Br_2," Phys. Rev. Lett. **87**, 193002 (2001). https://doi.org/10.1103/physrevlett.87.193002
[32] R.I. Tobey, M.E. Siemens, O. Cohen, M.M. Murnane, H.C. Kapteyn, and K.A. Nelson, "Ultrafast extreme ultraviolet holography: Dynamic monitoring of surface deformation," Opt. Lett. **32**, 286 (2007). https://doi.org/10.1364/ol.32.000286
[33] Y. Zhang, Z. Wang, Z. Nie, C. Li, H. Chen, K. Lu, and M. Xiao, "Four-wave mixing dipole soliton in laser-induced atomic gratings," Phys. Rev. Lett. **106**, 093904 (2011). https://doi.org/10.1103/physrevlett.106.093904
[34] Y. Zhang, Z. Wu, M.R. Belic, H. Zheng, Z. Wang, and M. Xiao, "Photonic Floquet topological insulators in atomic ensembles", Laser Photonics Rev. **9**, 331 (2015). https://doi.org/10.1002/lpor.201570039
[35] D.N. Gupta, A.K. Sharma, M. Hur, I. Hwang, and H. Suk, "Plasma density ramp for relativistic self-focusing of an intense laser," J. Opt. Soc. Am. B, **24**, 1155-1159 (2007). https://doi.org/10.1364/JOSAB.24.001155
[36] B. Hafizi, A. Ting, P. Sprangle, and R.F. Hubbard, "Relativistic focusing and ponderomotive channeling of intense laser beams", Phys. Rev. E, **62**, 4120 (2000). https://doi.org/10.1103/physreve.62.4120
[37] S.A. Akhmanov, A.P. Sukhorukov, and R.V. Kokhlov, "Self-focusing and diffraction of light in nonlinear media," Sov. Phys. Usp. 10, 609 (1968).
[38] M.S. Sodha, A.K. Ghatak, and V.K. Tripathi, "Self-focusing of laser beams in plasmas and semiconductors", Prog. Opt. **13**, 169 (1976). https://doi.org/10.1016/s0079-6638(08)70021-0
[39] M.S. Sodha, V.K. Tripathi, and A.K. Ghatak, *Self-Focusing of Laser Beams in Dielectrics, Plasmas and Semiconductors*, (Tata McGraw-Hill, New Delhi, 1974).
[40] H. Hora, "Theory of relativistic self-focusing of laser radiation in plasmas," J. Opt. Soc. Am. **65**, 882-886 (1975). https://doi.org/10.1364/josa.65.000882
[41] H. Hora, *Laser Interaction and Related Plasma Phenomena*, vol. 4B, (Plenum Press, New York, 1977).
[42] C. Tsallis, "Possible generalization of Boltzmann-Gibbs statistics," J. Stat. Phys. **52**, 479-487 (1988). https://doi.org/10.1007/BF01016429
[43] S. Ali, and P.K. Shukla, "Potential distributions around a moving test charge in quantum plasmas," Phys. Plasmas, **13**, 102112 (2006). https://doi.org/10.1063/1.2352974
[44] S. Na, and Y. Young, "Temperature effects on the nonstationary Karpman–Washimi ponderomotive magnetization in quantum plasmas", Phys. Plasmas, **16**, 074504 (2009). https://doi.org/10.1063/1.3176616
[45] A.R. Niknam, M. Hashemzadeh, and B. Shokri, "Weakly relativistic and ponderomotive effects on the density steepening in the interaction of an intense laser pulse with an underdense plasma," Phys. Plasmas, **16**, 033105 (2009). https://doi.org/10.1063/1.3081098

НЕЛІНІЙНЕ САМОФОКУСУВАННЯ q-ГАУСІВСЬКИХ ЛАЗЕРНИХ ПРОМЕНІВ У ПЛАЗМІ З РЕЛЯТИВІСТСЬКИМИ ТА ПОНДЕРОМОТОРНИМИ ЕФЕКТАМИ ПРИ ЛІНІЙНОМУ ПОГЛИНАННІ

Кешав Валья[1], Ніша Сінгх Ратхор[2], Вініт Каккар[3], Діпак Тріпаті[4]
[1]Кафедра фізики, Університет DAV, Джаландхар, Пенджаб, Індія
[2]Кафедра прикладних наук, Інститут технологій та менеджменту KCC, Велика Нойда, Індія
[3]Кафедра фізики, Міжнародна школа Lotus Valley, Сектор-50, Гургаон, Індія
[4]Кафедра фізики, USAR/USBS, Університет Гуру Гобінда Сінгха Індрапрастхи, кампус Східного Делі, Делі, Індія-110032

У цьому дослідженні представлено теоретичний аналіз нелінійного самофокусування q-гауссового лазерного променя, що поширюється через немагнічену плазму, враховуючи одночасний вплив релятивістської зміни маси та пондеромоторного механізму. Лінійне поглинання також враховується для врахування дисипації енергії під час поширення променя. Застосовуючи ВКБ-апроксимацію та параксіальне наближення, задача зводиться до диференціального рівняння 2-го порядку, яке описує еволюцію ширини лазерного променя як функції нормалізованої відстані поширення. Отримане рівняння розв'язується чисельно за допомогою методу Рунге-Кутти 4-го порядку. Проведено систематичний аналіз для вивчення впливу інтенсивності лазера, густини плазми, коефіцієнта поглинання, q-параметра та початкового радіуса променя на динаміку самофокусування q-гауссового лазерного променя. Ці результати показують, що параметри лазерної плазми суттєво впливають на динаміку променя та критично керують процесом самофокусування.

Ключові слова: *взаємодія лазера з плазмою; q-гауссовий промінь; нелінійне самофокусування; коефіцієнт поглинання; нелінійна динаміка*

East European Journal of Physics. 1. 112–126 (2026)
DOI: 10.26565/2312-4334-2026-1-09 ISSN 2312-4334

BENJAMIN–FEIR INSTABILITY OF INTERFACIAL GRAVITY–CAPILLARY WAVES IN A TWO-LAYER FLUID. PART II. SURFACE-TENSION EFFECTS

Olga Avramenko[1*,2], **Volodymyr Naradovyi**[3]
[1]*National University of Kyiv-Mohyla Academy, 2 Skovorody, Kyiv, 04070, Ukraine*
[2]*Vytautas Magnus University, 58 K. Donelaičio g., Kaunas 44248, Lithuania*
[3]*Volodymyr Vynnychenko Central Ukraine State University, 1 Shevchenka, Kropyvnytskyi, 25006, Ukraine*
[*]*Corresponding Author e-mail: o.avramenko@ukma.edu.ua*
Received November 17, 2025; revised January 12, 2026; accepted February 2, 2026

This second part of the study develops a complete geometric and asymptotic description of how surface tension governs the modulational stability of interfacial waves in a two-layer fluid. Extending the analytical framework of Part I, surface tension is treated as a freely adjustable parameter, making it possible to trace the nonlinear and dispersive properties of the system across the full range of depth ratios and density contrasts. Using the nonlinear Schrödinger reduction together with long-wave asymptotics, the mechanisms that shape the boundaries between stable and unstable regimes are identified and their dependence on surface tension is quantified. The long-wave structure is controlled by two special density values that mark the bases of the loop and the corridor on the stability diagrams. Their ordering switches at a threshold that exists only when the lower layer is deeper, and loop-type structures occur only in this regime. A second organising parameter is the classical Bond threshold, at which the dispersive and nonlinear singularities coincide. When surface tension exceeds this value and the upper layer is sufficiently deep, the interaction between resonant and dispersive effects produces a capillary cut that replaces the corridor and characterises strongly capillary, upper-layer-dominated configurations. To unify these observations, the full three-dimensional critical surfaces that separate different types of nonlinear and dispersive behaviour are computed. The familiar loop, corridor, and cut appear as planar sections of these surfaces, and their transitions follow directly from the deformation of the intersection between the resonant and dispersive sheets. Two depth ratios correspond to genuine geometric degeneracies: equal layer depths, where the intersection reduces to a straight line, and the golden-ratio configuration, where the critical surface becomes horizontally tangent at the Bond threshold. Overall, Part II completes the geometric and physical classification of modulational stability in two-layer interfacial waves and provides a framework for future extensions incorporating shear, external forcing, flexible boundaries, or variable bathymetry.

Keywords: *Modulational instability; Interfacial gravity–capillary waves; Two-layer fluid; Surface tension; Benjamin–Feir instability*

PACS: 47.20.Dr, 47.20.Ky, 47.35.Bb, 47.35.Pq

1. INTRODUCTION

In Part I [1], the modulational instability of interfacial waves in a two-layer fluid was examined for different depth ratios and density contrasts under the assumption of a fixed or characteristic interfacial tension. The present paper extends that analysis by investigating the effects of varying surface tension T on the stability and topology of modulational–stability domains.

The theoretical foundation of modulational instability originates from the classical works of Benjamin and Feir [2] and Zakharov [3], with extensions to interfacial waves by Grimshaw and Pullin [4] and by Christodoulides and Dias [5]. Dullin, Gottwald, and Holm further developed a unified long-wave shallow-water asymptotic framework linking several equivalent model equations (KdV, fifth-order KdV/Kawahara, and Camassa–Holm), clarifying the role of surface tension through the Bond-number parameter and identifying the parameter regimes where each model applies [6, 7]. Building on this foundation, more recent studies have explored the influence of surface tension in both surface and interfacial systems.

Sun and Wahlén [8] performed a rigorous spectral analysis of periodic gravity–capillary waves and showed that positive T excludes spectral instabilities at high-frequency crossings, yielding regions of spectral stability.In their analysis based on the Evans function method, Hur and Yang [9] examined the spectral properties of gravity–capillary waves, identifying regimes of Wilton-ripple instability and establishing the precise criteria for their onset. Ward et al. [10] examined the Faraday instability in a system with two interfaces, demonstrating experimentally and theoretically that surface tension governs excitation thresholds.

For interfacial waves in two-layer fluids, several recent studies have derived nonlinear Schrödinger (NLS) reductions and constructed stability diagrams. Li et al. [11] obtained the NLS equation for arbitrary depths and showed that stronger density contrast and thinner layers compress the modulational–instability region, while finite T shifts the instability boundary toward shorter waves. Li et al. [12] considered a linear shear profile and demonstrated that the combined effects of shear and T alter the sign of the nonlinear coefficient, changing the envelope–stability type. Murashige and Choi [13] performed a two-dimensional stability analysis of finite-amplitude waves and found competition between modulational and Kelvin–Helmholtz instabilities: surface tension suppresses the latter but alters the width of the modulational–instability

Cite as: O. Avramenko, V. Naradovyi, East Eur. J. Phys. 1, 112 (2026), https://doi.org/10.26565/2312-4334-2026-1-09

band. Pal and Dhar [14, 15] produced stability maps for oceanographic parameters and emphasized the sensitivity of instability boundaries to T. Boral, Ni, and Korobkin [16] studied the interaction between interfacial and flexural–gravity waves in the presence of a discontinuous background current, while Halder et al. [17] analyzed the effect of constant vorticity and showed that vorticity and surface tension jointly modify nonlinear corrections and stability.

Other studies have explored situations where capillarity interacts with external influences. Goldobin et al. [18] investigated interfacial waves in a two-layer system subjected to horizontal vibrations and showed that surface tension T influences the onset and stability of long-wave oscillatory modes. Doak et al. [19] considered gravity–capillary waves at the boundary between dielectric fluids under an external electric field, where surface tension modifies both the dispersion relation and the stability condition. Chow, Chan, and Grimshaw [20] analyzed long internal waves in smoothly stratified shallow fluids—although surface tension was absent, their approach is directly transferable to interfacial configurations. Liang, Zareei, and Alam [21] demonstrated resonant harmonic generation in internal waves, producing narrow instability windows analogous to those induced by capillarity. Boral, Sahoo, and Stepanyants [22] investigated surface waves under wind forcing and identified T as a key control parameter for the transition between stability and instability. Andreeva, Bulavin, and Tkachenko [23] investigated the Rayleigh–Plateau dissipative instability with viscous effects in both contacting fluids and showed that surface tension, together with dissipation, controls the transition between stable and unstable regimes.

Overall, existing research provides rigorous spectral criteria for gravity–capillary waves at $T > 0$, modulational–instability maps for two-layer systems with shear and currents, and analyses of auxiliary factors such as vorticity, vibrations, electric fields, wind forcing, and stratification. However, a consistent topological classification of stability diagrams in the (ρ, k) plane under varying T has not been established. The mechanisms governing the emergence and disappearance of corridors, loops, and cuts, as well as the limiting configurations HS–La, La–HS, and HS–HS (as defined in Part I), remain insufficiently understood. These questions are addressed in the present work.

2. PROBLEM FORMULATION, PRELIMINARY BACKGROUND, AND LIMITING CASES

2.1. Mathematical formulation and background assumptions

All variables and scaling follow the notation of Part I [1].

We consider the same two-layer inviscid, incompressible fluid system as in Part I, composed of a lower layer $\Omega_1 = \{(x, z) \mid -h_1 < z < 0\}$ and an upper layer $\Omega_2 = \{(x, z) \mid 0 < z < h_2\}$, separated by the interface $z = \eta(x, t)$ with surface tension T. The fluid densities are ρ_1 and ρ_2, and the density ratio is $\rho = \rho_2/\rho_1$. In Part I, the analysis was carried out for a fixed interfacial tension corresponding to $T = 1$. Here, T is treated as a free control parameter governing the capillary contribution.

Following the nondimensionalization adopted previously, all quantities are scaled with $L = (T_0/(\rho_1 g))^{1/2}$, $t_0 = (L/g)^{1/2}$, and $m_0 = \rho_1 L^3$, where T_0 is the reference interfacial tension. The dimensionless coefficient $T = T/T_0$ measures the relative magnitude of surface tension effects. Here we keep the same nondimensionalization as in Part I, where the choice $T = T_0$ led to the dimensionless value $T = 1$ in the dispersion relation.

The governing equations for the velocity potentials $\varphi_j(x, z, t)$ and the interface displacement $\eta(x, t)$ are identical to system (1) of Part I. The dependent variables are expanded in powers of the small steepness parameter $\alpha = a/l$, where a is the maximum interface displacement and l the wavelength:

$$(\eta, \varphi_j) = \sum_{n=1}^{3} \alpha^{n-1} (\eta_n, \varphi_{jn}) + O(\alpha^3), \qquad x_n = \alpha^n x, \quad t_n = \alpha^n t.$$

From the first-order approximation, one obtains the dispersion relation

$$\omega^2 = \frac{k\,(1 - \rho + Tk^2)}{\coth kh_1 + \rho\, \coth kh_2}, \tag{1}$$

in which T explicitly controls the curvature of $\omega(k)$.

At third order, the solvability condition gives the nonlinear Schrödinger equation

$$iA_t + i\omega' A_x + \tfrac{1}{2}\,\omega'' A_{xx} = -\alpha\,\omega^{-1} J\,|A|^2 A, \tag{2}$$

where $\omega' = \partial\omega/\partial k$ and $\omega'' = \partial^2\omega/\partial k^2$ are the first and second derivatives of the carrier frequency. The coefficient J is the Benjamin–Feir index, which depends on the system geometry and on the second-harmonic correction Λ (defined in Eq. (3) of Part I):

$$\begin{aligned} J = -\frac{1}{16(1-\rho)\,[\,\rho\,\coth kh_2 + \coth kh_1\,]} \Big\{ & 2k\omega^2(1-\rho)\Lambda[-3\rho\,\coth^2 kh_2 + 3\,\coth^2 kh_1 - 1 + \rho] \\ & - 4k\omega^4[\rho(\coth^2 kh_2 - 1) - (\coth^2 kh_1 - 1)]^2 \\ & - 4k^2\omega^2(1-\rho)[\rho\,\coth^3 kh_2 + \coth^3 kh_1 - 2\rho\,\coth kh_2 - 2\,\coth kh_1] - 3Tk^5(1-\rho) \Big\}. \end{aligned} \tag{3}$$

A purely temporal solution of Eq. (2), $A(t) = a\,\exp\left(i\alpha a^2\omega^{-1}Jt\right)$, with constant envelope amplitude a, is modulationally stable when

$$J\omega'' < 0, \tag{4}$$

while $J\omega'' > 0$ signals the onset of instability. In what follows, we examine how variations of T alter the loci $J = 0$ and $\omega'' = 0$ in the (ρ, k) plane, revealing new transitions between stable and unstable regimes as surface tension modifies both the nonlinear and dispersive characteristics of the interfacial mode.

2.2. Limiting case $\rho = 1$ for equal layer depths

We now consider the symmetric configuration of two layers with equal thickness $h_1 = h_2 = h$ and equal densities $\rho = 1$. In this limit the interface vanishes, and the system formally reduces to a single homogeneous fluid bounded by two free surfaces of equal curvature. Nevertheless, this configuration provides a convenient reference for analysing the nonlinear coefficient J and the structure of the Benjamin–Feir index near the symmetry line.

For $\rho = 1$ and $h_1 = h_2 = h$, substituting the dispersion relation (1),

$$\omega^2 = \frac{Tk^3}{2\,\coth kh},$$

into the general expression (3) for J, one obtains, after simplification,

$$J = -\frac{1}{32}\,T\,k^5\Big(\coth kh - \frac{5}{\cosh kh\,\sinh kh}\Big).$$

The factor T appears only as a multiplier and therefore does not affect the location of the zero of J. The condition $J = 0$ yields $\cosh^2(kh) = 5$, and hence the characteristic wavenumber at which J changes sign is

$$k_{\rm ch}(h) = \frac{1}{2h}\ln(9 + 4\sqrt{5}) \approx \frac{1.4436}{h}. \tag{5}$$

The independence of $k_{\rm ch}$ from the surface-tension coefficient T is a notable feature of this symmetric configuration. While T scales the dispersion relation, $\omega \propto \sqrt{T}$, so that the frequency increases as the square root of the surface tension, it does not modify the nonlinear geometry encoded in J. Consequently, the transition between focusing and defocusing nonlinearity in the Benjamin–Feir sense depends solely on the dimensionless depth parameter kh. For $k < k_{\rm ch}(h)$ the index $J > 0$, corresponding to one type of nonlinearity, whereas for $k > k_{\rm ch}(h)$ the sign reverses ($J < 0$). Because $\omega''(k)$ obeys the same scaling invariance ($\omega(k) \propto \sqrt{T}$, and thus $\omega''(k)$ scales identically and retains its sign), the overall modulational-stability criterion based on the product $J\,\omega''$ preserves the same threshold (5) for all $T > 0$.

The analytical symmetry of the perfectly symmetric configuration $\rho = 1$, $h_1 = h_2 = h$ implies that both $\omega(k)$ and $J(k)$ are even functions of the carrier wavenumber k. In this limit, the small-k expansion of the dispersion relation yields $\omega(k) \propto k^2$, so that $\omega''(k)$ tends to a finite positive constant as $k \to 0$. By contrast, for unequal densities $\rho \neq 1$ (with comparable layer depths) the long-wave behaviour is gravity-dominated: $\omega(k) \sim c(\rho)\,k$, and hence $\omega''(k)$ vanishes linearly with k as $k \to 0$. In both cases, the coefficient J remains finite at $k = 0$. In the long-wave regime $k \to 0$, the critical curves associated with the conditions $J \to \infty$ and $\omega'' = 0$ in the (ρ, k)-plane accumulate near the symmetry point $(\rho, k) = (1, 0)$. In the perfectly symmetric case $\rho = 1$, $h_1 = h_2$, both J and ω'' stay regular at $k = 0$, and the corresponding geometric degeneracy reduces to a simple linear intersection in the (ρ, k) plane, as observed in the three-dimensional representations discussed in Sec. 4.

To the best of our knowledge, the T-independence of the characteristic wavenumber $k_{\rm ch}$ in the symmetric limit $\rho = 1$, $h_1 = h_2$ has not been explicitly noted in the literature. This follows directly from the capillary scaling of the dispersion relation ($\omega \propto \sqrt{T}$) and the corresponding invariance of $\omega''(k)$. For a comprehensive discussion of modulational instability in gravity–capillary systems, see Dias and Kharif [25].

2.3. Mutual placement of the points $\rho_{\rm L}$ and $\rho_{\rm C}$ at $k = 0$

In the long-wave limit $k \to 0$, the intersection points of the conditions $J = 0$ and $J \to \infty$ with the density axis $O\rho$ are

$$\rho_{\rm L} = \frac{h_2^2}{h_1^2}, \tag{6}$$

$$\rho_{\rm C}(T) = \frac{-h_2h_1^2 + h_1h_2^2 - 3Th_1 + \sqrt{h_1^4h_2^2 + 2h_1^3h_2^3 + h_1^2h_2^4 + 6Th_1^3h_2 - 6Th_1^2h_2^2 - 12Th_1h_2^3 + 9T^2h_1^2}}{2h_1h_2^2}. \tag{7}$$

Geometry fixes the reference point $\rho_L = h_2^2/h_1^2$, while Capillarity shifts $\rho_C(T)$ leftward from $\rho = 1$ for small T, and, whenever the corresponding branch remains real, towards its asymptotic geometric limit for large T. The two curves intersect at a finite surface-tension value $T_\times$ defined by $\rho_C(T_\times) = \rho_L$. Solving this relation gives

$$T_\times = \frac{h_1^4 - h_1^3 h_2 + h_1 h_2^3 - h_2^4}{3h_1^2} = \frac{(h_1^2 - h_2^2)(h_1^2 + h_2^2 - h_1 h_2)}{3h_1^2},$$

whose sign determines the admissible configurations:

$$\operatorname{sign}(T_\times) = \begin{cases} > 0, & h_1 > h_2, \\ = 0, & h_1 = h_2, \\ < 0, & h_1 < h_2, \end{cases} \qquad \text{so that } T_\times > 0 \text{ exists only if } h_1 > h_2.$$

For physically relevant $T > 0$, three cases arise:

(i) $h_1 > h_2$: $T_\times > 0$, and

$$T < T_\times : \ \rho_L < \rho_C(T), \qquad T = T_\times : \ \rho_L = \rho_C(T_\times), \qquad T > T_\times : \ \rho_C(T) < \rho_L.$$

(ii) $h_1 = h_2 = h$: $\rho_L = 1$ and

$$\rho_C(T) = \frac{-3T + |3T - 2h^2|}{2h^2} = \begin{cases} 1 - \dfrac{3T}{h^2}, & 0 \le T < \dfrac{2h^2}{3}, \\ -1, & T \ge \dfrac{2h^2}{3}, \end{cases}$$

hence $\rho_C(T) \le 1 = \rho_L$ for all $T > 0$.

(iii) $h_1 < h_2$: $T_\times < 0$, so for admissible $T > 0$ the equality $\rho_C(T) = \rho_L$ cannot be reached. Along the real branch of $\rho_C(T)$ the dependence on T is continuous, and therefore, once $\rho_C(T)$ drops below ρ_L for $T > 0$, the inequality $\rho_C(T) < \rho_L$ persists for all admissible $T > 0$. Since $\rho_L = h_2^2/h_1^2 > 1$ while $\rho_C(T) \le 1$ for small T, the inequality $\rho_C(T) < \rho_L$ holds for all $T > 0$.

For small capillarity ($T \to 0$), a Taylor expansion of ρ_C yields

$$\rho_C(T) = 1 - \frac{3T}{h_1 h_2} + O(T^2),$$

so the curve $\rho_C(T)$ departs from unity with slope $-3/(h_1 h_2)$. Hence, for $h_1 > h_2$ the crossing $\rho_C(T) = \rho_L < 1$ occurs at a finite $T_\times > 0$, whereas for $h_1 \le h_2$ the ordering $\rho_C(T) \le 1 \le \rho_L$ is maintained even for arbitrarily small $T > 0$.

In the opposite, capillarity-dominated regime ($T \to \infty$), the leading terms in formula (7) cancel, yielding the simple asymptotic limit

$$\rho_C(T) = -\frac{h_2}{h_1} + O\left(\frac{1}{T}\right),$$

so that

$$\lim_{T\to\infty} \rho_C(T) = -\frac{h_2}{h_1} < 0, \qquad \rho_L = \frac{h_2^2}{h_1^2} \text{ is independent of } T.$$

Thus, for $h_2 \ge h_1$ one always has $\rho_C(T) \le 1 \le \rho_L$ throughout the entire range $T \ge 0$ along the real branch of $\rho_C(T)$. For $h_2 < h_1$, the inequality eventually reverses once $T > T_\times$.

The analytical relations derived above show that the relative placement of ρ_L and $\rho_C(T)$ at $k = 0$ depends on both geometry and surface tension: a positive threshold $T_\times$ satisfying $\rho_C(T_\times) = \rho_L$ exists only when $h_1 > h_2$. This behaviour underlies the long-wave topology of neutral-stability boundaries first noted by Grimshaw and Pullin [4], where the neutral curves separating focusing and defocusing regimes form closed contours in the (ρ, k) plane.

2.4. Long-wave critical surface tension T^* (Bond threshold Bo = 1/3)

To determine the long-wave threshold and introduce convenient notation, we define the Bond number $\mathrm{Bo} = T/h_1^2$ following the standard convention [24, 25]. The corresponding critical surface tension is

$$T^* = \frac{h_1^2}{3}, \tag{8}$$

which is equivalent to $\mathrm{Bo}^* = 1/3$ [6, 7]. This threshold separates the regimes of normal and anomalous dispersion in the long-wave limit: for $\mathrm{Bo} < \mathrm{Bo}^*$ ($T < T^*$) the small-k curvature $\omega''(k)$ is negative (normal dispersion), whereas for $\mathrm{Bo} > \mathrm{Bo}^*$ ($T > T^*$) it becomes positive (anomalous dispersion).

From the dispersion relation (1), in the limit of a light upper layer ($\rho \to 0$), corresponding to long gravity–capillary waves at the free surface of the lower layer, we obtain

$$\omega^2 = \frac{(1+Tk^2)\,k}{\coth(kh_1)} = (1+Tk^2)\,k\,\tanh(kh_1) = h_1k^2\Big[1+\Big(\mathrm{Bo}-\tfrac{1}{3}\Big)(kh_1)^2+O\Big((kh_1)^4\Big)\Big].$$

Hence,

$$\omega(k) = \sqrt{h_1}\,k\Big[1+\tfrac{1}{2}\Big(T-\tfrac{h_1^2}{3}\Big)k^2+O(k^4)\Big], \qquad \omega''(k) = 3\sqrt{h_1}\Big(T-\tfrac{h_1^2}{3}\Big)\,k+O(k^3).$$

At $T = T^*$ ($\mathrm{Bo} = \mathrm{Bo}^*$), the curvature $\omega''(k)$ vanishes, and the dispersion relation becomes degenerate. This is the classical long-wave, or shallow-water, threshold where the dispersive coefficient changes sign [6, 7].

The link between this linear threshold and the nonlinear modulation follows from the asymptotics of the Benjamin–Feir index (3). In the double limit $k \to 0$ and $\rho \to 0$ (long waves on a light upper layer),

$$\lim_{\rho\to 0}\lim_{k\to 0} J = \frac{9}{16\,h_1\,(-h_1^2+3T)},$$

so J diverges precisely at $T = T^*$, corresponding to $\mathrm{Bo} = \mathrm{Bo}^*$, in agreement with the long-wave shallow-water theory [6, 7]. At this value, the curves $J \to \infty$ and $\omega'' = 0$ intersect at the origin of the (ρ, k) plane: for $T < T^*$, the $J \to \infty$ branch is locally vertical, whereas for $T > T^*$ it becomes nearly horizontal. As T increases further, the curves $J \to \infty$ and $\omega'' = 0$ approach one another and nearly coincide, forming the degenerate "cut" structure observed in the modulational-stability diagrams.

2.5. Geometric condition for horizontal tangency of the critical surface

As shown in Subsec. 2.4, the long-wave Bond threshold $T^* = h_1^2/3$, $\mathrm{Bo}^* = 1/3$, marks the point where the singular conditions $J \to \infty$ and $\omega'' = 0$ coincide at $(\rho, k) = (0, 0)$. The geometry of the critical surface $T(\rho, k)$ near this point depends on the depth ratio of the layers.

Expanding the dispersion relation (1) for small k yields

$$\omega^2 = c_2(\rho)\,k^2 + c_4(\rho;T)\,k^4 + O(k^6),$$

with

$$c_2(\rho) = \frac{h_1h_2(1-\rho)}{h_1\rho+h_2}, \quad c_4(\rho;T) = \frac{h_1h_2\big[3T(h_1\rho+h_2)+h_1^2h_2(\rho-1)+h_1h_2^2(\rho^2-\rho)\big]}{3(h_1\rho+h_2)^2}.$$

The condition $c_4(\rho;T) = 0$ defines the critical surface-tension function

$$T^*(\rho) = \frac{h_1h_2\big(-h_1\rho+h_1-h_2\rho^2+h_2\rho\big)}{3(h_1\rho+h_2)}, \qquad T^*(0) = \frac{h_1^2}{3}.$$

In the long-wave limit, this degeneracy condition coincides with the singularity set $J \to \infty$; hence, the same function $T^*(\rho)$ locally describes both the linear dispersion surface $\omega'' = 0$ (green) and the nonlinear singular surface $J \to \infty$ (blue) in the vicinity of $(\rho, k) = (0, 0, T^*)$.

A horizontal tangency of $T(\rho, k)$ to the plane $T = T^*$ at $(\rho, k) = (0, 0)$ requires $\partial T^*/\partial\rho|_{\rho=0} = 0$, which gives

$$h_1^2 + h_2(h_1-h_2) = 0, \qquad \frac{h_2}{h_1} = \frac{1+\sqrt{5}}{2} \approx 1.618. \tag{9}$$

Hence, the critical surface is horizontally tangent at the origin when the depth ratio satisfies (9). This ratio corresponds to the *golden ratio* $\varphi = (1+\sqrt{5})/2$, representing a neutral balance between the inertial contributions of the two layers in the long-wave limit. For $h_2/h_1 < \varphi$, $\partial T^*/\partial\rho|_{\rho=0} < 0$, indicating a gravity-dominated regime; for $h_2/h_1 > \varphi$, the derivative is positive, corresponding to a capillarity-dominated regime, while the golden-ratio configuration $h_2/h_1 = \varphi$ defines the boundary between these two regimes.In particular, when the depth ratio exceeds the golden value $h_2/h_1 = \varphi$ and the surface tension is increased beyond the long-wave threshold T^*, the resulting change in the local geometry of the critical surfaces $J \to \infty$ and $\omega'' = 0$ leads to a qualitative restructuring of the modulational-stability diagrams, as will be illustrated in Sec. 4.

3. STABILITY DIAGRAMS: THE INFLUENCE OF SURFACE TENSION

3.1. General remarks and reference configuration

In Part I, modulational–stability maps were constructed for two representative sets of layer–depth combinations, $(h_1, h_2) \in \{1, 2, 3, 4\}$ and $(h_1, h_2) \in \{1, 5, 9, 13\}$, which together illustrated the main topological types of stable and

unstable regions and their evolution with varying density ratio ρ and wavenumber k. In the present part, attention is focused on the second, broader matrix $(h_1, h_2) \in \{1, 5, 9, 13\}$, which serves as a reference configuration for analysing the effect of surface tension. Other geometric and physical parameters of the system will be examined in the following subsections.

Figure 1 shows the modulational–stability diagrams for three representative values, $T = 1/2$, 1, and 2. The colour convention is the same as in Part I: black denotes the linear–stability boundary corresponding to the *critical wavenumber*

$$k = k_c = \sqrt{(\rho - 1)/T},$$

which separates the regions of linear stability and instability; red indicates the curve $J = 0$ separating focusing and defocusing nonlinearities; blue marks the singular curve $J \to \infty$ associated with resonance coupling; and green represents the dispersion–curvature line $\omega''(k) = 0$, where the sign of the group–velocity dispersion changes. Solid, dashed, and dotted lines correspond to $T = 1/2$, 1, and 2, respectively. This comparison highlights how an increase in surface tension gradually modifies the topology of stable and unstable domains across the parameter space (ρ, k).

3.2. Symmetric and asymmetric configurations of the upper unstable region

The influence of surface tension on the upper modulationally unstable domain (bounded above by the red locus $J = 0$) can be examined by comparing three representative values, $T = 1/2$ (solid), 1 (dashed), and 2 (dotted), across all panels of Fig. 1. As shown in Part I, deviations of T from the reference value $T = 1$ produce opposite yet comparable effects: doubling to $T = 2$ and halving to $T = 1/2$ deform the upper domain in reverse directions with nearly symmetric magnitudes.

For equal depths ($h_1 = h_2$), the upper region remains continuous at $\rho = 1$, without a vertical cut. In Fig. 1a ($h_1 = h_2 = 1$) the red boundaries for different T intersect twice, the left intersection occurring at relatively large wavenumbers ($k > 2$). For $\rho < 1$, the ordering of curves is dotted ($T = 2$) above dashed ($T = 1$) above solid ($T = 1/2$), indicating that increasing surface tension narrows the upper unstable domain, whereas decreasing T broadens it. This qualitative property persists along the diagonal of the matrix (Figs. 1f, k, p), where $h_1 = h_2 = h$: the asymptote at $\rho = 1$ does not appear, and the intersection point of the T-dependent boundaries shifts toward smaller k as h increases. The corresponding characteristic wavenumber

$$k_{ch}(h) = \frac{1}{2h} \ln(9 + 4\sqrt{5}),$$

given by formula (5), decreases monotonically with h and approaches $(\rho, k) = (1, 0)$ in the deep–water limit, consistent with the case of two hydrodynamic half–spaces. As can be seen in the panels corresponding to the equal–depth configurations (Figs. 1a, f, k, p), the point $(\rho, k) = \big(1,\, k_{ch}(h)\big)$ appears as the unique location at which all red boundaries ($J = 0$) corresponding to $T = 1/2$, 1, and 2 intersect. This common intersection is a distinctive geometric feature of the symmetric case $h_1 = h_2 = h$; for unequal layer depths such a point does not exist, and instead the line $\rho = 1$ becomes a vertical asymptote of the upper unstable region, as discussed below.

When depth symmetry is broken, the topology of the upper region changes at $\rho = 1$. In the first row of Fig. 1b–d ($h_1 = 1$, $h_2 > 1$), the intersection at $\rho = 1$ is replaced by a vertical asymptote that divides the upper domain, although the relative ordering of the T-dependent boundaries away from $\rho = 1$ remains similar to that in Fig. 1a. In contrast, Figs. 1e, i, m ($h_2 = 1$, $h_1 = 5, 9, 13$) exhibit a reversed response at small density ratios: the dotted curve ($T = 2$) lies below the dashed one ($T = 1$), while the solid curve ($T = 1/2$) lies above both, so increasing T expands the upper unstable domain and decreasing T contracts it. For larger ρ ($\rho \gtrsim 0.3$) this tendency reverses. In the remaining panels of Fig. 1 (rows 2–4, columns 2–4), the pairwise intersection points of the T-dependent boundaries cluster near $\rho \simeq 0.85$–0.99; within this range the order of curves is temporarily reversed, but just below $\rho = 1$ the usual sequence (dotted below dashed, solid above both) is restored.

The physical mechanism underlying these reorganizations is the redistribution of the balance between focusing and defocusing nonlinearities by capillarity under nearly fixed dispersion. The capillary contribution to the effective nonlinearity scales as $T\,k^5(1 - \rho)$: for a light upper layer ($\rho < 1$) an increase in T stiffens the interface and shifts the $J = 0$ boundary upward in k, narrowing the unstable region. Near and above density matching, particularly under pronounced depth asymmetry, the same increase in T can enhance the focusing component and expand the instability zone. Depth symmetry ($h_1 = h_2$) removes the singular response at $\rho = 1$, producing a smooth passage of the $J = 0$ locus across the density–matching line, whereas asymmetry restores a nearly singular sensitivity manifested as a vertical asymptote. The clustering of intersection points near $\rho \lesssim 1$ shows that, for small density contrast, variations in T mainly tune the high–k capillary stiffness without significantly changing the inertial balance between layers, leading to local, topology-preserving adjustments of the upper boundary rather than qualitative alterations of its shape.

3.3. Corridor and cut formation

The stability structures associated with the corridor and the cut, which represent additional stable regions, are absent in Fig. 1a for the symmetric case $h_1 = h_2 = 1$. In the subsequent panels (Figs. 1b–d) a narrow cut appears, terminating at both ends on the ρ-axis. For $h_1 = 1$ and $h_2 = 5$ only a single small cut is visible, corresponding to $T = 1/2$ (Fig. 1b).

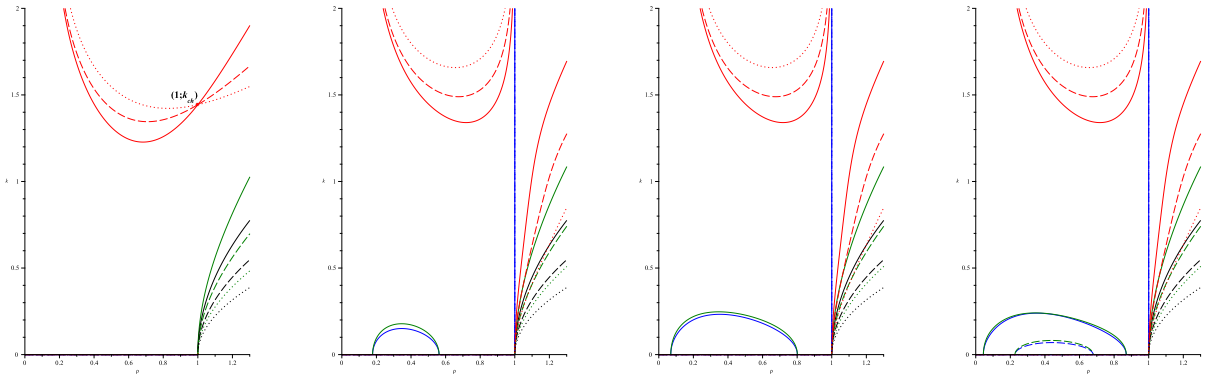

(a) $h_1 = 1,\ h_2 = 1$ **(b)** $h_1 = 1,\ h_2 = 5$ **(c)** $h_1 = 1,\ h_2 = 9$ **(d)** $h_1 = 1,\ h_2 = 13$

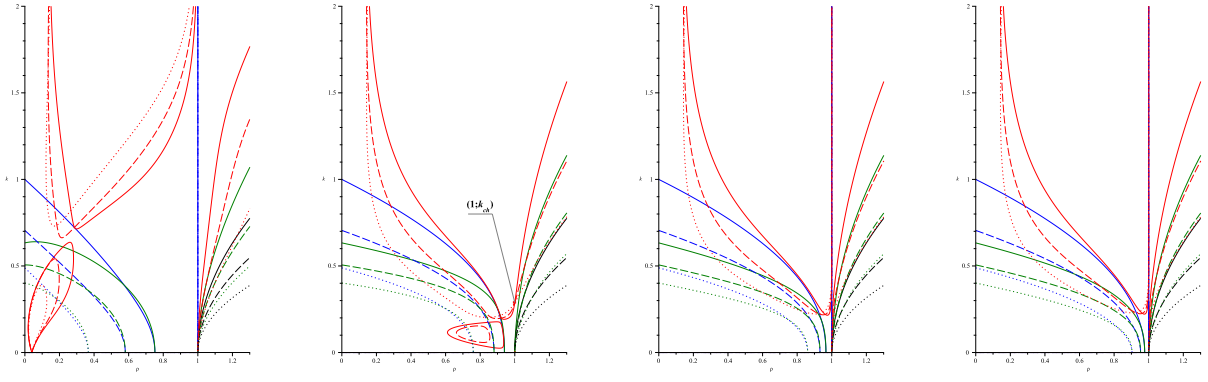

(e) $h_1 = 5,\ h_2 = 1$ **(f)** $h_1 = 5,\ h_2 = 5$ **(g)** $h_1 = 5,\ h_2 = 9$ **(h)** $h_1 = 5,\ h_2 = 13$

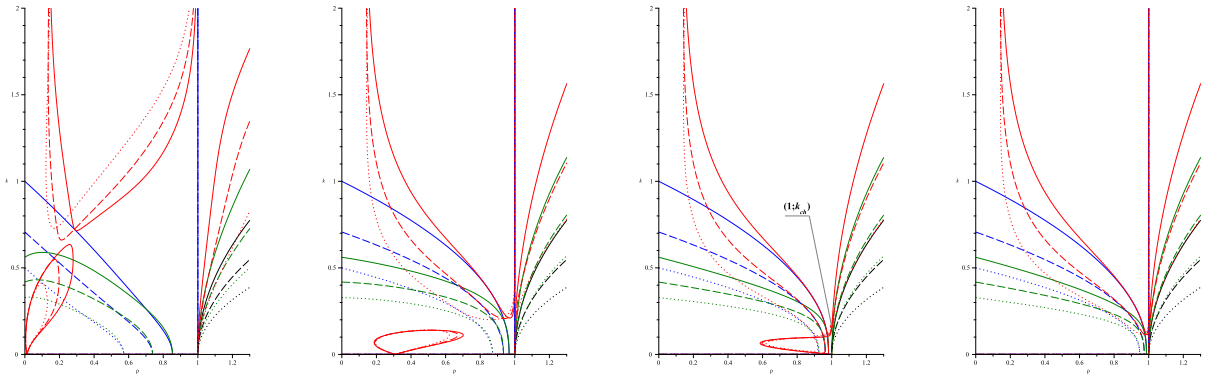

(i) $h_1 = 9,\ h_2 = 1$ **(j)** $h_1 = 9,\ h_2 = 5$ **(k)** $h_1 = 9,\ h_2 = 9$ **(l)** $h_1 = 9,\ h_2 = 13$

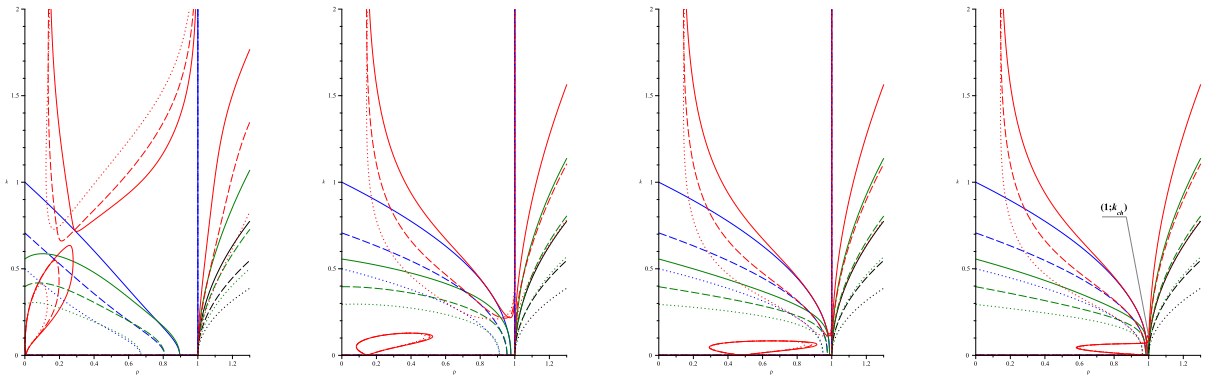

(m) $h_1 = 13,\ h_2 = 1$ **(n)** $h_1 = 13,\ h_2 = 5$ **(o)** $h_1 = 13,\ h_2 = 9$ **(p)** $h_1 = 13,\ h_2 = 13$

Figure 1. Modulational–stability diagrams for all combinations of $h_1, h_2 \in \{1, 5, 9, 13\}$ for $T = 1/2, 1, 2$.

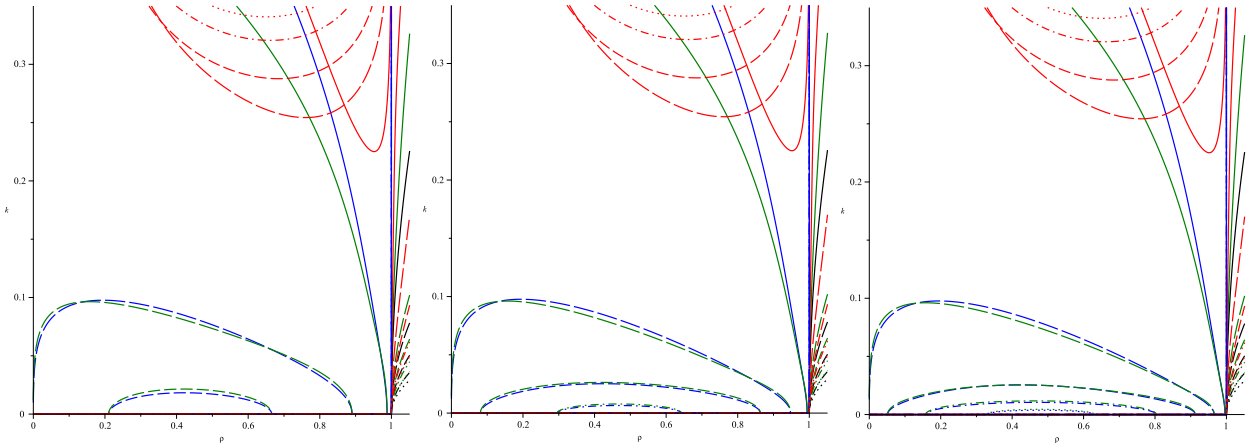

(a) $h_1 = 5,\ h_2 = 50$ **(b)** $h_1 = 5,\ h_2 = 100$ **(c)** $h_1 = 5,\ h_2 = 150$

Figure 2. The cut-type corridor for $h_1 = 5$ and $h_2 \in \{50, 100, 150\}$ for $T = 1,\ 25/3,\ 20,\ 40,\ 60$.

When the upper-layer thickness increases to $h_2 = 9$, the cut persists for $T = 1/2$, becomes noticeably longer, and extends to higher wavenumbers (Fig. 1c). At $h_2 = 13$ (Fig. 1d), two distinct cuts are observed: a broader one associated with $T = 1/2$ and a smaller one corresponding to $T = 1$.

At significantly higher depth ratios, the narrow cuts characteristic of moderate asymmetry transform into broad open corridors. This behaviour is consistent with the analytical result of Subsec. 2.5, which shows that the critical surface $T^*(\rho)$ develops a horizontal tangency at $(\rho, k) = (0, 0)$ when the depth ratio satisfies $h_2/h_1 = (1 + \sqrt{5})/2 \approx 1.618$. For depth ratios exceeding this value, the local geometry of the critical surfaces $J \to \infty$ and $\omega'' = 0$ changes in such a way that cut–type structures naturally emerge: in this regime the singular branch $J \to \infty$ bends toward the $k = 0$ axis, producing cuts that visibly rest on the ρ–axis. This effect is clearly seen in the moderately asymmetric panels of Fig. 1b–d and becomes even more transparent in the three–dimensional representations discussed in Sec. 4.

For $h_1 = 5$ and $h_2 = 50$, 100, and 150 (Figs. 2a–c), several distinct corridors are observed, their structure depending on the magnitude of surface tension ($T = 1$, $25/3$, 20, 40, and 60), represented by solid, long-dashed, dashed, dash-dotted, and dotted lines, respectively. The chosen five values of T play a key methodological role. They cover the reference case $T = 1$ used throughout Part I, the critical long-wave threshold (8)

$$T^* = \frac{h_1^2}{3} = \frac{25}{3}, \qquad \mathrm{Bo}^* = \frac{1}{3},$$

and three progressively higher values $T = 20$, 40, and 60, which extend the analysis well into the strongly capillary regime. This set allows one to track, within a single series of diagrams, the complete transition from gravity–capillary balance to capillary dominance and to identify the scaling of corridor width, shape, and position with increasing T.

For $h_2 = 50$ (Fig. 2a) only three corridors are present ($T = 1$, $25/3$, and 20); for $h_2 = 100$ (Fig. 2b) four corridors appear ($T = 1$, $25/3$, 20, 40); and for $h_2 = 150$ (Fig. 2c) all five corridors corresponding to $T = 1$, $25/3$, 20, 40, and 60 are clearly visible. At $T = 1$ the corridor remains broad and nearly invariant with h_2, while increasing T primarily affects the region of small k, where pronounced cuts develop in the central part of the ρ-range. As T exceeds the critical value T^*, the individual corridors converge toward the origin $(\rho, k) = (0, 0)$, producing a cut-type topology.

This behaviour marks the transition from a mixed gravity–capillary regime to a purely capillary one. For moderate surface tension ($T < T^*$), both restoring mechanisms act simultaneously, producing multiple corridors whose positions depend on the density ratio. As T approaches T^*, the capillary stress increasingly dominates, damping long-wave modulation and localizing the instability at short wavelengths. The cut-type corridor thus corresponds to the limit in which the interface behaves as a nearly rigid capillary sheet bounding a deep lower layer: nonlinear effects persist only within a narrow density interval, and the unstable band detaches from the ρ-axis. In this regime, the inertia of the lower layer provides the dominant response, while dispersion is governed exclusively by surface tension, resulting in the flattening and eventual disappearance of the loop.

3.4. Loop and its interaction with the corridor

From the second (Figs. 1e–h), third (Figs. 1i–l), and fourth (Figs. 1m–p) rows of the matrix diagrams corresponding to $h_1 = 5$, 9, and 13, respectively, it is seen that at a lower value of surface tension ($T = 1/2$) both stability structures—the

loop and the corridor—expand relative to the reference case $T = 1$, while the corridor shifts rightward along the ρ-axis. Its lower boundary, however, never crosses the line $\rho = 1$, approaching the point $(\rho, k) = (1, 0)$ asymptotically as the upper–layer thickness increases. At a higher value of surface tension ($T = 2$), both the loop and the corridor contract and become narrower, and the corridor moves leftward toward smaller density ratios. In the complete matrix of stability maps (Fig. 1), the loop is observed in Figs. 1e, f, i–k, m–p; in Fig. 1f it remains isolated, whereas in the other cases it touches the ρ-axis.

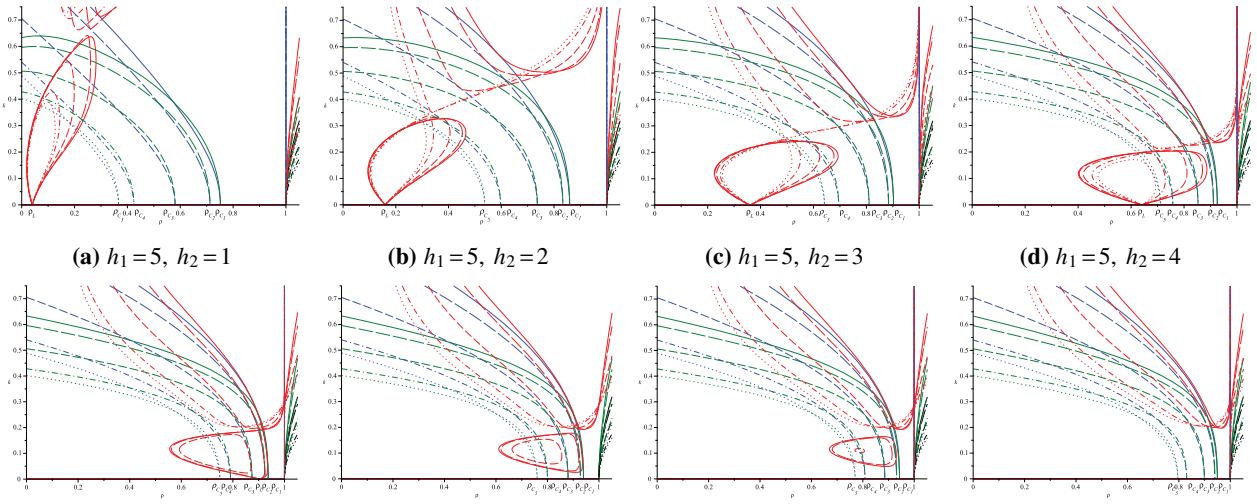

(a) $h_1 = 5,\ h_2 = 1$ **(b)** $h_1 = 5,\ h_2 = 2$ **(c)** $h_1 = 5,\ h_2 = 3$ **(d)** $h_1 = 5,\ h_2 = 4$

(e) $h_1 = 5,\ h_2 = 4.75$ **(f)** $h_1 = 5,\ h_2 = 5$ **(g)** $h_1 = 5,\ h_2 = 5.25$ **(h)** $h_1 = 5,\ h_2 = 6$

Figure 3. Stability diagrams for surface–tension coefficients $T = 1/2,\ 3/5,\ 1,\ 5/3,\ 2$ for $h_1 = 5$ and $h_2 \in \{1, 2, 3, 4, 4.75, 5, 5.25, 6\}$.

Figure 3 presents enlarged fragments of the modulational–stability maps for fixed $h_1 = 5$ and a sequence of upper–layer thicknesses $h_2 = 1, 2, 3, 4, 4.75, 5, 5.25, 6$ (Figs. 3a–h), computed for five values of surface tension, $T = 1/2$, $3/5$, 1, $5/3$, and 2, represented by solid, long-dashed, dashed, dash-dotted, and dotted lines. Each panel shows the relative configuration of the loop and the corridor near small wavenumbers k, illustrating how their positions vary with both geometry and surface tension. The loop–base point at $k = 0$ is determined solely by the depth ratio, $\rho_{\mathrm{L}} = h_2^2/h_1^2$, whereas the corridor–edge points ρ_{C_1}–ρ_{C_5} correspond to these five values of T and mark the roots of the corridor branches on the horizontal axis, that is, the intersections of the resonant ($J \to \infty$) and dispersive ($\omega'' = 0$) conditions at $k \to 0$.

For quantitative reference, the corresponding values of ρ_{L} and $\rho_{\mathrm{C}}(T)$ are summarized in Table 1.

Table 1. Loop–base ρ_{L} and corridor–edge $\rho_{\mathrm{C}}(T)$ coordinates for five representative surface–tension values at fixed $h_1 = 5$.

h_2	ρ_{L}	$\rho_{\mathrm{C}_1} = \rho_{\mathrm{C}}(1/2)$	$\rho_{\mathrm{C}_2} = \rho_{\mathrm{C}}(3/5)$	$\rho_{\mathrm{C}_3} = \rho_{\mathrm{C}}(1)$	$\rho_{\mathrm{C}_4} = \rho_{\mathrm{C}}(5/3)$	$\rho_{\mathrm{C}_5} = \rho_{\mathrm{C}}(2)$
1.00	0.040	0.752	0.712	0.580	0.424	0.367
2.00	0.160	0.859	0.833	0.737	0.597	0.537
3.00	0.360	0.903	0.884	0.810	0.695	0.641
4.00	0.640	0.926	0.911	0.853	0.758	0.711
4.75	0.902	0.937	0.924	0.874	0.791	0.749
5.00	1.000	0.940	0.928	0.880	0.800	0.760
5.25	1.103	0.943	0.931	0.885	0.809	0.770
6.00	1.440	0.950	0.940	0.899	0.831	0.796

The inclusion of the loop–base coordinate ρ_{L} in Fig. 3 clarifies the mutual placement of the loop and corridor edge points. For all configurations, the corridor–edge coordinate $\rho_{\mathrm{C}}(T)$ (corresponding to ρ_{C_1}–ρ_{C_5} in Table 1) decreases monotonically with increasing T. When $h_2 < h_1$, the values $\rho_{\mathrm{C}}(T)$ lie strictly above the loop base ρ_{L} and approach it from the right as T increases, indicating a gradual contraction of the corridor toward the loop. In contrast, when $h_2 > h_1$, the quantities $\rho_{\mathrm{C}}(T)$ remain strictly below unity and therefore stay well separated from the loop–base coordinate $\rho_{\mathrm{L}} > 1$ for all admissible values of T. In this regime, the loop and corridor bases do not approach one another as the surface tension varies; instead, their persistent separation reflects the dominance of geometric asymmetry over the capillary adjustment of the resonant and dispersive branches.

As shown in Figs. 3(a–d), for $h_2 = 1$–4 the loop–base coordinate $\rho_{\mathrm{L}} = h_2^2/25$ remains considerably smaller than the corresponding corridor–edge values ρ_{C_1}–ρ_{C_5} for all surface–tension magnitudes listed in Table 1. Hence, the corridor

always originates to the right of the loop base, satisfying $\rho_C(T) > \rho_L$. At small surface tension ($T = 1/2$) the corridor widens and its right edge extends well beyond ρ_L, forming a broad composite loop–corridor domain. As T increases, the corridor contracts and shifts leftward as $\rho_C(T)$ approaches ρ_L, and the loop correspondingly narrows. In the most asymmetric case ($h_2 = 1$) the loop remains detached from the ρ-axis, whereas for $h_2 = 2$–4 it touches the $O\rho$-axis and gradually enlarges with increasing h_2. This behaviour indicates that a thicker upper layer increases the effective inertia above the interface, thereby strengthening the dispersive response and widening the interval of nonlinear–dispersive balance at small k.

Fig. 3e corresponds to nearly symmetric configurations ($h_2 \simeq h_1$), where the loop–base point ρ_L approaches unity and the corridor–edge coordinates ρ_{C_i} ($i = 1-5$) remain slightly below 1 for all values of T. For $h_2 = 4.75$, one finds $\rho_L = 0.903$ and $\rho_{C_1} = 0.937$, indicating that at small T the corridor begins slightly to the right of the loop base, forming a large loop resting on the ρ-axis. As surface tension increases, the edge positions ρ_{C_i} shift left of ρ_L (e.g., for $T = 2$, $\rho_{C_5} = 0.749$), and the loop contracts. In the fully symmetric case $h_2 = 5$ (Fig. 3f), where $\rho_L = 1$ and all $\rho_{C_i} < 1$, no vertical asymptote appears at $\rho = 1$, and the loop always rests on the ρ-axis at $(1, 0)$. The corridor base lies to the left of this point and moves further left as T increases, showing that decreasing surface tension enlarges the corridor and enhances its overlap with the loop, whereas higher T suppresses this interaction. The convergence of ρ_L and ρ_{C_i} toward unity with increasing total depth explains the near coincidence of the loop and corridor bases in these quasi–symmetric configurations.

For $h_2 > h_1$ (Figs. 3(g, h)), the loop–base coordinate satisfies $\rho_L > 1$, while $\rho_{C_i} < 1$ for all T (see Table 1). Thus, the corridor originates to the left of the loop base, and their interaction depends on whether the corridor's right boundary at finite k extends beyond ρ_L. For slightly asymmetric configurations (h_2 close to h_1; Fig. 3(g)), this occurs only at small T, when ρ_{C_1} is closest to unity and the corridor is widest; under these conditions the loop persists in a degenerate form without reaching the ρ-axis. As the upper layer becomes thicker (h_2 further increases; Fig. 3(h)), even such degenerate loops no longer appear, and only the corridor structure remains.

These geometric dependences outline the quantitative trends governing the interaction between the loop and the corridor under varying surface tension. The corresponding physical interpretation is summarized in Sec. 3.5.

3.5. Summary and physical interpretation

The contrasting effects of surface tension in the two limiting geometries— loop formation in the HS–La system and cut development in the La–HS system— previously described in [27, 28], are consistently reproduced within the present unified two-layer framework. When the upper layer becomes thicker than the lower one, the interfacial mode acquires a predominantly capillary character: the restoring force is governed by surface tension rather than gravity, and increasing T enhances this dominance, narrowing the parameter range in which nonlinearity and dispersion compensate. Consequently, the loop shrinks and may disappear, leaving only the narrow stability corridor.

The joint analysis of ρ_L and $\rho_C(T)$ clarifies the structural transitions observed in Fig. 3. For $h_2 < h_1$ and small T, the corridor begins to the right of the loop base ($\rho_C(T) > \rho_L$), so that the loop lies entirely beneath the corridor in the (ρ, k)-plane. As T increases at fixed geometry ($h_2 < h_1$), the value $\rho_C(T)$ decreases monotonically, and the corridor correspondingly shifts leftward along the ρ-axis. When $\rho_C(T)$ drops below ρ_L (at $T = T_\times$; see Sec. 2.3), the loop ceases to exist and only the corridor remains. When $h_2 \geq h_1$, the condition $\rho_C(T) = \rho_L$ has no solution for any admissible $T > 0$, and the loop is absent for all surface–tension magnitudes.

Surface tension thus controls the relative positioning of the loop and corridor at small wavenumbers: decreasing T moves the corridor to the right and allows a loop to exist beneath it, whereas increasing T shifts the corridor leftward and eliminates the loop. In the symmetric geometric limit $h_2 \to h_1$ one has $\rho_L \to 1$, while for $T \to 0$ one obtains $\rho_C(T) \to 1^-$, so that both base points accumulate near the long–wave limiting point $(\rho, k) = (1, 0)$. In the additional deep–water limit $h_1, h_2 \to \infty$, this configuration approaches the classical model of two hydrodynamic half–spaces.

A three–dimensional perspective of these transitions is presented in Sec. 4, which shows how loops, corridors, and cuts merge or collapse as the surface–tension magnitude and the depth ratio h_2/h_1 increase.

4. THREE-DIMENSIONAL CRITICAL SURFACES $T(\rho, k)$

4.1. Analytical framework and Bond-threshold structure

A comprehensive understanding of the modulational–stability topology can be achieved by extending the two-dimensional maps of Sec. 3 into the full three-dimensional parameter space (ρ, k, T). The stability diagrams discussed earlier represent planar sections of this space at fixed T, showing how the upper stability region, the corridor, and the loop transform as the surface–tension coefficient varies. In three dimensions these structures arise from the three continuous critical surfaces defined by

$$J(\rho, k; h_1, h_2, T) = 0, \qquad J(\rho, k; h_1, h_2, T) \to \infty, \qquad \omega''(\rho, k; h_1, h_2, T) = 0,$$

and from their mutual arrangement in the (ρ, k, T) space. The first surface ($J = 0$, red) separates focusing and defocusing nonlinearities, the second ($J \to \infty$, blue) corresponds to the resonant singularity, and the third surface ($\omega'' = 0$, green)

marks the change of sign of group–velocity dispersion. Taken together, these three critical surfaces provide the geometric framework for the three–dimensional organisation of modulationally stable and unstable regions in the (ρ, k, T) space.

It is useful to distinguish between the long-wave critical value of surface tension and the full three-dimensional critical structure. The Bond threshold T^* is a scalar quantity: it specifies the value of T at which the curvature ω'' vanishes in the limit $k \to 0$, marking the transition between gravity- and capillarity-dominated dispersion. In contrast, the critical conditions $\omega'' = 0$ and $J \to \infty$ define two distinct two-dimensional surfaces in the (ρ, k, T) space. Their planar sections at fixed T give the neutral-stability curves that delimit modulationally stable and unstable regions in the (ρ, k) plane.

According to expression (8) in Subsec. 2.4, the long-wave Bond threshold $T^* = h_1^2/3$ (with $\mathrm{Bo}^* = 1/3$) is the unique value at which the long-wave limits of the resonant condition $J \to \infty$ and the dispersive condition $\omega'' = 0$ coincide at the point $(\rho, k) = (0, 0)$. In the three-dimensional space (ρ, k, T) this point lies on a one-dimensional intersection curve (a nodal line) along which the resonant (blue) and dispersive (green) surfaces meet.

Although the resonant and dispersive critical surfaces intersect along a one-dimensional curve and lie geometrically close to each other over wide regions of the (ρ, k) plane for many depth configurations, their local behaviour near $(\rho, k) = (0, 0)$ remains distinct for all $T < T^*$. At the Bond-critical value $T = T^*$, the two surfaces exhibit a local degeneracy at $(\rho, k) = (0, 0)$, where they meet at the same height and have a common tangent. For $T > T^*$, planar sections $T = \mathrm{const}$ intersect the two surfaces in a different manner, producing cut-type configurations; their detailed geometry will be discussed in Secs. 4.2–4.3.

In addition to the Bond threshold T^*, a second geometric degeneracy is associated with the depth ratio. As shown in Subsec. 2.5, the dispersive critical surface $T_{\omega''=0}(\rho, k)$ has a horizontal tangent at $(\rho, k, T) = (0, 0, T^*)$ when the layer depths satisfy the golden–ratio relation $h_2/h_1 = \varphi$. The consequences of this local geometric condition become evident in the three–dimensional structure discussed in Subsec. 4.2, where its impact on the critical surfaces is examined in detail.

4.2. Geometry of the critical surfaces and symmetry effects

Figure 4 shows the critical surfaces for the fixed lower-layer depth $h_1 = 5$ and a sequence of upper-layer thicknesses $h_2 \in \{1, 4, 5, 6, 5(1 + \sqrt{5})/2, 12, 50, 100, 150\}$. This set spans the transition from configurations with a thin upper layer to those in which the upper layer is effectively deep.

For $h_2 = 1$, the system is close to the HS–La limiting configuration, and the nonlinear surface $J = 0$ forms a pronounced loop near the origin [27]. The case $h_2 = 4$ represents moderate asymmetry, whereas $h_2 = 5$ gives the symmetric configuration discussed in Subsec. 2.2. Increasing the upper-layer thickness to $h_2 = 6$ introduces weak asymmetry. The value $h_2 = 5(1 + \sqrt{5})/2$ realises the golden–ratio depth ratio, at which both the dispersive ($\omega'' = 0$) and the resonant ($J \to \infty$) critical surfaces acquire a horizontal tangent at $(\rho, k, T) = (0, 0, T^*)$; see Subsec. 2.5. Larger values $h_2 = 12, 50, 100, 150$ correspond to progressively deeper upper layers and bring the system close to the La–HS regime, in which the dispersive (green) and resonant (blue) surfaces lie geometrically close over a wide region of the (ρ, k) domain (see Subsec. 3.3 and [28]).

In every panel the point $(\rho, k, T) = (0, 0, T^*)$ appears as the intersection of the dispersive ($\omega'' = 0$) and resonant ($J \to \infty$) surfaces. For $h_1 = 5$, its height is $T^* = 25/3$, in agreement with the analytic Bond threshold $T^* = h_1^2/3$ obtained in Subsec. 2.4.

In panels (a)–(f) of Fig. 4 the axes are scaled identically, which facilitates comparison of curvature and elevation. Panels (g)–(i) use an enlarged vertical scale that highlights the geometry of the critical surfaces for large values of h_2. These three-dimensional plots directly extend the detailed two-dimensional sections shown in Fig. 2 and analysed in Subsec. 3.3. In particular, the configurations with $h_2 = 50$, 100, and 150 correspond to planar diagrams in which three, four, and five cut-type corridors are present for the respective subsets of the surface-tension values $T = \{1, 25/3, 20\}$, $T = \{1, 25/3, 20, 40\}$, $T = \{1, 25/3, 20, 40, 60\}$. The three-dimensional representation thus visualises how these cut-type structures arise as intersections of the resonant ($J \to \infty$) and dispersive ($\omega'' = 0$) critical surfaces at the corresponding T-levels.

For small and moderate asymmetry (Figs. 4a–d), the red surface $J = 0$ forms a convex sheet that rises above the (ρ, k)-plane at small T, while the blue and green critical surfaces remain well separated. Sections at fixed T reproduce the loop– and corridor–type structures identified in the two-dimensional matrix of Subsec. 3.2. The closed intersections of $J = 0$ give the loop-type stability islands, whereas the region lying between the resonant ($J \to \infty$) and dispersive ($\omega'' = 0$) surfaces forms the open corridor that separates the low–k and high–k instability zones. Thus, in the regime of weak asymmetry these three-dimensional surfaces provide direct extensions of the characteristic curves forming the upper unstable region and the corridor in the planar diagrams of Subsecs. 3.2–3.4.

In panels (a)–(c) of Fig. 4, a grey horizontal plane marks the level $T = T_\times$ introduced in Subsec. 2.3. This plane intersects the upper part of the red surface $J = 0$ and separates the parameter ranges in which the loop has a well-defined base ($T < T_\times$) from those in which the loop becomes degenerate ($T > T_\times$), as illustrated in Fig. 3. For $h_2 = 1$ (panel (a)) and $h_2 = 4$ (panel (b)) the level $T_\times$ is positive and lies above most of the plotted region. In the symmetric case $h_2 = h_1 = 5$ (panel (c)) one has $T_\times = 0$, so the plane coincides with the coordinate plane $T = 0$. For $h_2 = 6$ (panel (d)), $T_\times < 0$, and the corresponding horizontal plane lies outside the plotted domain and is therefore not shown. A distant branch of the same red surface $J = 0$ is also visible in all panels of Fig. 4 as the remote background sheet forming the rear boundary of the three-dimensional plots. This rear branch exhibits its most noticeable deformation for small upper-layer

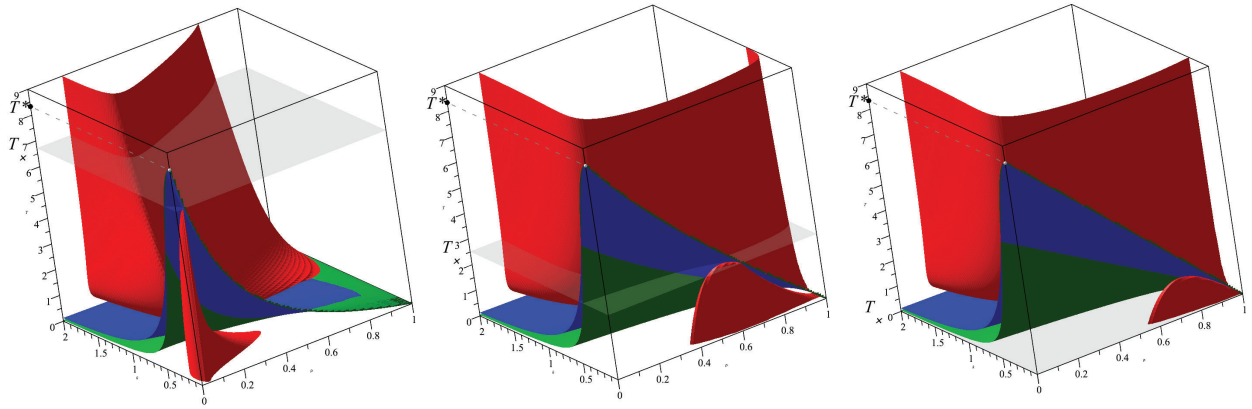

(a) $h_1 = 5,\ h_2 = 1$ **(b)** $h_1 = 5,\ h_2 = 4$ **(c)** $h_1 = 5,\ h_2 = 5$

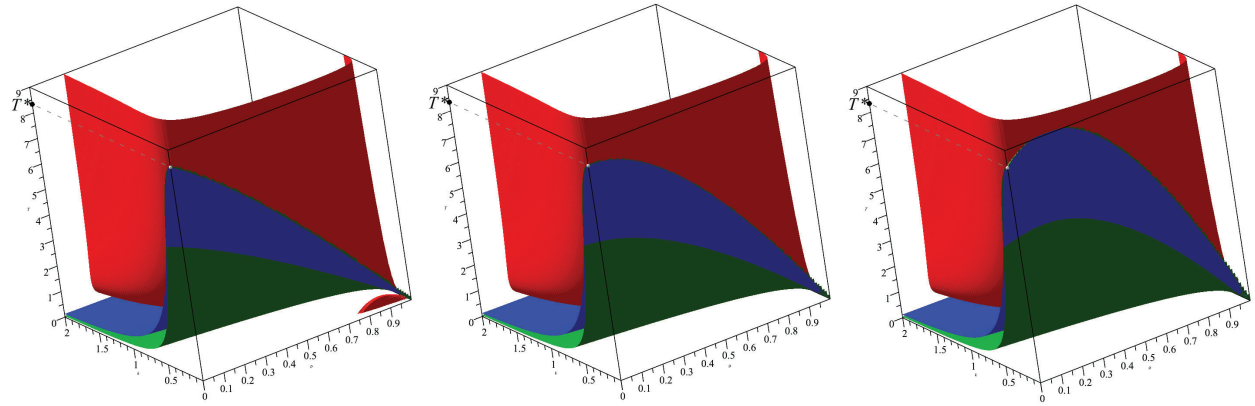

(d) $h_1 = 5,\ h_2 = 6$ **(e)** $h_1 = 5,\ h_2 = 5(1+\sqrt{5})/2 \approx 8.09$ **(f)** $h_1 = 5,\ h_2 = 12$

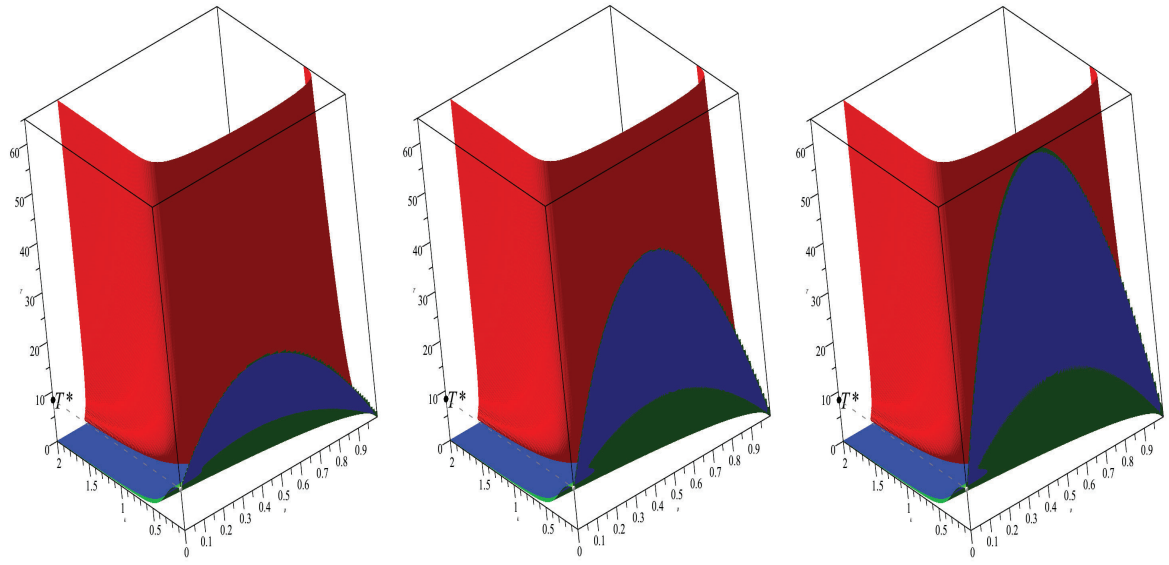

(g) $h_1 = 5,\ h_2 = 50$ **(h)** $h_1 = 5,\ h_2 = 100$ **(i)** $h_1 = 5,\ h_2 = 150$

Figure 4. Critical surfaces $T(\rho, k)$ for $h_1 = 5$ and $h_2 \in \{1, 4, 5, 6, 5(1+\sqrt{5})/2, 12, 50, 100, 150\}$.

depths: from panel (a) to panel (c) it gradually straightens, its curvature weakens, and the sheet approaches a more vertical orientation. For larger depth ratios $h_2 \geq h_1$, the subsequent changes of this background branch become smooth and relatively small; although the surface continues to deform as h_2 increases, the scale and perspective of the visualisation make these variations barely discernible in panels (d)–(i). Consequently, at large asymmetry the apparent geometry of this rear part of the red surface remains nearly unchanged, and the qualitative transformations of the modulational-stability topology are governed almost entirely by the behaviour of the blue and green surfaces.

In the vicinity of the level $T = T^*$, the singular surfaces $J \to \infty$ (blue) and $\omega'' = 0$ (green) lie geometrically close to each other and intersect along a one–dimensional curve in the three–dimensional (ρ, k, T) space. The point $(\rho, k, T) = (0, 0, T^*)$ is the lower endpoint of this curve and corresponds to the coincidence of the long–wave dispersive and nonlinear singularities. The geometry of the intersection line, as well as the shape of the adjacent upper parts of the blue and green surfaces, depends sensitively on the depth ratio h_2/h_1. For $h_2 < h_1$ the two surfaces bend downward near $(0, 0, T^*)$, giving a visibly concave intersection line (panels (a), (b)). In the symmetric case $h_2 = h_1 = 5$ (panel (c)) the intersection line becomes nearly straight, reflecting the even symmetry of the dispersive characteristics with respect to k. For $h_2 > h_1$ the line bends upward, producing a convex shape, as seen beginning from panel (d).

As h_2 increases further, the upward bending of the resonant $(J \to \infty)$ and dispersive $(\omega'' = 0)$ surfaces becomes more pronounced. At the golden–ratio depth ratio $h_2 = h_1(1 + \sqrt{5})/2$ (panel (e)), the common intersection line of the blue and green surfaces develops a horizontal tangent at the point $(\rho, k, T) = (0, 0, T^*)$, in agreement with the analytical condition of Subsec. 2.5. For $h_2 > h_1(1 + \sqrt{5})/2$, both surfaces acquire a distinct local maximum in their upper parts near small k; the same local maximum appears on their intersection line, as clearly visible in panels (f)–(i). This local extremum forces the intersection line to bend further upward in T, and its projections onto the planes $T = \text{const}$ give rise to the cut–corridor patterns described in Subsec. 3.3. In the two–dimensional stability diagrams, the intersection points of the cut boundaries correspond precisely to the projection of this three–dimensional blue–green intersection curve onto the (ρ, k) plane.

Overall, the evolution in panels (a)–(i) shows that the topological transitions in the (ρ, k)-plane are governed primarily by the geometry of the intersection line between the resonant $(J \to \infty)$ and dispersive $(\omega'' = 0)$ surfaces. For small and moderate depth ratios h_2/h_1 this line is concave or nearly straight, producing corridor–type structures, while the loop is generated independently by the front branch of the $J = 0$ surface. Once h_2 exceeds the golden–ratio value, a local maximum emerges on the upper parts of the blue and green surfaces and on their intersection line, causing it to bend upward; its projections onto $T = \text{const}$ planes then yield the characteristic cut–corridor patterns of Subsec. 3.3. Thus, the deformation of this intersection line provides the geometric link between the gravity–capillary and capillary regimes of modulational stability.

4.3. Physical interpretation and correspondence with planar maps

The red surface $J = 0$ marks the boundary between the two signs of the nonlinear NLS coefficient and therefore separates the focusing and defocusing regimes. Its geometry shows how sensitively the nonlinear response of the interface depends on the density ratio and the wavenumber. The front part of this surface, clearly visible in the three–dimensional plots, generates a closed intersection with constant–T planes, producing the loop observed in the planar diagrams. As the upper layer becomes thicker, the gravitational contribution to nonlinearity is increasingly masked by the inertia of the upper fluid, so that the capillary term in J becomes dominant. In this regime the variation of J with respect to ρ becomes much weaker, the $J = 0$ surface straightens in the ρ–direction and shifts toward larger density ratios, and the resulting loop progressively shrinks and eventually disappears.

The blue surface, corresponding to the near–resonant nonlinear response $(J \to \infty)$, and the green surface associated with the change of sign of the group–velocity dispersion $(\omega'' = 0)$, intersect along a one–dimensional curve that exists for all depth ratios. The mutual arrangement of these two surfaces, however, depends strongly on the ratio h_2/h_1. When the upper layer is thinner than the lower one, or only slightly thicker so that the depths remain comparable, the blue–green intersection line lies close to the density–matching region $\rho \simeq 1$. Away from this neighbourhood the surfaces separate, and their planar sections at fixed T produce two distinct branches whose projections bound a finite interval in ρ; this interval appears in the (ρ, k) plane as the *corridor*.

When the upper layer becomes much thicker than the lower one, the geometry changes qualitatively. For surface–tension magnitudes exceeding the long–wave threshold T^*, the upper parts of the blue and green surfaces rise in such a way that the projections of their intersection line onto the planes $T = \text{const}$ no longer bound a finite interval. In these sections the corridor collapses into a *cut*, which appears as a narrow band rooted at $k = 0$ and produced by the close proximity of the two critical surfaces in the three–dimensional geometry.

The curvature of the intersection line between the surfaces $J \to \infty$ and $\omega'' = 0$ in the neighbourhood of $k = 0$ is governed by the long–wave distribution of inertia between the two layers and therefore by the depth ratio. When the lower layer is thicker $(h_2 < h_1)$, most of the inertial mass resides in the lower fluid and the dynamical influence of the upper layer is weak. As the density ratio varies, the resonant nonlinear and dispersive mechanisms shift in different directions, and the long–wave portion of the intersection line acquires a downward concavity ($\bigcap$-shape), as seen in panels (a)–(b) of Fig. 4. In the symmetric configuration $h_2 = h_1$, the inertial contributions of the two layers become equivalent; in the long–wave limit the interface behaves as a single fluid column, and the response of the conditions $J \to \infty$ and $\omega'' = 0$ to variations in ρ is nearly synchronised. As a result, the intersection line becomes approximately straight, as in panel

(c). When the upper layer is thicker ($h_2 > h_1$), the inertial dominance reverses and the upper fluid governs the long–wave dynamics. The resonant and dispersive conditions then diverge in the opposite sense as ρ varies, and the intersection line becomes upward–concave ($\bigcup$-shape), as seen in panels (d)–(i). Thus, the change of convexity of the intersection line captures the transition from lower–layer dominance (downward concavity), through the symmetric regime (straight line), to upper–layer dominance (upward concavity).

The golden–ratio depth ratio $h_2/h_1 = \varphi$ does not by itself produce a cut. Rather, it marks the point at which the curvature of the blue–green intersection line changes sign and a horizontal tangent appears at $(\rho, k, T) = (0, 0, T^*)$. Only for depth ratios exceeding φ can a genuine local maximum develop on this line. As h_2 increases further, this maximum rises in T, and once it exceeds the level of a given plane $T = \text{const}$, the planar section exhibits a cut rooted at $k = 0$. This explains why cut–type structures appear only for sufficiently large h_2 (e.g. $h_2 = 12, 50, 100, 150$), even though the change of curvature originates at the golden–ratio configuration.

Thus, the loop, corridor, and cut correspond to three distinct physical–geometric regimes. The loop reflects a local balance between nonlinearity and dispersion. The corridor arises from a gentle separation between the resonant and dispersive mechanisms, produced when the corresponding critical surfaces remain well apart. The cut appears only when these two mechanisms become locally nearly simultaneous: for sufficiently large depth ratios and surface–tension magnitudes, the resonant and dispersive surfaces approach each other so closely that the intermediate region collapses into a narrow cut–type band rooted at $k = 0$.

5. CONCLUSIONS

Together with Part I, this study provides a unified geometric and asymptotic description of the modulational stability of interfacial gravity–capillary waves in a two-layer fluid. Treating the surface tension T as an independent control parameter reveals how capillarity modifies both the nonlinear coefficient J and the curvature of the dispersion relation ω'', and how these changes reorganise the neutral boundaries in the (ρ, k)–plane.

In the long-wave limit, the base of the loop is fixed by the geometric coordinate $\rho_{\mathrm{L}} = h_2^2/h_1^2$, whereas the base of the corridor is determined by $\rho_{\mathrm{C}}(T)$, the density at which the singular condition $J \to \infty$ meets $k = 0$ (Sec. 2.3). Their ordering is controlled by the threshold $T_\times$, which exists only when $h_1 > h_2$. Loops are possible only while $\rho_{\mathrm{L}} < \rho_{\mathrm{C}}(T)$. Once $T > T_\times$, the ordering reverses and the loop collapses. For $h_2 > h_1$, one has $\rho_{\mathrm{C}}(T) \le 1 < \rho_{\mathrm{L}}$ for all $T > 0$, so loop-type structures are excluded and only corridor-type formations remain.

A second organising parameter is the long-wave Bond threshold $T^* = h_1^2/3$, at which $\omega'' = 0$ and $J \to \infty$ coincide at $(\rho, k) = (0, 0)$. Below this value, gravity and capillarity act jointly, producing loop– and corridor–type structures with finite overlap. For $T > T^*$, the resonant ($J \to \infty$) and dispersive ($\omega'' = 0$) surfaces lie very close in a neighbourhood of the origin. When the depth ratio exceeds the golden value $h_2/h_1 = \varphi$, these surfaces develop a horizontal tangent at $(0, 0, T^*)$; for $h_2/h_1 > \varphi$, they acquire a local maximum in T. Planar sections then generate the capillary cut: a narrow corridor detached from the ρ–axis, characteristic of strongly capillary, upper–layer–dominated configurations.

The three-dimensional critical surfaces $J = 0$, $J \to \infty$ and $\omega'' = 0$ provide a single geometric framework for all observed structures. Loops, corridors, and cuts arise as planar intersections of these surfaces with planes $T = \text{const}$, and their evolution with varying T and depth ratio h_2/h_1 follows directly from the deformation of these surfaces. Two distinguished geometric configurations correspond to genuine degeneracies: equal layer depths ($h_1 = h_2$), where the resonant–dispersive intersection is a straight line, and the golden ratio ($h_2/h_1 = \varphi$), where the dispersive critical surface is horizontally tangent at $(0, 0, T^*)$. For $h_2/h_1 > \varphi$, this degeneracy evolves into a local maximum of the resonant–dispersive intersection curve and enables the onset of cut-type behaviour.

Overall, the results provide a coherent geometric framework for the classification of modulational stability in two-layer fluids with variable surface tension and extend the theory developed in Part I. They form a basis for future extensions involving shear, external forcing, flexible boundaries, or variable bathymetry.

Acknowledgments

Olga Avramenko thanks the Research Council of Lithuania for supporting this work.

ORCID

Olga Avramenko, https://orcid.org/0000-0002-7960-1436; **Volodymyr Naradovyi**, https://orcid.org/0000-0001-5187-8831

REFERENCES

[1] O. Avramenko and V. Naradovyi, East Eur. J. Phys. **3**, 239 (2025), https://doi.org/10.26565/2312-4334-2025-3-21.

[2] T. B. Benjamin, and J. E. Feir, J. Fluid Mech. **27**(3), 417 (1967). https://doi.org/10.1017/S002211206700045X

[3] V. E. Zakharov, J. Appl. Mech. Tech. Phys. **9**, 190 (1968). https://doi.org/10.1007/BF00913182

[4] R. H. J. Grimshaw, and D. I. Pullin, J. Fluid Mech. **160**, 297 (1985). https://doi.org/10.1017/S0022112085003494

[5] P. Christodoulides, and F. Dias, Phys. Fluids **7**, 3013 (1995). https://doi.org/10.1063/1.868678

[6] H. R. Dullin, G. A. Gottwald, and D. D. Holm, Fluid Dyn. Res. **33**, 73 (2003). https://doi.org/10.1016/S0169-5983(03)00046-7

[7] H. R. Dullin, G. A. Gottwald, and D. D. Holm, Physica D **190**, 1 (2004). https://doi.org/10.1016/j.physd.2003.11.004

[8] C. Sun, and E. Wahlén, arXiv:2509.17534 (2025). https://doi.org/10.48550/arXiv.2509.17534

[9] V. M. Hur, and J. Yang, arXiv:2311.01368 (2023). https://doi.org/10.48550/arXiv.2311.01368

[10] K. Ward, F. Zoueshtiagh, and R. Narayanan, Phys. Rev. Fluids **4**, 043903 (2019). https://doi.org/10.1103/PhysRevFluids.4.043903

[11] S. Li, A. Cao, J. Song, C. Yu, and J. Chen, Phys. Fluids **32**, 072104 (2020). https://doi.org/10.1063/5.0013225

[12] S. Li, X. Xie, D. Chen, and J. Song, Phys. Fluids **34**, 092105 (2022). https://doi.org/10.1063/5.0098077

[13] S. Murashige, and W. Choi, J. Fluid Mech. **938**, A13 (2022). https://doi.org/10.1017/jfm.2022.145

[14] T. Pal, and A. K. Dhar, Ocean Dyn. **72**, 241 (2022). https://doi.org/10.1007/s10236-022-01503-1

[15] T. Pal, and A. K. Dhar, Ocean Dyn. **74**, 133 (2024). https://doi.org/10.1007/s10236-023-01594-4

[16] S. Boral, B.-Y. Ni, and A.A. Korobkin, J. Fluid Mech. **1015**, A22 (2025). https://doi.org/10.1017/jfm.2025.10268

[17] S. Halder, M. Francius, A. K. Dhar, S. Mukherjee, H. C. Hsu, and C. Kharif, J. Fluid Mech. **1010**, A55 (2025). https://doi.org/10.1017/jfm.2025.318

[18] D. S. Goldobin, A. V. Pimenova, K. V. Kovalevskaya, D. V. Lyubimov, and T. P. Lyubimova, Phys. Rev. E **91**, 053010 (2015). https://doi.org/10.1103/PhysRevE.91.053010

[19] A. Doak, T. Gao, J.-M. Vanden-Broeck, and J. J. S. Kandola, Q. J. Mech. Appl. Math. **73**(3), 231 (2020). https://doi.org/10.1093/qjmam/hbaa009

[20] K. W. Chow, H. N. Chan, and R. H. J. Grimshaw, Nat. Hazards Earth Syst. Sci. **19**, 583 (2019). https://doi.org/10.5194/nhess-19-583-2019

[21] Y. Liang, A. Zareei, and M.-R. Alam, J. Fluid Mech. **811**, 400 (2017). https://doi.org/10.1017/jfm.2016.754

[22] S. Boral, T. Sahoo, and Y. Stepanyants, Symmetry **13**(4), 651 (2021). https://doi.org/10.3390/sym13040651

[23] O. L. Andreeva, L. A. Bulavin, and V. I. Tkachenko, East Eur. J. Phys. **2**, 38 (2020). https://doi.org/10.26565/2312-4334-2020-2-02.

[24] W. N. Bond, Philos. Mag. (Ser. 7) **4**(24), 889 (1927). https://doi.org/10.1080/14786441108564394

[25] F. Dias and C. Kharif, Annu. Rev. Fluid Mech. **31**, 301 (1999). https://doi.org/10.1146/annurev.fluid.31.1.301

[26] A. Davey and K. Stewartson, Proc. R. Soc. Lond. A **338**, 101 (1974). https://doi.org/10.1098/rspa.1974.0076

[27] O. Avramenko and V. Naradovyi, J. Appl. Math. Comput. Mech. **24**(2), 5 (2025), https://doi.org/10.17512/jamcm.2025.2.01.

[28] O. Avramenko and V. Naradovyi, Rend. Mat. Appl. (7) **47**, 55 (2026), https://doi.org/10.48550/arXiv.2411.15168.

НЕСТІЙКІСТЬ БЕНДЖАМІНА–ФЕЙРА МІЖФАЗНИХ ГРАВІТАЦІЙНО-КАПІЛЯРНИХ ХВИЛЬ У ДВОШАРОВІЙ РІДИНІ. ЧАСТИНА II. ВПЛИВ ПОВЕРХНЕВОГО НАТЯГУ

Ольга Авраменко[1,2], **Володимир Нарадовий**[3]

[1]*Національний університет "Києво-Могилянська академія вул. Сковороди, 2, Київ, 04070, Україна*

[2]*Університет Вітовта Великого, вул. К. Донелайчо, 58, Каунас, 44248, Литва*

[3]*Центральноукраїнський державний університет імені Володимира Винниченка, вул. Шевченка, 1, Кропивницький, 25006, Україна*

У другій частині дослідження розроблено повний геометричний та асимптотичний опис того, як поверхневий натяг визначає модуляційну стійкість інтерфейсних хвиль у двошаровій рідині. Розвиваючи аналітичну схему Частини I, поверхневий натяг розглядається як вільний керівний параметр, що дає змогу відстежувати нелінійні та дисперсійні властивості системи для широкого діапазону співвідношень глибин та контрастів густин. Використовуючи зведення до нелінійного рівняння Шредінгера разом із довгохвильовими асимптотиками, визначено механізми, що формують межі між стабільними та нестабільними режимами, та встановлено їхню залежність від величини поверхневого натягу. Довгохвильова структура контролюється двома спеціальними значеннями густини, які задають точки зародження петлі та коридору на діаграмах стійкості. Взаємне розташування цих точок змінюється за певного порогу, що існує лише тоді, коли нижній шар є глибшим, і саме в цьому випадку можливе існування петлі. Другим організувальним параметром є класичний поріг Бонда, за якого дисперсійна і нелінійна сингулярності збігаються. Коли поверхневий натяг перевищує це значення і верхній шар є достатньо глибоким, взаємодія резонансних та дисперсійних ефектів утворює капілярний розріз, який заміщує коридор і характеризує режими з домінуванням капілярності. Для об'єднання цих спостережень побудовано повні тривимірні критичні поверхні, що розмежовують різні типи нелінійної та дисперсійної поведінки. Петля, коридор і розріз постають як площинні перерізи цих поверхонь, а їхні топологічні переходи безпосередньо зумовлені деформацією лінії перетину між резонансною та дисперсійною поверхнями. Два співвідношення глибин відповідають справжнім геометричним виродженням: рівні товщини шарів, коли лінія перетину стає прямою, та конфігурація золотого перетину, коли критична поверхня набуває горизонтальної дотичної при порозі Бонда. У цілому, Частина II завершує геометричну та фізичну класифікацію модуляційної стійкості інтерфейсних хвиль у двошарових рідинах і формує основу для подальших узагальнень, що враховують зсувні течії, зовнішні збурення, гнучкі межі або змінну батиметрію.

Ключові слова: *модуляційна нестійкість; міжфазні гравітаційно–капілярні хвилі; двошарова рідина; поверхневий натяг; нестійкість Бенджаміна–Фейра*

EAST EUROPEAN JOURNAL OF PHYSICS. **1.** 127-133 (2026)
DOI:10.26565/2312-4334-2026-1-10 ISSN 2312-4334

SELF-FOCUSING DYNAMICS OF COSH-GAUSSIAN LASER BEAMS IN ABSORPTIVE COLD QUANTUM PLASMA UNDER RELATIVISTIC AND PONDEROMOTIVE NONLINEARITIES

Deepak Tripathi[1], Nisha Singh Rathore[2], Vinit Kakkar[3], Keshav Walia[4]*
[1]*Physics Department, USAR/USBS, Guru Gobind Singh Indraprastha University, East Delhi Campus, Delhi, India-110032*
[2]*Department of Applied Sciences, KCC institute of Technology and Management, Greater Noida, India*
[3]*Department of Physics, Lotus Valley International School, Sector-50, Gurgaon, India*
[4]*Department of Physics, DAV University Jalandhar, Punjab, India*
**Corresponding Author e-mail: keshavwalia86@gmail.com*
Received December 28, 2025; revised February 14, 2026; accepted February 16, 2026

The current study examines self-focusing behavior of Cosh-Gaussian laser beams in absorptive cold quantum plasma, incorporating merged influence of relativistic mass variation and ponderomotive effects. Applying WKB approximation in combination with paraxial theory, 2nd order propagation equation describing variation of beam width as a function of normalized distance is derived incorporating effect of linear absorption. The numerical solution of resulting differential equation is obtained by 4th order Runge-kutta method. Further, a comprehensive parametric study is performed to access effect of laser-plasma parameters such as beam intensity, plasma density, initial beam radius, decentered parameter and absorption coefficient on beam dynamics. The results show that relativistic and ponderomotive nonlinearities enhance self-focusing, whereas absorption reduces it. Comparison with classical relativistic plasma underscores the key role of quantum effects in laser propagation through dense plasmas.
Keywords: *Self-focusing dynamics; Cosh-Gaussian beam; Relativistic mass variation; Ponderomotive effects; Linear absorption*
PACS: 52.38.Hb, 52.35.Mw, 52.38.Dx

1. INTRODUCTION

Laser beam self-focusing in plasma is a fundamental nonlinear phenomenon attracting interest from theoretical/experimental groups. This phenomenon was first time reported by Askar'yan in 1962[1]. In self-focusing, the intensity of laser beam alters the refractive index of plasma medium, thereby causing beam to self-focus without any external optical components. This intrinsic focusing tendency plays a pivotal role in many advanced applications including laser driven fusion, X-ray lasers, high energy particle acceleration and nonlinear optical experiments [2-9]. It has been confirmed from past literature that self-focusing phenomenon may arise in distinct nonlinear media including plasmas, atomic clusters and related materials. There exist many mechanisms that lead to self-focusing in plasma media. These mechanisms include relativistic self-focusing, ponderomotive self-focusing and thermal self-focusing. In relativistic self-focusing, an intense laser beam induces an effective increase in electronic mass, thereby modifying plasma's dielectric response. In addition to relativistic effects, ponderomotive and thermal self-focusing also contribute significantly to beam's convergence. Each of these mechanisms induces refractive index modifications, thereby enhancing the beam's focusing. Early work in this area was conducted by Hora and Siegrist [10-11]. Relativistic and ponderomotive nonlinearities are often studied separately, through both can co-exist depending on pulse duration. Relativistic effects dominate for $\tau < \tau_e$, while for $\tau_e < \tau < \tau_i$, both act together. In this regime, ponderomotive nonlinearity strengthens relativistic self-focusing and plasma density modulation. Self-focusing often triggers secondary nonlinear phenomena including harmonic production, filamentation, and parametric instabilities, which are critical in high intensity laser plasma interactions [12-27].

Recent developments in plasma physics have focused on laser interactions with quantum plasmas, which are characterized by high electron densities and low temperatures. In quantum plasmas, some effects such as electron degeneracy, quantum tunneling and wave-function becomes significant. While classical plasmas are governed by Maxwell-Boltzmann statistics, whereas electrons in quantum plasmas obey Fermi-Dirac statistics, and their behavior is best described through Wigner formalism [28-32]. Quantum effects become dominant when electron De-Broglie wavelength is comparable to or greater than inter-particle spacing, leading to pronounced modifications in plasma properties. Quantum plasmas are of interest for astrophysical/cosmological systems, dense plasma devices, semiconductor systems, quantum dots, and inertial confinement fusion experiments [33-40].

Most previous studies on laser propagation in quantum plasmas have focused on cylindrical symmetric Gaussian beams, which provide limited control over beam's intensity profile [41-43]. Cosh-Gaussian (ChG) laser beams offer a more general and flexible intensity profile, with adjustable intensity distribution that better represents realistic laser pulses. Unlike conventional Gaussian beams, ChG beams provide extra control via decentered parameter, allowing precise manipulation of self-focusing. The enhanced control improves energy localization, reduces diffraction, and strengthens laser plasma interactions. Linear absorption further affects beam's energy distribution, altering plasma dielectric response and overall propagation. Understanding these effects is crucial for accurately modeling laser-plasma interactions under

Cite as: D. Tripathi, N.S. Rathore, V. Kakkar, K. Walia, East Eur. J. Phys. 1, 127 (2026), https://doi.org/10.26565/2312-4334-2026-1-10

practical experimental conditions. In this study, we investigate self-focusing of ChG laser beams in absorptive cold quantum plasma to achieve a more realistic description of laser-plasma dynamics. Both relativistic modification of electron mass and ponderomotive nonlinear effects are included to describe beam propagation under intense laser fields. The paper is structured as follows: Section 2 presents the derivation of governing 2nd order differential equation using WKB and paraxial approximations. Section 3 explains numerical method and discusses the influence of different parameters on beam dynamics. Finally, section 4 summarizes main results and highlights the important features observed due to quantum plasma effects.

2. NONLINEAR DYNAMICS OF LASER BEAM WIDTH

The transverse electric field distribution of a ChG laser beam at the input plane ($z = 0$) can be written as

$$E(r,0) = E_0 \exp\left(-\frac{r^2}{r_0^2}\right) Cosh(\rho_0 r) \tag{1}$$

Where r_0 is initial beam width, r denotes radial coordinate in a cylindrical coordinate system, E_0 represents peak field amplitude. The parameter $'\rho_0'$, known as Cosh-factor, governs the deviation of beam from standard Gaussian profile. Using the identity of hyperbolic cosine function, Eq. (1) can be equivalently expressed as superposition of two laterally displaced Gaussian beams as

$$E(r,0) = E_0 \exp\left(\frac{b^2}{4}\right)\left\{exp\left(-\left[\frac{r}{r_0}+\frac{b}{2}\right]^2\right) + exp\left(-\left[\frac{r}{r_0}-\frac{b}{2}\right]^2\right)\right\} \tag{2}$$

Where, $b = r_0\rho_0$ is denoted as decentered parameter. This parameter controls separation of Gaussian components, shaping beam profile and influencing self-focusing. During the propagation along z-direction, the ChG beam's transverse profile evolves under influence of diffraction and nonlinear plasma effects. The field distribution at an arbitrary propagation distance z is given by

$$E(r,z) = \frac{E_0}{2f} \exp\left(\frac{b^2}{4}\right)\left\{exp\left(-\left[\frac{r}{r_0 f}+\frac{b}{2}\right]^2\right) + exp\left(-\left[\frac{r}{r_0 f}-\frac{b}{2}\right]^2\right)\right\} \tag{3}$$

Where, $f(z)$ represents the normalized beam width parameter describing the dynamics of beam spot size during transition. The formulation clearly illustrates enhanced flexibility of Cosh-Gaussian beams over conventional Gaussian beams, enabling precise control of intensity distribution and nonlinear propagation characteristics in plasma media.

The transition of pump beam in plasma medium is described by wave equation for field vector. In non-uniform plasma, this equation takes the form

$$\nabla^2 E - \nabla(\nabla . E) + \frac{\omega^2}{c^2}\varepsilon E = 0 \tag{4}$$

Where, ε represents dielectric function of plasma, ω is beam's angular frequency, and c is light's speed. The second term accounts for spatial variations of dielectric function and becomes important only when the plasma inhomogeneity is strong. For slowly varying plasma density, the dielectric function changes smoothly in space. Under the condition, $\frac{1}{k^2}[\nabla^2 \ln \epsilon] \ll 1$, the contribution of second term in Eq. (4) can be neglected. Consequently, the wave equation simplifies to

$$\nabla^2 E + \frac{\omega^2}{c^2}\varepsilon E = 0 \tag{5}$$

As the laser beam propagates through cold quantum plasma, its oscillating electric field drives plasma electrons in to oscillatory motion. In the relativistic intensity regime, this motion leads to an effective increase in electron mass. The corresponding oscillatory velocity of electron is given by $v = \frac{eE}{m_0\omega\gamma}$. Here, $'\gamma'$ is relativistic Lorentz factor expressed as $\gamma = (1 + \alpha E E^*)^{1/2}$ with $\alpha = \frac{e^2}{m_0^2\omega_0^2 c^2}$ being nonlinear coefficient.

In the nonlinear regime of laser-plasma interaction, the dielectric response of medium becomes explicitly dependent on intensity of electromagnetic field. Accordingly, the dielectric function can be expressed in general form as

$$\epsilon = \varepsilon_0 + \Phi(E \cdot E^*) \tag{6}$$

Where, $\varepsilon_0 = 1 - \frac{\omega_p^2}{\omega^2}$ represents the linear, intensity-independent contribution, while $\Phi(E \cdot E^*)$ accounts for nonlinear modification arising due to relativistic electron mass variation and quantum mechanical effects induced by strong laser field. The plasma frequency is defined as $\omega_p = \sqrt{\frac{4\pi n e^2}{m}}$. For an unmagnetized cold quantum plasma (CQP), merged influence of relativistic and quantum corrections leads to dielectric function given by [44]

$$\epsilon = 1 - \frac{\omega_p^2}{\gamma\omega^2}\left(1 - \frac{\delta q}{\gamma}\right)^{-1} \tag{7}$$

Here, the parameter $'\delta q'$ measures the strength of quantum effects and is expressed as $\delta q = \frac{4\pi^4 \hbar^2}{m^2\omega^2\lambda^4}$. Where, $'h'$ denotes Planck's constant and λ is the wavelength of incident laser beam. In the classical limit, where quantum effects are negligible, $\delta q -> 0$, So, Eq. (6) reduces to well-known dielectric response of classical relativistic plasma (CRP).

$$\epsilon = 1 - \frac{\omega_p^2}{\gamma\omega^2} \tag{8}$$

The redistribution of electrons in plasma arises due to action of ponderomotive force associated with intense laser field. This force drives electrons away from portions of high field intensity, leading to a modification in local electron density. The resulting density variation can be expressed as [44]

$$n = n_0 exp\left(-\frac{mc^2}{T}(\gamma - 1)\right) \tag{9}$$

By substituting modified electron density given by Eq.(9) in dielectric function expressions and combining Eqs. (6), (7) and (9), the nonlinear contribution to dielectric function is obtained as

$$\Phi(E \cdot E^*) = \frac{\omega_{p0}^2}{\omega^2}\left[1 - \left(1 - \frac{\delta q}{\gamma}\right)^{-1} \exp\left(-\frac{mc^2}{T}(\gamma - 1)\right)\right] \tag{10}$$

Where $\omega_{p0} = \sqrt{\frac{4\pi n_0 e^2}{m_0}}$.

Following [41-43], the wave Eq.(5) is solved by adopting slowly varying envelope approximation, wherein the laser field is represented as a slowly varying amplitude modulating a oscillating carrier wave. Accordingly, the electric field is represented as

$$E = E_0(r, z)\exp[i(\omega t - k(S + z))] \tag{11}$$

The corresponding intensity distribution of propagating ChG beam is given by

$$E_0(r, z) = \frac{E_{00}}{2f} exp\left(\frac{b^2}{4}\right)\left\{exp\left(-\left[\frac{r}{r_0 f} + \frac{b}{2}\right]^2\right) + exp\left(-\left[\frac{r}{r_0 f} - \frac{b}{2}\right]^2\right)\right\} \tag{12}$$

The phase function $'S'$, which accounts for both curvature of wave-front and the accumulated longitudinal phase change during propagation, can be expressed as

$$S = \frac{1}{2}r^2\frac{1}{f}\frac{df}{dz} + \Phi_0(z) \tag{13}$$

Where, $\Phi_0(z)$ denotes cumulative longitudinal phase shift accumulated by laser beam during its propagation through plasma medium. The wave number k of laser beam inside plasma is defined as

$$k = \frac{\omega}{c}\sqrt{\varepsilon_0} \tag{14}$$

The transverse dynamics of laser beam is completely described by beam width parameter $'f(z)'$, which characterizes variation of beam spot size during propagation. To simplify analysis, a normalized propagation distance $'\eta'$ is introduced. In terms of this normalized variable, the evolution of beam width $'f(z)'$ along propagation direction is governed by 2nd order nonlinear differential equation, which captures combined effects of diffraction, nonlinear plasma response and absorption of beam propagation.

$$\frac{d^2 f}{d\eta^2} = \frac{1}{f^3} - \left(\frac{\omega_{p0} r_0}{c}\right)^2 (2 - b^2)\frac{\alpha E_{00}^2 exp(-2k_i\eta)}{2f^3}\frac{exp\left(-\frac{mc^2}{T_e}\left[\sqrt{1+\frac{\alpha E_{00}^2 exp(-2k_i\eta)}{f^2}} - 1\right]\right)}{\left(1+\frac{\alpha E_{00}^2 exp(-2k_i\eta)}{f^2}\right)^{3/2}\left(1-\frac{\delta q}{\sqrt{1+\frac{\alpha E_{00}^2 exp(-2k_i\eta)}{f^2}}}\right)^2}\left[1 + \frac{mc^2}{T_e}\sqrt{1+\frac{\alpha E_{00}^2 exp(-2k_i\eta)}{f^2}}\left(1 - \frac{\delta q}{\sqrt{1+\frac{\alpha E_{00}^2 exp(-2k_i\eta)}{f^2}}}\right)\right] \tag{15}$$

Eq. (15) describes how the normalized beam waist $'f(z)'$ evolves with the normalized distance. Diffraction, represented by 1st term, causes the beam to spread during propagation, whereas 2nd term arises from nonlinear relativistic-ponderomotive effects in cold quantum plasma, which promotes self-focusing by modifying plasma response. The balance between these opposing mechanisms determines whether the beam spreads, self-focuses, or show oscillatory behavior.

3. DISCUSSION

Due to the inherent nonlinearity of Eq. (15), an exact analytical solution is not feasible. Therefore, the numerical solution is obtained using the 4th-order Runge-Kutta method. The simulations are carefully performed for a chosen range of laser and plasma parameters corresponding to realistic experimental conditions, allowing a meaningful analysis of beam propagation behavior in plasma:

$$\alpha E_{00}^2 = 3.0, 4.0, 5.0; \frac{\omega_{p0}^2}{\omega^2} = 0.6, 0.7, 0.8; k_i = 0.1, 0.4, 0.7\ ; b = 1.0, 2.0, 3.0; r_0 = 10\ \mu m, 15\ \mu m, 20\ \mu m$$

The propagation dynamics of beam width described by Eq. (15) arises from interplay between diffraction and nonlinear focusing. Diffraction accounts for inherent tendency of beam to spread while propagating through plasma; its dominance leads to beam divergence and leading to a broadening of lateral dimensions of beam. On the other hand, high power laser field nonlinearly modifies plasma dielectric response, producing a self-focusing effect. When this mechanism dominates, the beam contracts and its width decreases. A balanced regime is achieved, when diffraction and nonlinear focusing exactly counteract each other. In this regime, the beam propagates in a stable manner with a constant transverse width.

Figure 1 presents variation of beam width f along propagation distance η for beam intensities $\alpha E_{00}^2 = 3.0, 4.0,$ and 5.0, shown by Black, Red, and Green respectively. In each case, the beam width displays a characteristic oscillatory pattern arising from saturation of plasma's dielectric response. With increasing laser intensity, diffraction effects become more significant against the nonlinear focusing effect, diminishing beam's ability to contract. As a result, at higher intensities, the beam reaches its minimum width farther along the propagation path, clearly indicating a reduction in self-focusing effect.

Figure 2 presents variation of beam width f along propagation distance η for plasma densities $\omega_{p0}^2/\omega^2 = 0.6, 0.7, 0.8$, shown by Black, Red, and Green respectively. In each case, the beam width displays a characteristic oscillatory pattern arising from saturation of plasma's dielectric response. With increasing plasma density, nonlinear focusing effects become more significant against diffraction effects, strengthening beam's ability to contract. As a result, at higher densities, the beam reaches its minimum width at an earlier point along the propagation, clearly indicating a amplification in self-focusing effect.

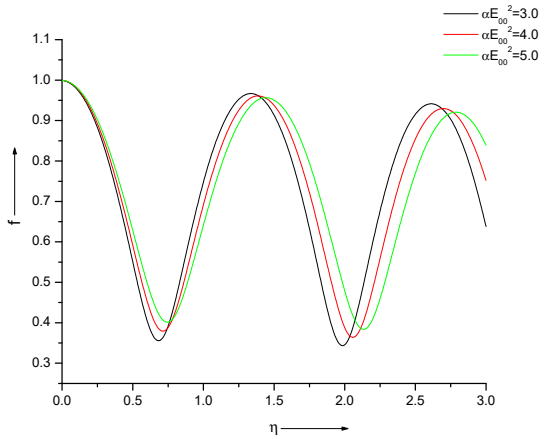

Figure 1. Variation of beam width f along propagation distance η for beam intensities $\alpha E_{00}^2 = 3.0, 4.0,$ and 5.0, shown by Black, Red, and Green respectively

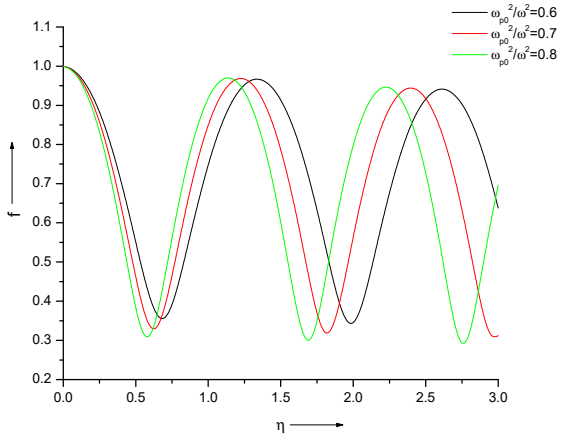

Figure 2. Variation of beam width f along propagation distance η for plasma densities $\omega_{p0}^2/\omega^2 = 0.6, 0.7, 0.8$, shown by Black, Red, and Green respectively

Figure 3 presents variation of beam width f along propagation distance η for beam radii $r_0 = 10\ \mu m,$ $15\ \mu m,$ and $20\ \mu m$, shown by Black, Red, and Green respectively. For each scenario, the beam width shows a regular oscillatory pattern caused by nonlinear saturation of plasma dielectric properties. With higher beam radius, the influence of nonlinear focusing grows compared to diffraction, promoting stronger beam convergence. Accordingly, at elevated beam radii, the beam achieves its minimum width at a shorter propagation distance, indicating strengthened self-focusing.

Figure 4 presents variation of beam width f along propagation distance η for decentered parameter, $b = 1.0,2.0,3.0$, shown by Black, Red, and Green respectively. For each scenario, the beam width shows a regular oscillatory pattern caused by nonlinear saturation of plasma dielectric properties. Increasing the decentered parameter amplifies the role of nonlinear focusing relative to diffraction, promoting tighter beam focusing. A higher decentered parameter increases local beam intensity, enhancing nonlinear plasma response. This strengthens self-focusing over diffraction, leading to tighter beam contraction and stronger confinement along propagation.

Figure 5 presents variation of beam width f along propagation distance η for distinct k_i values, $k_i = 0.1, 0.4, 0.7$, shown by Black, Red, and Green respectively. The figure demonstrates that an increase in k_i reduces beam's contraction driven by enhanced energy dissipation via absorption. With increasing absorption, the gradient of plasma refractive index

weakens, weakening nonlinear focusing mechanism. Consequently, diffraction predominates, causing the beam to converge less efficiently, and maintain a wider transverse profile during propagation.

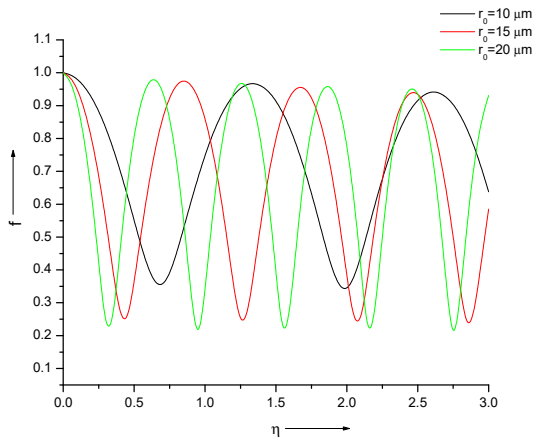

Figure 3. Variation of beam width f along propagation distance η for beam radii $r_0 = 10\ \mu m, 15\ \mu m,$ and $20\ \mu m$, shown by Black, Red, and Green respectively

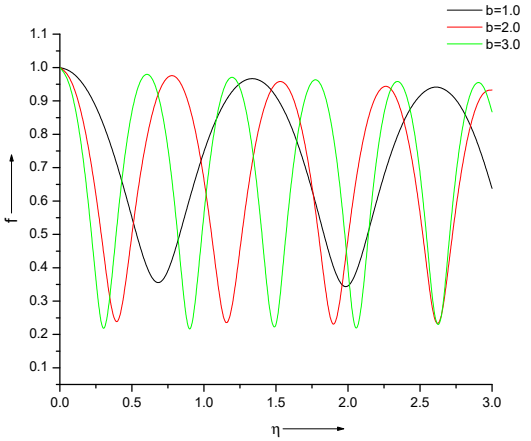

Figure 4. Variation of beam width f along propagation distance η for decentered parameter, $b = 1.0,2.0,3.0$, shown by Black, Red, and Green respectively

Figure 6 presents variation of beam width f along propagation distance η for three distinct plasma regimes. The black curve depicts the combined influence of relativistic-ponderomotive cold quantum plasma (RPCQPP), while red curve corresponds to cold quantum plasma (CQP) alone, and the green curve corresponds to classical relativistic plasma (CRP) alone. Beam focusing occurs earliest in the RPCQP case, compared to both CQP and CRP. In CQP regime, the beam exhibits stronger focusing than in CRP scenario. This behavior highlights the significant role of quantum effects, which enhance the nonlinear focusing contribution relative to diffraction, thereby improving the overall focusing of beam.

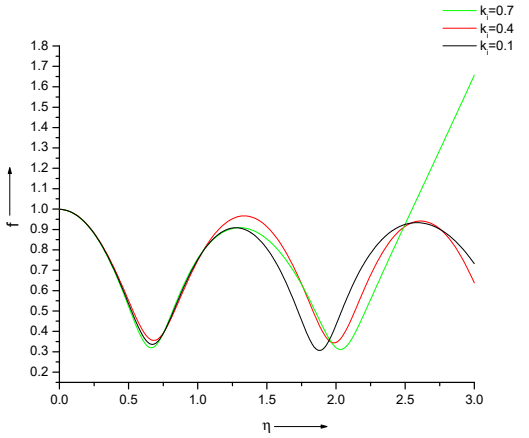

Figure 5. Variation of beam width f along propagation distance η for distinct k_i values, $k_i = 0.1, 0.4, 0.7$, shown by Black, Red, and Green respectively

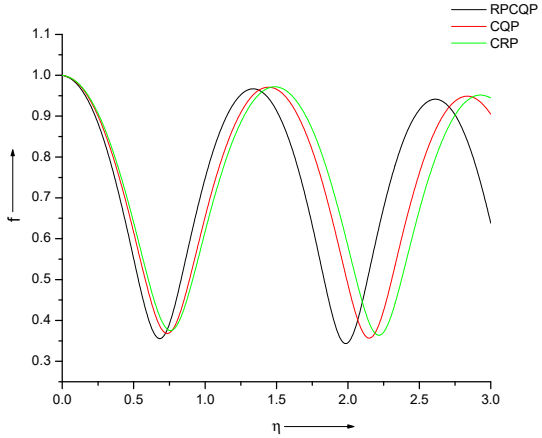

Figure 6. Variation of beam width f along propagation distance η for three distinct plasma regimes. The black curve depicts the combined influence of relativistic-ponderomotive cold quantum plasma (RPCQPP), while red curve corresponds to cold quantum plasma (CQP) alone, and the green curve corresponds to classical relativistic plasma (CRP) alone

4. CONCLUSIONS

This work presents a comprehensive study of self-focusing dynamics of ChG laser beams propagating through absorptive cold quantum plasma, incorporating RP force. Employing WKB and paraxial approximations, the self-focusing equation is derived. The results reveal that the beam's convergence is enhanced with increasing number density, beam radius, and decentered parameter, as these parameters strengthen nonlinear refractive index. Conversely, higher beam intensity reduces focusing effect. Furthermore, inclusion of quantum contribution amplifies nonlinear convergence term, leading to markedly stronger self-focusing of beam. These results help understand and control laser propagation in plasma, useful for improving laser-driven fusion and other high intensity laser applications.

Funding

No funding was received for conducting this study.

Conflict of Interest

The authors declare that there are no conflicts of interest.

ORCID

Deepak Tripathi, https://orcid.org/0000-0001-9945-4069; **Keshav Walia,** https://orcid.org/0000-0001-9547-3027

REFERENCES

[1] G.A. Askaryan, "Effects of the Gradient of a Strong Electromagnetic Beam on Electrons and Atoms," JETP, 15, 1088 (1962).
[2] D. Tripathi, S. Kaur, A. Vijay, and K. Walia, "Nonlinear Dynamics of q-Gaussian Laser Beam in Collisional Plasma: Effect of Linear Absorption," J. Contemp. Phys. **60**, 16 (2025). https://doi.org/10.1134/s1068337225700409
[3] K. Walia, N. Mehra, and S. Pandit, "Propagation Characteristics of q-Gaussian Laser Beam in Cold Collisionless Plasma," J. Contemp. Phys. **59**, 378(2024). https://doi.org/10.1134/s1068337225700203
[4] P.B. Corkum, C. Rolland, and T. Rao, "Supercontinuum Generation in Gases," Phys. Rev. Lett. **57**, 2268 (1986). https://doi.org/10.1103/physrevlett.57.2268
[5] P. Sprangle, E. Esarey, and J. Krall, "Laser driven electron acceleration in vacuum, gases, and plasmas," Phys. Plasmas, **3**, 2183 (1996). https://doi.org/10.1063/1.871673
[6] S.C. Wilks, J.M. Dawson, W.B. Mori, T. Katsouleas, and M.E. Jones, "Photon accelerator," Phys. Rev. Lett. **62**, 2600 (1989). https://doi.org/10.1103/physrevlett.62.2600
[7] K.A. Brueckner, and S. Jorna, "Laser-driven fusion", Rev. Mod. Phys. **46**, 325(1974). https://doi.org/10.1103/revmodphys.46.325
[8] J. Faure, Y. Glinec, A. Pukhov, S. Kiselev, S. Gordienko, E. Lefebvre, J.P. Rousseau, *et al*., "A laser-plasma accelerator producing monoenergetic electron beams," Nature, **431**, 541 (2004). https://doi.org/10.1038/nature02963
[9] P.E. Young, H.A. Baldis, R.P. Drake, E.M. Campbell, and K.G. Estabrook, "Direct Evidence of Ponderomotive Filamentation in a Laser-Produced Plasma," Phys. Rev. Lett. 61, 2336 (1988). https://doi.org/10.1103/physrevlett.61.2336
[10] H. Hora, "Self-focusing of laser beams in a plasma by ponderomotive forces," Z. Phys. **226**, 156(1969).
[11] M.R. Siegrist, "Self-focusing in a plasma due to ponderomotive forces and relativistic effects," Opt. Commun. **16**, 402 (1976).
[12] K. Walia, "Self-focusing of high power beam in unmagnetized plasma and its effect on Stimulated Raman scattering process," Optik, **225**, 165592 (2021). https://doi.org/10.1016/j.ijleo.2020.165592
[13] K. Walia, "Stimulated Brillouin Scattering of high power beam in unmagnetized plasma: Effect of relativistic and ponderomotive nonlinearities," Optik, **221**, 165365 (2020). https://doi.org/10.1016/j.ijleo.2020.165365
[14] K. Walia, "Propagation characteristics of a high-power beam in weakly relativistic-ponderomotive thermal quantum plasma", Commun. Theor. Phys. **75**, 095501 (2023). https://doi.org/10.1088/1572-9494/accf82
[15] K. Walia, "Self-focusing of q-Gaussian beam in unmagnetized plasma and its impact on second harmonic generation," Optik, **277**, 170681 (2023). https://doi.org/10.1016/j.ijleo.2023.170681
[16] K. Walia, "Nonlinear Dynamics of Intense Laser Beam in Unmagnetized Plasma and its Influence on Second Harmonic Generation," J. Fusion Energ. **41**, 21 (2022). https://doi.org/10.1007/s10894-022-00335-7
[17] H. Hora, "Theory of Relativistic Self-Focusing of Laser Radiation in Plasmas," J. Opt. Soc. Am. **65**, 882 (1975). https://doi.org/10.1364/josa.65.000882
[18] A.G. Litvak, "Self-focusing of Powerful Light Beams by Thermal Effects", JETP Lett. **4**, 230 (1966).
[19] W.B. Mori, C. Joshi, J. Dawson, D. Forslund, and J. Kindel, "Evolution of self-focusing of intense electromagnetic waves in plasma," Phys. Rev. Lett. **60**, 1298(1988). https://doi.org/10.1103/physrevlett.60.1298
[20] T. Singh, and K. Walia, "Impact of High-Power Cosh-Gaussian Beam on Second Harmonic Generation in Collisionless Magnetoplasma," J. Contemp. Phys. **59**, 254 (2024). https://doi.org/10.1134/s106833722470049x
[21] K. Singh, and K. Walia, "Second Harmonic Generation of High Power Cosh-Gaussian Beam in Thermal Quantum Plasma: Effect of Relativistic and Ponderomotive Nonlinearity", J. Contemp. Phys. **59**, 244 (2024). https://doi.org/10.1134/s1068337224700488
[22] K. Singh, K. Walia, "Influence of Self-Focused Elliptical Laser Beam on Second Harmonic Generation in Cold Quantum Plasma," J. Contemp. Phys. **59**, 154 (2024). https://doi.org/10.1134/s1068337224700300
[23] D. Tripathi, T. Singh, A. Vijay, and K. Walia, "Second Harmonic Generation of q-Gaussian Laser Beam in Thermal Quantum Plasma," J. Contemp. Phys. **60**, 171 (2025). https://doi.org/10.1134/s1068337225700574
[24] K. Walia, "Enhanced Brillouin scattering of Gaussian laser beam in collisional plasma: Moment theory approach," J. Nonlinear Opt. Phys. Mater. **23**, 1450011 (2014). https://doi.org/10.1142/s0218863514500118
[25] R.Y. Chiao, E. Garmire, and C.H. Townes, "Self-trapping of optical beams," Phys. Rev. Lett. **13**, 479 (1964). https://doi.org/10.1103/physrevlett.13.479
[26] P.L. Kelley, "Self-focusing of optical beams," Phys. Rev. Lett. **15**, 1005 (1965). https://doi.org/10.1103/physrevlett.15.1005
[27] H.M. Milchberg, C.G. Durfee III, and T.J. Mcllrath, "High-order frequency conversion in the plasma waveguide," Phys. Rev. Lett. **75**, 2494 (1995). https://doi.org/10.1103/physrevlett.75.2494
[28] N.S. Rathore, and P. Kumar, "Ponderomotive self-focusing of linearly polarized laser beam in magnetized quantum plasma," Laser Part Beams, **34**, 764 (2016). https://doi.org/10.1017/s0263034616000689
[29] S.D. Patil, M.V. Takale, S.T. Navare, M.B. Dongare, and V.J. Fulari, "Self-focusing of Gaussian laser beam in relativistic cold quantum plasma," Optik, **124**, 180 (2013). https://doi.org/10.1016/j.ijleo.2011.11.061
[30] P.K. Shukla, and B. Eliasson, "Nonlinear aspects of quantum plasma physics," Phys. Usp. **53**, 55 (2010).
[31] P.K. Shukla, and B. Eliasson, "Nonlinear collective interactions in quantum plasmas with degenerate electron fluids," Rev. Mod. Phys. **83**, 885 (2011).
[32] L. Bergamin, P. Alitalo, and S. Tretyakov, "Nonlinear transformation of optics and Engineering of Kerr effect," Phys. Rev. B, **84**, 205103 (2011). https://doi.org/10.1103/physrevb.84.205103
[33] S.X. Hu, and C.H. Keitel, "Spin signatures in intense laser-ion interaction," Phys. Rev. Lett. 83, 4709 (1999). https://doi.org/10.1103/physrevlett.83.4709

[34] P.K. Shukla, and L. Stenflo, "Stimulated scattering instabilities of electromagnetic waves in an ultracold quantum plasma," Phys. Plasmas, **13**, 044505 (2006). https://doi.org/10.1063/1.2196248
[35] G. Manfredi, "How to Model Quantum Plasmas," Fields Inst. Commun. **46**, 263 (2005). https://doi.org/10.1090/fic/046/10
[36] P.K. Shukla, S. Ali, L. Stenflo, and M. Marklund, "Nonlinear wave interactions in quantum magnetoplasmas," Phys. Plasmas, **13**, 112111 (2006). https://doi.org/10.1063/1.2390688
[37] G. Shpatakovskaya, "Semiclassical model of a one-dimensional quantum dot," J. Exp. Theor. Phys. Lett. **102**, 466 (2006). https://doi.org/10.1134/s1063776106030095
[38] A.K. Harding, and D. Lai, "Physics of strongly magnetized neutron stars," Rep. Prog. Phys. **69**, 2631 (2006). https://doi.org/10.1088/0034-4885/69/9/r03
[39] A.V. Andreev, "Self-consistent equations for the interaction of an atom with an electromagnetic field of arbitrary intensity,", J. Exp. Theor. Phys. Lett. **72**, 238 (2000).
[40] S.H. Glenzer, and R. Redmer, "X-ray Thomson scattering in high energy density plasmas," Rev. Mod. Phys. **81**, 1625(2009). https://doi.org/10.1103/revmodphys.81.1625
[41] S.A. Akhmanov, A.P. Sukhorokov, and R.V. Kokhlov, "Self-focusing and diffraction of light in nonlinear medium," Sov. Phys. Uspekhi, **10**, 609 (1968).
[42] M.S. Sodha, A.K. Ghatak, and V.K. Tripathi, "Self focusing of laser beams in plasmas and semiconductors," Progress in Optics, **13**, 169 (1976).
[43] M.S. Sodha, A.K. Ghatak, and V.K. Tripathi, *Self Focusing of Laser Beams in Dielectrics, Semiconductors and Plasmas*, (Tata-McGraw-Hill, Delhi, 1974).
[44] Y. Jung, and I. Murakami, "Quantum effects on magnetization due to ponderomotive force in cold quantum plasmas," Phys. Lett. A, **373**, 969 (2009). https://doi.org/10.1016/j.physleta.2009.01.024

ДИНАМІКА САМОФОКУСУВАННЯ КОШ-ГАУСІВСЬКИХ ЛАЗЕРНИХ ПРОМЕНІВ В АБСОРБЦІЙНІЙ ХОЛОДНІЙ КВАНТОВІЙ ПЛАЗМІ ПІД ДІЄЮ РЕЛЯТИВІСТСЬКИХ ТА ПОНДЕРОМОТОРНИХ НЕЛІНІЙНОСТЕЙ

Діпак Тріпаті[1], Ніша Сінгх Ратхор[2], Вініт Каккар[3], Кешав Валья[4]
[1]*Фізичний факультет, USAR/USBS, Університет Гуру Гобінд Сінгх Індрапрастха, кампус Східного Делі, Делі, Індія-110032*
[2]*Фізичний факультет, Інститут технологій та менеджменту KCC, Велика Нойда, Індія*
[3]*Фізичний факультет, Міжнародна школа Лотосової долини, Сектор-50, Гургаон, Індія*
[4]*Фізичний факультет, Університет DAV, Джаландхар, Пенджаб, Індія*

У цьому дослідженні розглядається поведінка самофокусування лазерних променів Коша-Гаусса в абсорбційній холодній квантовій плазмі, враховуючи об'єднаний вплив релятивістської зміни маси та пондеромоторних ефектів. Застосовуючи наближення ВКБ у поєднанні з параксіальною теорією, отримано рівняння поширення 2-го порядку, що описує зміну ширини променя як функцію нормалізованої відстані, враховуючи вплив лінійного поглинання. Чисельне рішення результуючого диференціального рівняння отримано методом Рунге-Кутти 4-го порядку. Далі проведено комплексне параметричне дослідження для оцінки впливу параметрів лазерної плазми, таких як інтенсивність променя, густина плазми, початковий радіус променя, параметр децентрування та коефіцієнт поглинання, на динаміку променя. Результати показують, що релятивістська та пондеромоторна нелінійності посилюють самофокусування, тоді як поглинання зменшує його. Порівняння з класичною релятивістською плазмою підкреслює ключову роль квантових ефектів у поширенні лазера через щільну плазму.
Ключові слова: *динаміка самофокусування; Кош-Гаусівський промінь; релятивістська зміна маси; пондеромоторні ефекти; лінійне поглинання*

East European Journal of Physics. 1. 134–142 (2026)
DOI: 10.26565/2312-4334-2026-1-11 ISSN 2312-4334

IMPACT OF HEXADECAPOLE DEFORMATION ON FUSION CROSS SECTIONS OF SOME SPHERICAL + DEFORMED SYSTEMS IN 3S-CMD MODEL

Jignasha Patel[1*], **Vipul Katariya**[2]
[1]*Veer Narmad South Gujarat University, Surat - 395007, Gujarat, INDIA*
[2]*Department of Physics, Atmanand Saraswati Science College, Surat - 395006, Gujarat, INDIA*
[*]*Corresponding Author e-mail: pateljignasha87@gmail.com*
Received October 28, 2025; revised December 17, 2025, accepted January 8, 2026

The effect of quadrupole deformation (β_2) on heavy ion fusion is a fact that is well recognized phenomenon. In addition to the influence of quadrupole deformation (β_2), the potential impact of hexadecapole deformation (β_4) on sub-barrier fusion has been a topic of frequent discussion. Recently, a theoretical analysis was performed to examine the impact of hexadecapole deformations (β_4), employing the simplified coupled channels code CCFUS, which incorporates static deformations. In this study, we analyze the effect of the β_4 of the target nucleus on fusion cross sections within the framework of the 3S-CMD model. For this purpose, we have chosen the reactions ^{16}O + ^{154}Sm and ^{16}O + ^{174}Yb. The present research has calculated the fusion cross sections using the SBPM model as well. The calculated fusion cross sections using 3S-CMD model and SBPM are compared with each other as well as experiment.

Keywords: *Deformed nuclei; Quadrupole; Hexadecapole; Fusion cross sections; Classical microscopic approaches; Heavy-ion reactions*

PACS: 24.10.-i; 25.70.De; 25.60.Pj

1. INTRODUCTION

The study of hexadecapole deformation (β_4)of deformed body is essential for understanding the creation of superheavy elements (SHEs). Thus, the deformation associated with the hexadecapole may considerably modify the height of the fusion barrier. This consequently affects the fusion probability and, as a result, the likelihood of superheavy elements (SHEs) [1] formation. Theoretically, it has been proposed that a hexadecapole deformation (β_4) could facilitate fusion, resulting in the formation of superheavy elements (SHEs), depending on the chosen reaction partners [2]. Moreover, it is expected that hexadecapole deformation (β_4) will have a meaningful impact on the fusion process. The fusion barrier distributions derived from experimental findings demonstrate that fusion reactions are notably influenced by quadrupole deformation (β_2) and even by minor adjustments in hexadecapole deformation (β_4) [3].

Recently, a theoretical analysis focused on the importance of hexadecapole deformation (β_4) was performed using the simplified coupled channels code CCFUS, which incorporates static deformations. The predictions highlight considerable changes in the fusion cross sections. Positive values of β_4 are expected to enhance fusion while negative values will decrease it with respect to the $\beta_4 = 0$ system [4, 5].

The process of experimentally obtaining hexadecapole deformation (β_4) is challenging, with results that depend heavily on the chosen models and considerably vary with significant inaccuracies. Conceptually, the method that combines macroscopic and microscopic perspectives [6, 7] has been utilized to compute the deformation of nuclei in their ground state. In the present work, we modify the "STATIC" code [8] to calculate hexadecapole deformation (β_4). The hexadecapole deformation and the other ground-state properties are calculated using this code. By using the obtained ground-state properties, fusion cross sections have been calculated in 3S-CMD [9] and SBPM [9] model. During the approach stage of a heavy-ion collision, the higher deformation (in this study hexadecapole deformation) of the nucleus near the fusion barrier changes the barrier parameters, which in turn affect fusion cross-section calculations. Therefore, the effect of deformation on fusion cross-section calculation is studied for Spherical + Deformed systems and is discussed in detail in this article.

The motivation of this study is to find the impact of hexadecapole deformation of various target nuclei keeping the projectile nucleus same on fusion cross sections in 3S-CMD model. Fusion cross sections have been calculated for ^{16}O + ^{154}Sm and ^{16}O + ^{174}Yb systems. As long as the doubly magic ^{16}O nucleus is thought of to be spherical, it is expected that any effects of nuclear shapes on fusion cross sections will arise solely from the target nuclei.

The structure of this study is outlined as follows: Section 2 contains calculation details which include calculation of NN-potential, construction of the nuclei in ground state,evaluation of fusion cross sections together with a brief summary of the models which is used to find fusion cross sections. Section 3 provides a summary of the results obtained through the dynamic simulation. The final section gives the conclusion of the findings.

Cite as: J. Patel, V. Katariya, East Eur. J. Phys. 1, 134 (2026), https://doi.org/10.26565/2312-4334-2026-1-11

2. CALCULATION DETAILS

2.1. Nucleon-Nucleon potential

The NN potential utilized in this research is a soft-core Gaussian potential, which is entirely phenomenological and can be described by the following equation [10],

$$V_N(r_{ij}) = -V_0\left(1 - \frac{C}{r_{ij}}\right)\exp\left(-\frac{r_{ij}^2}{r_0^2}\right), \tag{1}$$

where, V_0, C and r_0 are respectively, the depth parameter, repulsive-core radius and range parameter. The parameters V_0, C and r_0 are chosen so that the NN-potential reproduces gross characteristics of the nuclei in their ground state such as the ground state binding energy, the rms radius etc.

The Coulomb potential between protons

$$V_C\left(r_{ij}\right) = \frac{1.44}{r_{ij}}(\text{MeV}), \tag{2}$$

is also added to the nuclear potential.

2.2. Construction of nuclei in their ground state

Nuclei in the ground state are generated through the "STATIC" procedure, which starts with a random distribution of nucleon positions within a defined spherical radius. Subsequently, the total potential energy of these nucleon configurations is minimized cyclically by making slight displacements to the coordinates of each nucleon.

Total BE is the total potential energy and R_{rms} is calculated from all the nucleon positions. The quadrupole deformation parameter (β_2) is calculated from the expression [11],

$$\beta_2 = \sqrt{\frac{16\pi}{5}}\left(1 - \frac{R\,(90^\circ)}{R_0}\right), \tag{3}$$

where, R (90°) is the length of the two equal axes perpendicular to the symmetry axis and R_{rms} is the rms radius of the spherical nucleus.

For the given nucleus if its symmetry axis is greater than R_{rms}, R (90°) < R_{rms} in eq. (3) and hence the β_2 of that nucleus is positive (prolate deformation). Similarly, if the symmetry axis of the given nucleus is less than R_{rms}, R (90°) > R_{rms} in eq. (3) and hence the β_2 of that nucleus is negative (oblate deformation).

The hexadecapole deformation parameter (β_4) is calculated from the expression

$$\beta_4 = \left(\frac{16}{9}\sqrt{\pi}\right)\left[\frac{R(90)}{R_0} - 1 + \beta_2\left(\sqrt{\frac{5}{16\pi}}\right)\right], \tag{4}$$

in terms of rms radius of the nucleus and R(90°) which is the length of the axes along the direction of any one of the principal axes perpendicular to the symmetry axis.

The ultimate configuration of nucleon placements leads to a stable nucleus. Considering that for A ≥ 5, there may be multiple local minima in the binding energy, a nucleus is chosen that demonstrates the highest binding energy from a diverse range of configurations (the most-bound nucleus) [12]. Alternatively, a configuration that bears a strong resemblance to the properties of the experimental ground state is chosen [13].

A parameter set V_0 = 1155 MeV, C = 2.07 fm, r_0 = 1.2 fm is used in the present calculation which produces the ground state characteristics of the colliding nuclei is shown in Table 1.

Table 1. The characteristics of the produced nuclei in their ground state.

	Calculated				Experimental			
	B.E. (Mev)	RMS (fm)	β_2	β_4	B.E. (Mev)	RMS (fm)	β_2	β_4
^{16}O	-125.36	2.47	0.15	-0.08	-127.62	2.73	0.00	-0.12
^{154}Sm	-1375.86	5.46	0.20	-0.11	-1266.94	5.12	0.27	0.10
^{174}Yb	-1478.90	5.71	0.12	-0.06	-1406.60	5.41	0.28	-0.05

Fig. 1 shows the ground state characteristics of all the configurations of the ^{16}O, ^{154}Sm and ^{174}Yb nuclei generated by the "STATIC" method. Among the large set of generated configurations for the nuclei, those that exhibit ground state properties closely aligned with experimental values are chosen for collision calculations. These systems are indicated by bigger open circle and triangle in Fig. 1.

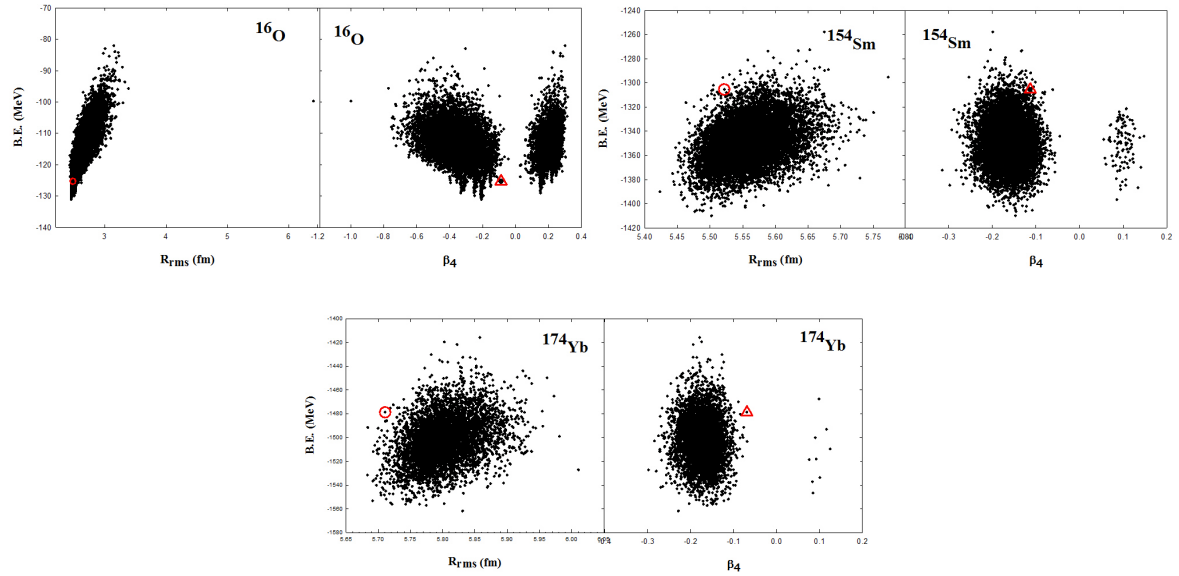

Figure 1. Ground state characteristics of the ^{16}O, ^{154}Sm and ^{174}Yb nuclei generated by the "STATIC" method. ◯ and △ indicate the ground state characteristics of the nuclei used in the present study.

2.3. Analysis of fusion cross sections involving hexadecapole deformation

Calculations of fusion cross sections have been performed for numerous reactions that involve nuclei displaying various collective degrees of freedom. Different models have been employed to calculate the fusion cross sections, such as Time Dependent Hartree Fock (TDHF) [14, 15], classical trajectory methods [16], and the coupled channel calculation software referred to as CCFULL [17]. However, methods based on quantum mechanics at the microscopic scale, such as TDHF calculations, are very compute-intensive, and CCFULL calculations, which are static, do not reflect the effects of dynamical reorientation.

The barrier parameters at b = 0 (indicating a head-on collision) which corresponds to a specific collision energy and the initial orientation of the two nuclei, are derived from a dynamically generated ion-ion potential. With these parameters, fusion cross-section is calculated using Wong's formula [18],

$$\sigma_{\text{fus}}\left(E_{CM}\right) = \left[\frac{R_B^2 \hbar\omega_0}{2E_{CM}}\right] \ln\left\{1 + \exp\left(2\pi \frac{E_{CM} - V_B}{\hbar\omega_0}\right)\right\}, \tag{5}$$

where V_B denotes the height of the barrier, R_B represents the radius of the barrier, and ω_0 signifies the oscillator frequency associated with the peak of the barrier. The method used to find barrier parameters affects the fusion cross-sections.

The calculations of heavy-ion fusion cross sections have been performed using SBPM and 3S-CMD methods within the context of classical approximations. ^{16}O + ^{154}Sm and ^{16}O + ^{174}Yb reaction has been studied in this approach with the potential parameter set P4 (V_0 = 1155 MeV, C = 2.07 fm and r_0 = 1.2 fm). The ^{16}O + ^{154}Sm system has been well studied in SBPM model in ref. [10] and in CRBD model in ref. [11] using the same NN potential parameter set P4.

2.4. Model Details

- **SBPM Model :** The ion-ion potential is formulated as a function of the center of mass separation (R_{CM}) of the two nuclei, as derived from the impulse approximation (i.e., keeping the configuration of the nucleons in the two nuclei frozen during their collision) [9]. The ion-ion potential consists of the total nuclear and Coulomb potentials that exist between all nucleons of the two ions. The parameters V_B and R_B represent the outer maximum of the ion-ion potential, while ω_B denotes the second derivative of this peak. This gives barrier parameters of head-on collision for a given orientation of the two nuclei. Large numbers of such randomly chosen orientations of the two nuclei are considered in this study. All the degree of freedom are explicitly neglected in this model.

- **3S-CMD Model :** The simulation of heavy-ion collisions within the present classical approach (3S-CMD) occurs in three sequential stages:
  (1) Rutherford Trajectory Calculation: The two nuclei, treated as charged point particles, are directed along their Rutherford trajectories with a defined collision energy (E_{CM}) and impact parameter (b) until they attain a separation of R_{CM} = 2500 fm.

(2) CRBD model Calculation: The two nuclei, considered as rigid bodies with a fixed arrangement of nucleon positions in their ground state, are subsequently permitted to evolve further through the CRBD model [19]. This is achieved by solving the translational and rotational equations of motion for their center of mass and the orientation angles of their principal axes. The process of CRBD calculation is carried on until a relatively small separation of R_{CM} = 50 fm is attained.
(3) CMD Calculation: The Rigid body constraints are relaxed at approximately R_{CM} = 50 fm, and the paths of all the participating nucleons are calculated using the coupled Newton's equations of motion for each particle within a CMD framework [20].

3. RESULT AND DISCUSSION

^{16}O + ^{154}Sm : The ^{16}O + ^{154}Sm system has been selected to investigate the impact of hexadecapole deformation, as it has been extensively examined through both experimental [21] and theoretical approaches [10, 11]. The phase of the collision as it approaches the barrier top is influenced by the center-of-mass energy, E_{CM}. Because barrier parameters are the key components in fusion cross-section calculations, a detailed understanding of the variations in the ion-ion potential V_{12} and the barrier parameters with respect to the collision energy E_{CM} is required.

Fig. 2 illustrates the ion-ion potential for the ^{16}O + ^{154}Sm system, calculated with an initial R_{in} = 2500 fm across various collision energies (E_{CM}), while maintaining the same arbitrary initial orientation for each case. This figure illustrates that both the barrier height V_B and the barrier radius R_B are influenced by the incident energy E_{CM}. Thus, it is essential to determine the barrier parameters (V_B, R_B, ω_0) based on a specified initial orientation and a defined collision energy. To determine the fusion cross section, it is essential to take the average of the barrier parameters across numerous initial random orientations. The fusion cross-section obtained is specific to the fusion cross-section at that particular collision energy only.

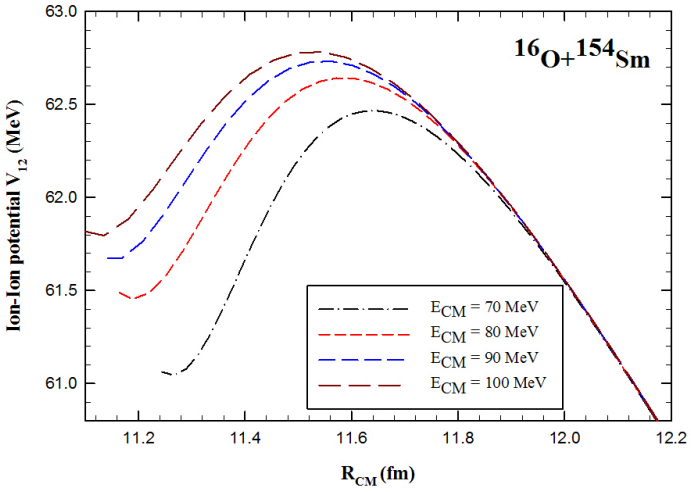

Figure 2. Ion-ion potential V_{12} as a function of center-of-mass separation R_{CM} for ^{16}O + ^{154}Sm system for different collision energy E_{CM} but same arbitrary orientation.

The fusion cross-section of the ^{16}O + ^{154}Sm system is calculated in SBPM calculations, utilizing the NN potential parameter set P4 (V_0 = 1155 MeV, C = 2.07 fm and r_0 = 1.2 fm) shown in Fig. 3 . This figure also shows the fusion cross sections calculated for^{16}O + ^{154}Sm system in 3S-CMD model with the same potential parameter set along with the experimental data of ref. [21]. Fusion cross-section are calculated for ^{16}O + ^{154}Sm system in 3S-CMD model for central collisions (b = 0). The ^{16}O and ^{154}Sm nucleus are dynamically evolved as a rigid body till the target-projectile separation is close to their barrier top (about 13 fm). At this separation the rigid body constraint on both the ^{16}O and ^{154}Sm are relaxed for further evolution of the entire system. Comparison of fusion cross sections calculated by considering the quadrupole deformation and hexadecapole deformation using both the models is also shown in Fig. 3.

It is evident from Fig. 3 that the fusion cross sections calculated for quadrupole deformation and hexadecapole deformation in the SBPM model agrees well with the experimental data as well as with each other at higher energy levels. At lower energy levels, the SBPM calculations tend to overestimate the experimental fusion cross-sections for both the deformations. Fusion cross sections calculated for the hexadecapole deformations are highly overestimated with the experimental data whereas fusion cross sections calculated for the quadrupole deformations are slightly overestimated with the experimental data at lower energy side. Fusion cross sections calculated for quadrupole deformation and hexadecapole deformation in 3S-CMD model are highly overestimated with the experimental data at all energy levels. At lower energy

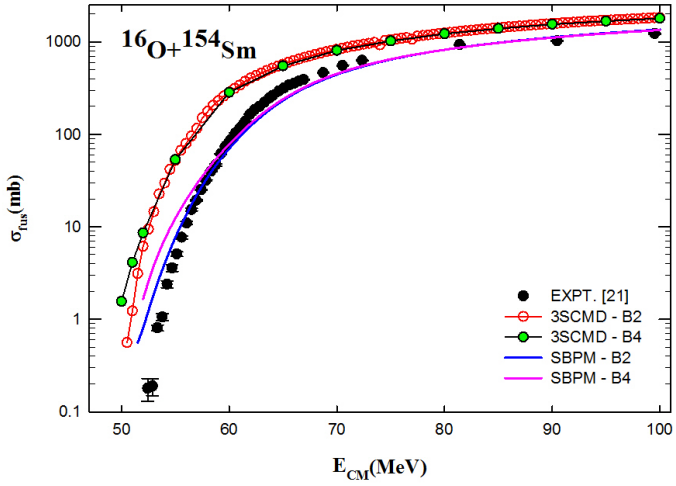

Figure 3. Comparison of fusion cross sections calculated for quadrupole and hexadecapole deformation using SBPM and 3S-CMD model with experimental fusion cross sections for ^{16}O + ^{154}Sm system.

side, the fusion cross section calculated quadrupole deformation and hexadecapole deformation in 3S-CMD model shows same trend as in SBPM calculation.

At low collision energy levels, the duration of interaction between the colliding nuclei becomes longer. This causes the reorientation of the deformed ^{154}Sm in relation to the spherical ^{16}O nucleus. However, the extent of reorientation is small because the target nucleus (^{154}Sm) is medium heavy and has large moment of inertia. As mentioned in ref. [11], at lower energy the fusion cross sections calculated using CRBD model and SBPM model shows small difference. Because the CRBD model only considered rotational degree of freedom. This research calculates the fusion cross sections through the 3S-CMD model, which incorporates both the long-range rotational excitation (reorientation effect) and the vibrational excitations that occur in proximity to or within the barrier and this could be one of the reason in difference of fusion cross sections between SBPM and 3S-CMD model.

Additionally, the fusion cross sections calculated using 3S-CMD model overestimated at all energies with the experimental fusion cross sections. In order to examine this anomaly, we carry out an examination of the ground state properties of the nuclei involved in the above calculations. Ground state properties of the nuclei used in present calculation are shown in the Table 1.

From the Table 1, it is noted that experimentally determined values of β_2 indicate that ^{16}O is spherical while the ^{16}O nucleus generated in present study is being prolate (β_2 = 0.157). The experimental β_4 value for ^{154}Sm is positive while the calculated β_4 value is negative. Calculated rms radius of ^{16}O nucleus is found to be smaller than the experimental rms value by about 10 % while that for ^{154}Sm is larger by about 6 %. Thus, the smaller dimensions of the lighter nucleus, when combined with the larger dimensions of the heavier nucleus, contribute to an overestimation of the fusion cross sections for this particular reaction.

T_{rot} for non-rigid case with E_{CM} = 100 MeV and b = 0 fm are shown in Fig. 4. At b = 0 fm, T_{rot} is higher initially but soon it reduces to very low values because for central collision T_{rot}(^{16}O) and T_{rot}(^{154}Sm) dissipates very soon as shown in Fig. 4. The light prolate ^{16}O acquire comparatively high T_{rot} initially on the contact with the heavy-medium deformed ^{154}Sm but it dissipates soon to very low level.

Fig. 5 shows the total vibrational excitation energy (T_{vib}) of ^{16}O + ^{154}Sm system at b = 0.0 fm. From the Fig. 4 and Fig. 5 we can see that for the central collision ^{154}Sm acquire a small T_{rot} but large T_{vib} resulting from the maximum change in the internal potential energy (binding energy) of the ^{154}Sm.

^{16}O + ^{174}Yb : In order to clearly bring out the effect of hexadecapole deformation on fusion cross sections, we replace the medium-heavy target nucleus (^{154}Sm) with heavy nucleus (^{174}Yb) with same projectile (^{16}O). In this system both the projectile and target nuclei having prolate quadrupole deformation with β_2 = +0.157 (^{16}O) and β_2 = +0.123 (^{174}Yb). For ^{16}O + ^{174}Yb system, the mass asymmetry between ^{16}O and ^{174}Yb is somewhat greater than that observed between ^{16}O and ^{154}Sm. The ground state configuration of generated nuclei are shown in Fig. 1 and the ground state properties of the generated nuclei are shown in Table 1. From the Table 1, it has been observed that the binding energy and rms radius of ^{174}Yb nucleus are overestimate by 5% where as quadrupole deformation parameter β_2 is reduced by 1%. The experimental and calculated β_4 value is negative for both the projectile and target nuclei.

Fusion cross-sections for ^{16}O + ^{174}Yb system is calculated using SBPM and 3S-CMD model are shown in Fig. 6. From this figure it is clear that the fusion cross sections calculated using SBPM model with quadrupole and hexadecapole deformation shows good agreement at higher energies with the experimental data while below the barrier energies it

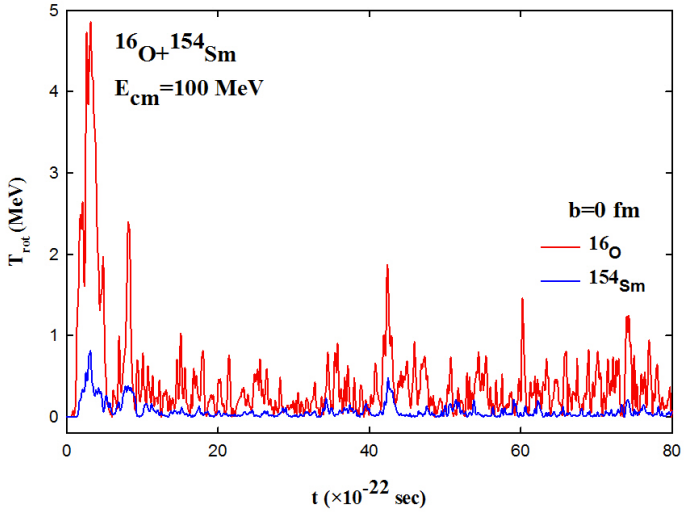

Figure 4. Total rotational kinetic energy (T_{rot}) of ^{16}O + ^{154}Sm system at b = 0.0 fm.

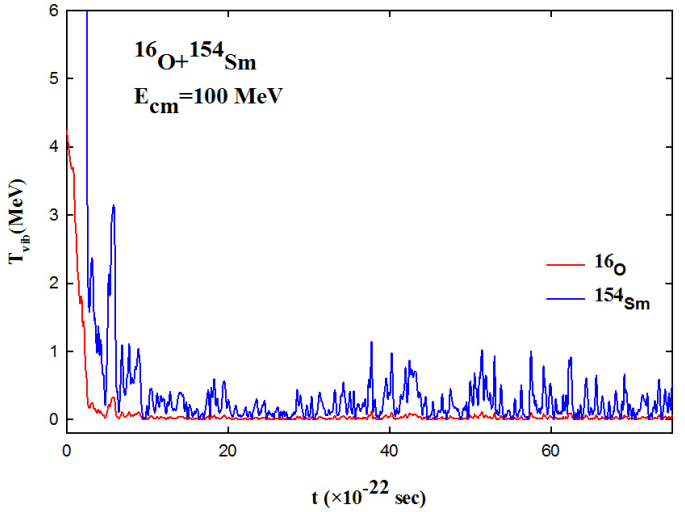

Figure 5. Total vibrational excitation energy (T_{vib}) of ^{16}O + ^{154}Sm system at b = 0.0 fm.

over estimates the experiment. The result of fusion cross sections calculated using 3S-CMD model with quadrupole and hexadecapole deformation are close to the experiment at higher energies. At sub-barrier energies, the fusion cross sections calculated using 3S-CMD model with both the deformations are highly overestimated.

The fusion cross sections corresponding to a particular collision energy in the 3S-CMD calculation are derived by averaging the orientations of the fusion cross sections determined through Wong's formula, utilizing barrier parameters specific to that energy simulation. About 500 initial random orientation were considered for $E_{CM} \geq 80$ Mev and 1000 for $E_{CM} < 80$ MeV.

As the reorientation and vibrational effects are likely to be prominent at collision energies near the Coulomb barrier, it is essential to investigate fusion cross-sections at energy levels that are significantly below the lowest E_{CM} indicated in ref. [14] . To effectively highlight both the effect of reorientation + vibration, fusion cross-sections are calculated in 3S-CMD for energies as low as 60.0 MeV, which is significantly lower than the minimum energy used in experiment [14]. For E_{CM} at 59.5 MeV, an analysis of 2000 randomly selected initial orientations indicates that there is no pocket present in the ion-ion potential. Consequently, the fusion cross section is considered to be zero for $E_{CM} \leq 59.5$ MeV in the 3S-CMD calculation.

From Fig. 6, it has been observed that at higher energy levels, the variation in fusion cross-sections computed using the SBPM and 3S-CMD models is small. When energy levels decrease, the fusion cross-sections calculated from the 3S-CMD model show an enhancement compared to those obtained from the SBPM, where all dynamic effects are explicitly ignored. The shift from the SBPM calculations is clearly a result of the reorientation + vibrational effect occurring in the 3S-CMD model.

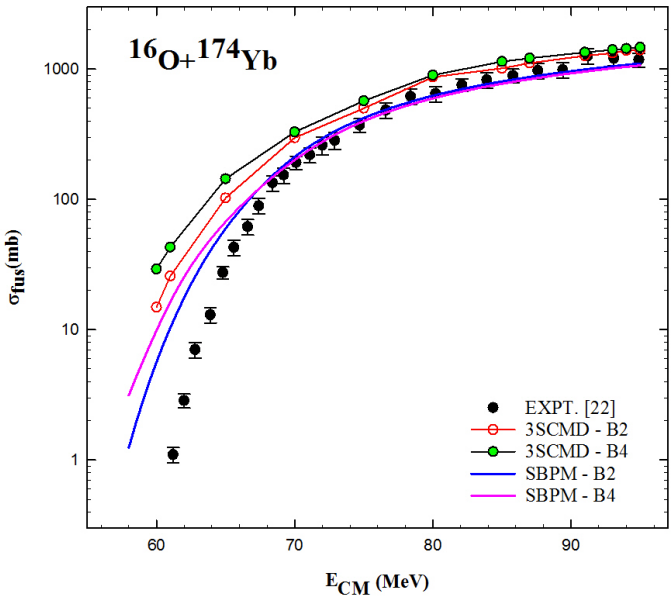

Figure 6. Comparison of fusion cross sections calculated for quadrupole and hexadecapole deformation using SBPM and 3S-CMD model with experimental fusion cross sections for ^{16}O + ^{174}Yb system.

Since the target nucleus (^{174}Yb) used in the above calculation is heavy and has principal moment of inertia components I_1 = 3474.112 u fm^2; I_2 = 3826.939 u fm^2 and I_3 = 3902.096 u fm^2, the extent of reorientation is small as shown in Fig. 7. The principal moment of inertia components of projectile nucleus (^{16}O) are I_1 = 59.182 u fm^2; I_2 = 68.651 u fm^2 and I_3 = 68.806 u fm^2. The evolution of these two nuclei begins at a distance of 2500 fm, influenced by the Coulomb field of each other. The reorientation of the deformed ^{174}Yb nucleus at different collision energies is shown in Fig. 7 , where the initial orientation angle is set at β_0 = 0, α_0 = 0, γ_0 = 0 and R_{in} = 2500 fm. This figure clearly indicates that the extent

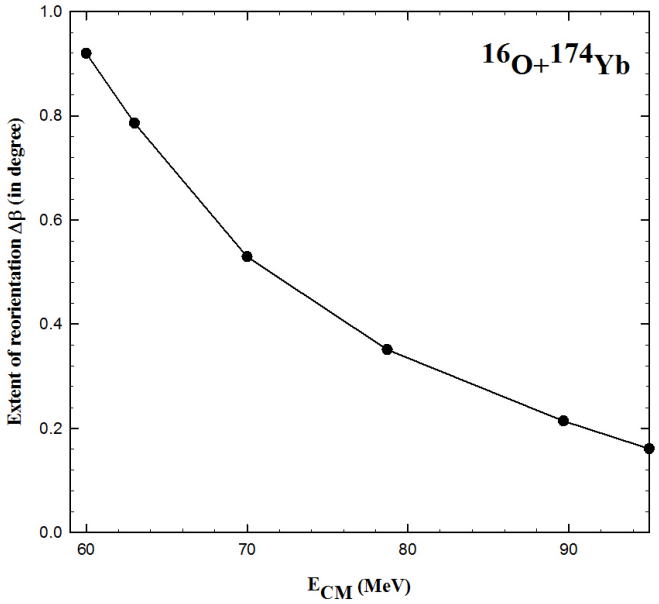

Figure 7. Extent of reorientation $\Delta\beta$ at the barrier top against E_{CM} for ^{16}O + ^{174}Yb system.

of reorientation of the ^{174}Yb nucleus is less than 1°, even at the lowest energy of 60 MeV. The reorientation value of the deformed nucleus, ^{174}Yb, is too small to have a significant effect on the fusion cross-sections. Therefore, the enhancement in fusion cross sections in 3S-CMD model with SBPM model is due to the vibrational excitations which occur close to the barrier or inside of it.

4. CONCLUSIONS

The above study explains the effect of hexadecapole deformation (β_4) on fusion cross sections of different systems in heavy ion collision. Although quadrupole deformation (β_2) is the most commonly examined type of deformation in nuclear fusion reactions, hexadecapole deformation (β_4) can also significantly influence fusion cross sections, particularly in systems where higher-order deformations play a crucial role.

From the above study, it is clear that the fusion cross section calculated with the quadrupole deformation shows smaller enhancement at lower energies than the fusion cross sections calculated with the hexadecapole deformation with the experiment. At higher energies heavy mass nucleus system (i.e., ^{16}O + ^{174}Yb) gives better agreement with experiment than the medium-heavy mass nucleus system (i.e., ^{16}O + ^{154}Sm).

ORCID

Jignasha Patel, https://orcid.org/0009-0008-1454-4283; **Vipul Katariya**, https://orcid.org/0009-0001-7215-8128

APPENDIX A CALCULATION OF HEXADECAPOLE DEFORMATION (β_4)

The nuclear surface can be characterized by the radius vector $\overrightarrow{R}$ in the direction (θ, ϕ) as given below [23],

$$\mathrm{R}(\theta,\phi) = \mathrm{R}_0\left[1 + \sum_{\lambda=0}^{\infty}\sum_{\mu=-1}^{\lambda} \alpha_{\lambda\mu} Y_\mu^\lambda(\theta,\phi)\right], \tag{6}$$

where R_0 is the radius of the spherical nucleus, and the terms containing $\alpha_{\lambda\mu}$ represent the expansion of any general function of the angles (θ, ϕ) in terms of the complete set of spherical harmonics $\mathrm{Y}_\mu^\lambda(\theta,\phi)$. For the deformed partner, we shall restrict ourselves to only axially symmetric deformations of nucleus characterized by nuclear quadrupole and hexadecapole deformation parameters β_2 and β_4 respectively. In this case the nucleus can only rotate around an axis perpendicular to the symmetry axis. In terms of these, the radius of a deformed system is written as,

$$\begin{aligned}\mathrm{R}(\theta) &= \mathrm{R}_0\left[1 + \beta_2 \mathrm{Y}_2^0(\theta,\phi) + \beta_4 \mathrm{Y}_4^0(\theta,\phi)\right] \\ &= \mathrm{R}_0\left[1 + \beta_2\left(\frac{1}{4}\sqrt{\frac{5}{\pi}}\left(3\cos^2\theta - 1\right)\right) + \beta_4\left(\frac{3}{16}\sqrt{\frac{1}{\pi}}\left(35\cos^4\theta - 30\cos^2\theta + 3\right)\right)\right],\end{aligned} \tag{7}$$

where,

R_0 in the present study is taken as rms radius of the nucleus.

$\mathrm{Y}_2^0(\theta,\phi)=\frac{1}{4}\sqrt{\frac{5}{\pi}}\left(3\cos^2\theta - 1\right)$

$\mathrm{Y}_4^0(\theta,\phi) = \frac{3}{16}\sqrt{\frac{1}{\pi}\left(35\cos^4\theta - 30\cos^2\theta + 3\right)}$

$\mathrm{R}(\theta)$ is the magnitude of the radius vector of the nucleus at an angle θ with respect to the symmetry axis of the nucleus. Substituting $\theta = 90°$ in the eq. (7), we get,

$$\begin{aligned}\mathrm{R}(90) &= \mathrm{R}_0\left[1 - \beta_2\left(\frac{1}{4}\sqrt{\frac{5}{\pi}}\right) + \beta_4\left(\frac{3}{16}\sqrt{\frac{1}{\pi}}(3)\right)\right] \\ &= \mathrm{R}_0\left[1 - \beta_2\left(\sqrt{\frac{5}{16\pi}}\right) + \beta_4\left(\frac{9}{16}\sqrt{\frac{1}{\pi}}\right)\right]\end{aligned}$$

or

$$\frac{\mathrm{R}(90)}{\mathrm{R}_0} = 1 - \beta_2\left(\sqrt{\frac{5}{16\pi}}\right) + \beta_4\left(\frac{9}{16}\sqrt{\frac{1}{\pi}}\right)$$

$$\beta_4\left(\frac{9}{16}\sqrt{\frac{1}{\pi}}\right) = \left[\frac{\mathrm{R}(90)}{\mathrm{R}_0} - 1 + \beta_2\left(\sqrt{\frac{5}{16\pi}}\right)\right]$$

which gives an expression for the hexadecapole deformation parameter β_4 as

$$\beta_4 = \left(\frac{16}{9}\sqrt{\pi}\right)\left[\frac{\mathrm{R}(90)}{\mathrm{R}_0} - 1 + \beta_2\left(\sqrt{\frac{5}{16\pi}}\right)\right], \tag{8}$$

in terms of rms radius of the nucleus and R(90°) which is the length of the axes along the direction of any one of the principal axes perpendicular to the symmetry axis.

REFERENCES

[1] A. Iwamoto, and P. Moller, Nucl. Phys. A, **605**, 334 (1996). https://doi.org/10.1016/0375-9474(96)00155-8

[2] R. K. Gupta, *et al*., Journal of Physics G: Nucl. Part. Phys. **31**, 631 (2005). 10.1088/0954-3899/31/7/009

[3] R. C. Lemmon, *et al*., Phys. Lett. B, **316**, 32 (1993). https://doi.org/10.1016/0370-2693(93)90653-Y

[4] J.F. Niello, and C. H. Dasso, Lecture Notes in Physics **317**, 56-60 (2005). https://link.springer.com/book/10.1007/3-540-50578-4

[5] H. Sharma, *et al*., The European Physical Journal A, **59**, 71 (2023). https://link.springer.com/article/10.1140/epja/s10050-023-00981-1

[6] P. Moller, Nucl. Phys. A, **142**, 1 (1970). https://doi.org/10.1016/0375-9474(70)90469-0

[7] U. Gotz, *et al*., Nucl. Phys. A, **192**, 1 (1972). https://doi.org/10.1016/0375-9474(72)90002-4

[8] S. S. Godre, and Y. R. Waghmare, Phys. Rev. C, **36**, 1632 (1987). https://doi.org/10.1103/PhysRevC.36.1632

[9] S. S. Godre, Pramana J. Phys. **82**, 879 (2014). https://doi.org/10.1007/s12043-014-0741-6

[10] S. S.Godre, Nucl. Phys. A, **734**, E17 (2004). https://doi.org/10.1016/j.nuclphysa.2004.03.009

[11] P. R. Desai, Ph.D. Thesis, "Effect of Coulomb reorientations on fusion crosssections and barrier distributions of some heavy-ion reactions," Veer Narmad South Gujarat University, Surat (2009).

[12] I. B. Desai, and S. S. Godre, Proc. Int. Symp. on Nucl. Phys. **54**, 196 (2009). https://www.sympnp.org/proceedings/54/A72.pdf

[13] S.S. Godre, and P.R. Desai, Proc. Symp. on Nucl. Phys. **53**, 341 (2008).

[14] C. Simenel, *et al*., Phys. Rev. Lett. **93**, 102701 (2004). https://doi.org/10.1103/PhysRevLett.93.102701

[15] S. E. Koonin, *et al*., Phys. Rev. C, **15**, 1359 (1977). https://doi.org/10.1103/PhysRevC.15.1359

[16] R. Birkelund, *et al*., Phys. Rep. **56**, 107 (1979). https://doi.org/10.1016/0370-1573(79)90093-0

[17] N. I. Chauhan, "A Study of near-barrier fusion of some heavy-ion collisions using coupled-channel calculation," M. Phil. Dissertation, Veer Narmad South Gujarat University, Surat (2012).

[18] C. Y. Wong, Phys. Rev. Lett. **31**, 766 (1973). https://doi.org/10.1103/PhysRevLett.31.766

[19] P. R. Desai, and S. S. Godre, Eur. Phys. J. A, **47**, 146 (2011). https://doi.org/10.1140/epja/i2011-11146-8

[20] S. S. Godre, and Y. R. Waghmare, Phys. Rev. C, **36**, 1632 (1987). https://doi.org/10.1103/PhysRevC.36.1632

[21] J. R. Leigh, *et al*., Phys. Rev. C, **47**, R437 (1993). https://doi.org/10.1103/PhysRevC.47.R437

[22] T. Rajbongshi, *et al*., Phys. Rev. C, **93**, 054622 (2016). https://doi.org/10.1103/PhysRevC.93.054622

[23] M. K. Pal, *Theory of Nuclear Structure*, 382, (Allied East-West press Pvt. Ltd., 1982).

ВПЛИВ ГЕКСАДЕКАПОЛЬНОЇ ДЕФОРМАЦІЇ НА ПОПЕРЕЧНІ ПЕРЕРІЗИ СИНТЕЗУ ДЕЯКИХ СФЕРИЧНИХ + ДЕФОРМОВАНИХ СИСТЕМ У МОДЕЛІ 3S-CMD

Джігнаша Патель[1], **Віпул Катарія**[2]

[1]*Вір Нармад, Університет Південного Гуджарату, Сурат - 395007, Гуджарат, Індія*

[2]*Кафедра фізики, Науковий коледж Атмананд Сарасваті, Сурат - 395006, Гуджарат, Індія*

Вплив квадрупольної деформації (β_2) на синтез важких іонів є добре відомим явищем. Окрім впливу квадрупольної деформації (β_2), потенційний вплив гексадекапольної деформації (β_4) на суббар'єрний синтез був предметом частих обговорень. Нещодавно було проведено теоретичний аналіз для вивчення впливу гексадекапольних деформацій (β_4) з використанням спрощеного коду зв'язаних каналів CCFUS, який враховує статичні деформації. У цьому дослідженні ми аналізуємо вплив β_4 цільового ядра на перерізи синтезу в рамках моделі 3S-CMD. Для цього ми обрали реакції ^{16}O + ^{154}Sm та ^{16}O + ^{174}Yb. У цьому дослідженні перерізи синтезу також розраховано за допомогою моделі SBPM. Розраховані перерізи синтезу за допомогою моделі 3S-CMD та SBPM порівнюються між собою, а також з експериментом.

Ключові слова: *деформовані ядра; квадруполь; гексадекаполь; перерізи синтезу; класичні мікроскопічні підходи; реакції важких іонів*

East European Journal of Physics. 1. 143–147 (2026)
DOI: 10.26565/2312-4334-2026-1-12 ISSN 2312-4334

FUSION OF WEAKLY-BOUND ^{9}Be WITH HEAVY NUCLEI ^{208}Pb : A MULTI-BODY THREE-STAGE CLASSICAL MOLECULAR DYNAMICS APPROACH

Vipul B. Katariya[1*], **Jignasha A. Patel**[2], **Hardip R. Mahida**[3], **Pinank H. Jariwala**[2]
[1]*Department of Physics, Atmanand Saraswati Science College, Surat, Gujarat, 395006, India*
[2]*Department of Physics, Navyug Science College, Surat, Gujarat, 395009, India*
[3]*Department of Physics, Veer Narmad South Gujarat University, Surat, Gujarat, 395007, India*
[*]*Corresponding Author e-mail: vipulkatariya5611@gmail.com*
Received October 25, 2025; revised December 23, 2025; accepted January 12, 2026

The fusion of the weakly bound ^{9}Be nucleus with ^{208}Pb is investigated using a multi-body three-stage classical molecular dynamics (3S-CMD) approach. This model explicitly treats ^{9}Be as a cluster of ^{4}He and ^{5}He, allowing for the relaxation of rigid-body constraints on both projectile fragments and the target. In this paper, the influence of these constraints on the complete fusion (CF) cross-section, considering both central and non-central collisions is studied. Systematic removal of rigidity constraints, particularly on the target and the ^{9}Be fragments, significantly affects the CF cross-section, especially at sub-barrier energies. Calculations show that relaxing these constraints enhances CF, indicating the important role of breakup and internal degrees of freedom. The multibody 3S-CMD model provides a tool for understanding the interplay of breakup and fusion in reactions involving weakly bound nuclei.

Keywords: *Weakly-bound nuclei; Heavy-ion collisions; Fusion reactions; Classical Molecular Dynamics*

PACS: 25.70.Jj, 25.60.Gc, 24.10.Lx

1. INTRODUCTION

Investigations of nuclear reactions involving weakly bound nuclei have been made possible due to recent developments in experimental techniques and the availability of radioactive beams. Weakly bound nuclei exhibit unique phenomena like increased breakup probabilities, neutron transfer, and complete and incomplete fusion processes. In complete fusion, the entire charge of the projectile is captured by the target, irrespective of the breakup of the projectile. Incomplete fusion refers to the capture of one or more fragments of the projectile taking place, followed by the breakup of the projectile. So, it is essential to understand the effects of breakup on fusion reaction, as it significantly changes the possibilities of various reaction channels.

Fusion reactions near the Coulomb barrier are strongly influenced by the intrinsic degrees of freedom, such as the rotational and vibrational modes of the interacting nuclei [1]. Numerous studies have also explored how breakup processes impact fusion outcomes [2–7]. Significant suppression of complete fusion and an enhancement in incomplete fusion at energy over the fusion barrier have been shown by precision measurements for the ^{9}Be + ^{208}Pb reaction [4]. These behaviors are attributed to the breakup of the ^{9}Be, which can occur through channels such as ^{8}Be + n (S_n = 1.67 MeV) and ^{5}He + ^{4}He (S_α = 2.42 MeV).

Reactions involving weakly bound nuclei, such as ^{6}Li + ^{209}Bi and ^{7}Li + ^{209}Bi have been studied using the Multi-Body Three-Stage Classical Molecular Dynamics (3S-CMD) model [8]. In this paper, we investigate the role of various rigidity constraints and their relative importance in determining the fusion cross-section for the ^{9}Be + ^{208}Pb system using the multi-body 3S-CMD model. This study includes calculations of complete fusion (CF) while systematically relaxing the rigid-body constraints on the nuclei involved in the collisions. The details of the model are presented in § 2, while the results for fusion cross-sections for ^{9}Be + ^{208}Pb are discussed in § 3. Finally, conclusions are summarized in § 4.

2. MODEL DETAILS

The multibody 3S-CMD model is used to simulate the collision of ^{9}Be + ^{208}Pb. In this model, ^{9}Be is made up of a cluster of ^{4}He and ^{5}He nuclei held together in a way that matches the observed break-up energy of ^{9}Be into ^{4}He and ^{5}He (2.42 MeV). A potential minimization code using a soft-core Gaussian NN potential given by,

$$V_{ij}(r_{ij}) = -V_0\left(1 - \frac{C}{r_{ij}}\right)\exp\left(-\frac{r_{ij}^2}{r_0^2}\right)\ \text{MeV}, \tag{1}$$

is used to create projectile fragments and targets where the typical form of the Coulomb potential between protons is,

$$V_C(r_{ij}) = \frac{1.44}{r_{ij}}\ \text{MeV}. \tag{2}$$

Cite as: V.B. Katariya, J. A. Patel, H. R. Mahida, P. H. Jariwala, East Eur. J. Phys. 1, 143 (2026), https://doi.org/10.26565/2312-4334-2026-1-12

However, a purely phenomenological potential is selected, and its parameters are set to approximately match the ground state properties of the target and projectile fragments. The potential parameter set V_0 = 710.0 MeV, C = 1.88 fm, and r_0 = 1.15 fm is used to produce ground state properties of projectile fragments and target mentioned in Table 1.

Table 1. Ground-state properties.

Nucleus	Calculated		Experimental	
	B.E. (MeV)	R (fm)	B.E. (MeV) [9]	R (fm) [10]
^{4}He	14.48	1.32	28.29	1.68
^{5}He	22.34	1.46	27.41	–
^{9}Be (^{4}He + ^{5}He)	39.23	1.87	58.16	2.51
^{208}Pb	1841.92	6.04	1636.46	5.50

These three stages are involved in the simulation of the multibody 3S-CMD model:

(1) Rutherford Trajectories: Initially, the target and projectile are brought together along their classical Rutherford trajectories, considering their Coulomb interaction.
(2) Classical Rigid Body Dynamics (CRBD): The system is dynamically evolved using CRBD to approach a distance close to the fusion barrier, accounting for the collective motion and interactions.
(3) Classical Molecular Dynamics (CMD): The entire multibody system undergoes CMD evolution, allowing for interactions and dynamic evolution of the system.

In stage 3, one or more projectile fragments are constrained to remain rigid, those nuclei are dynamically evolved as in the CRBD calculation. For ^{9}Be, the rigidity constraint on the bond between ^{4}He and ^{5}He, as well as on the target ^{208}Pb are relaxed when the center of mass distance, $R_{\rm cm}$ becomes less than 14 fm. One of the fragments of projectile ^{4}He is always kept rigid. Allowing ^{5}He in the projectile to be non-rigid enables the possibility of its breakup.

3. FUSION CROSS SECTION

The complete fusion cross-section is calculated for weakly bound ^{9}Be induced collisions to enable a quantitative comparison between model calculations and experimental results. Theoretically, the colliding nuclei are assumed to fuse when they overcome the potential barrier between them and become trapped in a potential pocket. The fusion cross section for a given collision energy $E_{\rm cm}$ is calculated using Wong's formula [11]. Classically, fusion cross sections vanish at energies below the barrier, but here the barrier penetrability is accounted for in the calculation using Wong's formula,

$$\sigma_{\rm fus}(E_{\rm CM}) = \frac{R_B^2\,\hbar\omega_0}{2E_{\rm CM}} \ln\left[1 + \exp\left(\frac{2\pi(E_{\rm CM} - V_B)}{\hbar\omega_0}\right)\right], \tag{3}$$

where, $V_{\rm B}$, $R_{\rm B}$, and ω_0 represent the barrier parameters. For higher energies, the Wong's formula can be approximated to classical formula,

$$\sigma_{\rm fus}(E_{\rm c.m.}) = \pi R_B^2\left[1 - \frac{V_B}{E_{\rm c.m.}}\right]. \tag{4}$$

So, at higher energies, the fusion cross sections obtained using the classical formula and Wong's formula are nearly the same; however, below the barrier, Wong's formula accounts for barrier penetrability, making it more suitable for our calculations [12].

The complete fusion cross section, $\sigma_{\rm CF}$ is defined as the capture of the total projectile charge. This process includes two mechanisms: direct complete fusion, which involves the capture of the projectile charge without breakup, and sequential complete fusion, which involves the capture of the entire projectile charge following the breakup of the projectile.

For head-on collisions (b = 0), the orientation-averaged fusion cross section is computed by averaging over a large number of Monte Carlo-sampled initial orientations, spanning collision energies both above and below the barrier. Calculated $\sigma_{\rm CF}$ for ^{9}Be + ^{208}Pb reaction with various assumptions of rigid body constraints for projectile fragments (^{4}He + ^{5}He), the bond between them and target (^{208}Pb), is shown in Figure 1 comparing it with experimental CF cross sections. In the SBPM (Static Barrier Penetration Model) [13] calculations, the nuclei are assumed to be rigid, and all rotational and vibrational degrees of freedom are suppressed, thereby neglecting any dynamical effects. As a result, the calculated complete fusion cross section ($\sigma_{\rm CF}$) is suppressed across all energies, as shown in Figure 1. To investigate the influence of rigidity constraints, three cases are considered. In Case (a), the rigidity constraint on ^{208}Pb is removed, while the projectile ^{9}Be remains rigid. In Case (b), along with the removal of the rigidity constraint on ^{9}Be + ^{208}Pb, the bond between the projectile fragments ^{4}He and ^{5}He (constituents of ^{9}Be) is removed, while ^{4}He and ^{5}He are kept rigid. In Case (c), the rigidity constraint on ^{5}He is also relaxed.

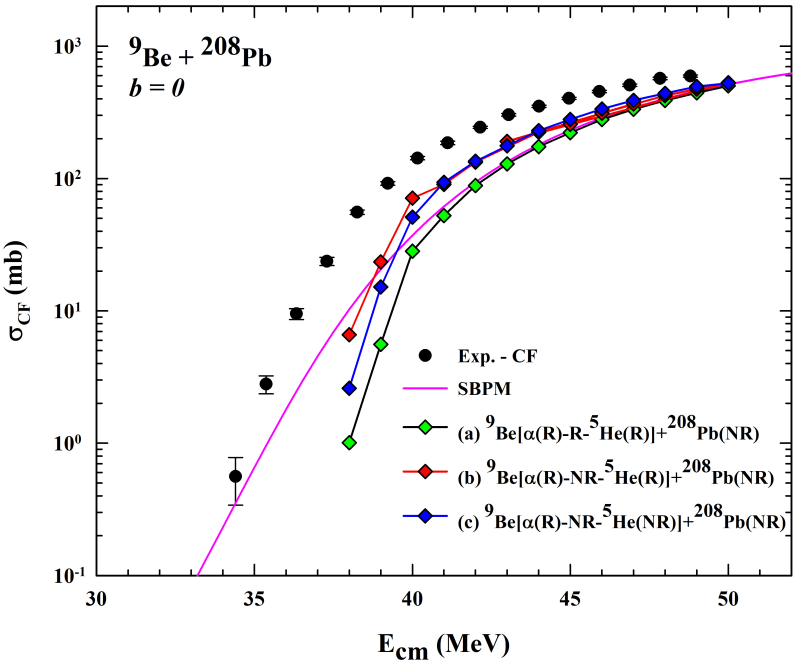

Figure 1. For (b = 0), σ_{CF} for ^{9}Be + ^{208}Pb reaction with various assumptions of rigid body constraints for a projectile, the bond between them, and the target. Experimental Complete Fusion Cross section (Exp.-CF) [14].

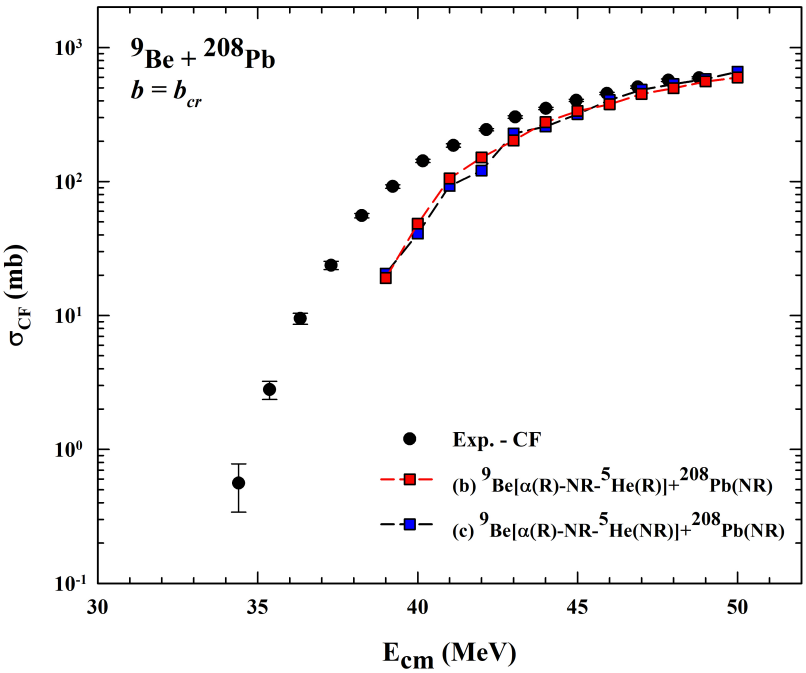

Figure 2. For (b = b_{cr}), σ_{CF} for ^{9}Be + ^{208}Pb reaction with various assumptions of rigid body constraints for a projectile, the bond between them, and the target. Experimental Complete Fusion Cross section (Exp.-CF) [14].

As seen in Figure 1, although (σ_{CF}) is suppressed at all energies, the suppression is particularly pronounced at below-barrier energies. Near the barrier energies, (σ_{CF}) improves as the rigidity constraints on the target and projectile are systematically removed, compared to the SBPM calculation. This signifies the dissipation of energy at below-barrier energies as rigidity constraints are relaxed. However, the multibody 3S-CMD calculations appear to follow the trend as the experimental results. For below- and near-barrier energies (σ_{CF}) in case (b) shows improvements compared to cases (a) and (c).

The CF cross-section is also calculated for non-central collisions ($b > 0$). The critical impact parameter for CF, (b_{cr} – CF), is determined dynamically during simulation, using the sharp cutoff approximation, where, all trajectories with ($b < b_{cr}$ – CF) result in complete fusion, while those with ($b > b_{cr}$ – CF) either lead to scattering or incomplete fusion (ICF). The CF cross section determined from (b_{cr} – CF) for cases (b) and (c) and shown in Figure 2. As evident from Figure 2, the fusion cross sections for non-central collisions are larger than those for central collisions at higher energies, while at lower energies they nearly coincide. This behavior indicates that as energy increases, non-central trajectories with finite orbital angular momentum can overcome the centrifugal barrier and contribute more to fusion, whereas central collisions correspond only to zero angular momentum $l = 0$. At lower energies, higher angular momentum contributions are strongly suppressed, making the fusion cross sections for central and non-central collisions nearly identical. This energy-dependent behavior is consistent with Wong's formula, where higher angular momentum partial waves become significant only above the Coulomb barrier. Furthermore, for near- and sub-barrier energies, the CF cross section in case (b) shows an improvement compared to case (c), reflecting the influence of different modeling assumptions on fusion probability.

4. CONCLUSIONS

The effects of various degrees of freedom on the ^{9}Be + ^{208}Pb reaction are studied using the multi-body Three-Stage Classical Molecular Dynamics (3S-CMD) approach. By appropriately modelling the weakly bound ^{9}Be and systematically relaxing rigidity constraints on the projectile and target, fusion cross sections for both central ($b = 0$) and non-central ($b > 0$) collisions are calculated. The complete fusion (CF) cross-section, σ_{CF}, is significantly influenced by various levels of rigidity constraints both on the target and projectile. For below-barrier energies, the complete fusion cross section is suppressed, while for near-the-barrier energy, it enhances as rigidity constraints are relaxed, indicating the importance of internal degrees of freedom. Mainly for below and near the barrier energies, trends of the multibody 3S-CMD model calculation are consistent with experimental data. Complete fusion cross sections, σ_{CF}, further enhance for non-central collisions. This demonstrates the applicability of this model to study systems with weakly bound nuclei in fusion dynamics.

ORCID

Vipul B. Katariya, https://orcid.org/0009-0001-7215-8128; **Jignasha A. Patel**, https://orcid.org/0009-0008-1454-4283; **Hardip R. Mahida**, https://orcid.org/0009-0001-7113-5848; **Pinank H. Jariwala**, https://orcid.org/0000-0003-1141-0761

REFERENCES

[1] M. Beckerman, Reports on Progress in Physics, **51**(8), 1047 (1988). https://doi.org/10.1088/0034-4885/51/8/001.

[2] C. Signorini, A. Andrighetto, M. Ruan, J.Y. Guo, L. Stroe, F. Soramel, K.E.G. Löbner, *et al.*, Physical Review C, **61**(6), 061603 (2000). https://doi.org/10.1103/PhysRevC.61.061603

[3] S. B. Moraes, P.R. S. Gomes, J. Lubian, J. J. S. Alves, R. M. Anjos, M. M. Sant'Anna, I. Padrón, *et al.*, Physical Review C, **61**(6), 064608 (2000). https://doi.org/10.1103/PhysRevC.61.064608

[4] M. Dasgupta, D. J. Hinde, R. D. Butt, R. M. Anjos, A. C. Berriman, N. Carlin, P. R. S. Gomes, *et al.*, Physical Review Letters, **82**(7), 1395 (1999). https://doi.org/10.1103/PhysRevLett.82.1395

[5] C. Signorini, Z. H. Liu, Z. C. Li, K. E. G. Löbner, L. Müller, M. Ruan, K. Rudolph, *et al.*, *et al.*, The European Physical Journal A – Hadrons and Nuclei, **5**(1), 7 (1999). https://doi.org/10.1007/s100500050250

[6] J. Takahashi, M. Munhoz, E. M. Szanto, N. Carlin, N. Added, A. A. P. Suaide, M. M. de Moura, *et al.*, Physical Review Letters, **78**(1), 30 (1997). https://doi.org/10.1103/PhysRevLett.78.30

[7] A. Mukherjee, M. Dasgupta, D. J. Hinde, H. Timmers, R. D. Butt, and P. R. S. Gomes, Physics Letters B, **526**(3), 295 (2002). https://doi.org/10.1016/S0370-2693(01)01505-2

[8] M. R. Morker, and S. S. Godre, EPJ Web of Conferences, **117**, 08013 (2016). https://doi.org/10.1051/epjconf/201611708013

[9] A. H. Wapstra, and K. Bos, Atomic Data and Nuclear Data Tables, **19**(3), 177 (1977). https://doi.org/10.1016/0092-640X(77)90020-1

[10] I. Angeli, and K. P. Marinova, Atomic Data and Nuclear Data Tables, **99**(1), 69 (2013). https://doi.org/10.1016/j.adt.2011.12.006

[11] C. Y. Wong, Physical Review Letters, **31**(12), 766 (1973). https://doi.org/10.1103/PhysRevLett.31.766

[12] P. R. Desai, and S. S. Godre, DAE Symp. Nucl. Phys. **55**, 400 (2010). https://www.sympnp.org/proceedings/55/B88.pdf

[13] S. S. Godre, Nuclear Physics A, **734**, E17 (2004). https://doi.org/10.1016/j.nuclphysa.2004.03.009

[14] M. Dasgupta, P. R. S. Gomes, D. J. Hinde, S. B. Moraes, R. M. Anjos, A. C. Berriman, R. D. Butt, *et al*., Physical Review C, **70**(2), 024606 (2004). https://doi.org/10.1103/PhysRevC.70.024606

ЗЛИТТЯ СЛАБКОЗВ'ЯЗАНИХ ^{9}Be З ВАЖКИМИ ЯДРАМИ ^{208}Pb: БАГАТОЧАСТИНКОВИЙ ТРЬОХЕТАПНИЙ ПІДХІД КЛАСИЧНОЇ МОЛЕКУЛЯРНОЇ ДИНАМІКИ

Віпул Б. Катарія[1*], **Джигнаша А. Патель**[2], **Хардіп Р. Махіда**[3], **Пінанк Х. Джарівала**[2]

[1]*Кафедра фізики, Науковий коледж Атмананд Сарасваті, Сурат, Гуджарат, 395006, Індія*

[2]*Кафедра фізики, Науковий коледж Нав'юг, Сурат, Гуджарат, 395009, Індія*

[3]*Кафедра фізики, Університет Віра Нармада Південного Гуджарату, Сурат, Гуджарат, 395007, Індія*

Злиття слабозв'язаного ядра ^{9}Be з ^{208}Pb досліджується за допомогою багаточастинкового тристадійного підходу класичної молекулярної динаміки (3S-CMD). Ця модель явно розглядає ^{9}Be як кластер ^{4}He та ^{5}He, що дозволяє послабити обмеження твердого тіла як на фрагментах снаряда, так і на мішені. У цій статті досліджується вплив цих обмежень на поперечний переріз повного злиття (CF), враховуючи як центральні, так і нецентральні зіткнення. Систематичне видалення обмежень жорсткості, зокрема на мішені та фрагментах ^{9}Be, суттєво впливає на поперечний переріз CF, особливо при підбар'єрних енергіях. Розрахунки показують, що послаблення цих обмежень посилює CF, що вказує на важливу роль розпаду та внутрішніх ступенів свободи. Багаточастинкова 3S-CMD-модель надає інструмент для розуміння взаємодії розпаду та синтезу в реакціях, що включають слабозв'язані ядра.

Ключові слова: *слабкозв'язані ядра; зіткнення важких іонів; реакції синтезу; класична молекулярна динаміка*

EAST EUROPEAN JOURNAL OF PHYSICS. 1. 148-155 (2026)
DOI:10.26565/2312-4334-2026-1-13 ISSN 2312-4334

RELATIVISTIC CONFIGURATION-INTERACTION PHOTOIONIZATION DATA FOR Ne-LIKE ISOELECTRONIC SEQUENCE

O. Abu-Haija[1]*, G.A. Alna'washi[2], S.M. Hamasha[2], M.T. Gning[3,4], I. Sakho[3,4], M. Al Shorman[1]
[1]*Applied Physics Department, Tafila Technical University, P. O. Box 179, Tafila 66110, Jordan*
[2]*Department of Physics, Faculty of Science, The Hashemite University, P. O. Box 330127, Zarqa 13133, Jordan*
[3]*Department of Physics Chemistry, UFR Sciences and Technologies, University Iba Der Thiam, Thies, Senegal*
[4]*African Center for Applied Atomic and Nuclear Technologies (CAFTANA), Dakar, Senegal*
**Corresponding Author email: oabuhaija@ttu.edu.jo*
Received October 12, 2025; revised February 4, 2026; accepted February 7, 2026

Photoionization data for the $1s^2\ 2s^2\ 2p^6\ (^1S_0)$ ground state of neon like Ca^{10+}, Sc^{11+}, Ti^{12+}, V^{13+}, and Cr^{14+} ions are reported. The values of ionization threshold limits, resonance energies, quantum defects, transition rates, and oscillator strengths for various Rydberg series are tabulated. The Relativistic configuration-interaction (RCI) approach, implemented in the Flexible Atomic Code (FAC), was used for all calculations. The RCI results for $2s\ 2p^6\ (^2S_{1/2})$ np resonance series show very good agreement with reported values in the literature. In addition, new calculations on K-shell photoexcitations ($1s\ 2s^2\ 2p^6\ (^2S_{1/2})$ np) in these ions are reported. These results would be valuable for high-precision spectral modeling in astrophysical or laboratory plasmas.
Keywords: *Photoexcitation; Resonance energy; Rydberg series; Relativistic configuration-interaction*
PACS: 31.15.ag

1. INTRODUCTION

Since the majority of matter in the Universe exists in an ionic form, the study of photoionization of positive ions is essential for improving our understanding and modeling of both fusion [1] and astrophysics [2] plasmas. In astrophysical nebulae, photoionization is an important process in controlling the ionization balance and, consequently, determining elemental abundances. In particular, the photoionization of Ne-like isoelectronic sequence is of astrophysical importance because the spectra of these ions serve as a key diagnostic tool for probing plasma conditions. Moreover, Ne-like ions of middle and high atomic numbers are found in various plasma environments, including electron-beam ion trap, tokamak, and solar atmosphere [3] [4]. In addition to their astrophysical relevance, these ions have practical significance in X-ray laser research, where photoionization of these ions has been utilized to explain the resonant photo-pumping scheme for driving lasing action [5]. Thus, ions belonging to the Ne isoelectronic sequence have attracted considerable experimental and theoretical studies [6] [7] [8] [9] [10] across a wide range of Z due to their broad application in plasma physics and astrophysics, as well as their stable closed-shell electronic structure. Among these, the neon like Ca^{10+}, Sc^{11+}, Ti^{12+}, V^{13+}, and Cr^{14+} ions are of particular interest. Goyal et al. [11] reported resonance energies and natural widths in the photoionization of Ne-like isoelectronic sequence (Z = 19 to 26) using the Screening Constant by Unit Nuclear Charge (SCUNC) approach. Liang et al. [12] employed the Breit–Pauli Hamiltonian within the R-matrix (B-P R-matrix) method to calculate the photoionization cross sections, resonance positions and widths for Ne-like Ca XI. In addition, the 2s to np autoionizing resonance transitions in various Ne-like ions were studied by Nrisimhamurty et al. [13] using the relativistic multichannel quantum-defect theory (RMQDT) and relativistic random-phase approximation (RRPA). More recently, Alna'washi et al. [14] [15] [16] presented new atomic data identifying 1s → np resonances in Ne and Ne-like ions, based on calculations performed within the relativistic configuration-interaction (RCI) method.

Given that achieving high accuracy for spectral modeling and high-resolution X-ray interpretation remains a significant challenge in astrophysical interest, this work extends our previous study [14] [15] [16] by performing new calculations for the Ne-like Ca^{10+}, Sc^{11+}, Ti^{12+}, V^{13+}, and Cr^{14+} ions. Specifically, the present study focuses on the $1s^2\ 2s\ 2p^6\ (^2S_{1/2})$ np $(^1P_1)$ and $1s\ 2s^2\ 2p^6\ (^2S_{1/2})$ np $(^1P_1)$ resonance series of these ions. To achieve this, the Relativistic Configuration Interaction (RCI) method, as implemented in the Flexible Atomic Code (FAC) [17], was employed for all calculations. The computed quantities include the ionization threshold, resonance energy, oscillator strength, and electric dipole (E1) transition rate corresponding to the 1s to np and 2s to np transitions with principal quantum number ranging from n = 3 to n = 22. Section 2 presents a brief outline of the theoretical framework. Section 3 presents and discusses our results in comparison with available literature data. Finally, we summarize and conclude in section 4.

2. THEORY

The RCI approach, as implemented in the FAC code, has already been extensively detailed in some literatures [14] [15] [16] [17] [18] [19]. Hence, a concise overview is provided here to outline the key aspects relevant to the present study.

Cite as: O. Abu-Haija, G. A. Alna'washi, S. M. Hamasha, M. T. Gning, I. Sakho, M. M. Al Shorman, East Eur. J. Phys. 1, 148 (2026), https://doi.org/10.26565/2312-4334-2026-1-13

2.1. Atomic structure: framework of the Dirac equation

For N electrons atom or ion, the relativistic Hamiltonian (H), expressed in atomic units, can be written as:

$$H = \sum_{i=1}^{N} H_D(i) + \sum_{i<j}^{N} \frac{1}{r_{ij}}, \tag{1}$$

where $H_D(i)$, the one electron Dirac Hamiltonian, is given by:

$$H_D = c\boldsymbol{\alpha}_i \cdot \boldsymbol{\alpha}_j + \beta m_e c^2 - \frac{Z}{r} \tag{2}$$

In Eq. (2), the term $c\boldsymbol{\alpha}_i \cdot \boldsymbol{\alpha}_j$ represents the electron's kinetic energy where $\boldsymbol{\alpha_i}$ and $\boldsymbol{\alpha_j}$ are Dirac matrices. The term $\beta m_e c^2$ denotes the rest-mass energy, and $(-\frac{Z}{r})$ corresponds to the Coulomb potential of the nucleus. The energy levels of any atomic ion can be obtained by diagonalizing the relativistic Hamiltonian (H).

In FAC, atomic processes are treated with basis state functions generated from a single potential. The basis states (Φ_v), referred as configuration state functions (CSFs), are built as antisymmetric sums of the products of N single-electron Dirac spinors φ_{nkm}.

The approximate atomic state functions are constructed by linearly combining basis states, Φ_v, with same symmetries as follows:

$$\psi = \sum_v b_v \Phi_v \tag{3}$$

where b_v are the mixing coefficients, which can be determined by diagonalizing the total Hamiltonian. The single-electron Dirac spinors are defined as:

$$\varphi_{n\kappa m} = \frac{1}{r}\begin{pmatrix} P_{n\kappa}(r)\chi_{\kappa m}(\theta,\phi,\sigma) \\ iQ_{n\kappa}(r)\chi_{-\kappa m}(\theta,\phi,\sigma) \end{pmatrix}. \tag{4}$$

Here, n denotes the principal quantum number, m represents the z-component of total angular momentum, and $\chi_{\kappa m}$ is the spin-angular function. The relativistic angular quantum number κ is expressed as:

$$\kappa = (l-j)(2j+1). \tag{5}$$

The functions $P_{n\kappa}$ and $Q_{n\kappa}$ are the Dirac spinor's radial part components. These radial functions are obtained as solutions to the Dirac differential equation for the local central potential $V(r)$ as follows:

$$\left(\frac{d}{dr} + \frac{\kappa}{r}\right) P_{n\kappa} = \alpha \left(\varepsilon_{n\kappa} - V + \frac{2}{\alpha^2}\right) Q_{n\kappa}(r) \tag{6}$$

$$\left(\frac{d}{dr} - \frac{\kappa}{r}\right) Q_{n\kappa} = \alpha(-\varepsilon_{n\kappa} + V) P_{n\kappa}(r). \tag{7}$$

Here, α is the fine-structure constant, and $\varepsilon_{n\kappa}$ represents the energy eigenvalues associated with the corresponding radial functions.

2.2. Radiative transition rates

The electric dipole (E1) transition rates are calculated within the single multipole approximation, which neglects the interference between different multipole orders. The transition rates, A_{fi}^{E1}, is related to the transition line strength, S_{if}, and wavelength of the transition, λ, by the expression:

$$A_{fi}^{E1} = \frac{2.0261\times10^{18}}{(2J+1)\lambda^3} S_{if}^{E1} \tag{8}$$

Here, the generalized line strength of the transition S_{fi} is defined as the squared matrix element $S_{fi} = \left|\langle\varphi_f|O_M^L|\varphi_i\rangle\right|^2$, where O_M^L is the multipole operator, φ_i, and φ_f are the wavefunctions of the initial and final states, respectively. Furthermore, the weighted oscillator strength, gf_{fi}, for different radiative channels is given by:

$$gf_{fi} = \frac{\omega}{L}(\alpha\omega)^{2L-2} S_{fi}, \tag{9}$$

where $\omega = E_f - E_i$ is the energy of transition.

2.3. Resonance energy and quantum defect

The quantum defect concept is introduced in the treatment of highly excited Rydberg states, which in turn accounts for the effects of core polarization and penetration. Within this framework, the revised Rydberg formula gives the energy level of an electron E_n (in eV) as:

$$E_n = E_\infty - \frac{R(Z-N_c)^2}{(n-\delta_n)^2}, \tag{10}$$

In this equation, R is the Rydberg constant, N_c is the number of core electrons, δ_n represents quantum defect, and E_∞ denotes the threshold limit.

2.4. Calculation procedure

Our configuration interaction (CI) expansion includes the ground state configuration ($1s^2\ 2s^2\ 2p^6$) and excited configurations ($1s^2\ 2s\ 2p^6$ np and $1s\ 2s^2\ 2p^6$ np) involving n goes to 22. To ensure convergence, we systematically increased the configuration set and monitored the resonance energies and oscillator strengths. This process guaranteed convergence for energy positions to within approximately 0.02 eV and for line strengths to within 2%. As mentioned in the FAC manual, the estimated uncertainties in the radiative rates and oscillator strengths range from 10 to 20%, while the accuracy within a few (eV) for the calculated energy levels. It is important to point out that the higher-order quantum electrodynamic (QED) effects are excluded from the RCI approach, as their impact is negligible compared to that of electron correlations. Furthermore, within FAC's RCI methodology, autoionizing resonances are treated as bound-like states, neglecting explicit continuum coupling. This approximation eliminates Fano interference and energy-dependent continuum effects, causing systematic shifts in resonance positions.

3. RESULTS AND DISCUSSION

3.1 Threshold limits

The $1s^2\ 2s\ 2p^6$ ($^2S_{1/2}$) and $1s\ 2s^2\ 2p^6$ ($^2S_{1/2}$) series limits for the Ne-like ions with nuclear charge Z = 20 – 24 are listed in Table 1, in addition to other theoretical results obtained by Goyal et al. [11] and Nrisimhamurty et al. [13], as well as tabulated data from the NIST database [20], for comparison.

Table 1. Energy limit E_∞ (eV) of the $1s^22s2p^6(^2S_{1/2})$ and $1s2s^22p^6(^2S_{1/2})$ thresholds of Ca^{10+}, Sc^{11+}, Ti^{12+}, V^{13+}, and Cr^{+14} ions.

Ion	Configuration	E_∞^a	E_∞^b	E_∞^c	E_∞^d
Ca^{10+}	$1s^2\ 2s\ 2p^6\ (^2S_{1/2})$	679.7839	680.800	679.509	682.642
	$1s\ 2s^2\ 2p^6\ (^2S_{1/2})$	4298.5845			
Sc^{11+}	$1s^2\ 2s\ 2p^6\ (^2S_{1/2})$	781.2269	782.758	782.0369	
	$1s\ 2s^2\ 2p^6\ (^2S_{1/2})$	4794.2941			
Ti^{12+}	$1s^2\ 2s\ 2p^6\ (^2S_{1/2})$	889.6942	891.543	889.3088	
	$1s\ 2s^2\ 2p^6\ (^2S_{1/2})$	5317.9877			
V^{13+}	$1s^2\ 2s\ 2p^6\ (^2S_{1/2})$	1005.2103	1007.146	1004.828	1008.297
	$1s\ 2s^2\ 2p^6\ (^2S_{1/2})$	5869.7555			
Cr^{14+}	$1s^2\ 2s\ 2p^6\ (^2S_{1/2})$	1127.7993	1129.556	1127.871	1130.993
	$1s\ 2s^2\ 2p^6\ (^2S_{1/2})$	6449.6768			

[a] : Present work.
[b] : Goyal et al. [11].
[c] : National Institute of Standards and Technology (NIST) [20].
[d] : Nrisimhamurty et al. [13].

For these ions, it can be seen that the present results for the $1s^2\ 2s\ 2p^6$ ($^2S_{1/2}$) limit are in good agreement with the results reported in the literature. The computed RCI energy limits show excellent agreement with the NIST data but lie approximately 1–1.8 eV below the values obtained using SCUNC method. In contrast, the results from RMQDT by Nrisimhamurty et al. [13] are slightly higher than the present RCI, SCUNC and NIST data for Ca^{10+}, V^{13+}, and Cr^{14+} ions. This discrepancy is likely attributed to omission of electron correlation effects in their RMQDT calculations. To the best of our knowledge, the threshold limits of the $1s\ 2s^2\ 2p^6$ ($^2S_{1/2}$) series have not been previously published for these five neon-like ions (Ca, Sc, Ti, V and Cr). Consequently, the calculated RCI $1s\ 2s^2\ 2p^6$ ($^2S_{1/2}$) series limits presented here may provide new findings for these K-shell excitations and may guide future theoretical and experimental studies.

3.2 The $1s^22s2p^6(^2S_{1/2})$ np ($^1P_1$) series

Following the determination of the energy thresholds, we investigate the resonance series associated with E1 transitions from the ground state to the $1s^2\ 2s\ 2p^6$ ($^2S_{1/2}$) np ($^1P_1$) excited states of the Ca^{10+}, Sc^{11+}, Ti^{12+}, V^{13+}, and Cr^{14+} ions. For these resonances, we present RCI-calculated resonance energies (E_n), transition rates (A_{fi}^{E1}), weighted oscillator strengths (gf_{ij}), and the quantum defects (δ_n) obtained from Eq. (10) using the corresponding computed RCI series limits. A comparison of our RCI results for the $2s\ 2p^6$ ($^2S_{1/2}$) np Rydberg series with those from Goyal et al. [11] is provided in Tables 2–6 for all five ions. For Ne-like Ca^{10+} ion, Table 2 also includes reference values from the (B-P R-matrix) method [12]. The B-P R-matrix resonance energies for Ca^{10+} ion show excellent agreement with our results for $n = 5 - 15$, with energy differences ranging from 0.08 eV to 0.42 eV. For all five ions, one can see from Tables 2–6 that our RCI-calculated resonance energy values for the $2s\ 2p^6$ ($^2S_{1/2}$) np ($^1P_1$) series agree well with the SCUNC data with energy differences remaining below 1.9 eV. In addition, the RCI and SCUNC resonance energies converge to nearly identical series limits with remarkably small differences of 1.02 eV, 1.53 eV, 1.85 eV, 1.94 eV, and 1.76 eV for Ca^{10+}, Sc^{11+}, Ti^{12+}, V^{13+}, and Cr^{14+} ions, respectively. This close agreement confirms the reliability of the present RCI predictions, particularly for higher states. Based on the preceding comparisons, the absolute uncertainties in the resonance energies are estimated as follows: ± 1.0 eV, ± 1.5 eV, ± 1.9 eV, ± 1.9 eV, and ± 1.8 eV for Ca^{10+}, Sc^{11+}, Ti^{12+}, V^{13+}, and Cr^{14+} ions, respectively.

Table 2. Calculated Spectroscopic Parameters: Resonance energies (E_n), quantum defects (δ_n), transition rates (A_{fi}^{E1}), and oscillator strengths (gf_{ij}) for $1s^2 2s 2p^6$ np ($^1P_1$) resonances in Ca^{10+}

n	E_n^a (eV)	δ_n^a	A_{fi}^{E1} (s^{-1})	gf_{ij}	E_n^b (eV)	δ_n^b	E_n^c (eV)
3	460.7453	0.25847	1.2562×10^{12}	4.091×10^{-1}			
4	562.8209	0.24829	5.3983×10^{11}	1.178×10^{-1}			
5	606.9299	0.24636	2.7276×10^{11}	5.119×10^{-2}			607.3513
6	630.0417	0.24705	1.5547×10^{11}	2.708×10^{-2}	630.92	0.255	630.2552
7	643.6609	0.24911	9.6801×10^{10}	1.615×10^{-2}	644.62	0.254	643.8187
8	652.3546	0.25278	6.4248×10^{10}	1.044×10^{-2}	653.37	0.253	652.4828
9	658.2414	0.25812	4.4782×10^{10}	7.146×10^{-3}	659.29	0.252	658.3523
10	662.4117	0.26523	3.2439×10^{10}	5.111×10^{-3}	663.48	0.252	662.5115
11	665.4738	0.27415	2.4241×10^{10}	3.784×10^{-3}	666.55	0.251	665.5660
12	667.7881	0.28511	1.8584×10^{10}	2.881×10^{-3}	668.87	0.251	667.8749
13	669.5799	0.29813	1.4559×10^{10}	2.245×10^{-3}	670.67	0.251	669.6641
14	670.9954	0.31340	1.1618×10^{10}	1.784×10^{-3}	672.09	0.250	671.0763
15	672.1331	0.33103	9.4165×10^{9}	1.441×10^{-3}	673.23	0.250	672.2124
16	673.0612	0.35120	7.7381×10^{9}	9.800×10^{-4}	674.16	0.250	
17	673.8283	0.37391	6.4359×10^{9}	8.223×10^{-4}	674.93	0.250	
18	674.4695	0.39947	5.4102×10^{9}	8.549×10^{-4}	675.57	0.250	
19	675.0110	0.42787	4.5914×10^{9}	6.967×10^{-4}	676.12	0.250	
20	675.4724	0.45936	3.9298×10^{9}	5.955×10^{-4}	676.58	0.250	
21	675.8688	0.49397	3.3895×10^{9}	5.130×10^{-4}	676.98	0.250	
22	676.2118	0.53202	2.9439×10^{9}	4.451×10^{-4}	677.32	0.250	
⋮							
∞	679.7839				680.800		

[a] : Present RCI results.
[b] : SCUNC calculations of Goyal et al. [11].
[c] : B-P R-matrix code calculations of Liang et al. [12].

Table 3. Calculated Spectroscopic Parameters: E_n, δ_n, A_{fi}^{E1} and gf_{ij} for $1s^2 2s\ 2p^6$ np ($^1P_1$) resonances in Sc^{11+}.

n	E_n^a (eV)	δ_n^a	A_{fi}^{E1} (s^{-1})	gf_{ij}	E_n^b (eV)	δ_n^b
3	523.5293	0.24269	1.6887×10^{12}	4.260×10^{-1}		
4	643.1629	0.23295	7.2497×10^{11}	1.213×10^{-1}		
5	695.0858	0.23090	3.6641×10^{11}	5.243×10^{-2}		
6	722.3511	0.23136	2.089×10^{11}	2.768×10^{-2}	723.75	0.238
7	738.4419	0.23301	1.3014×10^{11}	1.650×10^{-2}	739.91	0.238
8	748.7241	0.23608	8.6406×10^{10}	1.066×10^{-2}	750.25	0.237
9	755.6920	0.24060	6.0251×10^{10}	7.294×10^{-3}	757.25	0.237
10	760.6314	0.24662	4.3653×10^{10}	5.216×10^{-3}	762.21	0.236
11	764.2599	0.25419	3.2632×10^{10}	3.863×10^{-3}	765.85	0.236
12	767.0035	0.26347	2.5021×10^{10}	2.941×10^{-3}	768.60	0.236
13	769.1282	0.27458	1.9606×10^{10}	2.291×10^{-3}	770.73	0.236
14	770.8072	0.28759	1.5647×10^{10}	1.821×10^{-3}	772.42	0.236
15	772.1571	0.30253	1.2684×10^{10}	1.471×10^{-3}	773.77	0.235
16	773.2585	0.31964	1.0422×10^{10}	1.205×10^{-3}	774.87	0.235
17	774.1689	0.33901	8.6718×10^{9}	1.000×10^{-3}	775.79	0.235
18	774.9301	0.36069	7.2907×10^{9}	8.394×10^{-4}	776.55	0.235
19	775.5730	0.38481	6.1879×10^{9}	7.112×10^{-4}	777.19	0.235
20	776.1209	0.41150	5.2967×10^{9}	6.079×10^{-4}	777.74	0.235
21	776.5916	0.44097	4.5687×10^{9}	5.237×10^{-4}	778.21	0.235
22	776.9990	0.47321	3.9685×10^{9}	4.545×10^{-4}	778.62	0.235
⋮						
∞	781.2269				782.758	

[a] : Present RCI results.
[b] : SCUNC calculations of Goyal et al. [11].

Table 4. Calculated Spectroscopic Parameters: E_n, δ_n, A_{fi}^{E1} and gf_{ij} for $1s^2 2s\ 2p^6$ np ($^1P_1$) resonances in Ti^{12+}.

n	E_n^a (eV)	δ_n^a	A_{fi}^{E1} (s^{-1})	gf_{ij}	E_n^b (eV)	δ_n^b
3	590.2818	0.22879	2.2147×10^{12}	4.3945×10^{-1}		
4	728.8120	0.21950	9.4955×10^{11}	1.236×10^{-1}		
5	789.1685	0.21739	4.7996×10^{11}	2.808×10^{-2}		
6	820.9233	0.21769	2.7370×10^{11}	2.708×10^{-2}	822.64	0.223
7	839.6881	0.21902	1.7058×10^{11}	1.673×10^{-2}	841.47	0.224
8	851.6902	0.22162	1.1329×10^{11}	1.080×10^{-2}	853.52	0.223
9	859.8293	0.22549	7.9025×10^{10}	7.390×10^{-3}	861.69	0.223
10	865.6021	0.23064	5.7265×10^{10}	5.284×10^{-3}	867.49	0.223
11	869.8445	0.23717	4.2818×10^{10}	3.913×10^{-3}	871.75	0.223
12	873.0535	0.24513	3.2840×10^{10}	2.979×10^{-3}	874.97	0.223
13	875.5393	0.25469	2.5735×10^{10}	2.321×10^{-3}	877.46	0.223
14	877.5042	0.26585	2.0541×10^{10}	1.844×10^{-3}	879.43	0.223
15	879.0842	0.27871	1.6655×10^{10}	1.490×10^{-3}	881.01	0.222
16	880.3736	0.29342	1.3689×10^{10}	1.221×10^{-3}	882.31	0.223

n	E_n^{a} (eV)	δ_n^{a}	A_{fi}^{E1} (s^{-1})	gf_{ij}	E_n^{b} (eV)	δ_n^{b}
17	881.4396	0.31003	1.1388×10^{10}	1.013×10^{-3}	883.37	0.223
18	882.3310	0.32863	9.5759×10^{9}	8.504×10^{-4}	884.27	0.223
19	883.0839	0.34939	8.1282×10^{9}	7.206×10^{-4}	885.02	0.223
20	883.7256	0.37239	6.9583×10^{9}	6.160×10^{-4}	885.66	0.223
21	884.2770	0.39768	6.002×10^{9}	5.307×10^{-4}	886.22	0.223
22	884.7542	0.42553	5.2142×10^{9}	4.605×10^{-4}	886.69	0.223
⋮						
∞	889.6942				891.543	

[a] : Present RCI results.
[b] : SCUNC calculations of Goyal et al. [11].

Table 5. Calculated Spectroscopic Parameters: E_n, δ_n, A_{fi}^{E1} and gf_{ij} for $1s^22s\ 2p^6$ np ($^1P_1$) resonances in V^{13+}

n	E_n^{a} (eV)	δ_n^{a}	A_{fi}^{E1} (s^{-1})	gf_{ij}	E_n^{b} (eV)	δ_n^{b}
3	661.0276	0.21648	2.8432×10^{12}	4.499×10^{-1}		
4	819.7928	0.20761	1.2174×10^{12}	1.252×10^{-1}		
5	889.2021	0.20549	6.1534×10^{11}	5.381×10^{-2}		
6	925.7824	0.20569	3.5104×10^{11}	2.832×10^{-2}	927.60	0.210
7	947.4239	0.20678	2.1882×10^{11}	1.685×10^{-2}	949.29	0.211
8	961.2773	0.20901	1.4538×10^{11}	1.088×10^{-2}	963.19	0.211
9	970.6776	0.21234	1.0142×10^{11}	7.442×10^{-3}	972.62	0.211
10	977.3480	0.21682	7.3513×10^{10}	5.321×10^{-3}	979.32	0.211
11	982.2519	0.22251	5.4977×10^{10}	3.940×10^{-3}	984.24	0.211
12	985.9625	0.22942	4.2174×10^{10}	2.999×10^{-3}	987.96	0.211
13	988.8376	0.23772	3.3054×10^{10}	2.337×10^{-3}	990.84	0.211
14	991.1106	0.24745	2.6385×10^{10}	1.857×10^{-3}	993.12	0.211
15	992.9387	0.25863	2.1397×10^{10}	1.500×10^{-3}	994.95	0.211
16	994.4308	0.27144	1.7589×10^{10}	1.230×10^{-3}	996.45	0.211
17	995.6646	0.28584	1.4634×10^{10}	1.021×10^{-3}	997.69	0.211
18	996.6964	0.30201	1.2305×10^{10}	8.564×10^{-4}	998.72	0.211
19	997.5679	0.32015	1.0446×10^{10}	7.257×10^{-4}	999.59	0.211
20	998.3109	0.34004	8.9434×10^{9}	6.204×10^{-4}	1000.34	0.211
21	998.9493	0.36205	7.7156×10^{9}	5.346×10^{-4}	1000.98	0.211
22	999.5019	0.38620	6.7026×10^{9}	4.639×10^{-4}	1001.53	0.211
⋮						
∞	1005.2103				1007.146	

[a] : Present RCI results.
[b] : SCUNC calculations of Goyal et al. [11].

Table 6. Calculated Spectroscopic Parameters: E_n, δ_n, A_{fi}^{E1} and gf_{ij} for $1s^22s\ 2p^6$ np ($^1P_1$) resonances in Cr^{14+}.

n	E_n^{a} (eV)	δ_n^{a}	A_{fi}^{E1} (s^{-1})	gf_{ij}	E_n^{b} (eV)	δ_n^{b}
3	735.7920	0.20550	3.5833×10^{12}	4.576×10^{-1}		
4	916.1298	0.19703	1.5323×10^{12}	1.262×10^{-1}		
5	995.2111	0.19494	7.7450×10^{11}	5.406×10^{-2}		
6	1036.9528	0.19506	4.4200×10^{11}	2.842×10^{-2}	1038.60	0.199
7	1061.6735	0.19597	2.7559×10^{11}	1.690×10^{-2}	1063.35	0.200
8	1077.5096	0.19789	1.8314×10^{11}	1.091×10^{-2}	1079.24	0.200
9	1088.2609	0.20082	1.2779×10^{11}	7.460×10^{-3}	1090.02	0.200
10	1095.8933	0.20475	9.2648×10^{10}	5.333×10^{-3}	1097.68	0.200
11	1101.5063	0.20975	6.9296×10^{10}	3.949×10^{-3}	1103.31	0.200
12	1105.7546	0.21582	5.3168×10^{10}	3.006×10^{-3}	1107.57	0.200
13	1109.0471	0.22310	4.1676×10^{10}	2.343×10^{-3}	1110.87	0.200
14	1111.6506	0.23162	3.3272×10^{10}	1.861×10^{-3}	1113.48	0.200
15	1113.7448	0.24144	2.6984×10^{10}	1.504×10^{-3}	1115.58	0.201
16	1115.4543	0.2527	2.2185×10^{10}	1.233×10^{-3}	1117.29	0.201
17	1116.8680	0.26539	1.8459×10^{10}	1.023×10^{-3}	1118.71	0.201
18	1118.0504	0.27959	1.5523×10^{10}	8.585×10^{-4}	1119.89	0.201
19	1119.0493	0.29544	1.3179×10^{10}	7.256×10^{-4}	1120.89	0.201
20	1119.9008	0.31301	1.1283×10^{10}	6.220×10^{-4}	1121.75	0.201
21	1120.6326	0.33231	9.7348×10^{9}	5.359×10^{-4}	1122.48	0.201
22	1121.2661	0.35346	8.4571×10^{9}	4.651×10^{-4}	1123.11	0.201
⋮						
∞	1127.7993				1129.556	

[a] : Present RCI results.
[b] : SCUNC calculations of Goyal et al. [11].

The quantum defects calculated for Ne-like isoelectronic sequence reveal a noticeable increase with the principal quantum number n. This behavior indicates the growing dominance of the core polarization effect as n increases. In contrast, $\delta_n^{\mathrm{SCUNC}}$ values for all ions exhibit no noticeable change across $n = 6 - 22$. As expected for high-n Rydberg states, the transition rate values for all studied ions drop by at least two orders of magnitude. Meanwhile, the oscillator strength values exhibit an even more pronounced decline of over three orders of magnitude, indicating the reduced overlap associated with the state wavefunctions.

3.3 The $1s2s^22p^6(^2S_{1/2})$ np ($^1P_1$) series

Tables 7-11 present the RCI-calculated resonance parameters for the inner shell 1s → np excitations ($n = 3 - 22$) for Ne-like ions with $10 \leq Z \leq 14$, respectively. It can be seen that the calculated energies demonstrate a clear convergence trend toward their respective series limits with increasing n. In addition, the quantum defect values display minimal variation, with average values of 0.27 for Ca^{10+}, 0.25 for Sc^{11+}, 0.24 for Ti^{12+}, 0.22 for V^{13+}, and 0.21 for Cr^{14+}. The stability of δ_n indicates that the core polarization effect is largely independent of n. Both the transition rates and oscillator strengths follow similar decreasing trend with increasing the principal quantum number. The behavior of the transition rates is in accordance with that of electric dipole-allowed transitions in Rydberg series, whereas the trend of the oscillator strengths can be attributed to the reduced overlap between the initial and final states.

Table 7. Present RCI Spectroscopic Parameters: E_n, δ_n, A_{fi}^{E1} and gf_{ij} for the $1s2s^22p^6$ ($^2S_{1/2}$) np ($^1P_1$) series in Ca^{10+} ion.

n	E_n (eV)	δ_n	A_{fi}^{E1} (s^{-1})	gf_{ij}
3	4075.7419	0.28197	2.1720×10^{13}	9.040×10^{-2}
4	4180.3278	0.26887	8.3378×10^{12}	3.299×10^{-2}
5	4225.1686	0.26459	4.0696×10^{12}	1.576×10^{-2}
6	4248.5758	0.26240	2.2961×10^{12}	8.795×10^{-3}
7	4262.3341	0.26098	1.4173×10^{12}	5.394×10^{-3}
8	4271.1030	0.26015	9.3575×10^{11}	3.546×10^{-3}
9	4277.0341	0.25972	6.4991×10^{11}	2.456×10^{-3}
10	4281.2325	0.25957	4.6963×10^{11}	1.771×10^{-3}
11	4284.3130	0.25966	3.5035×10^{11}	1.320×10^{-3}
12	4286.6401	0.25993	2.6830×10^{11}	1.009×10^{-3}
13	4288.4409	0.26037	2.0998×10^{11}	7.894×10^{-4}
14	4289.8630	0.26093	1.6741×10^{11}	6.289×10^{-4}
15	4291.0057	0.26152	1.3561×10^{11}	5.092×10^{-4}
16	4291.9376	0.26222	1.1139×10^{11}	4.181×10^{-4}
17	4292.7076	0.26295	9.2608×10^{10}	3.475×10^{-4}
18	4293.3511	0.26378	7.7824×10^{10}	2.919×10^{-4}
19	4293.8945	0.26445	6.6026×10^{10}	2.476×10^{-4}
20	4294.3574	0.26525	5.6500×10^{10}	2.118×10^{-4}
21	4294.7550	0.26606	4.8722×10^{10}	1.826×10^{-4}
22	4295.0990	0.26696	4.2308×10^{10}	1.586×10^{-4}
⋮				
∞	4298.5845			

Table 8. Present RCI Spectroscopic Parameters: E_n, δ_n, A_{fi}^{E1} and gf_{ij} for the $1s2s^22p^6$ ($^2S_{1/2}$) np ($^1P_1$) series in Sc^{11+} ion.

n	E_n (eV)	δ_n	A_{fi}^{E1} (s^{-1})	gf_{ij}
3	4532.3767	0.26499	2.7733×10^{13}	9.334×10^{-2}
4	4654.7836	0.25253	1.0695×10^{13}	3.299×10^{-2}
5	4707.5176	0.24839	5.2325×10^{12}	1.632×10^{-2}
6	4735.1112	0.24635	2.9595×10^{12}	9.126×10^{-3}
7	4751.3567	0.24503	1.8287×10^{12}	5.600×10^{-3}
8	4761.7228	0.24425	1.2083×10^{12}	3.684×10^{-3}
9	4768.7402	0.24386	8.3970×10^{11}	2.553×10^{-3}
10	4773.7109	0.24370	6.0710×10^{11}	1.842×10^{-3}
11	4777.3599	0.24379	4.5304×10^{11}	1.372×10^{-3}
12	4780.1176	0.24407	3.4705×10^{11}	1.050×10^{-3}
13	4782.2526	0.24439	2.7170×10^{11}	8.214×10^{-4}
14	4783.9390	0.24488	2.1667×10^{11}	6.546×10^{-4}
15	4785.2944	0.24540	1.7555×10^{11}	5.300×10^{-4}
16	4786.4000	0.24602	1.4422×10^{11}	4.352×10^{-4}
17	4787.3137	0.24666	1.1992×10^{11}	3.618×10^{-4}
18	4788.0775	0.24727	1.0079×10^{11}	3.040×10^{-4}
19	4788.7224	0.24800	8.5524×10^{10}	2.578×10^{-4}
20	4789.2720	0.24856	7.3192×10^{10}	2.206×10^{-4}
21	4789.7441	0.24915	6.3122×10^{10}	1.902×10^{-4}
22	4790.1526	0.24983	5.4818×10^{10}	1.652×10^{-4}
⋮				
∞	4794.2941			

Table 9. Present RCI Spectroscopic Parameters: E_n, δ_n, A_{fi}^{E1} and gf_{ij} for the $1s2s^22p^6$ ($^2S_{1/2}$) np ($^1P_1$) series in Ti^{12+} ion.

n	E_n (eV)	δ_n	A_{fi}^{E1} (s^{-1})	gf_{ij}
3	5013.9358	0.25002	3.4800×10^{13}	9.571×10^{-2}
4	5155.5039	0.23817	1.3474×10^{13}	3.505×10^{-2}
5	5216.7516	0.23420	6.6055×10^{12}	1.678×10^{-2}
6	5248.8680	0.23230	3.7449×10^{12}	9.398×10^{-3}
7	5267.8036	0.23106	2.3161×10^{12}	5.770×10^{-3}

n	E_n (eV)	δ_n	A_{fi}^{E1} (s^{-1})	gf_{ij}
8	5279.8982	0.23036	1.5313×10^{12}	3.798×10^{-3}
9	5288.0921	0.22999	1.0647×10^{12}	2.632×10^{-3}
10	5293.8994	0.22987	7.7015×10^{11}	1.900×10^{-3}
11	5298.1646	0.22995	5.7489×10^{11}	1.416×10^{-3}
12	5301.3892	0.23020	4.4050×10^{11}	1.084×10^{-3}
13	5303.8863	0.23054	3.4495×10^{11}	8.478×10^{-4}
14	5305.8594	0.23096	2.7514×10^{11}	6.757×10^{-4}
15	5307.4454	0.23151	2.2298×10^{11}	5.473×10^{-4}
16	5308.7395	0.23206	1.8320×10^{11}	4.494×10^{-4}
17	5309.8091	0.23266	1.5235×10^{11}	3.736×10^{-4}
18	5310.7034	0.23318	1.2806×10^{11}	3.139×10^{-4}
19	5311.4586	0.23377	1.0868×10^{11}	2.663×10^{-4}
20	5312.1022	0.23431	9.3018×10^{10}	2.279×10^{-4}
21	5312.6551	0.23489	8.0228×10^{10}	1.965×10^{-4}
22	5313.1336	0.23547	6.9679×10^{10}	1.707×10^{-4}
⋮				
∞	5317.9877			

Table 10. Present RCI Spectroscopic Parameters: E_n, δ_n, A_{fi}^{E1} and gf_{ij} for the $1s2s^22p^6$ ($^2S_{1/2}$) np ($^1P_1$) series in V^{13+} ion

n	E_n (eV)	δ_n	A_{fi}^{E1} (s^{-1})	gf_{ij}
3	5520.5112	0.23673	4.3008×10^{13}	9.757×10^{-2}
4	5682.5795	0.22547	1.6709×10^{13}	3.577×10^{-2}
5	5752.9610	0.22166	8.2062×10^{12}	1.714×10^{-2}
6	5789.9367	0.2199	4.6630×10^{12}	9.617×10^{-3}
7	5811.7652	0.21874	2.8860×10^{12}	5.907×10^{-3}
8	5825.7200	0.21808	1.9092×10^{12}	3.889×10^{-3}
9	5835.1804	0.21773	1.3282×10^{12}	2.697×10^{-3}
10	5841.8886	0.21763	9.6104×10^{11}	1.947×10^{-3}
11	5846.8176	0.2177	7.1759×10^{11}	1.451×10^{-3}
12	5850.5453	0.21791	5.4996×10^{11}	1.111×10^{-3}
13	5853.4327	0.21823	4.3076×10^{11}	8.692×10^{-4}
14	5855.7148	0.21858	3.4366×10^{11}	6.929×10^{-4}
15	5857.5496	0.21901	2.7854×10^{11}	5.613×10^{-4}
16	5859.0468	0.21953	2.2888×10^{11}	4.610×10^{-4}
17	5860.2846	0.21997	1.9037×10^{11}	3.832×10^{-4}
18	5861.3195	0.22048	1.6004×10^{11}	3.221×10^{-4}
19	5862.1936	0.22098	1.3583×10^{11}	2.733×10^{-4}
20	5862.9386	0.22143	1.1626×10^{11}	2.338×10^{-4}
21	5863.5787	0.22187	1.0029×10^{11}	2.017×10^{-4}
22	5864.1326	0.22249	8.7106×10^{10}	1.751×10^{-4}
⋮				
∞	5869.7555			

Table 11. Present RCI Spectroscopic Parameters: E_n, δ_n, A_{fi}^{E1} and gf_{ij} for the $1s2s^22p^6$ ($^2S_{1/2}$) np ($^1P_1$) series in Cr^{14+} ion.

n	E_n (eV)	δ_n	A_{fi}^{E1} (s^{-1})	gf_{ij}
3	6052.1823	0.22485	5.2439×10^{13}	9.898×10^{-2}
4	6236.0900	0.21414	2.0435×10^{13}	3.633×10^{-2}
5	6316.2251	0.21051	1.0051×10^{13}	1.742×10^{-2}
6	6358.3963	0.20888	5.7238×10^{12}	9.788×10^{-3}
7	6383.3321	0.20721	3.5450×10^{12}	6.015×10^{-3}
8	6399.2671	0.20718	2.3464×10^{12}	3.961×10^{-3}
9	6410.0840	0.20687	1.6329×10^{12}	2.748×10^{-3}
10	6417.7575	0.20679	1.1819×10^{12}	1.984×10^{-3}
11	6423.3979	0.20686	8.8278×10^{11}	1.479×10^{-3}
12	6427.6648	0.20707	6.7668×10^{11}	1.132×10^{-3}
13	6430.9708	0.20733	5.3010×10^{11}	8.862×10^{-4}
14	6433.5841	0.20769	4.2298×10^{11}	7.065×10^{-4}
15	6435.6856	0.20810	3.4291×10^{11}	5.724×10^{-4}
16	6437.4008	0.20851	2.8181×10^{11}	4.702×10^{-4}
17	6438.8188	0.20900	2.3440×10^{11}	3.909×10^{-4}
18	6440.0047	0.20938	1.9708×10^{11}	3.285×10^{-4}
19	6441.0063	0.20988	1.6727×10^{11}	2.788×10^{-4}
20	6441.8601	0.21027	1.4319×10^{11}	2.386×10^{-4}
21	6442.5937	0.21070	1.2352×10^{11}	2.057×10^{-4}
22	6443.2287	0.21108	1.0729×10^{11}	1.787×10^{-4}
⋮				
∞	6449.6768			

To the best of our knowledge, no experimental and/or theoretical data exists for the K-shell excitations of the studied ions. Consequently, the results presented here may provide a valuable benchmark for future studies. In the absence of benchmark data, estimating the uncertainty for these 1s excitations is challenging. We therefore base our uncertainty estimate of approximately ± 2.0 eV on our recent work for neutral neon [14], where the electronic configuration is the same.

4. CONCLUSIONS

The 1s → np and 2s → np resonances for several members of the neon isoelectronic sequence have been investigated using the RCI approach within the FAC code. The RCI calculations show good agreement with available theoretical data, confirming the accuracy and reliability of the present results. This study has reported new data for K-shell transitions to the 1s $2s^2$ $2p^6$ ($^2S_{1/2}$) np ($^1P_1$) excited states in all studied ions, thereby addressing a longstanding gap in the atomic data. The present results constitute important data for advancing spectral modeling of high-resolution X-ray emissions in both astrophysical and laboratory plasmas.

ORCID

O. Abu-Haija, https://orcid.org/0009-0005-4702-8080; **G.A. Alna'washi,** https://orcid.org/0000-0003-2860-7552;
S.M. Hamasha, https://orcid.org/0000-0001-5472-7801; **M.T. Gning,** https://orcid.org/0000-0003-3456-2717;
I. Sakho, https://orcid.org/0000-0003-2983-1396; **M.M. Al Shorman,** https://orcid.org/0009-0005-7760-7681

REFERENCES

[1] H.E. Mason, and B.C. Monsignori-Fossi, Astron. Astrophys. Rev. **6**, 123 (1994). https://doi.org/10.1007/bf01208253
[2] H.P. Summers, Adv. Atom. Mol. Opt. Phys. **33**, 275 (1994). https://doi.org/10.1016/S1049-250X(08)60039-7
[3] P. Beiersdorfor, M.H. Chen, R.E. Marrs, and M.A. Levine, Phys. Rev. A, **41**, 3453 (1990). https://doi.org/10.1103/physreva.41.3453
[4] D.D. Dietrich, A. Simionovici, M.H. Chen, G. Chandler, C.J. Hailey, P.O. Egan, P.H. Mokler, *et al.*, Phys. Rev. A, **41**, 1450 (1990). https://doi.org/10.1103/PhysRevA.41.1450
[5] J. Nilsen, J. Quant. Spectrosc. Radiat. Transf. **47**, 171 (1992). https://doi.org/10.1016/0022-4073(92)90026-Z
[6] J.A. Santana, J.K. Lepson, E. Trabert, and P.Beiersdorfer, Phys. Rev. A, **91**, 012502 (2015). https://doi.org/10.1103/PhysRevA.91.012502
[7] M.C. Simon, M. Schwarz, S.W. Epp, C. Beilmann, B.L. Schmitt, Z. Harman, T.M. Baumann, *et al.*, J. Phys. B: At. Mol. Opt. Phys. **43**, 065003 (2010). https://doi.org/10.1088/0953-4075/43/6/065003
[8] K. Schulz, M. Domke, R. Püttner, A. Gutiérrez, G. Kaindl, G. Miecznik, and C.H. Greene, Phys. Rev. A, **54**, 3095 (1996). https://doi.org/10.1103/PhysRevA.54.3095
[9] L.C. Gao, D.H. Zhang, L.Y. Xie, J.G. Wang, Y.L. Shi, and C.Z. Dong, J. Phys. B, **46**, 175402 (2013). https://doi.org/10.1088/0953-4075/46/17/175402
[10] I. Sakho, J. Electron Spectrosc. & Relat. Phenom. **222**, 40 (2018). https://doi.org/10.1016/j.elspec.2017.09.011
[11] A. Goyal, I. Khatri, M. Sow, I. Sakho, S. Aggarwal, A.K. Singh, and M. Mohan, Rad. Phys. Chem. **125**, 50 (2016). https://doi.org/10.1016/j.radphyschem.2016.03.017
[12] L. Liang, W.-J. Gao., and C. Zhou, Phys. Scr. **87**, 015301 (2013). https://doi.org/10.1088/0031-8949/87/01/015301
[13] M. Nrisimhamurty, G. Aravind, P.C. Deshmukh, and S.T. Manson, Phys. Rev. A, **91**, 13404 (2015). https://doi.org/10.1103/PhysRevA.91.013404
[14] G. A. Alna'washi, S.M. Hamasha, and O. Abu-Haija, Chem. Phys. Impact, **11**, 100926 (2025). https://doi.org/10.1016/j.chphi.2025.100926
[15] G. A. Alna'washi, O. Abu-Haija, and S.M. Hamasha, Phys. Open, **25**, 100317 (2025). https://doi.org/10.2139/ssrn.5744890
[16] G. A. Alna'washi, O. Abu-Haija, and S.M. Hamasha, J. Electron Spectrosc. & Relat. Phenom. **283**, 147574 (2025). https://doi.org/10.1016/j.elspec.2025.147574.
[17] M.F. Gu, Can. J. Phys. **86**, 675 (2008). https://doi.org/10.1139/p07-197
[18] A. Goyal, R. Sharma, A. Singh, and M. Mohan, Can. J. Phys. **95**, 10 (2017). https://doi.org/10.1139/cjp-2016-0812
[19] M.J. Seaton, Rep. Prog. Phys. **46**, 167 (1983). https://doi.org/10.1088/0034-4885/46/2/002
[20] A.E. Kramida, Yu. Ralchenko, and J. Reader, "NIST Atomic Spectra Database, version 5.2, (NIST ASD Team, 2024). https://www.nist.gov/pml/atomic-spectra-database

ДАНІ ФОТОНІЗАЦІЇ РЕЛЯТИВІСТСЬКОЇ КОНФІГУРАЦІЙНОЇ ВЗАЄМОДІЇ ДЛЯ Ne-ПОДІБНОЇ ІЗОЕЛЕКТРОННОЇ ПОСЛІДОВНОСТІ

О. Абу-Хайджа[1], Г.А. Ална'ваші[2], С.М. Хамаша[2], М.Т. Гнінг[3,4], І. Сахо[3,4], М. Аль Шорман[1]
[1]Кафедра прикладної фізики, Технічний університет Тафіли, а/с 179, Тафіла 66110, Йорданія
[2]Кафедра фізики, Факультет природничих наук, Хашимітський університет, а/с 330127, Зарка 13133, Йорданія
[3]Кафедра фізики та хімії, Університет УФР, Університет Іба Дер Тіам, Тієс, Сенегал
[4]Африканський центр прикладних атомних та ядерних технологій (CAFTANA), Дакар, Сенегал

Наведено дані фотоіонізації для основного стану $1s^2$ $2s^2$ $2p^6$ ($^1S_0$) неону, такого як іони Ca^{10+}, Sc^{11+}, Ti^{12+}, V^{13+} та Cr^{14+}. Значення порогових меж іонізації, резонансних енергій, квантових дефектів, швидкостей переходів та сил осциляторів для різних серій Ридберга наведено в таблиці. Для всіх розрахунків було використано підхід релятивістської конфігураційної взаємодії (RCI), реалізований у Гнучкому атомному коді (FAC). Результати RCI для резонансних серій 2s $2p^6$ ($^2S_{1/2}$) np демонструють дуже добру відповідність зі значеннями, наведеними в літературі. Крім того, повідомляється про нові розрахунки фотозбудження K-оболонки (1s $2s^2$ $2p^6$ ($^2S_{1/2}$) np) у цих іонах. Ці результати будуть цінними для високоточного спектрального моделювання в астрофізичній або лабораторній плазмі.

Ключові слова: *фотозбудження; резонансна енергія; серії Ридберга; релятивістська конфігураційна взаємодія*

EAST EUROPEAN JOURNAL OF PHYSICS. 1. 156-160 (2026)
DOI:10.26565/2312-4334-2026-1-14 ISSN 2312-4334

PHOTOMETRIC OBSERVATIONS OF SYMBIOTIC STAR AG PEG

Kh.M. Mikailov[1], R.T. Mammadov[2,3]*, A.B. Rustamova[4], L.R. Mammadova[5]
[1]*Baku State University, Baku, AZ-1148, Azerbaijan*
[2]*Nakhchivan State University, Nakhchivan, AZ-7012, Azerbaijan*
[3]*Batabat Astrophysics Observatory under Nakhchivan State University, Nakhchivan, AZ-7000, Azerbaijan*
[4]*Tusi Shamakhy Astrophysical Observatory of Science and Education Ministry, Baku, AZ-1148, Azerbaijan*
[5]*Nakhchivan State Technical College under Nakhchivan State University, Nakhchivan, AZ-7000, Azerbaijan*
**Corresponding Author e-mail: ruslan_rtm@yaho.com*
Received January 04, 2026; revised January 20, 2026; accepted February 5, 2026

In the article, using the AAVSO (American Association of Variable Star Observers) photometric database of the AG Pegasi symbiotic star, a light curve was constructed in the Vis filter for a period of 68 (1954-2022) years. During this period, the brightness of the Ag Peg star changed by approximately 2 magnitudes, reaching from 7.5^m to 9.5^m. Using the Scargle method, the possible periodicities in the light curve were investigated by applying statistical spectral Fourier analysis. Two $P=17857^d$ long and $P=815^d$ short periodic variations were detected in the light curve.
Keywords: *Symbiotic star; AG Peg; Photometric variable; Light curve; Photometry; Period; Observation*
PACS: 97.80.−d; 97.80 Fk; 97.80. Gm; 97.80.hn

1. INTRODUCTION

Symbiotic stars are interacting binary systems surrounded by cover. They consist of an advanced Red Giant and a hot component – White Dwarf. The material source of the cloud is Red Giant, which loses its substance by stellar wind and pulsation, and the energy source is the hot White Dwarf. Red Giants are stars that have reached the necessary temperature for helium fusion in their cores. White Dwarfs, on the other hand, are stars nearing the end of their life cycle and are highly compressed. These stars are so dense that, despite having nearly the same mass as the Sun, their size is comparable to that of Earth. [1, 2, 3, 4].

AG Pegasi (HD 207757, BD +11°4673) is a symbiotic star which is situated in the constellation Pegasus. This star is a dense binary system consisting of a red giant and a white dwarf [5]. The entire system is surrounded by a gas-dust nebula. The orbital period of the star is assumed to be ~818 days [1, 6]. The mass of the red giant: $M_g=2.6M_\odot$, the mass of the white dwarf: $M_d=0.6M_\odot$, the ratio of the masses of the components Mg/Md = 4.33. Kenyon et al. (1993) estimated a distance of 800 pc to AG Peg from the calibration of absolute bolometric magnitudes, assuming the M3 giant has a luminosity class III [7]. In 1967-1972, work was published by Boyarchuk et al. and by Hutchings et al. The spectroscopic studies have been interpreted as corresponding to a binary whose components can be approximated as an WN 6 and an M3 III, with a period of around 800 days [8, 9].

AG Peg belongs to the symbiotic new group. Currently, only 8 nova-like symbiotic stars are known. When stars ignite, the representatives of this class reach very high brightness and remain in this state for tens, sometimes hundreds of years. The strong shock waves that occur during ignition heat the surrounding plasma to 10^6 K and serve as a source of emission lines at various degrees of ionization [10]. In the spectrum of the star, coronal lines such as FeX, FeXI, [NiXV] are observed as well as [NII], [OII], and lines with low excitation potential, such as the Balmer series of hydrogen. AG Peg can confidently be an example of "symbiotic new".

Symbiotic stars can show ‘classical’ outbursts lasting weeks to years where they brighten by ∼1–3 mag [11, 12]. AG Peg has been studying since the middle of the 19th century. The fact that the AG Peg symbiotic star is bright enough ($V \approx 8.5^m$) allowed it to be well studied both photometrically and spectrally. Allen, who analyzed the light curve starting in the 1850s, called the AG Peg star a symbiotic nova. Burning in the star began in 1850. Then its star size increased from 9^m to 6^m. It reached its maximum luminosity of ~ 6^m in about 1885. Later, the gradual decrease in the star's brightness, to the level observed before ignition, continued for about 130 years [13]. Second-best, AG Peg continued to weaken until 2000 and showed variations in the V filter in the stellar size interval $8.5^m \div 9.0^m$ by June 2015. Along with other spectrophotometric parameters, this evolution of the light curve (LC-light curve) is characteristic of the slowest nova ever recorded [10, 11].

Despite the well-studied AG Peg symbiotic star, the daily acquisition of new observational data and new approaches allows for obtaining more reliable results about the star, as well as refining previously obtained values of the star's parameters.

The main purpose of our work is to investigate the periodic changes in the light curve of the symbiotic star AG Peg. For this, using the AAVSO photometric database, the light curve of the AG Peg symbiotic star was constructed in

Cite as: Kh.M. Mikailov, R.T. Mammadov, A.B. Rustamova, L. R. Mammadova, East Eur. J. Phys. 1, 156 (2026), https://doi.org/10.26565/2312-4334-2026-1-14

the Vis filter over 68 years, and possible periodic variations in luminosity were investigated using Fourier analysis. Photometric observations of the AG Peg symbiotic star were taken from the AAVSO (American Association of Variable Star Observers) database [14].

2. RESEARCH METHOD

We constructed a light curve in the Vis filter for a period of 68 years based on the AAVSO database of the AG Peg nova-like symbiotic star (Figure 1) [14].

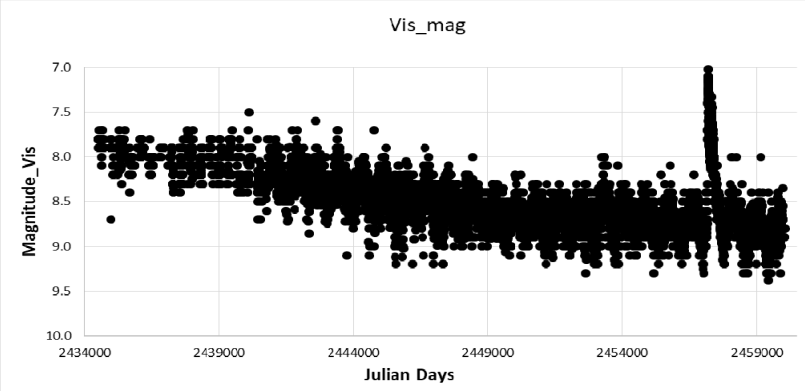

Figure 1. The light curve of the symbiotic star AG Peg for the period 1954-2022.
Each point in the figure is the average value of measurements for one day

As can be seen from the picture, the brightness of the star was 8^m stars in the years 1954-1970. After 1970, the star's brightness gradually decreased. The star AG Peg had one strong flare in 2015 (between 2457050 and 2457400 Julian date). At this time, the magnitude of the star increased from 8.7^m to 6.9^m. That is, it has changed by 1.8^m stars. In the rest of the time, as can be seen from the light curve of the star, small modulations, i.e., changes, happened in the star in the interval of 1^m star size. Currently, the magnitude of the star is 8.5^m.

We have divided the light curve in Figure 1 into two parts to better illustrate the periodic variations in the symbiotic star AG Peg. The first part covers the period 1954-1990, and the second part covers the period 1990-2022 (Figure 2) [14]. From Figure 2, certain periodic changes are visible in the light curve.

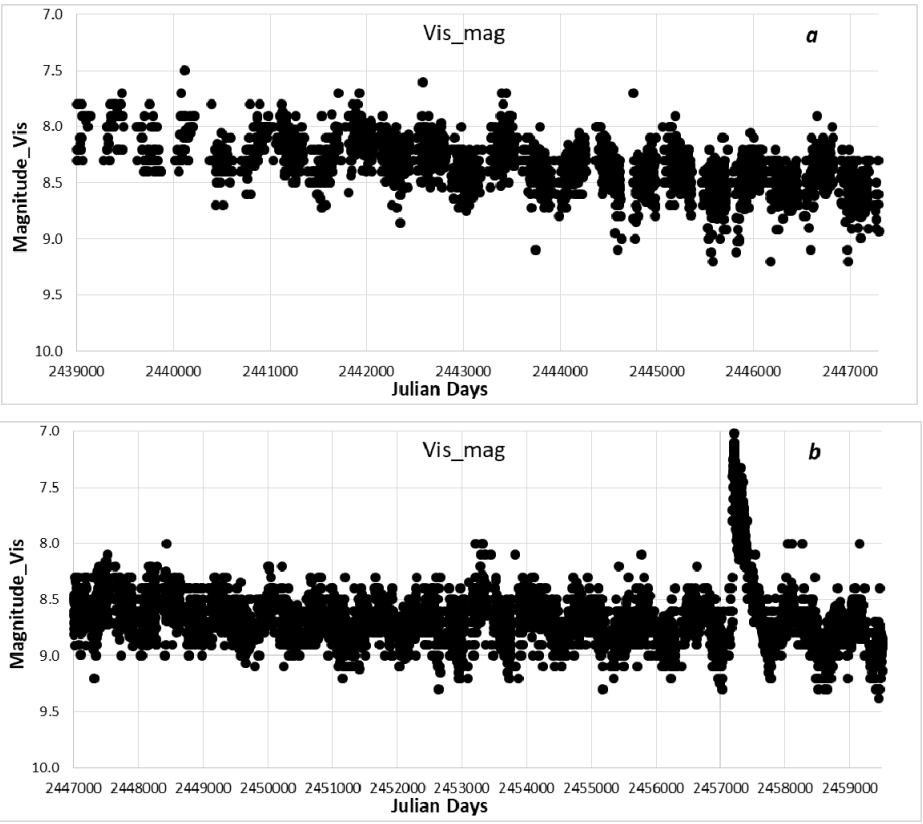

Figure 2. Age of the symbiotic star AG Peg 1954-2022 based on AAVSO datalight curve for the period
a) 1954-1990; b) 1990-2022

In figure 3, we have plotted the light curve for the JD 2440000-JD 2460000 interval. The time interval is taken as 10 days. On the flipside, each point is the average value of 10 days of measurements [15]. As can be seen from the picture, in this case, period-periodic changes in the brightness of the star are better seen.

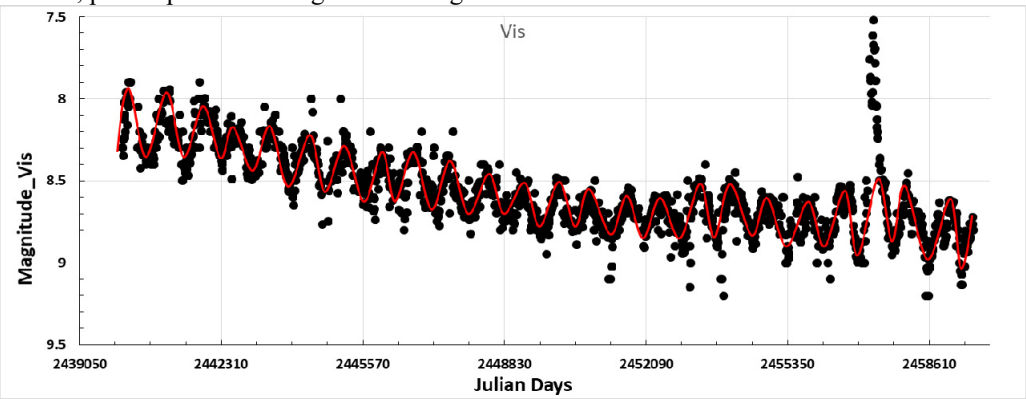

Figure 3. The light curve of the star AG Peg for 1968-2022 (JD 2440000-2459000).
Each point in the figure is the average value of 10 days of measurements.

As you can see from the figure, periodic changes are thorough seen during quiet periods. The wrinkled curve shown in red corresponds to a period of about 815 days. This curve fits very well on the points.

Fourier analysis was performed using Scargle software to find the period [16]. Classic Scargle can only work on Norton. We used the version developed by Kh. Mikailov and H. Mikailov for Windows [15]. The sequence of finding the period is as follows: 1. We add the file about the size of the star depending on time to the program. 2. Click the calculate button. 3. We enter the maximum frequency and step. 4. We consider the trend.

Figure 4 shows the power spectrum for the period 1994-2005.

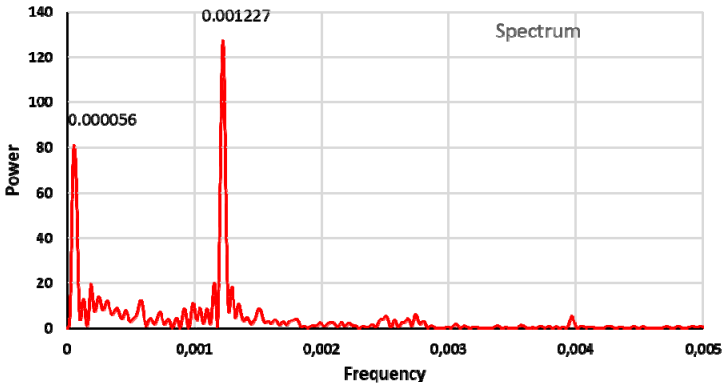

Figure 4. Power spectrum for the selected interval JD 2449400-JD2453400 (1994-2005).

As it is shown in the figure, there are two maxima in the power spectrum: **0.000056** and **0.001227**. Knowing that the period is inversely proportional to the frequency, we get the subsequent values of the period: **1.** Short period P=814.99 days, **2.** Long period P=17857.148 days. As you can see, mainly 2 periods are taken.

A phase diagram for the light curve of the symbiotic star AG Peg in the selected interval (1968-2012, and for the Julian date range 2440014÷2455953, i.e. for a period of 44 years) was constructed (Figure 5).

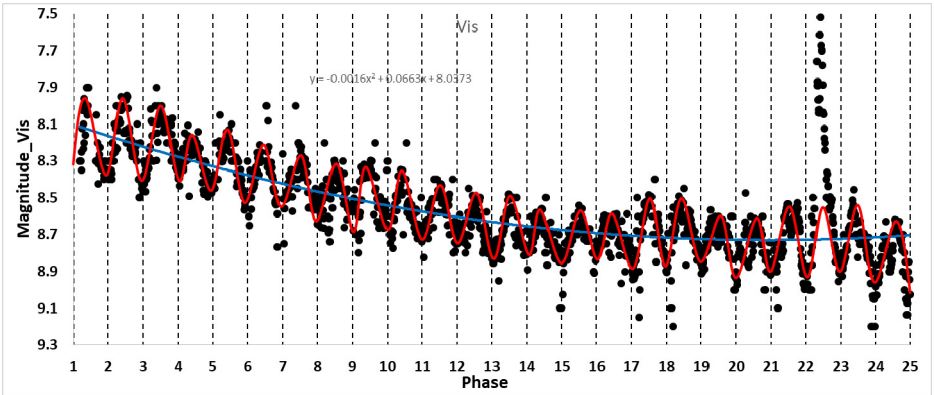

Figure 5. Phase diagram for the 44-year period 1968-2012.
The phase diagram spans 25 full cycles. Each period is 814.99 days.

We have drawn the trend curve for the selected time interval. The function of the curve:

$$y=-0.0016x^2+0.0663x+8.0373$$

Using this function, the deviation value of the Vis star size from the mean (O-C, Observed-Calculated) for each time was calculated. On the flipside, the value in the trend curve for that time was subtracted from each value of the star size of the AG Peg (figure 6).

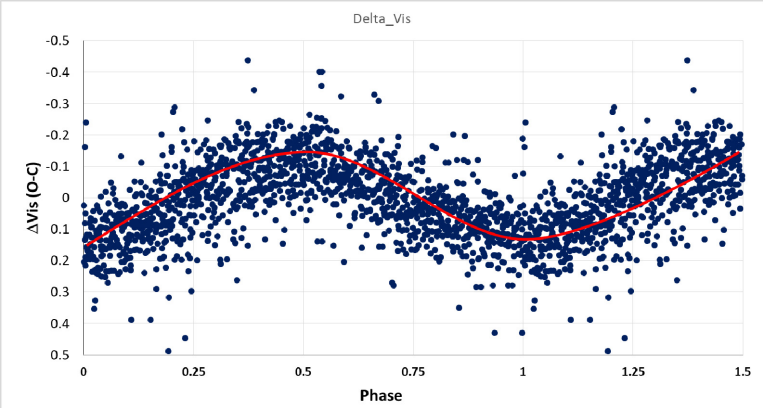

Figure 6. Total phase diagram of the Vis star size of the simbiotic star AG Peg

As shown in the figure, the points for the 44-year period fit the phase diagram very well. Thus, we assume that the Vis stellar magnitude of the AG Peg simbiotic star varies with a period of P = 814.99^d. Epoch start T_0 = 2439050. The minimum phase is calculated as: Min = JD2439050 + 814.99E.

3. CONCLUSIONS

A light curve of the symbiotic star AG Peg has been constructed for a period of 68 years (1954-2022). The long-term light curve of AG Peg shows two types of optical variability. One of them is a large-amplitude change, and the second is regular periodic modulations. Modulations with small amplitude are better seen in the interval 1968-2012. Using Fourier analysis, the problem of finding periods in the light curve of a star was considered. 2 periodic changes were found in the light curve: 1. P=17857.148 days for a long period. 2. For a short period, P=814.99 days.

It is believed that the short period is related to the binary system's orbital motion. That is, it is connected to the orbital motion of this system around the common center of mass of the red giant and the white dwarf. The long period can be revealed by the accretion (i.e., collection) of material lost by the red giant through its stellar wind onto the white dwarf.

Acknowledgements

We acknowledge with thanks the variable star observations from the **AAVSO** (American Association of Variable Star Observers) International Database contributed by observers worldwide and used in this research.

ORCID

Khidir Mikailov, https://orcid.org/0000-0003-1277-7370; **Ruslan Mammadov,** https://orcid.org/0000-0001-5879-1368
Aysel Rustamova, https://orcid.org/0009-0003-9043-985X; **Leylan Mammadova** https://orcid.org/0009-0003-8859-6274

REFERENCES

[1] A. Skopal, S. Shugarov, M. Vanko, et al., "Recent photometry of symbiotic stars", Astronomische Nachrichten, **333**, 242-255. (2012). https://doi.org/10.1002/asna.201111655

[2] Kh. M. Mikailov, R. T. Mammadov. "Photometric flickering of the CH Cyg in 2018", East European Journal of Physics, **2**, 38-42, (2025). https://periodicals.karazin.ua/eejp/article/view%20/25766/23443

[3] Kh. M. Mikailov, A.J. Orujova, R.T. Mammadov, I.A. Alakbarov, and O.V. Khalilov, "Analysis of spectral and photometric observations of the CH Cyg symbiotic star in 2018," Astronomical Journal of Azerbaijan, **16**(1) 4-21 (2021). https://aaj.shao.az/vol16_n1/AAJ_2021_V16_N1.pdf

[4] Kh. M. Mikailov, and R.T. Mammadov, "95-day variability in the light curve of the symbiotic star CH Cyg," in: *Proceedings of the XXI International Multidisciplinary Conference "Prospects and Key Tendencies of Science in Contemporary World*," (Bubok Publishing S.L., Madrid, 2022), pp. 67-71. https://www.internauka.org/conf/spain/21/343943

[5] W. P. Fleming, "Stars having peculiar spectra", The Observatory, **56**(6), 165-226 (1912). https://adsabs.harvard.edu/full/1912AnHar..56..165F

[6] G. Ramsay, J. L. Sokoloski, G. J. M. Luna, et al. and N.E.Nunez, "Swift observations of the 2015 outburst of AG Peg – from slow nova to classical symbiotic outburst", Monthly Notices of the Royal Astronomical Society, **461**(4), 3599-3606 (2016). https://doi.org/10.1093/mnras/stw1546

[7] S. J. Kenyon, J. Mikolajewska, M. Mikolajewski, R. S. Polidan, & M. H. Slovak, "Evolution of the symbiotic binary system AG Pegasi - The slowest classical nova eruption ever recorded", Astronomical Journal, **106**(4), 1573-1598 (1993).https://articles.adsabs.harvard.edu/full/1993AJ....106.1573K

[8] A. A. Boyarchuk, "The Nature of AG Pegasi", Soviet Astronomy, **11,** 8-15 (1967). https://adsabs.harvard.edu/full/1967SvA....11....8B
[9] D. L. Hutchings and R. O. Redman, "The spectrum of the symbıotıc star AG Pegası 1970-71", Pub. Astron. Soc. Pacific, **84,** 240-247 (1972). https://adsabs.harvard.edu/full/1972PASP...84..240H
[10] S. A. Zhekov & T.V. Tomov, "An XMM–Newton observation of the symbiotic star AG Peg: the X-ray emission after the end of its 2015 outburst" Monthly Notices of the Royal Astronomical Society, **481**(4). 5156-5162 (2018). https://doi.org/10.1093/mnras/sty2644
[11] Kh.M. Mikailov, R.T. Mammadov, B.N. Rustamov, and A.B. Rustamova, "Spectral Variability of the Symbiotic Star CH Cyg". Proceedings of the Pakistan Academy of Sciences: Part A: PS-671, **60**(1), 9-13 (2023). https://doi.org/10.53560/PPASA(60-1)671
[12] Kh. M. Mikailov, R.T. Mammadov, I. A. Alakbarov and O. V. Khalilov, "High velocity absorption in the spectra of CH Cyg in 2017", Astronomıcal Journal of Azerbaıjan, **15**(2), 82-90 (2020). https://aaj.shao.az/vol15_n2/AAJ_2020_V15_N2.pdf
[13] T. V. Tomov, K. A. Stoyanov and R. K. Zamanov, "AG Pegasi – now a classical symbiotic star in outburst?", Monthly Notices of the Royal Astronomical Society, **462**(4), 4435-4441 (2016). https://doi.org/10.1093/mnras/stw2012
[14] The American Association of Variable Star Observers (AAVSO), 185 Alewife Brook Parkway, Suite 410, Cambridge, MA 02138, USA, https://www.aavso.org/LCGv2/
[15] Kh. M. Mikailov, R.T. Mammadov and I.A. Alakbarov, "750-Days Variability of the CH Cyg," Astronomıcal Journal of Azerbaıjan, **16**(2) 37-43 (2021). https://aaj.shao.az/vol16_n2/AAJ_2021_V16_N2.pdf#page=36
[16] J. D. Scargle, "Studies in astronomical time series analysis. Fourier transforms. Autocorrelation function and cross-correlation functions of unevenly spaced data", The Astrophysical Journal, **343**, 874-887 (1989). https://articles.adsabs.harvard.edu/pdf/1989ApJ...343..874S

ФОТОМЕТРИЧНІ СПОСТЕРЕЖЕННЯ СИМБІОТИЧНОЇ ЗІРКИ AG PEG

Х.М. Мікайлов[1], Р.Т. Мамедов[2,3], А.Б. Рустамова[4], Л.Р. Мамедова[5]
[1]*Бакинський Державний Університет, Баку, AZ-1148, Азербайджан*
[2]*Нахічеванський Державний Університет, Нахічевань, AZ-7012, Азербайджан*
[3]*Батабатська Астрофізична Обсерваторія при Нахічеванському Державному Університеті, Нахічевань, AZ-7000, Азербайджан*
[4]*Шамахинська Астрофізична Обсерваторія імені Тусі, Міністерство Науки та Освіти, Баку, AZ-1148, Азербайджан*
[5]*Нахічеванський Державний Технічний Коледж при Нахічеванському Державному Університеті, Нахічевань, AZ-7000, Азербайджан*

У статті, використовуючи фотометричну базу даних AAVSO (Американської асоціації спостерігачів змінних зірок) симбіотичної зірки AG Pegasi, у фільтрі Vis було побудовано криву блиску за період 68 (1954-2022) років. Протягом цього періоду яскравість зірки Ag Peg змінилася приблизно на 2 зоряні величини, досягнувши від 7.5^m до 9.5^m. За допомогою методу Скаргла було досліджено можливі значення періодичних змін кривої блиску шляхом застосування статистичного спектрального Фур'є-аналізу. На кривій блиску було виявлено дві періодичні варіації тривалістю P=17857 днів та короткочасну варіацію P=815 днів.

Ключові слова: *симбіотична зірка; AG Peg; фотометрична змінна; крива блиску; фотометрія; період; спостереження*